

first 2nd last PPT

MSB microphone switch matrix (MSH)

81080 2 CH

SV 8
MMIC direct sync PPT

MSB
MSB keyboard keyboard journal entry
for MSB

2

COMSAT

Technical Review

Volume 4 Number 2, Fall 1974

COMSAT TECHNICAL REVIEW

Volume 4 Number 2, Fall 1974

Advisory Board Joseph V. Charyk
William W. Hagerty
John V. Harrington
Sidney Metzger

Editorial Board Pier L. Bargellini, Chairman
Robert D. Briskman
S. Browne
S. J. Campanella
William L. Cook
Denis J. Curtin
Joachim Kaiser
R. W. Kreutel
H. J. Meyerhoff
Akos G. Revesz

Editorial Staff Larry G. Hastings
MANAGING EDITOR
Leonard F. Smith
TECHNICAL EDITOR
Edgar Bolen
PRODUCTION

The COMSAT TECHNICAL REVIEW is published twice a year by the Communications Satellite Corporation (COMSAT). Subscriptions including postage, \$5.00 U.S. per year; single copies, \$3.00 U.S. Bulk rates are available upon request. Remittances for subscriptions should be made payable to the Treasurer, COMSAT, and addressed to COMSAT TECHNICAL REVIEW, Room 5273, 950 L'Enfant Plaza, S. W., Washington, D.C. 20024, U.S.A.

- 205 AN UNATTENDED EARTH TERMINAL FOR SATELLITE COMMUNICATIONS **L. Pollack** AND **W. Sones**
- 231 THE UNATTENDED EARTH TERMINAL MULTIPLE-BEAM TORUS ANTENNA **G. Hyde**, **R. Kreutel** AND **L. Smith**
- 263 STRUCTURAL ANALYSIS OF THE UNATTENDED EARTH TERMINAL ANTENNA **A. Abu-Taha**
- 283 HIGH-PERFORMANCE CORRUGATED FEED HORN FOR THE UNATTENDED EARTH TERMINAL **R. Price**
- 303 DESIGN CONSIDERATIONS FOR THE UNATTENDED EARTH TERMINAL WIDEBAND FM MODEM **M. Grossman**
- 319 THE BUTLER MATRIX TRANSPONDER **W. Sandrin**
- 347 AN EXPERIMENTAL INVESTIGATION OF 8-PHASE CPSK SIGNAL TRANSMISSION IN BAND-LIMITED SATELLITE CHANNELS **D. Chakraborty** AND **G. Robertson**
- 371 RESULTS AND ANALYSIS OF THE SPEECH PREDICTIVE ENCODING COMMUNICATIONS SYSTEM FIELD TRIAL
H. Suyderhoud, **J. Jankowski** AND **R. Ridings**
- 393 QUANTIZATION NOISE AND DISTORTION POWER SPECTRA OF PCM SYSTEMS **J. Su** AND **S. Campanella**
- 413 ANTENNA DESIGN STUDIES FOR A U.S. DOMESTIC SATELLITE **R. Gruner** AND **W. English**
- 449 PRESCREENING TECHNIQUES FOR FLIGHT GERMANIUM TUNNEL DIODES **P. Fleming**
- 461 IONOSPHERIC SCINTILLATION AT FREQUENCIES ABOVE 1 GHz **R. Taur**
- 477 THE INTELSAT GLOBAL SATELLITE COMMUNICATIONS SYSTEM **S. Browne**
- 489 CTR NOTES:
CHEMISTRY OF THE OXIDE CATHODE REVISITED
E. Rittner 489

A NULL TECHNIQUE FOR ACCURATELY DETERMINING THE
DRIVE LEVEL REQUIRED TO SATURATE A TWT

A. Standing 493

BLOCKING BUBBLES IN THE INTELSAT IV FUEL LINES

G. Gordon, G. Huson AND V. Slabinski 499

507 TRANSLATIONS OF ABSTRACTS

FRENCH 507

SPANISH 514

**Index: unattended earth terminals, multiple-beam
antennas, communications satellites.**

An unattended earth terminal for satellite communications

L. POLLACK AND W. SONES

(Manuscript received May 24, 1974)

Abstract

Changing system constraints and developments in microwave technology have led to a new satellite communications earth terminal designed for unattended operation. Synchronous orbit satellite stationkeeping tolerances of less than $\pm 0.5^\circ$, grouping of satellites in 10° to 20° of orbital arc to serve earth terminal communities, and the need to operate with two or more satellites and ensure service continuity have been the major factors leading to the unattended earth terminal (UET) concept.

The fixed reflector multiple-beam torus antenna (MBTA), which is an integral part of the UET, uses steerable feeds coupled to several filter-multiplexed, low-power, air-cooled transmitters and a broadband and uncooled low-noise receiver. All-solid-state frequency conversion, IF amplification, and modulation equipment are incorporated into microwave integrated circuits. With appropriate quality assurance during implementation, this design is extremely reliable.

This paper describes the rationale that determined the major features of the overall design and the performance of the terminal.

Introduction

Communications satellite earth terminal characteristics have evolved over the past decade from the requirements imposed by the early medium-altitude or nearly geosynchronous earth-orbiting satellites. To track

these satellites, earth terminal antennas had to provide full hemispheric tracking and communications capabilities. With the establishment of geosynchronous satellites and orbital positions maintained within $\pm 0.5^\circ$, the earth terminal antenna requirements have changed. Satellites are now grouped along 10° to 20° of the synchronous orbit arc to serve many earth terminals located around the oceans or within major land regions. Thus, hemispheric tracking is no longer required, and only limited steering is needed for narrow-beam antennas.

As communications satellite use has expanded, earth terminal operation has had to be extended to two or more satellites in each orbit community to meet the traffic demand and also to ensure service reliability. Communications satellite traffic is expected to increase substantially during the next decade. Although individual satellite communications capacity will also increase, the use of multiple satellites and multibeam earth terminals will undoubtedly continue.

With the number of earth terminals increasing, greater operating economy can be achieved with terminals left unattended for long periods of time. However, to maintain the high overall service continuity now achieved with manned terminals, the reliability of all the earth terminal components must be substantially improved.

These considerations led to the initiation of a research project at COMSAT Laboratories to develop a highly reliable unattended earth terminal (UET). The program began during the fourth quarter of 1970 and reached the engineering test phase by mid-1973, with experimental operation of the new terminal through INTELSAT IV satellites.

The program has incorporated the following major developments:

a. A multiple-beam torus antenna (MBTA) capable of providing two orthogonally polarized receive and two transmit beams from each of the one or more steerable feeds illuminating the fixed reflector.

b. A wideband parametric amplifier operating at room temperature with a noise temperature less than 75 K. Synchronously tuned, interchangeable stages are arranged so that failure of any stage does not interrupt the signal, but only reduces the system margin by no more than 1 to 2 dB. This precludes the need for a redundant amplifier and low-loss switch.

c. A 6-GHz, 400-W, 500-MHz bandwidth power amplifier using a single traveling wave tube (the only vacuum tube in the terminal) designed for 25,000 hours of life and with sufficient gain to be driven by a solid-state up-converter.

d. A directional-filter multiplexer capable of combining 10 power amplifiers, each assigned to a 40-MHz portion of the band, with guardbands not exceeding the 4 MHz assigned to the channelized transponder.

e. An up-converter with a 30-mW output level, sufficient to drive a single power amplifier to saturation, over the 500-MHz band.

f. Crystal-controlled local oscillators driving MIC frequency multipliers with a 500-MHz bandwidth. Thus, the frequency can be changed without retuning by simply changing crystals.

g. 500-MHz-bandwidth IF amplifiers at 855-MHz center frequency incorporating parallel hybrid-coupled MIC transistor stages to obtain "fail-soft" reliability.

h. A remote monitoring and control unit based on the choice of essential parameters and nondiagnostic monitoring and control, functions designed and constructed not to jeopardize the overall system reliability.

System model

To define the terminal parameters, it was first necessary to postulate an overall system and to apportion impairments among the major subsystems. The model assumed a network which included 400–500 earth terminals, each operating with two or more satellites spaced 3° to 5° apart. The satellite characteristics are listed in Table 1 and assume a channelized transponder.

TABLE 1. ASSUMED SATELLITE PARAMETERS

Operating Frequencies	3.7–4.2 GHz, transmit 4.925–6.425 GHz, receive
Antenna Gain	27 dB
Receive G/T	–6.8 dB/K
e.i.r.p.	34 dBW
Type of Transponder	Channelized
Bandwidth	36 MHz/output amplifier

Although the modulation, multiplexing, and multiple-access technique to be used in the system is assumed to be FM/FDM/FDMA with param-

eters chosen to conform to INTELSAT standards, transition to wider band digital modulation TDM/TDMA is possible. Therefore, to accommodate future systems characteristics and to obtain reliability through large performance margins, the bandwidth specified for all RF and IF subsystems at the terminal is 500 MHz. Frequency and channel bandwidth selection are determined by passive filters at IF.

Each station is to be monitored and controlled from a manned control center serving a region containing 10 to 50 earth terminals. The region encompasses a limited area so that a serviceman can travel by surface transportation to a terminal in eight hours or less. (Helicopter transportation would obviously reduce this time or extend the area of coverage.) It is assumed that service specialists will perform routine inspection and maintenance once every three months.

Earth terminal performance objectives

The characteristics of earth terminals operating with INTELSAT IV [1] provided a general guide for determining performance objectives. However, the trend toward higher satellite G/T, increased interference (cross polarization and adjacent beams), reduced baseband channel noise for high-quality point-to-point or multipoint networks, and low-error-rate digital transmission was also taken into account. These considerations led to the performance objectives specified in Table 2.

The reliability objective of each subsystem is based on an overall terminal, 10 transmitting and 10 receiving chains, achieving an availability of 0.999 during a 3-month period of unmanned operation. This implies that, of 100 terminals with 1,000 links, only one link would fail during the 3-month period. Components subject to wearout, such as the traveling wave tube, would have a minimum life of 25,000 hours.

Earth terminal configuration

With unattended operation as a principal objective, simplicity became a major factor in the choice of the terminal design. In addition, the ability to accommodate future growth and modifications required to operate in the 11/14- and 20/30-GHz bands contributed to the choice of the actual configuration. Figure 1 is a block diagram of the earth terminal which includes the components described in the following subsections.

TABLE 2. EARTH TERMINAL OBJECTIVES (FM)

Total System Noise	5,600 pWp
Total System Thermal Noise plus Intermodulation	3,600 pWp
External Noise Sources	1,000 pWp
Earth Terminal Noise Allocation (excluding thermal noise)	1,000 pWp
Earth Terminal Noise Breakdown	
Transmit Baseband	50 pWp
Modulator	100 pWp
Local Oscillators	75 pWp
Channel Filter Group Delay	125 pWp
Multiplexer and High-Power Amplifier	150 pWp
Receive Baseband	50 pWp
Demodulator	100 pWp
Local Oscillators	75 pWp
Channel Filters	125 pWp
Low-Noise Amplifier, Transistor Amplifiers, and Channel Splitters	150 pWp
	TOTAL
	1,000 pWp
Crosstalk	< 65 dB
Receive G/T	30 dB/K at 4 GHz, 10° elevation
Transmit Antenna Gain	54 dB at 6 GHz
Transmit Power/36-MHz Bandwidth	400 W

High-power amplifier

An examination of the problems associated with high-power (8- to 12-kW), liquid-cooled, traveling wave tube amplifiers required for multi-carrier operation led to the decision to designate single-carrier-per-amplifier operation as the primary operating mode. Hence, it was possible to avoid the 7- to 8-dB output power backoff required of traveling wave tubes in multichannel operation to meet the limitation on "out-of-band" intermodulation power, i.e., $p_i = 26 - 0.06 (\alpha - 10)$ dBW/4kHz.*

The communications capacity (number of telephone channels per 36-MHz bandwidth) versus earth terminal power for a 32-ft (11.7-m) antenna was examined by using the satellite model, as shown in Figure 2.

* α is the elevation angle of the earth terminal antenna.

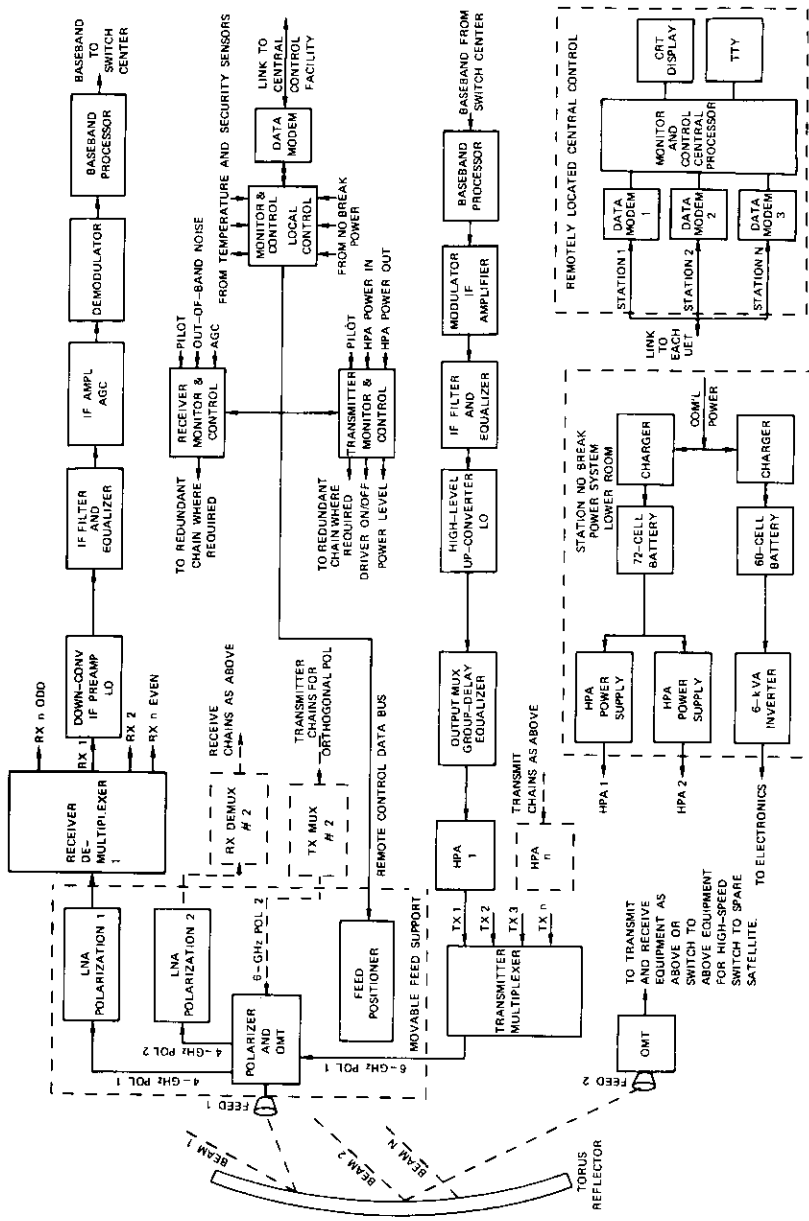


Figure 1. Overall Block Diagram of the UET

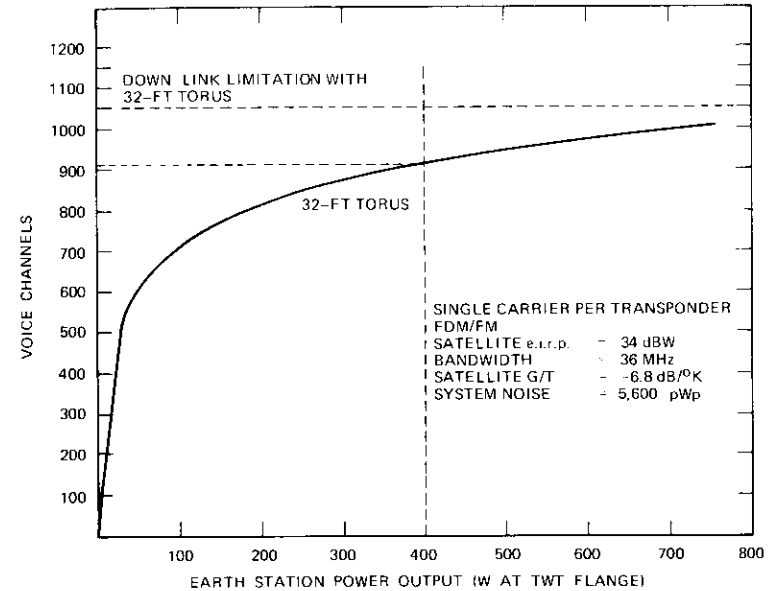


Figure 2. UET Voice Channel Capacity vs Transmitter Power

At 400 W, the number of voice channels was about 10 percent lower than the asymptotic capacity established by the down-link thermal noise alone. With the likelihood of future satellites providing greater receive sensitivity, it was decided to accept the communications capacity limitation of the 400-W amplifier since at this power level it was feasible to achieve a long-life, air-cooled, high-gain traveling wave tube. This power level would also be useful for as many as 100 voice channels in single-channel-per-carrier multicarrier operation with adequate saturation power backoff to meet in-band and out-of-band intermodulation limits.

The power amplifier traveling wave tube (type 6361J1 developed by Varian for COMSAT) has a minimum saturated power gain of 5 dB over the 5.925- to 6.425-GHz band at a power output of 400 W. An overall primary-power-input-to-RF-output conversion efficiency of 24 percent has been achieved. The impregnated dispenser cathode emission current density of $<900 \text{ mA/cm}^2$ at an operating temperature of $1,070^\circ\text{C}$ ensures the specified minimum lifetime of 25,000 hours. The permanent-magnet-focused tube is conduction cooled by an air-cooled cold plate. Each tube is energized by lead-acid rechargeable batteries through an inverter-type supply operating at 1,500 Hz. This frequency in conjunction with elec-

tronic regulation of the series-connected anode and depressed collector supplies (each about 5,000 V) ensures constant power output and a low ripple voltage with small filtering components (see Figure 3).

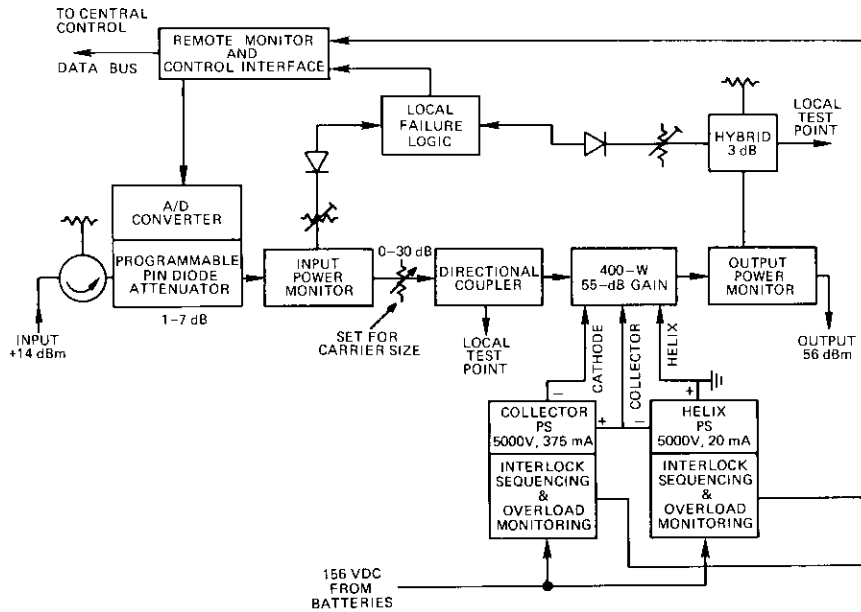


Figure 3. UET High-Power Amplifier Block Diagram

The high-power amplifier monitoring and test access design is consistent with the general philosophy adopted for the UET. The subsystems do not incorporate any metering, on-off switches, or indicator lamps, since operation is by remote control. As a safety measure, the high-power amplifier does include a high-voltage ON lamp and emergency high-voltage OFF switch. A service test panel can be connected through a multipin connector mounted on the front panel of the amplifier to permit access to and measurement of important voltages and currents. To enable checking while in service, RF test access is through directional couplers with test ports brought out to the front panel.

High-power amplifier filter-multiplexer

The key to the suitability of the power level chosen for the high-power amplifier is an arrangement of filter-multiplexer units which permits ad-

jacent channel amplifier operation. The dual-mode elliptic function filter-multiplexer developed at COMSAT Laboratories [3] fulfills this requirement. The design achieves a useful bandwidth of 36 MHz with 40-MHz spacing between center frequencies to match the frequency plans of the INTELSAT IV, IV-A, and presently operating and planned U.S. domestic satellites. The output multiplexer is group-delay equalized at the input to the traveling wave tube with a 3-pole coupled waveguide cavity unit. Equalization at this point is possible because of the small phase versus drive factor of the traveling wave tube (35° with drive variation from -20 dB to saturation). The noise contribution due to the filter group delay shown in Figure 4 is held to less than 150 pWp for an 1,800-channel carrier. The loss per multiplexer section is 0.3 dB.

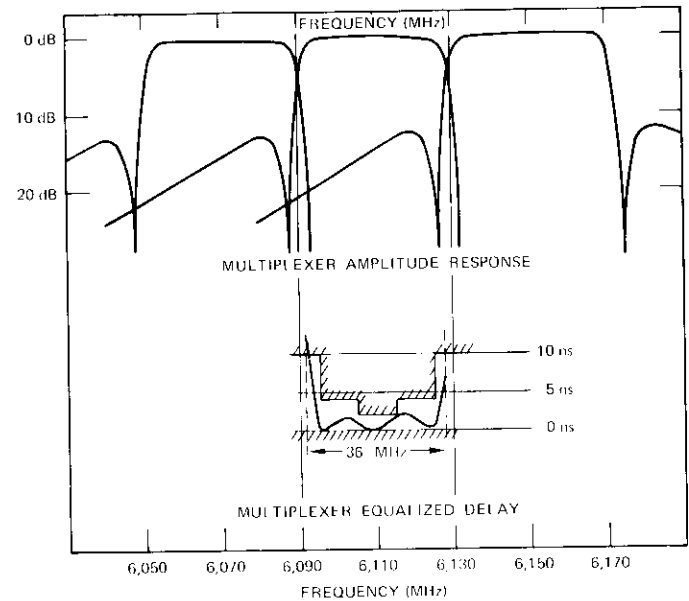


Figure 4. Output Multiplexer Amplitude and Group-Delay Response

Up-converter

The varactor upper sideband up-converter [2] is capable of driving the power amplifier to saturation. With the up-converter's minimum measured signal gain of 4.8 dB, the IF amplifier drive is 10 mW for maximum transmitter output. The pump-to-output-port response varies less than 1 dB

over the 500-MHz band. Similarly, the IF signal-to-output response is within 1 dB, ± 250 MHz, with the pump at 5.32 GHz. The wide bandwidth permits channel switching simply by changing the local oscillator frequency.

An alternate design using a low-level varistor mixer followed by a medium-powered Gunn diode amplifier was considered, and a 500-mW Gunn diode amplifier was developed. However, because of the early state of the Gunn diode amplifier development and the critical transmission performance required in the 6-GHz signal chain, contrasted with the ruggedness of the up-converter varactor, the latter was chosen.

Local oscillator

To ensure reliability and to obtain the required frequency stability, the chosen local oscillator design uses a crystal-controlled oscillator operating at VHF followed by frequency multipliers and a transistor amplifier at 2 GHz with sufficient power to drive the final step recovery diode frequency doubler to an output level of 400 mW (see Figure 5).

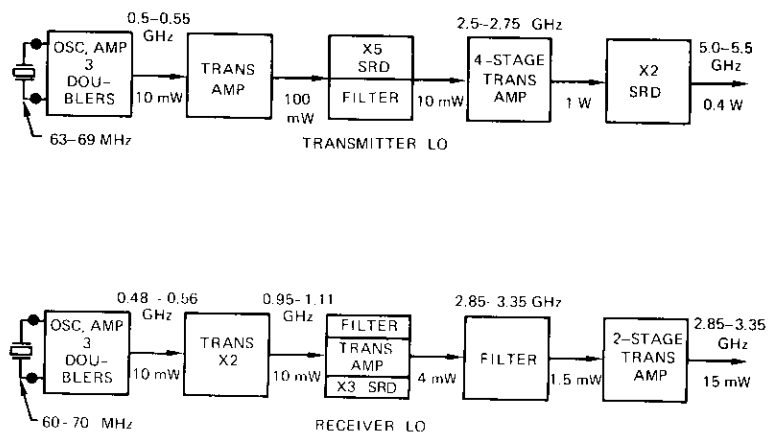


Figure 5. Transmitter and Receiver Local Oscillators

Designing all interstage filter and impedance matching circuits with bandwidths in excess of 9 and 16 percent of the operating frequency for the transmit and receive chains, respectively, has made it possible to achieve a noncritical fixed tuned local oscillator. The output frequency can be set, without tuning, by choosing a crystal at the appropriate frequency. The crystal can be plugged in, or alternatively, a series of crystals with the desired frequency selected by a remotely operated switch can be provided.

The thermal noise introduced by a chain of broadband frequency multipliers and amplifiers has been reduced to an acceptable value by using low-noise field effect transistors (FETs) in the master oscillator and buffer amplifier stages and appropriate interstage filters. The local oscillator noise contribution has been measured as less than 75 pWp with respect to 419-kHz deviation in a 4-kHz channel.

Each of the five modules shown in Figure 5 is a 2- x 2-in. (5.08- x 5.08-cm) microwave integrated circuit using discrete parts. Other forms of local oscillators, such as synthesizers employing phase-lock loops or oscillators directly at the operating frequency using high-stability cavities, were evaluated and rejected for this application because of an undesirable failure mode, i.e., loss of frequency lock with consequent potential interference to other carriers.

855-MHz IF amplifier

With the trend toward systems with higher capacity and larger bandwidths operating at higher frequencies, it seemed logical to reconsider the use of the usual 70-MHz intermediate frequency. It was desirable to select the lowest intermediate frequency which would permit future wideband operation (up to 500 MHz) with economical filtering and amplification. These factors, in conjunction with the usual mixer considerations for reducing spurious frequency generation, led to the selection of an intermediate frequency of 855 MHz. With this intermediate frequency, local transmitter mixing products and all mixer products below the seventh order would be placed outside the mixer filter passband responses.

Figure 1 indicates the insertion channel filters following IF amplification. A series of stripline, 6-pole, Chebychev filters and 3- or 5-section group-delay equalizers (depending on the bandwidth) has been designed to cover a range of bandwidths from 2.5 to 36 MHz.

Parametric amplifier

At the present state-of-the-art, a noise temperature < 75 K can be achieved with varactors operating at room temperature and pump diodes that are qualified for long life and high reliability.

The parametric amplifier, shown in Figure 6, uses the fail-soft approach. Each stage, complete with varactor and pump diodes and diode bias regulators, is included in a temperature-controlled module coupled to a 9-port circulator. Temperature, and consequently paramp gain, is stabilized by Peltier thermoelectric devices (TEDs). Current direction and magnitude through the TED are controlled by a solid-state feedback controller which

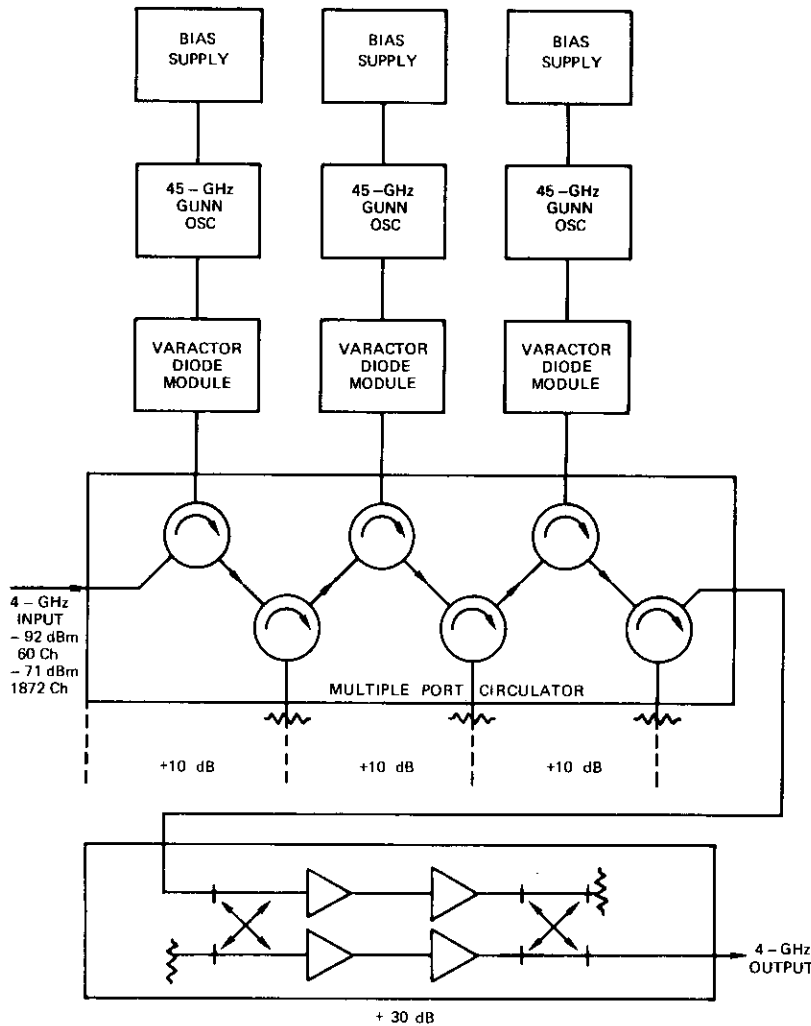


Figure 6. 4-GHz Low-Noise Amplifier Block Diagram

will hold the 45-GHz Gunn diode pump and varactor diodes to within 2°C over an ambient range of 10°C to 50°C.

In the event of a stage failure, the signal is circulated to the next stage, and the gain loss is automatically compensated by the IF amplifier automatic gain control. Failure of the first stage results in a maximum noise

temperature degradation of 1.5 dB, while failure of the later stages results in correspondingly less degradation. The design implemented employs three identical parametric amplifier stages followed by a 4-stage transistor amplifier.

Transistor amplifier

The low-noise solid-state amplifiers following the paramp use silicon NPN bipolar transistors (HP 35876 E, option 100). Two of these modules are cascaded to obtain 30-dB gain. The measured performance of each module is shown in Table 3.

TABLE 3. MEASURED PERFORMANCE OF TRANSISTOR AMPLIFIER MODULE

Frequency	3.7-4.2 GHz
Gain	15 ± 0.2 dB over frequency, ±0.3 dB over 0°C-50°C
Noise Figure	3.8 dB maximum
C/I Two-Tone	>50 dB at P _{out} = 5 dBm

The amplifier incorporates an FET constant-current regulator to prevent overvoltage and to stabilize performance over temperature. The circuit is etched on a 2- x 2-in. (5.08- x 5.08-cm) copper-clad polyphenylene-oxide substrate.

Receiver multiplexer-mixer preamp

A separate down-converter is assigned to each RF channel through a stripline filter-multiplexer. The insertion loss (0.4 dB per section) of the suspended substrate photo-etched filter can be tolerated at the low-power levels in the receiver, and has a negligible effect on receiver noise temperature because of the preceding 60 dB of gain. The 3-pole filter provides >30-dB rejection to the alternate channels on either side of the desired carrier, thus eliminating concern that higher order intermodulation products could contribute to channel noise if the mixer were presented with several large carriers.

The multiplexer approach permits modular addition of carriers with relatively low loss, i.e., 5 dB for the filter multiplexer versus 12 dB for the hybrid-coupled 12-port divider.

The microstrip mixer-preamp shown in Figure 7 includes the single mixer diode and three hybrid-coupled transistor amplifiers. The hybrid-coupled stages yield higher reliability as well as an improved dynamic range. The net gain is 27 ± 0.5 dB over the 3.7- to 4.2-GHz band. The wide bandwidth provides noncritical performance when the mixer is used in the present 36-MHz/carrier application and will be directly applicable to future systems with wider bandwidths.

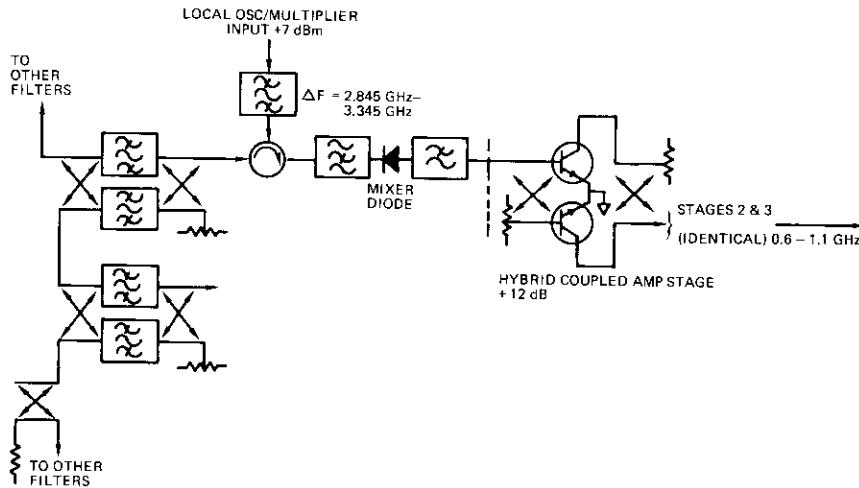


Figure 7. Multiplexer-Mixer-IF Preamp

Frequency selection, as described in the transmitter section, is achieved by switching or inserting the appropriate crystal into the local oscillator unit. Carrier bandwidth selection is accomplished with passive filters identical to the stripline units in the transmitter chain.

IF amplifier-automatic gain control

The 60-dB gain required between the mixer preamp output and the 0-dBm demodulator input to accommodate a range of signals from 24 to 1,872 channels is obtained with two amplifier units of the 3-stage hybrid-coupled transistor amplifier [4] identical to those of the mixer pre-amplifier. As shown in Figure 8, the automatic gain control (AGC) PIN diode attenuators preceding the IF amplifier units maintain the input to the demodulator within ± 1 dB over a +10- to -30-dB level change. Thus the AGC range compensates for gain loss incurred when a para-

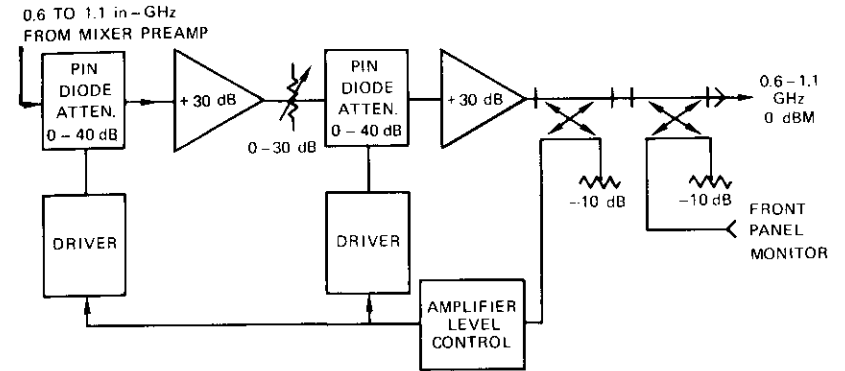


Figure 8. IF Amplifier Multiplexer Automatic Gain Control

metric amplifier, 4-GHz transistor amplifier, and/or IF amplifier stage fails.

Wideband modulator-demodulator and baseband module

The wideband modem and baseband processors shown in Figure 9 are divided into four modules. The transmit baseband module controls the baseband level and the frequency response of the signals to be transmitted. The baseband limiter sets a predetermined upper limit on the deviation and holds that level within ± 1 dB. It also controls the output level of the spreading waveform generator so that the ultimate carrier flux density is within FCC and ITU limits. This is accomplished by adding to the baseband input a 20- to 150-Hz triangular waveform with a level inversely proportional to the baseband level. The spreading waveform also acts as the carrier signature. In addition, within the baseband module, a 60-kHz pilot signal and pre-emphasis are applied to the baseband. The baseband module contributes no more than 10 pW of noise and distortion to the modem output.

The wideband modulator employs two varactor-controlled oscillators (1.4 and 2.25 GHz) in a push-pull circuit. This method of operation yields high modulator sensitivity (226 MHz/V) and, by mixing these signals, effects a cancellation of the even harmonics produced in the modulator. Deviation from the 855-MHz modulator center frequency in excess of ± 40 MHz peak-to-peak with baseband from DC to 10 MHz is possible with less than 1.0-percent intelligible AM.

The phase-locked-loop demodulator employs the same dual oscillators

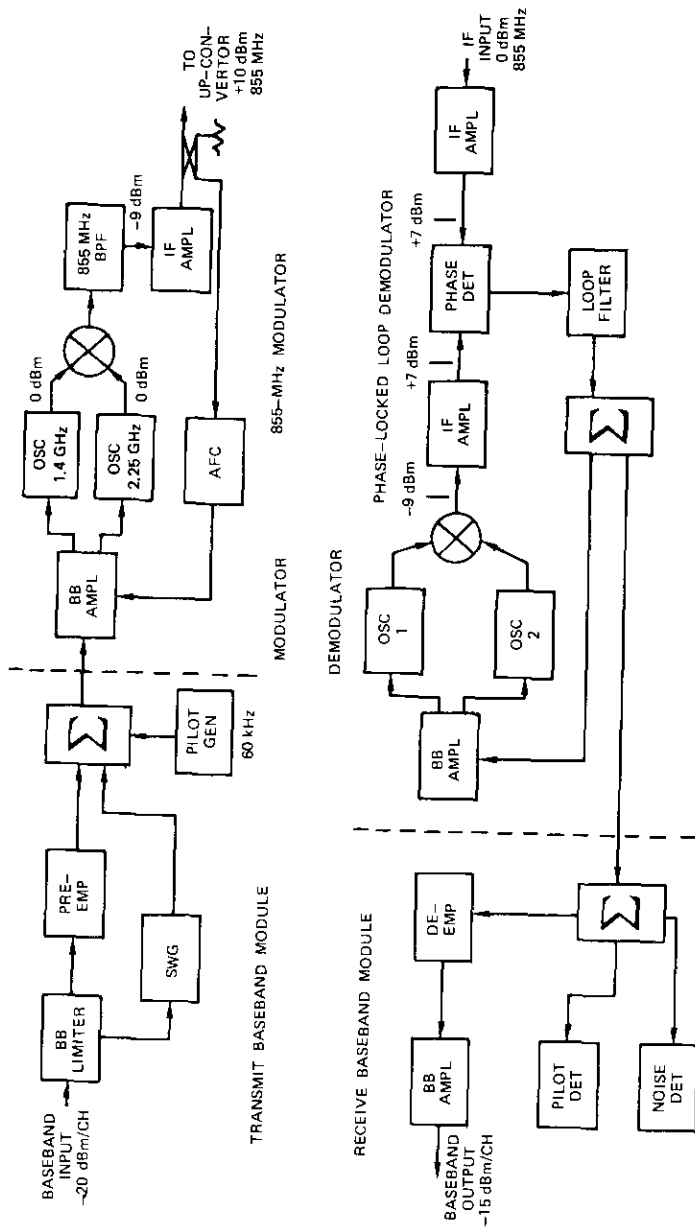


Figure 9. Wideband FM Modulator/Demodulator Baseband Processor

as the modulator. The phase detector sensitivity is 0.05 V/rad. The modem has been implemented for a 612-channel carrier, although it is capable of handling 1,872 channels as well as TV. For the 612-channel implementation, the modulator-demodulator contributed less than 200 pW in the worst channel (14 kHz), met all INTELSAT IV operating specifications, and provided a threshold improvement of 1.5 dB over a conventional discriminator.

The receive baseband module provides the de-emphasis and amplification. It also contains the pilot detector, loss of pilot alarm, and out-of-band noise detector circuitry.

All circuits are solid state and implemented in printed circuit and MIC form.

Antenna

As indicated earlier, earth station location and antenna elevation angle limitations plus the need for two or more satellites in the orbital arc to serve a community of users have resulted in increased restrictions on satellite orbital positions. These restrictions suggest the use of a fixed reflector multiple-beam antenna. Previous studies [5] of multibeam antennas had shown that a conical torus reflector with offset feeds would provide multiple steerable beams at a lower cost than separate antennas for each beam, as well as improved reliability and performance.

The surface of the reflector is generated by a parabolic arc rotated about an axis appropriately oriented at the earth site to obtain uniform scanning of the geosynchronous arc. This surface yields higher efficiency but less out-of-plane scanning flexibility [6] than that of a spherical reflector. The feeds are positioned along an arc matching the reflector paraxial arc and at a distance from the reflector located between the paraxial and parabolic focal arcs. Beam steering in equivalent hour angle motion is accomplished simply by sliding a carriage which supports the feed assembly and low-noise amplifiers along a pair of bearing rods formed to match the feed arc. The declination motion required to follow out-of-plane satellite drift is guided by a pair of parallel rods perpendicular to the first set, as shown in Figure 10.

The antenna feed geometry has been designed so that the simple X-Y motion of the feed scans as much as 40° of the geosynchronous arc with negligible error. Mechanical interference limits adjacent feed (beam) spacing to about 2° .

The engineering model shown in Figure 11 has a lightweight structure that has been analytically developed by using NASTRAN programs. The

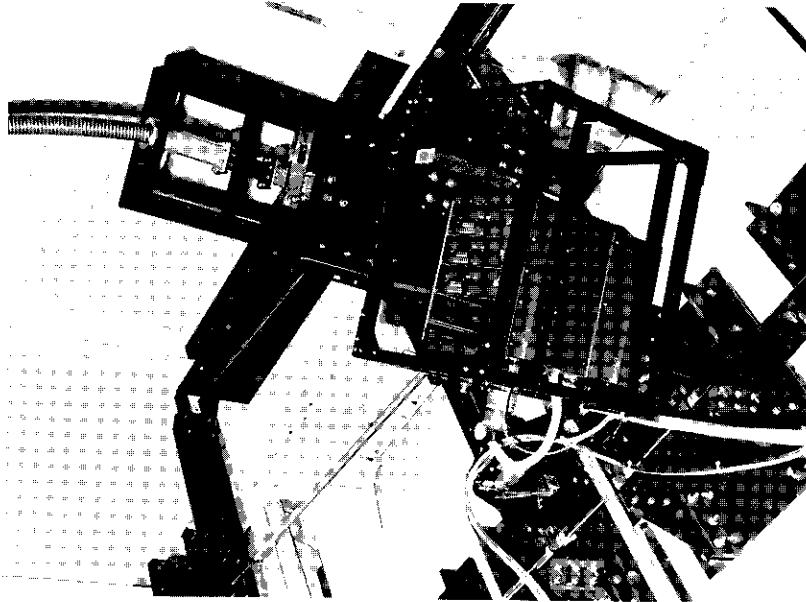


Figure 10. *Feed and Paramp Support and Guides*

32- x 55-ft (9.6- x 16.5-m) aperture provides beams to scan 20° of the geostationary arc. The reflector is positioned to cover the orbital arc from 18° to 38° west longitude.

The reflector backup structure is formed of standard steel angle which can be easily assembled in the shop and checked for proper curvature. The tubular steel curved spline which determines the circular curvature of the reflector backup structure and provides the 4-point attachment to the support structure (see Figure 11) is fabricated in three sections so that it can be shipped to the site via conventional trucks. The tubular steel support structure utilizes a tripod of fixed length for the right front support point, an A-frame for the left front support point, and an inverted A for the rear two points. For a particular location, the A-frame members are fabricated to the required length. Small adjustments to account for installation inaccuracies are accommodated by the locking nuts on the foundation mounting studs.

To provide greater insight into fabrication and installation problems, detailed drawings and separate work statements were prepared for steel structures, aluminum reflector surface, foundation, and erection and

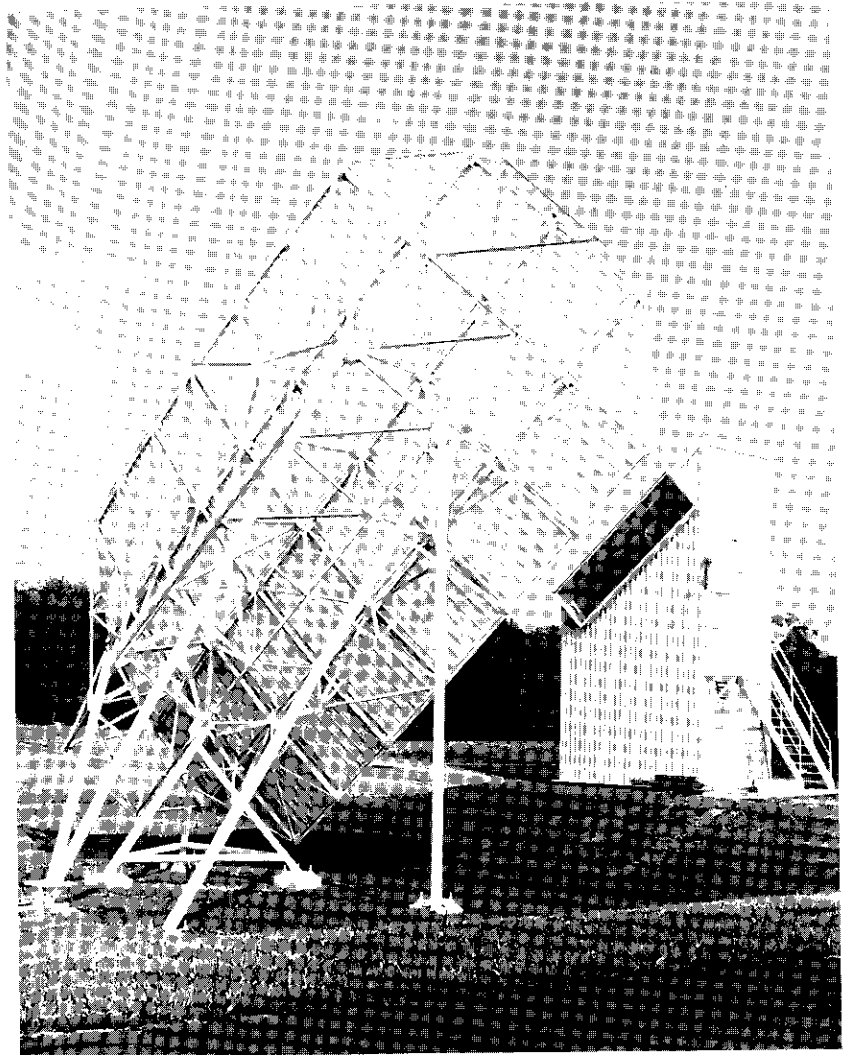


Figure 11. *UET/MBTA*

adjustment on-site. Separate contracts were let for each activity.

The reflector was assembled in the horizontal position (focal point up) on four concrete piers corresponding to the four reflector backup structure support points. After final alignment of the 32 panels, the reflector

was lifted into position on the support tripod and A-frames previously aligned by star observations and standard surveying techniques, as shown in Figure 12.

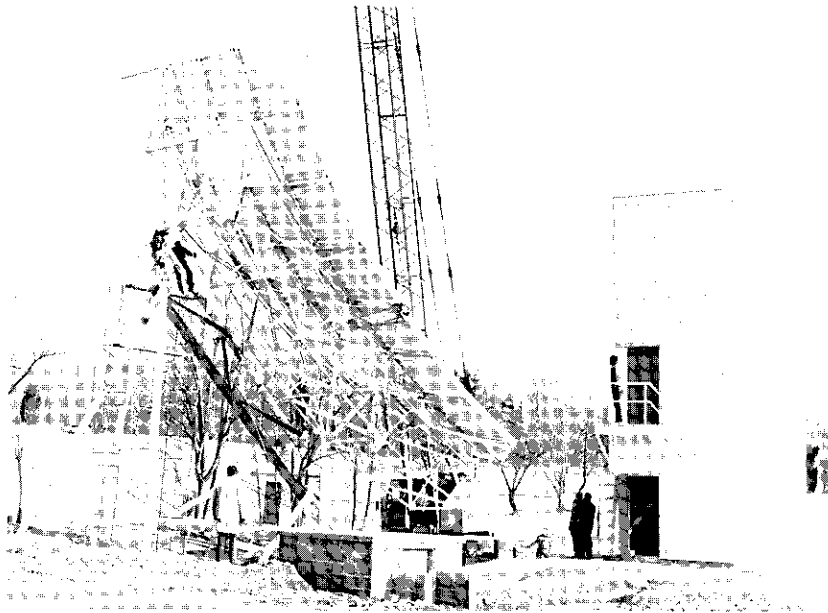


Figure 12. Antenna Reflector Being Lifted Into Position

Measurements of the reflector surface indicate that it is better than 0.015 in. (0.381 mm) rms with respect to a true parabolic vertical section. The structure is designed to maintain surface errors over the entire surface within less than 0.035 in. (0.889 mm) rms of the true parabolic torus surface for wind loads up to 35 mph (56 km/hr) with gusts up to 45 mph (72 km/hr). The reflector support structure and feed equipment tower stiffness result in signal variations of less than 0.1 dB in winds of 60 mph (96 km/hr) and no permanent deformation in winds of 100 mph (160 km/hr).

A broadband corrugated horn feed and a 5-port orthomode transducer have been developed to illuminate the 32-ft (9.6-m) aperture. This effort has resulted in a more complete understanding of corrugated feed design. Exceptional symmetry of E- and H-plane radiation patterns, low sidelobes, constant phase center with frequency, and octave band impedance match have been obtained with a considerably smaller feed than had previously been possible.

Feed position versus satellite motion has been calibrated against the orbital motion of INTELSAT IV F-2 and F-7. The feed positioning worm screws provide $\pm 1^\circ$ of beam steering, corresponding to ± 8 in. (20.32 cm) of travel along the X and Y guide rails. Position adjustment can be held to ± 0.04 in. (1.016 mm) or 0.005° . The north-south feed travel versus time follows a sine function with a period of 24 hours. The X-plane motion, which corresponds to satellite in-plane drift, although it has constant velocity until a satellite drift correction is made, is slight. Therefore, it is necessary to correct this position only once or twice a day. The feed is behind a mylar window completely protected from the weather and directly connected to the parametric amplifier. The major antenna performance characteristics are shown in Table 4.

TABLE 4. ANTENNA PERFORMANCE CHARACTERISTICS

Frequency	
Transmit	5.925-6.425 GHz
Receive	3.70-4.20 GHz
Gain	
at 6 GHz	53.8 dB
at 4 GHz	50.5 dB
Sidelobes	
First	>25 dBi below beam peak
$1^\circ \leq \theta \leq 48^\circ$ Profile	32-30 log θ
$\theta > 48^\circ$	less than 20 dBi
VSWR	
Output of Orthomode Transducer (receive)	1.2:1
Input to Orthomode Transducer (transmit)	1.2:1
Polarization	linear or circular with axial ratio <0.5 dB in transmit and receive bands
Isolation	
Feed-to-Feed	>40 dB
Transmit-to-Receive	>80 dB
Polarization-to-Orthogonal Polarization	>40 dB
Noise Temperature	
(total antenna + feed + polarizer and orthomode transducer)	20 K at 29° elevation
Structure	
Gain Loss (winds 60 mph, or 112 km/hr)	<0.1 dB
Temperature	-20°F to $+120^\circ\text{F}$
No Permanent Distortion	winds 100 mph (160 km/hr)

Monitoring and control

Based on the premise that telemetry and command monitoring will not be diagnostic, but will determine only the terminal's operational status, the number of subsystem parameters to be monitored has been kept to a minimum. The essential parameters monitored and the operations commanded are shown in Figure 13. In case of monitoring and control system failure, the terminal will operate "blind" until monitoring and control are restored, although the radiator power can be monitored through the satellite.

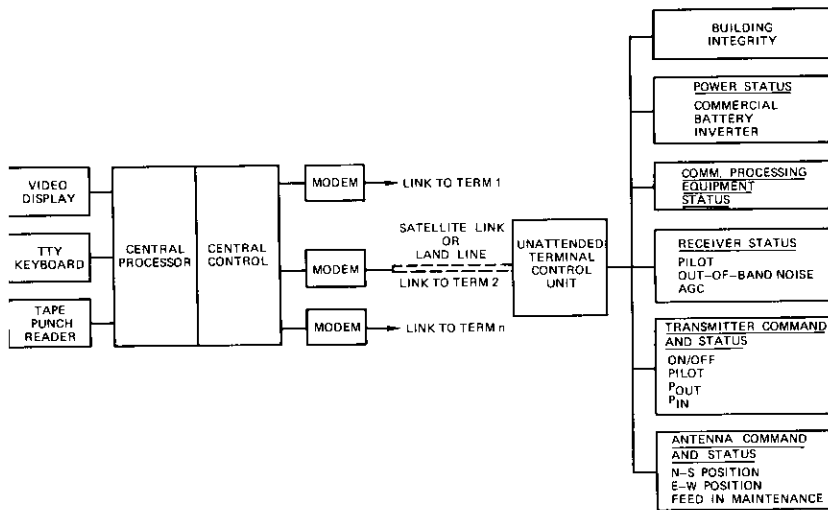


Figure 13. Monitoring and Control System Block Diagram

The control system operates through a voice channel that can be transmitted via satellite. Antenna pointing information, transmitter ON/OFF, and power level adjustment of each terminal are centrally controlled.

Prime power

For reliable operation, it is necessary to isolate the transmission equipment from power transients and to continue operation during power interruptions. Therefore, prime power is taken from two lead-acid battery banks which are constantly being recharged by the AC power line. One battery bank has 72 cells, each with a capacity of 32.5 Ah, to yield 156 V.

This battery will supply up to three power amplifier modules for two hours. The second battery has 60 cells, each with a capacity of 73 Ah, to yield 129 V. This second battery operates all the other equipment except building lighting, heating, and cooling through an inverter which generates 117 V, 60 Hz, single phase. All of the low-power equipment operates from this 60-Hz source with standard self-contained power supplies.

This arrangement permits redundancy, as shown in Figure 14, since either of the two battery banks may be used directly for the traveling wave tube amplifier power supplies, the 60-Hz inverter can be bypassed, and all the low-voltage equipment can be operated directly from the power line. The battery watt-hour capacity depends on the depth of discharge permitted; battery operation for long life has dictated a discharge limita-

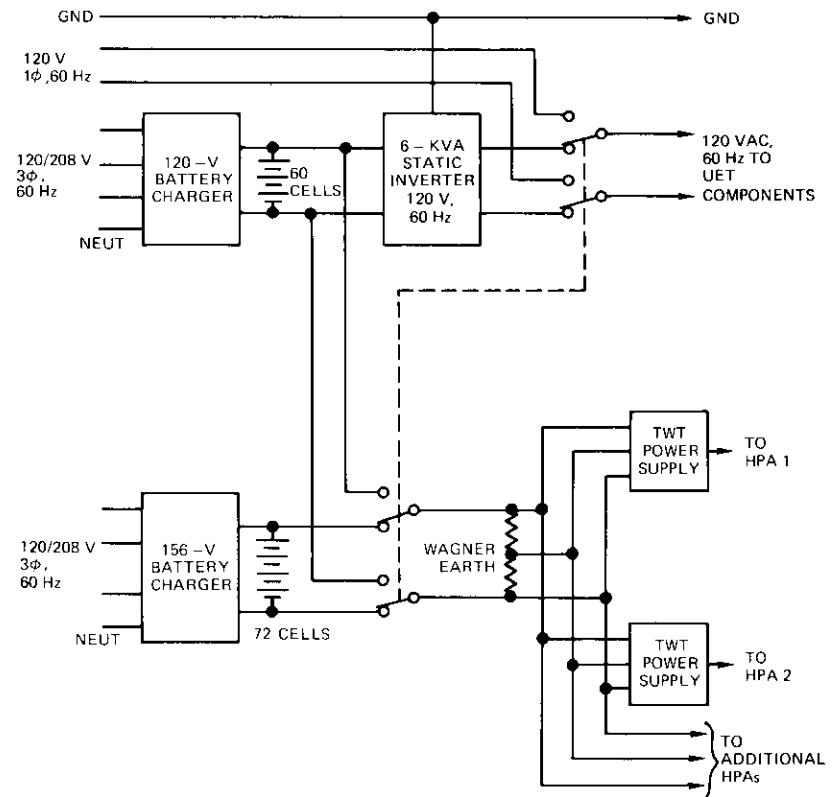


Figure 14. Uninterrupted Power System Block Diagram

tion of 126 V for the 72-cell system and 105 V for the 60-cell system. With this depth of discharge, two complete transmit and receive chains will operate for two hours in the absence of line power.

Initial tests

In early 1973, as an initial test, circuits were established between Clarksburg and a small terminal aboard the *S.S. HOPE* in Maceio, Brazil, through the global beam of the INTELSAT IV F-3 satellite. Three telephone channels, 300 Hz to 4 kHz, 12 to 16 kHz, and 16 to 20 kHz, were used for slow-scan television, facsimile, telecopier, and voice communications. Frequency modulation with a peak deviation of 75 kHz per channel was used. The occupied bandwidth was 300 kHz. For e.i.r.p. and G/T values of 59.8 and 75 dBW and 14.2 and 30 dB/K at the *S.S. HOPE* and Clarksburg, respectively, the operating C/T was 160.5 dBW/K, resulting in signal-to-noise ratios of 48 dB in each channel. The direct and reliable communications enabled doctors on board the *S.S. HOPE* to consult with specialists in the United States, and to obtain information directly from the Library of Medicine of the National Institute of Health and various universities.

A television test transmission was conducted through the INTELSAT IV F-3 spot beam between the UET and a 15-ft (4.5-m) receiving station at COMSAT Headquarters in Washington, D.C. The RF bandwidth from the video signal was reduced to 18 MHz through a 6-dB reduction of the color subcarrier at the UET transmitter and corresponding restoration at the Washington receiver. The sound was transmitted on a separate carrier with 15 dB less power and at a frequency 14 MHz higher than the video carrier. Although the signal-to-noise ratios (47 dB at Washington and 50 dB at the UET) were lower than current INTELSAT IV system standards, the quality was judged adequate for many purposes.

Initial operating experience has been gratifying in terms of reliability. Almost all parts except special microwave components were selected from the NASA PPL-11* high-reliability list, and all parts were derated according to satellite practice. Although strict quality assurance practices such as those which would apply to parts, source control, and burn-in in the production phase were not followed for the engineering model, failures have been few. For instance, the paramp has operated over 6,000 hours without failure. Since the feed and all radio equipment have been mounted in an enclosure, well protected from the weather, operation through rain, snow, and wind storms has been uneventful.

* Now replaced by PPL-12.

The terminal will undergo further testing to evaluate remote supervision and control, equipment performance, and reliability. The UET will also be used to test polarization isolation measurement techniques using the dual polarization feed, polarizer and orthomode transducers.

Conclusion

A complete earth terminal based on new concepts has been developed to achieve the high reliability required for unattended operation. These basic concepts include broadband microwave integrated circuit amplifiers with fixed tuning, a fixed reflector antenna with multiple steerable feeds enclosed in the equipment room, passive multiplexing of low-power broadband final amplifiers and receivers, hybrid-coupled active redundancy in all signal amplifiers except the traveling wave tube, and remote control and monitoring of each terminal from a central point.

Acknowledgments

This project has reached its present state of development only through the dedicated efforts of many individuals at COMSAT Laboratories. The authors are particularly pleased to acknowledge Laurence Gray for able direction of the high-power amplifier, frequency conversion and modem development, and assembly of the UET engineering model.

Many others too numerous to list have contributed to the design and implementation, and the authors express their sincere appreciation to these individuals.

Some of the subsystems of the UET have been previously reported, as indicated in the references; others are reported in this issue and more will be reported in forthcoming issues of the COMSAT Technical Review.

References

- [1] "Performance Characteristics of Earth Stations in the INTELSAT IV System," ICSC-45-13, W/1/70 (Rev. 1), June 23, 1972.
- [2] R. L. Sicotte, "A 6-GHz Broadband Varactor Up-converter," *COMSAT Technical Review*, Vol. 3, No. 2, Fall 1973, pp. 387-411.
- [3] A. E. Atia and A. E. Williams, "New Types of Waveguide Bandpass Filters for Satellite Transponders," *COMSAT Technical Review*, Vol. 1, No. 1, Fall 1971, pp. 21-43.
- [4] C. B. Cotner, "A Microstrip Balanced Transistor Amplifier with Collector-Base Feedback for 0.6-1.1 GHz," *COMSAT Technical Review*, Vol. 3, No. 2, Fall 1973, pp. 431-437.

- [5] Geoffrey Hyde, "A Novel Multiple-Beam Earth Terminal Antenna for Satellite Communication," IEEE 1970 International Conference on Communications, San Francisco, California, June 8-10, 1970, Paper No. 70-CP-386-COM, *Proceedings*, pp. 38-24-28-33.
- [6] G. Hyde, W. Korvin, and R. Price, "A Fixed Multiple-Beam Toroidal Reflector Antenna Operating at Frequencies Above 12 GHz," IEEE International Conference on Communications, Montreal, Canada, June 14-16, 1971, *Proceedings*, pp. 27-11-27-16.



Louis Pollack, with COMSAT Laboratories for seven years, is Assistant Director-Technical, responsible for the technical direction of the Spacecraft, Communications Processing, Microwave, Applied Sciences, and Transmission Systems Laboratories. For 23 years he was with ITT Federal Laboratory, where his last position was Director, Transmission System Operations, concerned with design and development of space communications equipment and other microwave

transmission equipment.

He received his B.E.E. degree from the C.C.N.Y. in 1953, and is a Fellow of the IEEE, an associate member of the National Society of Professional Engineers, and a member of the AIAA.

William K. Sones received a B.Sc. degree with honors from London University, and an M.S. and a Ph.D. degree with distinction from Johns Hopkins University. His professional career includes seven years at Westinghouse, Baltimore, where he participated in the design of HF, VHF, and microwave communications systems. At Johns Hopkins University five years were spent jointly as supervisor in charge of the communications and data processing group at their radiation laboratory and as professor in the school of graduate engineering, where his main interests were optimum detection and adaptive maximum likelihood techniques.

In the five years Dr. Sones has been at the COMSAT Laboratories he has worked principally on earth terminal design for satellite systems. He is presently a Senior Staff Scientist.



Index: unattended earth terminals, reflector antennas, structural design, toroidal reflectors, feed horns, steering.

The unattended earth terminal multiple-beam torus antenna

G. HYDE, R. W. KREUTEL, AND L. V. SMITH

(Manuscript received August 1, 1974)

Abstract

This paper deals first with the electrical characteristics of the front-fed conical torus antenna as developed analytically and verified by scale-model antenna measurements. The unattended earth terminal multiple-beam torus antenna (UET MBTA) design and measurements are then discussed. Noise temperature performance is estimated. Next, the corrugated horn used to feed the MBTA is briefly reviewed. The orthomode transducer and polarizer requirements, design, and performance are then developed. The beam steering mechanism is described in detail. This is followed by a discussion of the structural requirements, analysis, and design. Finally, the erection and checkout of the structure are described.

Introduction

The unattended earth terminal multiple-beam torus antenna (UET MBTA) shown in Figure 1 and described herein is designed to meet the overall antenna requirements of the UET.* As such, it provides for multiple steerable beams to view satellites in geosynchronous orbit with

*The UET is described in detail in a companion paper in this issue, "An unattended earth terminal for satellite communications," by L. Pollack and W. Sones.

improved reliability and wide-angle sidelobe performance at a cost lower than that of antennas of conventional design.

The MBTA is a fixed reflector, multiple-beam, offset-fed, conical torus antenna. The fixed reflector design gives improved reliability and lower cost by eliminating the reflector pedestal and using more efficient load paths, resulting in a lighter but stronger reflector. The multiple beams provide simultaneous RF connections with several satellites at reduced cost through reflector reuse by the overlapping illuminated areas. The offset-fed geometry results in an unblocked aperture which gives rise to very low wide-angle sidelobes as well as convenient access to feeds and the nearby RF equipment. The circular symmetry of the conical torus geometry permits identical beams to be generated by the feed system along the geostationary arc; further, it leads to cost-effective structural design by permitting eightfold iterative panel and truss sections.

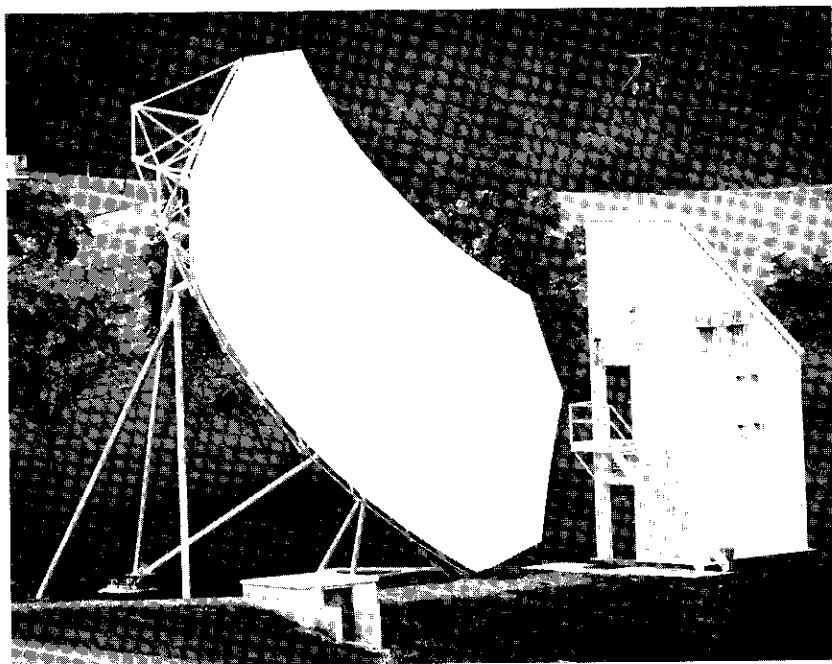


Figure 1. UET MBTA

The front-fed conical torus antenna

Consider the geometric optics of the generalized toroidal reflector antenna [1]—[3] with a simple point feed, as shown in Figure 2. For the MBTA, the section M is a parabola; V is its vertex; F is its focus; z is the direction of its axis; R is the radius of rotation at the vertex, V ; d is the offset of the reflector; and the x - y plane is a plane perpendicular to its axis. The parabolic section collimates a fan of rays originating at the focus and lying in the x - y plane so that they emerge parallel to the z -axis, which can therefore be thought of as the beam direction.

The angle between the axis of rotation (the z' -axis) and the beam direction is α . The parabola, M , is rotated about the z' -axis to form the torus. For $\alpha = 95.5^\circ$, the reflector is a "generalized" parabolic torus whose beam directions closely approximate the direction of the geostationary arc. It has been shown that, for a 40° field of view and locations between 30° and 50° north latitude, an angle of 95.5° between the axis of the conic section and the axis of rotation of the generalized torus reflector is nearly

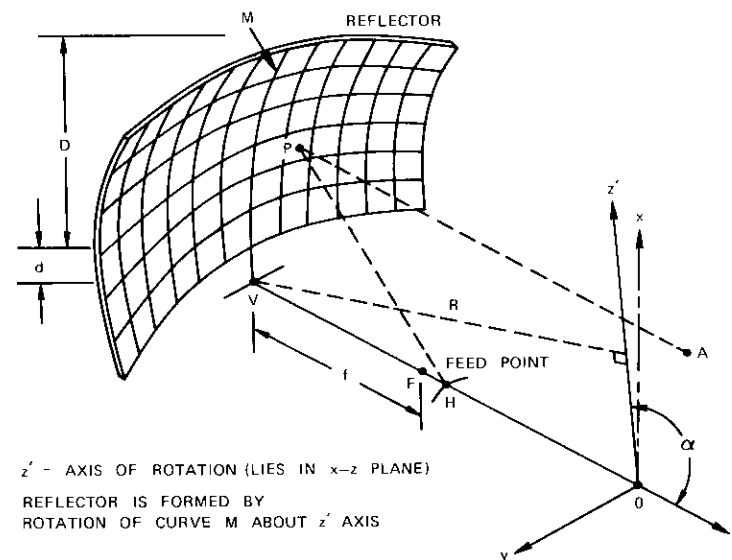


Figure 2. Torus Antenna Geometry

optimum. It results in a reflector whose beams, when moving on the scan cone, depart from the geostationary arc by much less than a beamwidth (for the proposed reflector size and desired field of view) for sites in the contiguous U.S. [4].

In Figure 2, when the feed point F is moved, it sweeps out a curve parallel to and near the focal arc. This feed curve is a circle. Because of the circular symmetry, feeds placed anywhere on this feed arc form identical beams which lie on the surface of a cone. (The cone arises from the relationship between z' , the axis of rotation, and z , the axis of the parabola, which causes the latter to sweep out the surface of a cone as the parabola sweeps out the torus.) As a consequence, because a given portion of the reflector illuminated by a given feed is geometrically and optically identical to any other section illuminated by another feed on the focal arc, no performance degradation is incurred when using several feeds to place several beams on the orbital arc. There is of course a mechanical limit to the number of feeds which may be conveniently placed on the focal arc. (At present the feed systems have been designed for a 3° minimum spacing.)

As a further consequence of this symmetry, moving a feed along the feed arc steers the corresponding beam along the orbital arc, i.e., east-west, with no performance degradation. Feed motion perpendicular to the focal arc moves the beam across the orbital arc, i.e., north-south, and results in a small amount of performance degradation comparable to off-axis defocusing of a paraboloid of similar geometry.

To obtain these desired symmetries, which provide degradation-free east-west scanning and permit the use of identical feeds, it is necessary to use optical systems, such as the torus, which have some aberration. For aperture diameters up to about 200 wavelengths, the front-fed configuration, used in the 10-ft (3.04-m) scale model and the 32-ft (9.75-m) design, may be employed. For larger apertures, the use of aberration correction is profitable, and this feature is presently under investigation.

Sections of the reflector taken by plane cuts including the z' -axis are all identical to M . Sections obtained by planar cuts perpendicular to the z' -axis are circular. Thus it can be seen that, in the plane cuts including the z' -axis, focusing is similar to that of a parabola, while in the plane of the circle, focusing is similar to that of a circular section. $M(x, y)$ can be written as a parabola of the form

$$x^2 = 4f(z_0 - f)$$

where f is the focal length, the focus is at $F(0, z_0)$ on the z' -axis, and the

vertex is at $V(0, z_0 - f)$. It should be noted that, in the x' - y plane, the reflector sections are circles,

$$x'^2 + y^2 = x_0'^2$$

where x_0' is the x' coordinate of the parabola in the x' - y' plane.

For nearly constant path lengths from the feed point $H(x_n, z_n)$ to the aperture plane, the path length, L , can be approximated by

$$L \simeq z + [(z - z_n)^2 + (x - x_n)^2]^{1/2}$$

The change in path length is

$$\Delta L = L - |z_0 - f| - f$$

For normalization purposes the calculation was performed in units of R ($R = OV \sin \alpha$), where R is the radius of curvature in the x' - y' plane at the vertex. The results of the computations are presented as contour plots, where the contours are marked in units of $10^{-3}R$ to permit freedom of choice in terms of D/λ , the aperture diameter in wavelengths, and D/R , the curvature parameter (which also fixes f/D). Calculations were performed over a wide range of parameters. In addition to the variations in α ($\alpha = 90^\circ, 95.5^\circ$, and 101.1°), the relative focal length was varied [$0.450 < (f \sin \alpha)/R \leq 0.525$]. From these calculations it appeared that $(f \sin \alpha)/R = 0.485$, i.e., $f/R = 0.487$, was the best choice. Exploration of feed position yielded optimum field coordinates $H(x, y) = H(0.001, -0.518)$.

Figures 3a and 3b are contour plots of aperture path length distribution and radiation field. The circle in Figure 3a delineates a circular aperture in which the path length variation is sufficiently small to be useful. The tendency of the main beam around the -15 -dB contour in Figure 3b to become triangular is characteristic of the radiation pattern of offset toroidal reflectors.

Consider now the variation of gain as a function of frequency. The parameter D/λ , which is proportional to frequency, is preferable for this purpose. For a torus defined by $\alpha = 95.5^\circ$, $R/D = 2$, and $f/R = 0.487$, with the feed at $H(x, y, z) = H(0.001R, 0.0, -0.5204R)$, gain has been evaluated for a wide range of D/λ and several illumination functions of the form $E_{\text{feed}} = A(\cos)^n$. The results of this evaluation for $n = 1$ and 2 are shown in Figure 4.

It is evident from these curves that the variation of gain with normalized aperture diameter, D/λ , falls into two regions. For larger D/λ ($D/\lambda > 400$),

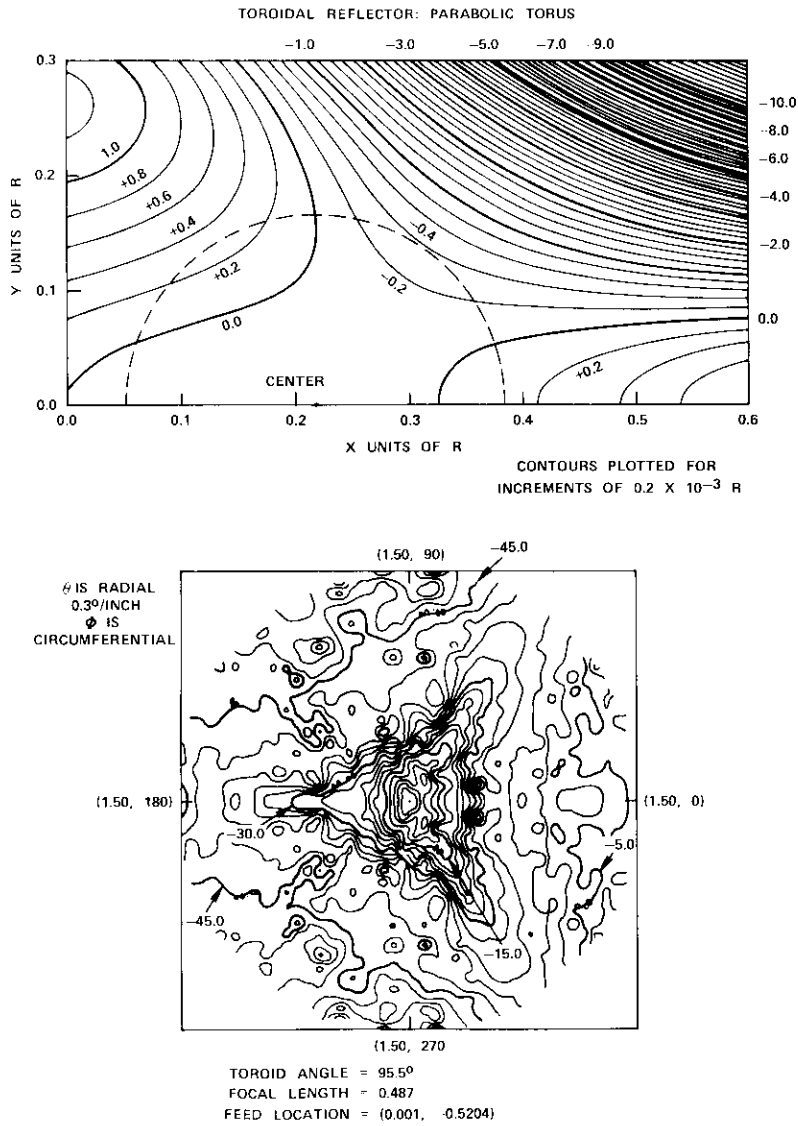


Figure 3. Path Length Difference Contours and Far-Field Radiation Pattern Contour Plot for Feed at (0.001, -0.5204)

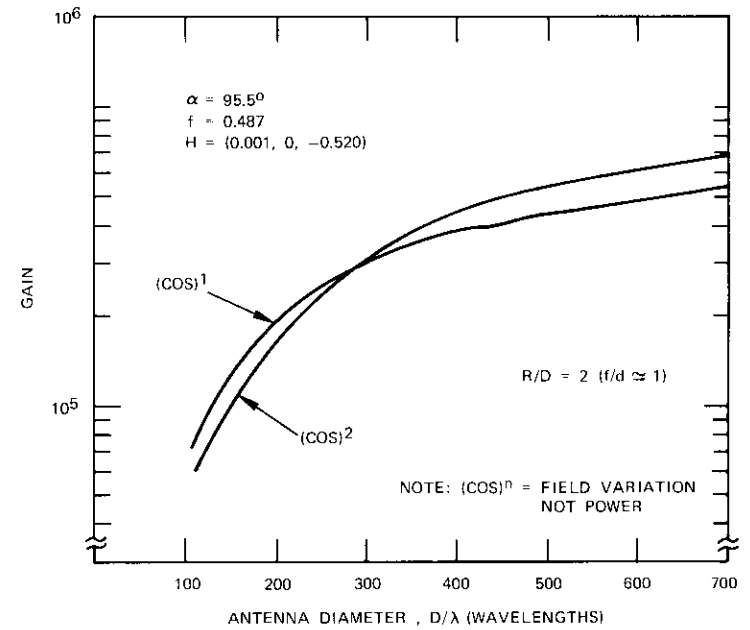


Figure 4. Parabolic Torus Gain vs Antenna Diameter with Illumination as a Parameter

there is a region where aberration dominates. In contrast, for smaller normalized apertures ($D/\lambda < 250$), a more uniform illumination function results in higher efficiency and antenna gain. This clearly implies that all of the illuminated region is adding to the gain. And so it may be concluded that the aberration is sufficiently low and that the system behavior is akin to that of focused systems. Between the two regions discussed above, there is a transition where neither regimen is dominant. It is clear that, for the parameters discussed, only for smaller reflectors, i.e., $(D/\lambda)_{\text{max}} \approx 220$, are good aperture efficiencies obtained without compensating for aberration or increasing the value of the parameter R/D .

Experimental model

Based on the preceding computations, the 10-ft scale model shown in Figure 5 was designed and fabricated to permit the detailed performance evaluation [2], [5] essential to verify the analytic design and provide an experimental basis for a full-scale design. The parameters of this scale

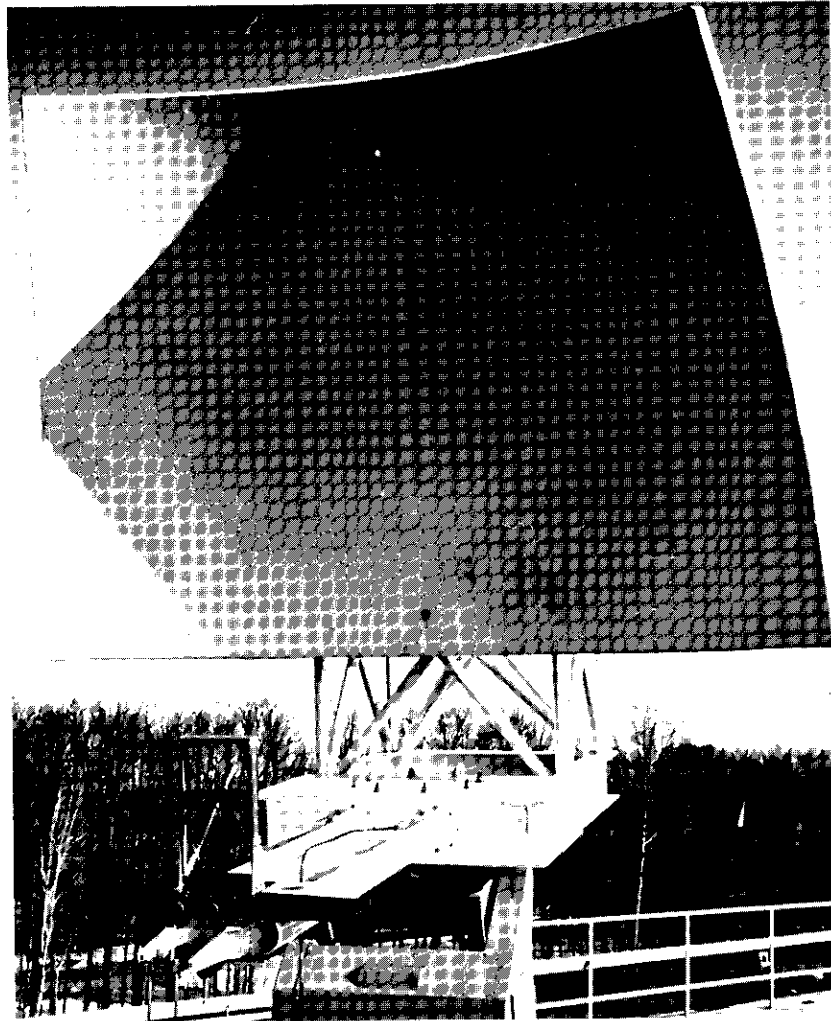


Figure 5. *Experimental Torus Reflector*

model are $f/R \approx 0.487$, $R/D = 2.0$, $\alpha = 95.50^\circ$, and antenna field of view = 15° . Figure 6 shows measured gain as a function of the frequency used in the scale model. Two gain points computed using an exact path length model are shown for comparison. The comparison is very good, within a few tenths of a decibel.

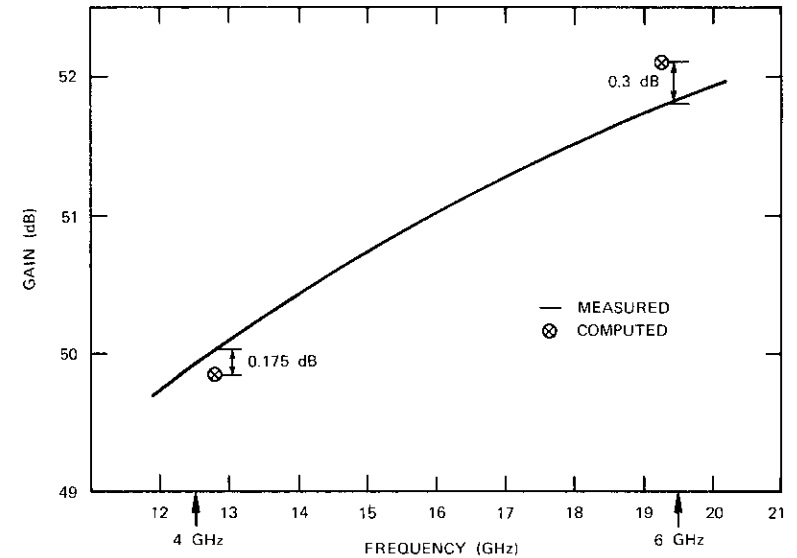


Figure 6. *Gain as a Function of Frequency*

Wide-angle radiation patterns were measured at several frequencies, and the peaks of the sidelobes plotted. The envelope of the peaks, shown in Fig. 7, is always below the line for a sidelobe level equal to $(32 - 25 \log_{10} \theta^\circ)$ dB, which is a widely accepted standard [6] for the sidelobe envelope representation of the "smoothed" peaks. In fact, the smoothed envelope falls off at $-30 \log_{10} \theta^\circ$ or better.

It has already been noted that the circular symmetries of the torus configuration permit the feed to be moved on a feed circle while scanning the unchanged beam over a scan cone defining the field of view of the antenna. Figure 8, which shows radiation patterns measured for the center beam (at 0°) and for a beam near one edge of the reflector (at 6° scan), demonstrates this property.

Again, as noted earlier, to obtain the necessary field of view, scanning orthogonal to the symmetry cone is required to follow the out-of-plane motion of the satellite. Here the geometry exacts a loss of gain comparable to the off-axis defocusing of a parabola of similar geometry. The results of measurements of this loss of gain are shown in Figure 9.

It has also been noted earlier that, because of the overlapping of illuminated regions on the toroidal reflector, less reflector area is required for several beams, with a consequent potential savings. The reflector surface

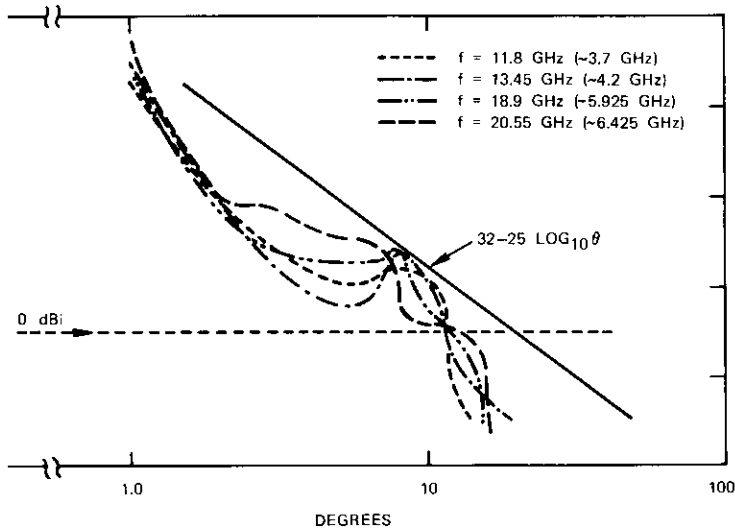


Figure 7. Pattern Envelopes for Torus Sidelobes

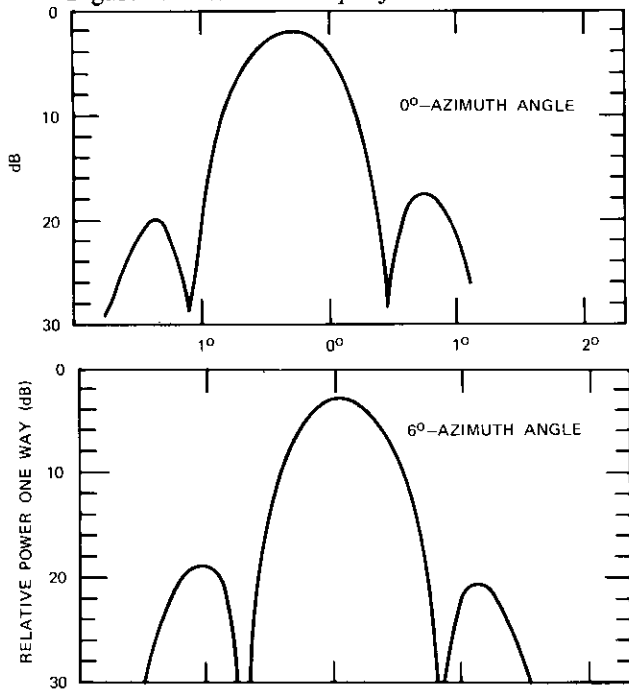


Figure 8. Azimuth Scan Characteristics (0° and 6°)

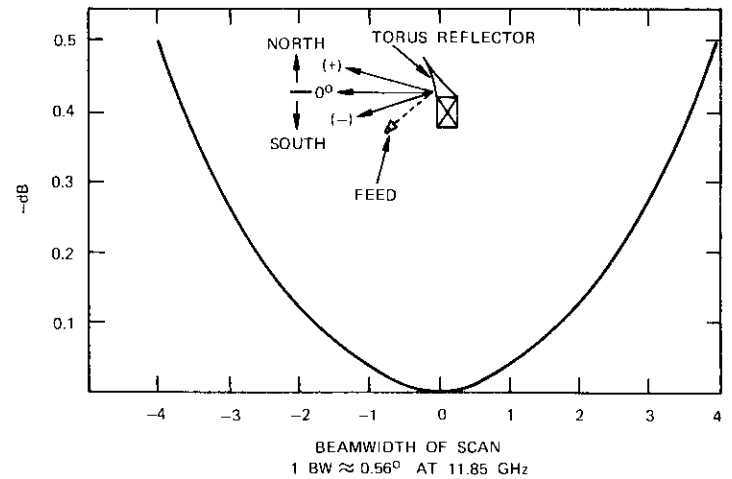


Figure 9. Gain Loss vs Elevation Scan

area has been calculated for a 32-ft torus and a typical 32-ft paraboloid. The results shown in Figure 10 clearly indicate that, for only two beams, the torus antenna surface is smaller than that of the paraboloid for fields of view approaching 20°. For three or more beams, the area of the torus antenna is significantly smaller for fields of view less than 37°.

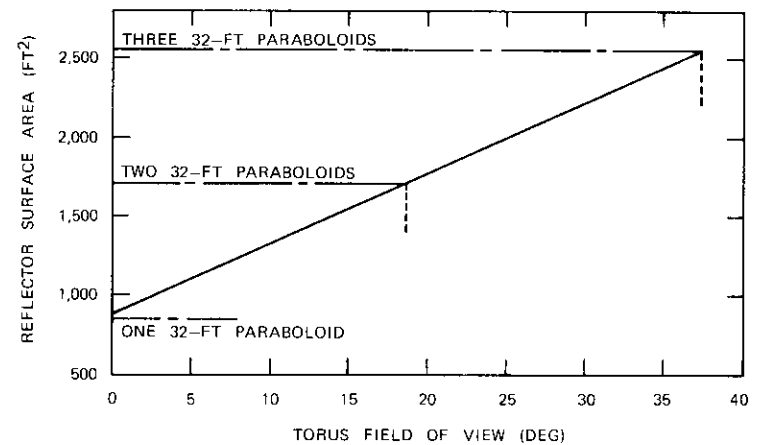


Figure 10. Torus Reflector Surface Area as a Function of Field of View

The UET torus antenna

The improved computer model [7] developed and verified using the scale model was applied to the design of the 32-ft UET MBTA. The results of a parametric study of variation of gain as a function of the parameters D/R , f/R , and feed displacement from the focus, Δ/R , versus frequency are shown in Figure 11. It is clear that aberration correction was not needed. Because it was desired to closely match the requirements of a domestic system ($G/T \geq 30$ dB/K), the values of f/R and R/D were chosen as 0.488 and 2.5, respectively (where $R = 80$ ft or 24.4 m), yielding a computed gain of about 54 dB at 6 GHz.

The UET MBTA (shown in Figure 1) was designed and fabricated to these electrical parameters as discussed below. Gain and far-field radiation patterns were measured by moving the feed horn and measuring the signal

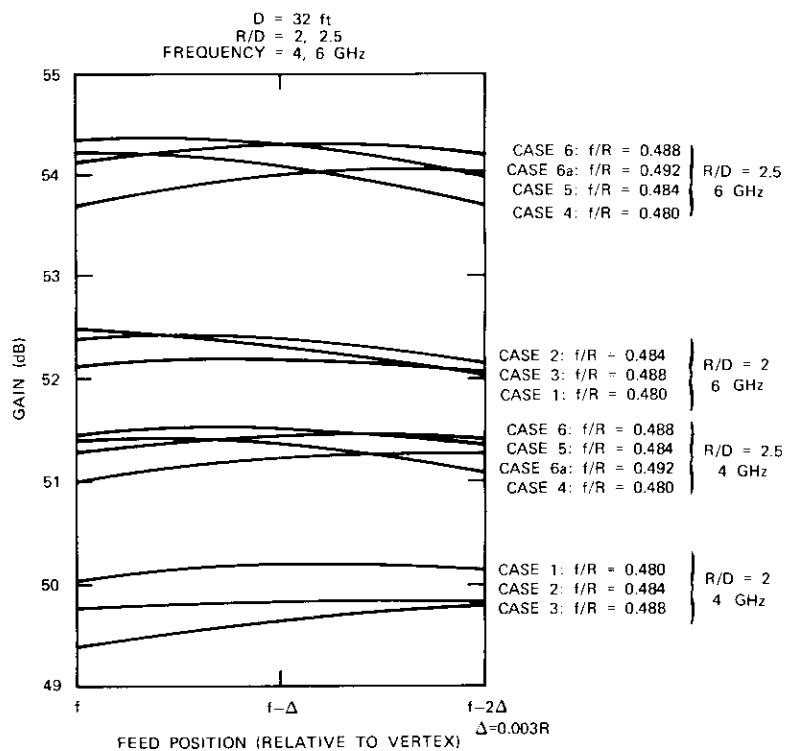


Figure 11. Gain Analysis for Front-Fed Torus

from an INTELSAT IV spacecraft. As discussed below, feed motions are in hour angle and declination. The hour-angle pattern (half-power beamwidth = 0.47°) with its characteristically low sidelobes is shown in Figure 12. The declination pattern shown in Figure 13 has a half-power beamwidth of 0.58° , with somewhat higher sidelobes since the scan motion introduces more aberration.

Gain and beamwidth were measured at several frequencies in the receive band. These data, shown in Figure 14, are remarkably consistent with external verification. A gain of 50.3 dB was calculated by using the formula $gain = 30,000/\text{beamwidth product}$. System loop measurements with a cooperating earth station at Andover, Maine, yielded a gain of 50.2 dB at 3,876 MHz. A gain of 50.5 dB was measured by comparison with another antenna (whose gain had been measured with some care) working the same satellite at the same frequency. Previous independent calculations based on computer modeling with due allowance for surface tolerance, feed efficiency, and waveguide losses gave an estimated gain of 50.3 dB at 3,900 MHz.

In the transmit band, the gain at 6,200 MHz was measured as 53.6 dB, while the computation-based estimate was 54 dB. The correspondence is still quite good.

The system G/T for a 32-ft earth terminal is calculated assuming a low-noise receiver noise temperature of 75 K, where the low-noise receiver is an uncooled paramp/receiver. Since

$$T_{\text{system}} = t_a + t_L + t_{\text{RCVR}}$$

the estimated torus antenna noise temperature, t_a , is

$$\begin{aligned} \text{spillover} &= 5 \text{ K} \\ \text{blockage} &= 0 \text{ K} \\ \text{main beam (10}^\circ \text{ elevation)} &= 12 \text{ K} \\ t_a &= 17 \text{ K} \end{aligned}$$

where t_L = feed, orthmode transducer (OMT), filter, and waveguide noise temperature
 $= 0.2 \text{ dB} = 13 \text{ K}$
 t_{RCVR} = uncooled paramp/receiver noise temperature
 $= 75 \text{ K}$.

Therefore, $T_{\text{system}} = 17 \text{ K} + 13 \text{ K} + 75 \text{ K} = 105 \text{ K}$. Taking the measured gain as 50.3 dB, a G/T of 30.1 dB/K is obtained for a 32-ft torus with a 75-K uncooled paramp.

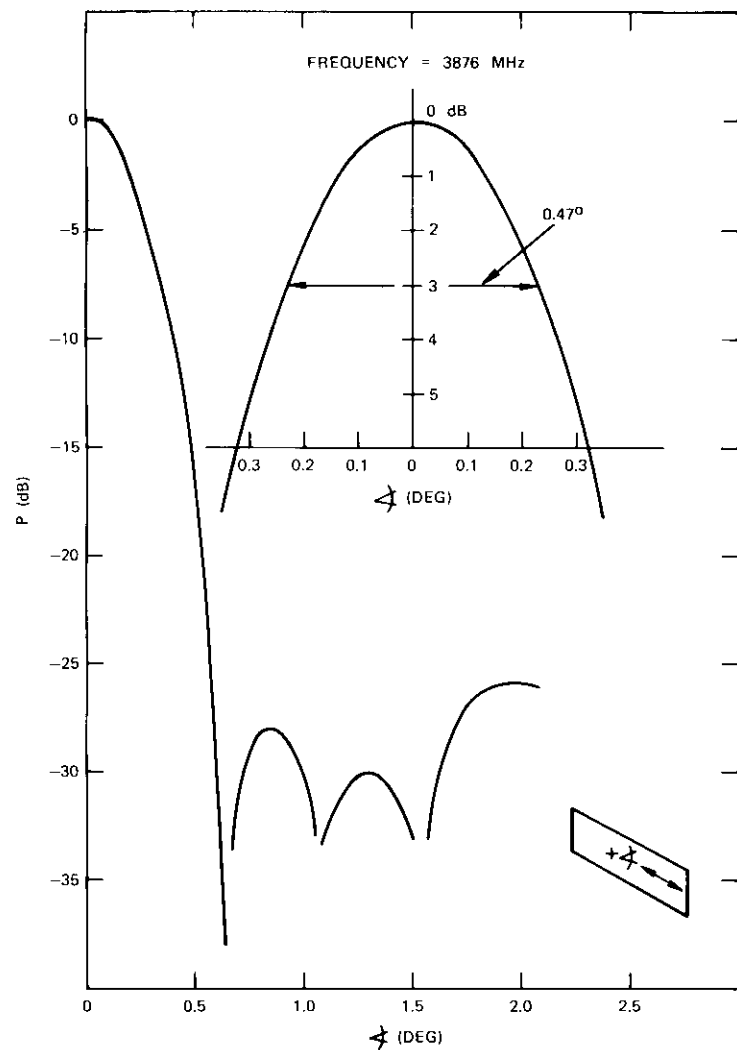


Figure 12. UET Antenna, Scan Plane Pattern

Corrugated horn feed

Tests of the scale model have shown that a torus antenna fed by a corrugated horn gives better performance than the same antenna fed by other feeds. The corrugated horn shown in Figure 15 provides axial symmetry

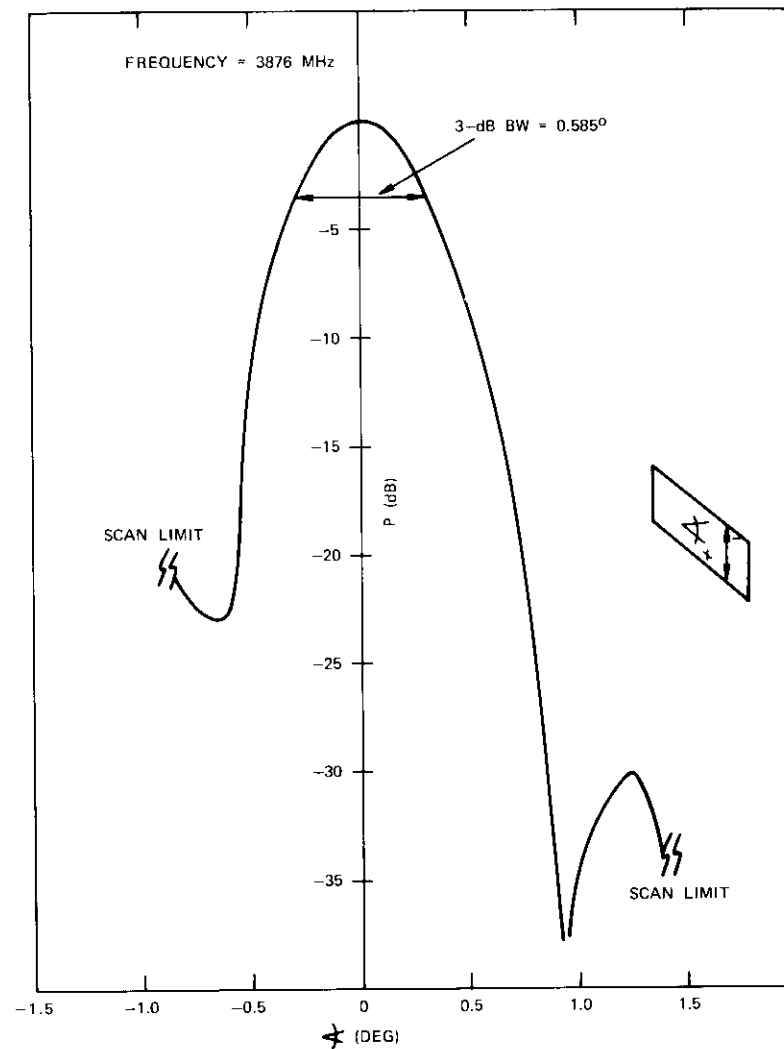


Figure 13. UET Antenna, Out-of-Plane Scan Pattern

(equal E- and H-plane patterns), sidelobe levels below 30 dB, appropriate amplitude taper, a beamwidth essentially independent of frequency over wide ranges of frequency, and negligible cross-polarized radiation. These properties are illustrated in Figure 16. The E- and H-plane radiation patterns shown are typical of this horn over the frequency band of 3.7 to

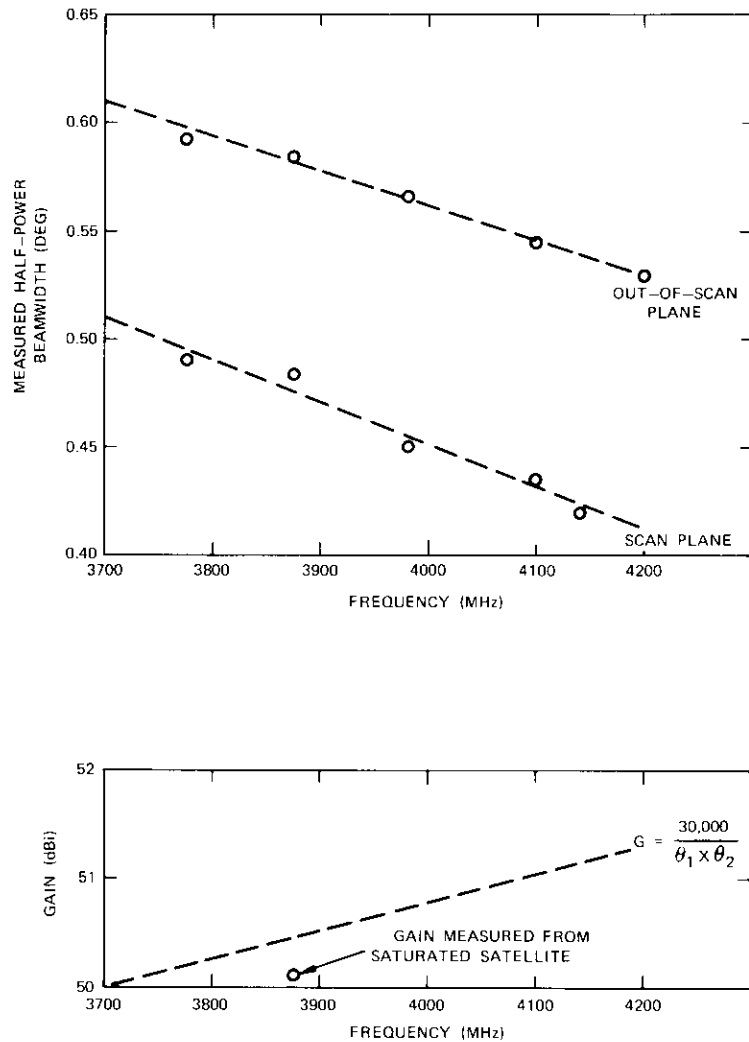


Figure 14. UET Antenna, Gain and θ_3 dB Summary

6.425 GHz. The horn has a true phase center whose location does not change with frequency.

The axial symmetry of the radiation patterns, together with the phase center properties, describes a polarization character which is identical to

the elemental Huygens source. This behavior results from the field distributions built up principally in the center of the horn by hybrid modes which are generated near the throat of the horn and propagate along the corrugated structure.*

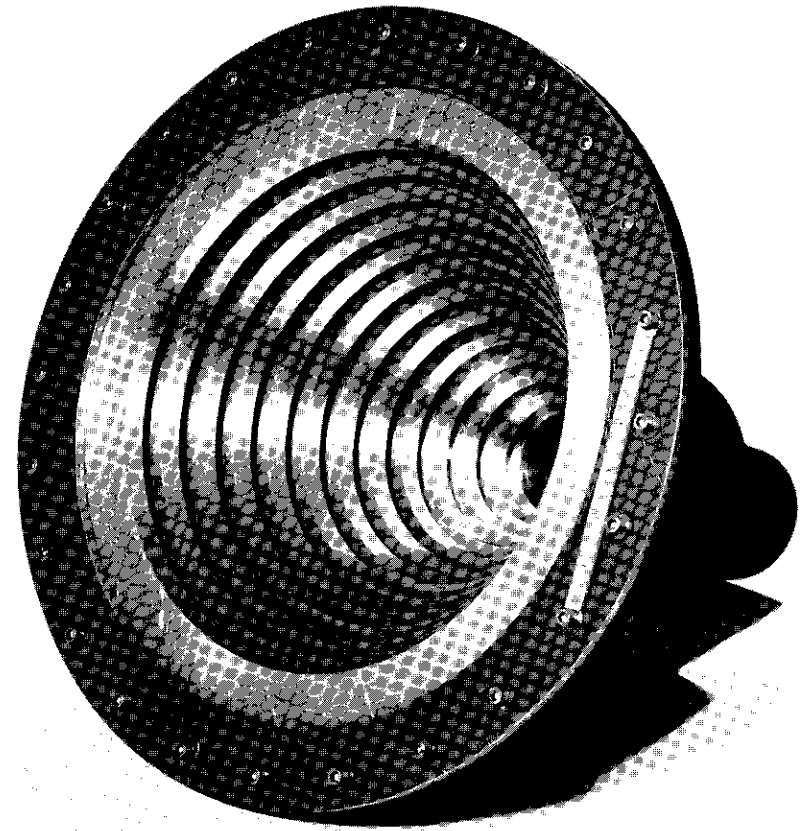


Figure 15. Corrugated Horn

*A more detailed discussion of the corrugated horn is given in the paper by R. Price, "High-performance corrugated feed horn for the unattended earth terminal," which also appears in this issue.

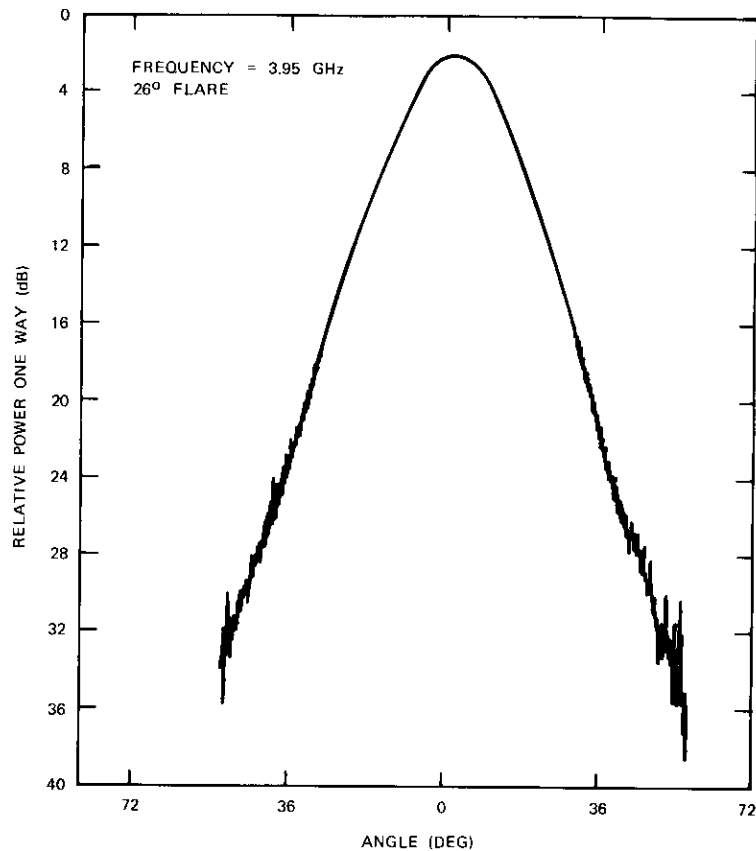


Figure 16. *E- and H-Plane Radiation Patterns of Corrugated Feed Horn*

Orthomode transducer and polarizer

There are basically two sets of requirements imposed on the OMT and polarizer design for the UET. The first set pertains to the INTELSAT IV operational requirements: receive on right-hand circular polarization, transmit on left-hand circular polarization, axial ratio less than 0.3 dB, and isolation adequate for receive protection (typically 80 dB). Figure 17 is a photograph of the OMT and polarizer designed to these requirements.

Far more interesting is the set of requirements imposed by frequency reuse using orthogonal polarizations, which enables theoretical doubling of

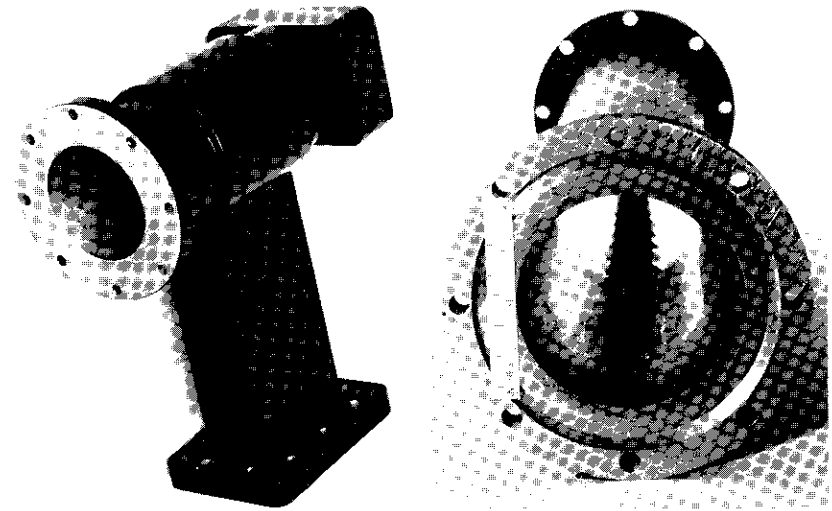


Figure 17 a. *OMT* b. *Polarizer*

the communications capacity. Implied in this operation are the requirements imposed on the OMT and polarizer circuits: simultaneous reception and transmission on orthogonal polarizations and a high degree of isolation between waves which are nominally orthogonally polarized.

The system requirements imposed on OMT/polarizer designs for frequency reuse are as follows:

polarization mode:	dual linear polarization (LP) or dual circular polarization (CP)
polarization rotation (LP only):	$\pm 10^\circ$ transmit relative to receive
axial ratio:	CP: <0.5 dB; LP: >40 dB
insertion loss:	<0.1 dB
VSWR:	<1.15:1

These specifications apply to both transmit and receive bands.

The design approach selected to meet these requirements centers on the use of a novel junction to separate the transmit and receive frequency bands. Once the frequency separation has been achieved, the remaining components, e.g., the polarizers, can be designed for relatively narrowband

operation, thus attaining the required polarization characteristics. The successful design of the directional junction is fundamental to the successful design of the network.

The directional junction is based on coupling between circular and coaxial waveguide sections using a short section of corrugated waveguide as a transition. The basic junction geometry is illustrated in Figure 18. As indicated, the circular waveguide section supports both transmit and receive frequencies in the TE_{11} mode, the coaxial waveguide supports the TE_{11} mode in coaxial guide, and the center conductor supports only the TE_{11} 6-GHz mode. The design problem then is to funnel the 4-GHz fields in the circular grid into the coaxial guide while simultaneously coupling the transmit fields from the conductor guide to the larger circular waveguide. The corrugated waveguide section is used to perform this function.

The actual design of the junction entailed a substantial amount of detailed effort relating to such problems as impedance matching, achieving 6- to 4-GHz isolation, and mode purity.

Once frequency band separation has been achieved by means of the directional junction, the remaining components are designed on the basis of a 10- to 12-percent bandwidth. Figure 19 is a sketch of the complete OMT/polarizer assembly implemented for circular polarization. For linear polarization the polarizer sections are removed and a rotary joint is mounted on the transmit waveguide to permit relative isolation rotation.

The design of the transmit band ortho-coupler was matched to better than 1.15 and had more than 40-dB/in. (15.8-dB/cm) linear or about 25-dB/in. (9.8-dB/cm) circular polarization isolation between ports. The polarizer was designed with a maximum axial ratio of about 0.15 dB. The

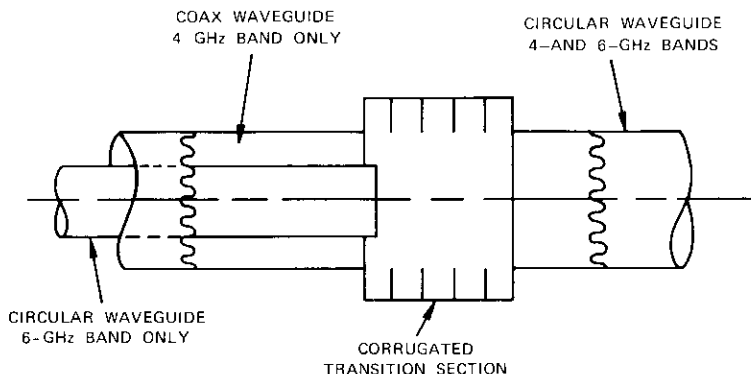


Figure 18. Directional Junction Geometry

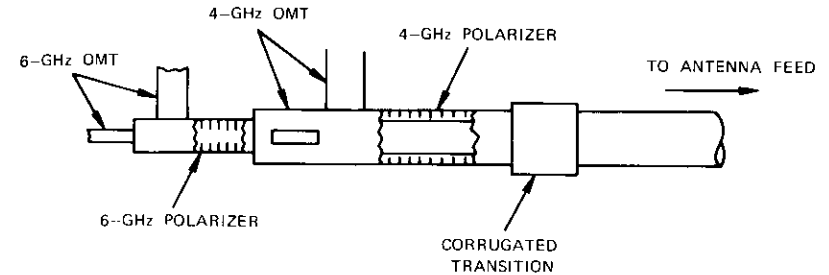


Figure 19. OMT/Polarizer Assembly (CP mode)

ortho-coupler and polarizer together had an insertion loss of about 0.06 dB.

On the receive side a considerable effort was required to design the ortho-coupler and polarizer in coaxial waveguide. The ortho-coupler consisted of a pair of displaced unbalanced waveguides shunt coupled to the coaxial waveguide. The guides were displaced to prevent evanescent TE_{21} mode coupling and a vane was employed to provide appropriate reactive loading to the guides. To increase the 6- to 4-GHz isolation to that required for receive protection, waffle-iron low-pass filters were designed in each of the coupled waveguides with reference planes essentially at the junction.

The polarizer design in the coaxial guide utilizes periodic reactive elements. On the basis of extensive experimental evaluation, a simple iris has been selected as the reactive element. The final design of the polarizer embodies 12 iris pairs in a tapered distribution. The design achieves an axial ratio of less than 0.20 dB over the entire receive band.

The complete OMT and polarizer design meets all the requirements discussed earlier. The overall insertion loss is 0.5 dB in the transmit band and 0.15 dB in the receive band. The axial ratio is less than 0.25 dB (CP mode) in either band and all ports are matched to better than 1.15 CP.

Beam steering mechanism

It has been noted in the previous section that, for feed positions along the geostationary arc, the feed point sweeps out a circular arc (see Figure 2). This arc is the same arc used for in-plane scanning of a single feed to follow the motions of a single satellite, and it almost exactly simulates hour-angle motion in a satellite tracking hour-angle/declination mount. Moving the feed orthogonal to this trajectory closely corresponds to declination scan-

ning. Because of the torus geometry, these are the natural ways to move the feed; the feed mechanism has been constructed accordingly. The requirement for feed steering [8] has been given careful consideration. Table 1 shows the history of satellite box size, and Table 2 indicates the gain loss as a function of satellite station box size. For the UET MBTA in an INTELSAT IV environment with stationkeeping of about $\pm 0.5^\circ$, gain loss would be prohibitive without steering. However, for future applications involving stationkeeping within $\pm 0.1^\circ$, this question will be reopened.

The feed support shown in Figure 20 has been designed and built to support several feeds on the focal arc of the reflector and to look through a

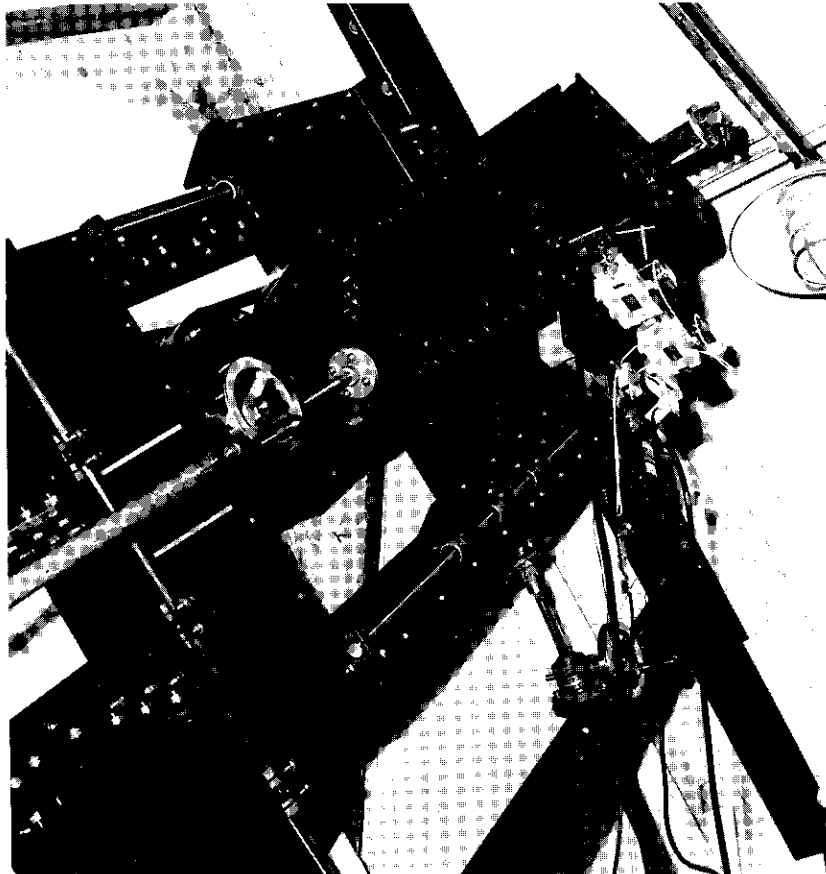


Figure 20. Feed Support

TABLE 1. HISTORY OF SATELLITE BOX SIZE

Satellite	Epoch	Satellite Box Size	
		East-West (in-plane)	North-South (out-of-plane)
EARLY BIRD	1965	12°	no control
INTELSAT II	1967	4°	3°
INTELSAT III	1969	2°	2°
INTELSAT IV	1971	1°	1°
Domestic Satellite (COMSAT GENERAL)	1975	0.2°	0.2°

window in the side of the upper room. The window is about 40 in. (1.01 m) wide and runs just below and parallel to the sloping roof of the tower. The roof slope is determined by the tilt of the reflector, which is set by the satellite geostationary arc as seen from the antenna location. The feed support consists of two bearing rails, one attached to the roof and the other attached to brackets just below the window. The rails are curved to follow the focal arc of the torus reflector. They support an azimuth plate through several roller bearings. Motion of the plate assembly along the curved rails provides hour-angle steering. Two similar straight rails are mounted on the back of this plane and an elevation plate is supported on these to provide declination steering. The feed and its associated paramps and other equipment are supported on a truss structure mounted on the elevation plate. Provisions are made for mechanically adjusting the feed toward and away from the reflector to coincide with the focal point.

TABLE 2. GAIN LOSS* VERSUS SATELLITE STATIONKEEPING

Uncertainty Box Size (deg)	Minimum Half-Power Beamwidth (deg)				
	0.5-dB	1-dB	2-dB	3-dB	4-dB
	Gain Loss	Gain Loss	Gain Loss	Gain Loss	Gain Loss
0.03 × 0.03	0.075	0.052	0.037	0.03	0.026
0.1 × 0.1	0.25	0.17	0.12	0.1	0.09
0.2 × 0.2	0.49	0.35	0.25	0.2	0.17
0.3 × 0.3	0.75	0.52	0.37	0.3	0.26
0.5 × 0.5	1.2	0.87	0.61	0.5	0.43
1 × 1	2.5	1.7	1.2	1.0	0.9

* Gain loss is 1-way loss in directive gain.

Once the feed is adjusted to its focal point, it remains fixed and all other steering is provided by moving the elevation and azimuth plates. Jactuators are provided on each plate to steer the feed $\pm 1^\circ$ on each axis. These have been motorized with a small AC motor so that the feed can be remotely positioned using the communications signal as a reference for peaking. If the feed is to be moved to another satellite, the Jactuator support for the azimuth steering can be relocated and the whole mechanism can be slid along the focal arc to the new position. A readout synchro has been provided to remotely indicate the feed position.

Structure

The structural requirements of the MBTA were predicated upon the desire to view synchronous satellites within a 20° sector of the synchronous arc. The 32-ft-aperture antenna was to operate in winds of 45 mph (72 km/hr) with full capabilities and up to 60 mph (96 km/hr) with a small degradation in performance. The structure was designed to survive 100-mph (160-km/hr) winds without exceeding stress levels which allow normal safety factors. In the operational environment, the antenna, after alignment, was to be capable of pointing at a given satellite to within one tenth of a beamwidth (0.05°). A surface accuracy of 0.035 in. (0.09 cm) rms was required.

The requirement to look at satellites in a 20° longitude band has established the width of the antenna as approximately 55 ft (16.76 m). This allows the feed or multiple feeds to be located anywhere along the feed arc $\pm 10^\circ$ from the center satellite position (see Figure 21). An additional requirement is imposed for beam steering to follow individual satellites which may vary $\pm 1^\circ$ in hour angle and declination.

The wind environment imposes the major loads on the antenna structure. An analysis was made to determine the distorted shape of the reflector while subjected to steady 45-mph wind loads from the front and back. Nonsymmetrical wind loads were also analyzed. Survival wind load stress levels were easily met in most members, since the reflector design had to be very stiff to meet the pointing and surface accuracy requirements. Although the dead load of the structure in its final position contributes to the member stresses only at survival, distortions were calculated for faceup and look angle positions to determine the contour change between the reflector surface alignment faceup in position and final position. This contour change was budgeted in the total error allowed in the look angle position. A 10° temperature differential between the front and back structural mem-

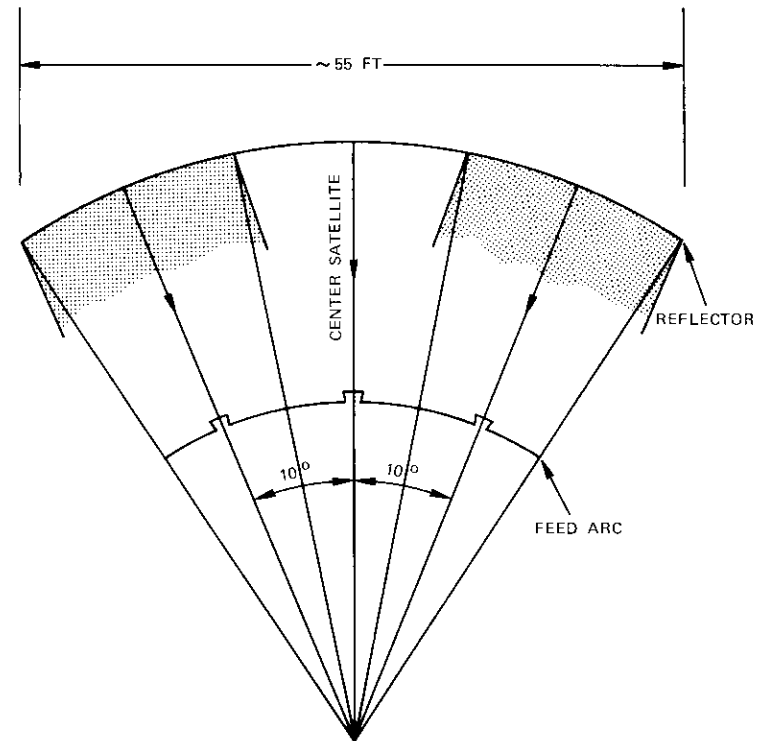


Figure 21. Location of Feeds Along the Feed Arc

bers was used to determine the solar differential effects on the surface tolerance while operating.

A preliminary design concept provided a modular type of structure that realized economy of fabrication. Hand calculations established the first estimate of member sizes. With these calculations and the design concept it was possible to calculate the coordinates of node points in the truss structure for analysis by the NASTRAN program created by NASA for analysis of complicated 3-dimensional structures.* Once the program was established it was possible to vary member sizes to optimize them for the desired surface accuracy and pointing errors. A typical set of rms values obtained

* A more detailed discussion of this analysis is included in the paper by A. Abu-Taha, entitled "Structural analysis of the unattended earth terminal antenna," which also appears in this issue.

from such an analysis is shown in Table 3. The surface accuracy budget was established to allocate the allowable error to various factors which had to be included. The budgeted and measured values for 45- and 30-mph (62- and 48-km/hr) wind are shown in Table 4.

Since a sandbag test indicated that the panel design was not as stiff as anticipated, the actual achieved surface error was higher than desired, but within the original design goal. The numbers shown in Table 4 are based on consideration of the full reflector. If only the 32-ft aperture had been included, an improvement in surface accuracy would have been realized. The

TABLE 3. SUMMARY OF ANTENNA SURFACE RMS CALCULATIONS

Loading Condition	rms (in.)				
	Case I ^a	Case II ^a	Case III ^a	Case IV ^a	Case V ^a
Gravity Loading at Look Angle	0.023	0.022	0.017	0.020	0.015
45 mph, Horizontal to Beam Axis	0.010	0.008	0.007	0.009	0.006
100 mph, Horizontal to Beam Axis	0.042	0.034	0.028	0.034	0.022
45 mph, Horizontal to Ground	0.024	0.021	0.017	0.020	0.013
100 mph, Horizontal to Ground	0.095	0.082	0.069	0.082	0.052
Gravity Loading + 45 mph Horizontal to Ground, Front Face of Antenna	0.015	0.015	0.012	0.014	0.013
Gravity Loading + 45 mph Horizontal to Ground, Back Side of Antenna	0.032	0.030	0.022	0.027	0.019
Gravity Loading + 100 mph Horizontal to Beam Axis, Front Face of Antenna	0.025	0.017	0.020	0.022	0.018
Gravity Loading + 100 mph Horizontal to Beam Axis, Back Side of Antenna	0.063	0.054	0.042	0.051	0.033
Gravity Loading + 45 mph Horizontal to Ground, Front Face of Antenna	0.007	0.005	0.007	0.007	0.007
Gravity Loading + 45 mph Horizontal to Ground, Back Side of Antenna	0.046	0.043	0.033	0.040	0.028
Gravity Loading + 100 mph Horizontal to Ground, Front Face of Antenna	0.073	0.061	0.054	0.063	0.039
Gravity Loading + 100 mph Horizontal to Ground, Back Side of Antenna	0.117	0.104	0.084	0.100	0.066
10° ΔT	0.014	0.014	0.014	0.014	0.014
Gravity Loading, Antenna Looking Horizontally	0.007				
Gravity Loading, Antenna Looking Faceup	0.005				

^a Cases I through V represent the original configuration and sizing and four subsequent connect rod configurations, respectively, used in NASTRAN computations.

TABLE 4. SURFACE ACCURACY

	rms (in.)		
	Budget	45 mph (measured)	30 mph (measured)
Panel Manufacturing	0.015	0.015	0.015
Panel Alignment	0.015	0.015	0.015
Panel Wind Load and Dead Load	0.015	0.030 0.007	0.015 0.007
Structure Wind Load at Look Angle	0.015	0.016*	0.008*
Structure Dead Load at Look Angle	0.015	0.013*	0.013*
Support Alignment	0.010	0.013	0.013
TOTAL	0.035	0.044	0.034

* Calculated.

panels could be designed to be stiffer or more intermediate supports could be used if a tighter surface accuracy were required.

The pointing error is subject to reflector alignment, feed alignment, and relative positions between the reflector and feed. The pointing errors calculated for a 39.4-ft (12-m) antenna are shown in Table 5. The values for a 32-ft antenna are smaller.

The foundation and structure were aligned to better than 0.01°. After

TABLE 5. POINTING ERRORS

	Error (deg)
Reflector and Support	
Elevation	0.013
Azimuth	0.004
Vector	0.013
Tower Foundation	0.007
Reflector Foundation	0.005
Tower	0.006
TOTAL (Algebraic)	0.031

installation it was realized that the fine alignment of the structure was not as significant as originally thought since the steering capability allows for a $\pm 1^\circ$ adjustment of the beam. As a result, beam positioning can be used to compensate for some of the misalignment.

The desire to develop an antenna which could be used anywhere in the U.S. has resulted in a universal reflector structure design. It consists of a triangular spine truss with nine vertical flat trusses, each identical to the others, to provide a modular structure. The spine truss is supported on four points by the reflector support structure. This structure is a universal design, but requires changes in the lengths of some members to fit the orientation for each specific site. The foundation center line dimensions and the tower location with respect to the reflector must also be varied for different locations. Only four different reflector panels are used in the reflector surface, eight units of each.

This modular concept for the panels and reflector backup structure simplifies the shop tooling and lowers the fabrication costs. The reflector structure is shop welded whenever possible and field bolted with high-strength bolts. The spine truss is shipped in three pieces and bolted together in the field. The flat trusses are shipped as subassemblies and bolted to the spine truss with intermediate bracing. The panels come as complete units, which are supported on four stud bolts welded in the field to the backup structure. These studs provide the adjustment mechanism to set the surface to the required accuracy and reduce secondary stresses and distortions due to differential expansion of the steel backup structure and the aluminum panels.

The field alignment of the reflector surface was performed with the antenna on four temporary foundation supports and the reflector looking at the zenith. A special jig was mounted on the reflector to support the theodolite used for surveying the panels, and a special theodolite mount with a bearing mounted tape attachment permitted a tape to be stretched from the center of the instrument to the panel corners where the targets were fixed at precalculated positions. A 1-second theodolite was used to survey azimuth and elevation angles to establish the position of the targets to within 0.015 in. (0.04 cm) rms of the desired surface. All final surveying was performed at night to prevent distortions and nonrepeatable readings which would have resulted from temperature changes due to solar radiation. After the surface alignment the entire reflector was picked up by a crane and set on the four support points (see Figure 22), which were then aligned to be at the proper slope and to lie within a plane, duplicating the alignment condition during the surface accuracy survey.

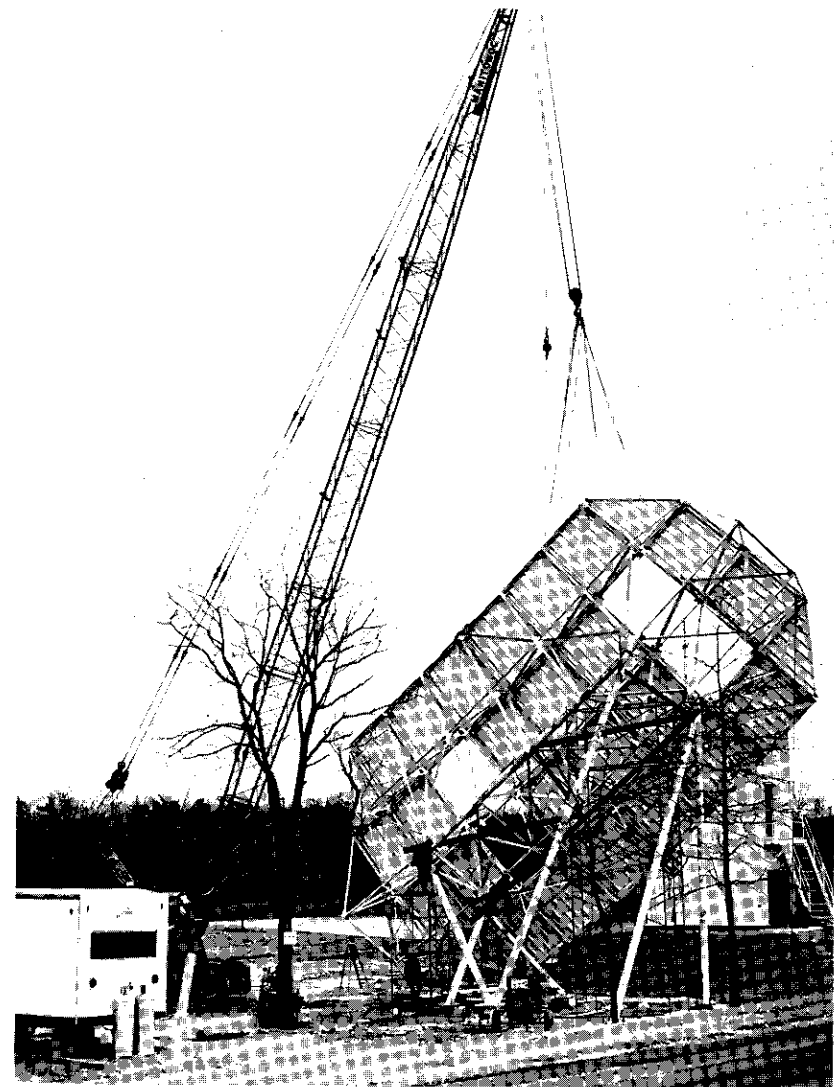


Figure 22. *Placement of Reflector on Support Points*

The tower has been designed to provide a stiff structure to prevent beam misalignment due to focal length changes with respect to the reflector. It provides space for batteries, power equipment, transmitters, feed horn, and

receivers. The batteries and power equipment are located on the ground floor and the RF equipment is located in the upper room. To minimize the tower height and provide easier access, the ground has been filled about 5 ft so that the ground floor is level with the adjacent road. The tower is a simple steel structure with diagonal bracing for stiffening. The upper floor is metal decking covered with fireproof plywood and vinyl tile. The roof and walls are corrugated steel, insulated with flat steel interior panels. The walls and roof are galvanized and prefinished in the shop. They are fitted, cut, and attached to the steel with stainless steel self-tapping nylon hex head screws.

The engineering model built at Clarksburg was manufactured and erected with COMSAT acting as the general contractor. Contracts were awarded separately for the fabrication of the steel structure and for the panels. Another contractor aligned and installed the reinforced concrete foundations by using a north-south baseline established by COMSAT Laboratories and a surveying subcontractor. The steel and aluminum for the reflector and tower were aligned and erected by still another contractor.

Panel alignment using theodolite and tape was accomplished at night in a conventional manner, although the lack of complete circular symmetry required more individual attention to each panel point adjustment. Only two points could be set with each tabulated elevation angle, and azimuth angles were more important than usual for a paraboloidal reflector, since they established the spacing between panels in the wide dimension of the reflector. The unique alignment problem for this type of antenna is the requirement to place the four points of support in a plane once the reflector was mounted at the look angle. This requirement resulted from the desire to obtain a surface accuracy at the look angle that is the same as that built into the surface when it was adjusted on the ground. These four points were surveyed from a baseline oriented with respect to north using a 1-second theodolite and surveyor's tapes. After alignment the points were found to be in a plane within 0.024 in. (0.06 cm). This resulted in an overall surface misalignment of 0.013 in. (0.03 cm) rms, which was considered acceptable. Since the engineering model was to be used for experiments at higher frequencies, the alignment requirements were more rigorous than those which would be necessary for an antenna to be used in the 4- to 6-GHz range.

The MBTA reflector structure and tower were designed and built using standard techniques of analysis, fabrication, and erection to produce an economical and useful antenna system which would demonstrate the feasibility of a multiple-beam system.

Acknowledgments

The work described herein covers the efforts of many people. W. Korvin directed the experimental torus measurements and contributed to the design phase of the MBTA. The feeds used in the experimental model as well as in the UET MBTA were developed and designed by R. Price. R. Gruner was responsible for the efforts on the OMT and polarizer. The computer programs used in the earlier work were developed by J. Jih. The General Antenna Program used in later analysis and verification was developed by W. Cook, who also assisted in the application of NASTRAN to the structural analysis performed by A. Abu-Taha. M. Vlissides assisted ably in all phases of the structural design. C. Crane contributed heavily to the site preparation work. This effort was part of the overall UET program under the direction of L. Pollack and W. Sones.

References

- [1] G. Hyde, "A Novel Multiple-Beam Earth Terminal Antenna for Satellite Communications," IEEE 1970 International Conference on Communications, San Francisco, California, June 8-10, 1970, *Conference Proceedings*, Paper No. 70-CP-386-COM, pp. 38-24-38-33.
- [2] G. Hyde and W. Korvin, "The Front-fed Toroidal Multiple Beam Earth Terminal Antenna," to be published.
- [3] K. S. Kelleher and N. H. Hibbs, "A New Microwave Reflector," NRL Report 4141, Naval Research Laboratory, May 11, 1953.
- [4] R. W. Kreutel, Private Communication.
- [5] G. Hyde, W. Korvin, and R. Price, "A Fixed Multiple Beam Toroidal Reflector Antenna Operating at Frequencies Above 12 GHz," IEEE International Conference on Communications, Montreal, Canada, June 11-14, 1971, *Conference Proceedings*, pp. 27-11-27-16.
- [6] International Radio Consultative Committee (C.C.I.R.), "Radiation Diagrams of Antennas at Communication-Satellite Earth Stations for use in Interference Studies," Report 390-1, XIIth Plenary Assembly, New Delhi, 1970, Vol. IV, Pt. 2, pp. 183-188, Geneva: International Telecommunication Union, 1970.
- [7] W. L. Cook and G. Hyde, "A General Purpose Interactive Antenna Analysis Program," 1973 G-AP International Symposium, Boulder, Colorado, August 22-24, 1973, *Symposium Tech Program*, pp. 91-94.
- [8] G. Hyde, "Considerations in the Choice of Parameters for a Small Satellite Communications Earth Station Antenna," IEEE International Conference on Communications, Philadelphia, Pennsylvania, June 19-21, 1972, *Conference Record*, pp. 18-21-18-26.

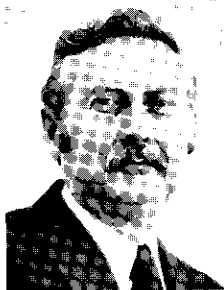


Geoffrey Hyde received his B.A.Sc. in engineering physics and M.A.Sc. in electrical engineering from the University of Toronto in 1953 and 1959, and his Ph.D. in electrical engineering from the University of Pennsylvania in 1967. Prior to joining COMSAT Laboratories in 1968, he worked on antennas, microwaves, and propagation for RCA, for Avro Aircraft Co., and at Sinclair Radio Labs in Canada. At COMSAT he has worked on development of the torus antenna, a general antenna analysis computer program and the UET. He is

Manager, Propagation Studies Department.

Dr. Hyde received David Sarnoff Fellowships (1965 and 1966) and (jointly with Dr. Roy C. Spencer) the IEEE G-AP award for best paper, 1968. He is a member of IEEE, the IEEE Antenna and Propagation Society (Adcom) and a member of Commission II of URSI.

Randall W. Kreutel, Jr. received B.S.E.E. and M.S.E.E. degrees from Northeastern University. Prior to joining COMSAT, he was a research engineer with the Antenna and Microwave Lab of Sylvania Electronic Systems. He joined COMSAT in 1966 as a member of the technical staff. As Manager of the Antennas Department he is currently responsible for research and development of antennas and antenna-related equipment. He is a senior member of IEEE, a member of Eta Kappa Nu, and a member of Commission I of the International Scientific Radio Union.



Lewis V. Smith, Jr. received his B.C.E. from Cooper Union in 1947 after serving with the Army, and his M.C.E. from the Polytechnic Institute of Brooklyn in 1954. He is a registered professional engineer in New York and Maryland and a member of Sigma Xi. He worked with Edwards & Hjorth Consulting Engineers, General Bronze Cbrp. and American Machine and Foundry, and has specialized in antenna structures and mechanisms since 1955. He joined COMSAT in 1965, as a member of the Earth Station Engi-

neering Division, involved with international technical advisory service and COMSAT Laboratories. He is Manager of the RF Systems Engineering Department and technical officer for the new antennas at Etam and Andover.



Index: unattended earth terminals, multiple-beam antennas, structural analysis, computer systems programs.

Structural analysis of the unattended earth terminal antenna

A. ABU-TAHA

(Manuscript received April 9, 1974)

Abstract

This paper describes the semiautomated structural analysis of the fixed unattended earth terminal (UET) multiple-beam torus antenna (MBTA). The iterative analysis cycle has resulted in a lightweight engineering model that meets design requirements. The stringent design criteria are surface accuracy under operational loading conditions and structural integrity under survival loading conditions.

NASTRAN, the NASA structural analysis program, is used as the analysis tool in the design procedure. The design procedure includes the formulation of a representative structural model, the NASTRAN static and normal mode analyses, and processing of the results. The use of additional software in concert with NASTRAN has improved the accuracy of the analysis and enhanced the convergence on a final design.

Introduction

General-purpose digital computer programs based on finite-element techniques have proved to be valuable tools for determining the behavior of large elastic structures. One such program which provides a wide range of analytical capability is the NASA structural analysis program, NASTRAN. The basic idea of the finite-element method is to divide a

complex structure into simple interrelated structural elements. The usefulness of the method is best realized by employing the digital computer to solve the resulting matrix equations. Additional software used in concert with NASTRAN and resulting in a semiautomatic design procedure can greatly improve the speed and accuracy of the analysis of structures having many degrees of freedom. Such a design procedure has been used in the iterative design cycle of the unattended earth terminal (UET) multiple-beam torus antenna (MBTA).*

The UET antenna, shown in Figure 1, is a fixed torus antenna with satellite tracking accomplished by independent steering of the feed horns. Surface accuracy under operational loading and structural integrity under survival loading have been the major controlling design factors.

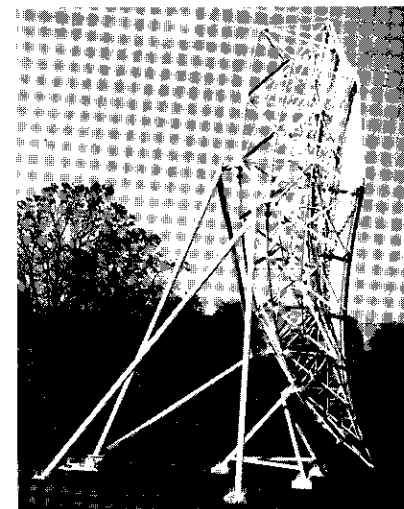
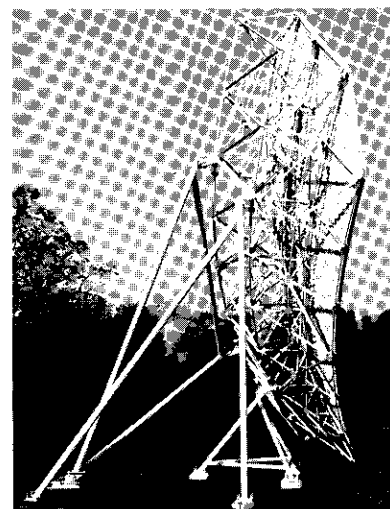
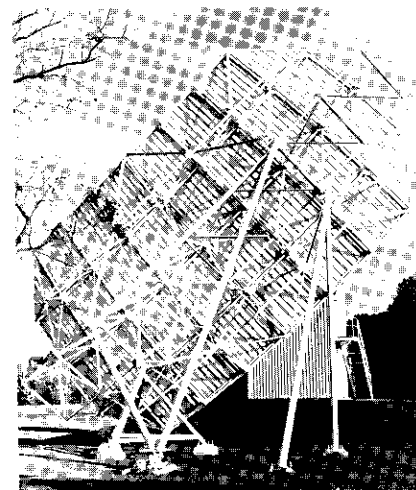
The NASTRAN program has been used as the analysis tool in the structural design of the UET antenna structure, which includes a reflecting surface, a backup structure, and a fixed support structure. The final results of each design cycle have been evaluated and structural modifications incorporated where necessary. Four different configurations have been analyzed, and approximately six redesign cycles of the selected configuration have been required to converge on a final design. The final configuration and one redesign cycle are described in this paper.

General description of the UET antenna

A typical synchronous satellite communications antenna consists of a parabolic reflecting surface and a backup structure supported and driven by a steerable mount. The elevation/azimuth steering is essential to maintain line-of-sight with the synchronous satellite as it experiences perturbation in its geostationary orbit. Such an antenna system is capable of receiving and transmitting signals to one satellite at a time. For simultaneous links with three satellites, three such antennas are necessary.

A novel multiple-beam earth terminal [1] can provide simultaneous links with three or more satellites occupying a 20° segment of the geostationary arc. The reflecting surface is a fixed torus with satellite tracking accomplished by independent movements of several feed horns. This configuration eliminates the driving gear needed to steer the typical 10- to 30-m (32.8- to 98.4-ft) parabolic antennas and replaces it with a simple feed steering mechanism.

*See the papers entitled "An unattended earth terminal for satellite communications" and "The unattended earth terminal multibeam torus antenna," which also appear in this issue.



THE TWO PHOTOS IMMEDIATELY ABOVE CAN BE VIEWED AS A STEREOSCOPIC PAIR. SEE FIGURE 9 FOR METHOD

Figure 1. UET/MBTA Fixed Antenna

The UET/MBTA reflecting surface and backup structure are mounted on a fixed support structure which is designed to orient the reflecting surface so that a given segment of the geostationary orbit is scanned. The orientation (look angle) of the torus, which depends on the location of the antenna relative to the central satellite point, consists of two rotations of the aperture plane from the local vertical plane: an elevation angle, ξ , and a tilt angle, Ω , shown in Figure 2. The orientation of several torus

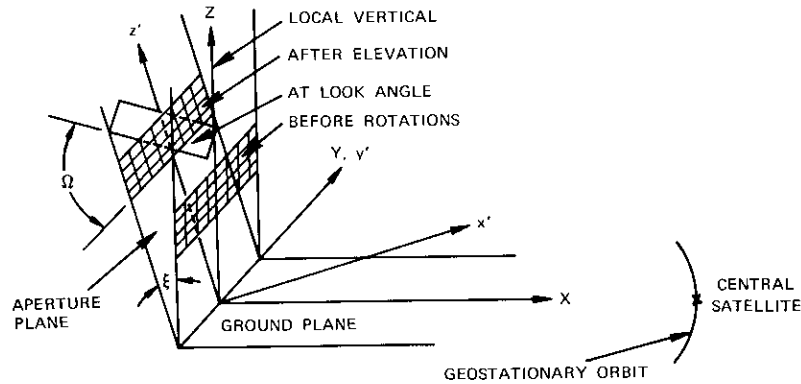
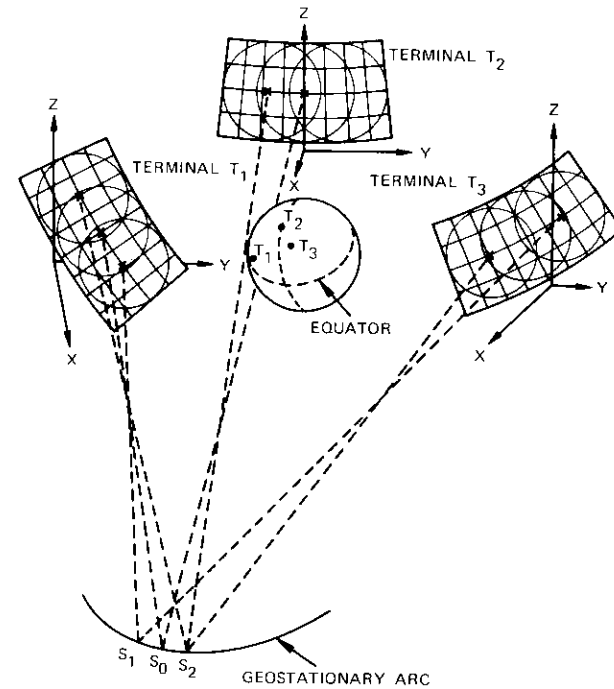


Figure 2. UET/MBTA Look Angle

antennas at different earth locations to scan the segment S_1S_2 of the geostationary arc is shown in Figure 3. The latitude, λ , and longitude, L , of the terminals, and the longitude of the central satellite, S_0 , are as indicated in the figure. The torus reflecting surface and backup structure described here can be used at different locations. Only the support structure members and feed support require modification so that the look angle at the desired location is obtained.

The toroidal reflecting surface is generated by rotating a parabolic section about an offset axis of rotation, as shown in Figure 4. The parabolic section is divided into four equal parts along its directrix, and the circular arc is divided into eight equal parts, resulting in a total of 32 quadrilateral panels. Figure 5 shows a cross section of the truss supporting the reflecting panels. An equilateral triangle (indicated by heavy lines) composes the main spine of the backup structure. The geometry of the foundation plan is shown in Figure 6, where p_1 and p_2 are the projections of the lower pickup points on the backup structure onto the ground plane.



S_0 = CENTRAL SATELLITE AT 333° EAST LONGITUDE
 λ = LATITUDE LOCATION OF TERMINAL
 L = LONGITUDE LOCATION OF TERMINAL
 ξ = ANGLE OF ELEVATION AT SITE
 Ω = ANGLE OF TILT AT SITE
 Z = LOCAL VERTICAL AT SITE
 XY = GROUND PLANE AT SITE

	λ	L	ξ	Ω
T_1	27N	279E	23	57
T_2	70N	333E	11	0
T_3	47N	11E	24	28

Figure 3. Orientation at Different Earth Locations

Figure 7 shows the support structure that connects the pickup points of the backup structure to the foundation.

Formulation of the structural model

The idealized model of the antenna structure consists of a finite number of nodal points defined in pertinent coordinate systems. Structural elements with given properties connect these points. Three local coordinate

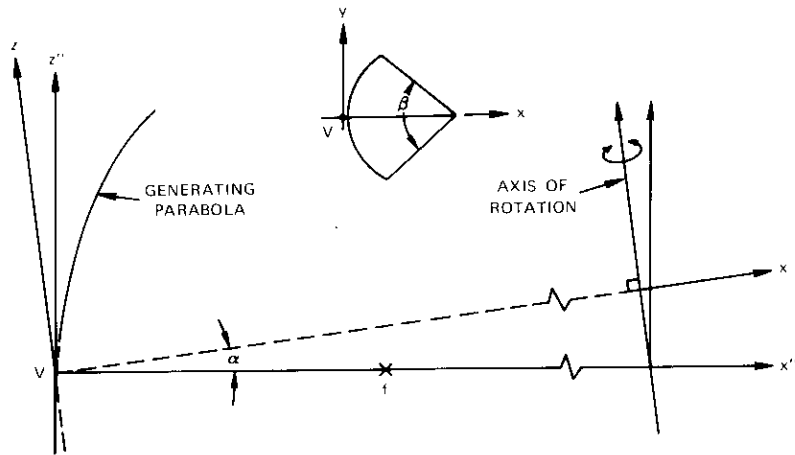


Figure 4. *The Generating Parabola Section*

systems, referenced to a basic coordinate system, are needed to completely define the UET model. The basic system is a rectangular cartesian system designated XYZ. The Z axis denotes the local vertical at the site, while the X axis is the projection of the axis of the parabola on the ground plane.

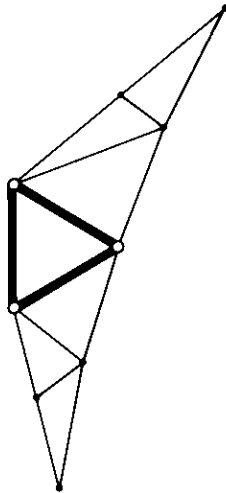


Figure 5. *The Generating Truss*

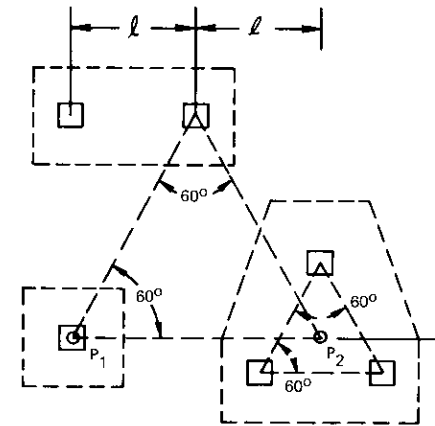


Figure 6. *The Foundation Plan*

The local coordinate systems account for the offset axis of rotation and the angles of elevation and tilt. The vertex of the generating parabola is assumed to be the origin of all coordinate systems used.

A digital computer program has been written to generate the data necessary to define a model for the NASTRAN analysis. The input to the program consists of the RF defining parameters, the location of the terminal and central satellite, and the geometry of the generating truss and foundation. The program generates the necessary elevation and tilt angles for the specified location, the coordinates of the grid points in the pertinent coordinate systems, the magnitude of loads to be applied to the grid points, and other pertinent data.

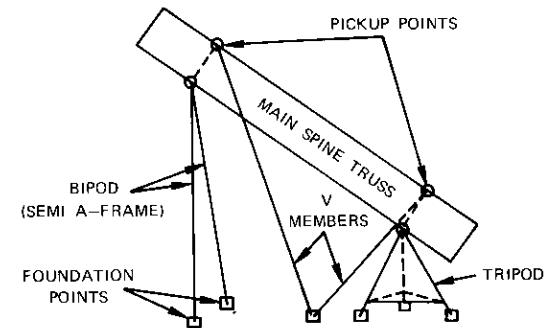


Figure 7. *The Support Structure*

The structural model was assumed to be a pin-jointed framework and the contribution of the panels to the total stiffness of the structure was neglected. These assumptions were intended to simplify the mathematical model and reduce the computation times without significant loss of accuracy. The bending rigidity of the joints was either negligible or nonexistent because of the method of connection. The actual structure should exhibit deflections that are smaller than those calculated here because of the extra stiffness, although small in value, contributed by the panels.

Loading conditions

The three basic forces that affect the behavior of the structure are gravity loads, wind loads, and temperature gradients. These loads have been applied to the model individually and in various combinations. The distributed forces acting on the reflecting surface panels have been converted into equivalent joint loads and applied to the backup structure grid points.

The operational and survival wind loads for the UET antenna have been specified as 72 km/hr (45 mph) and 160 km/hr (100 mph), respectively. Wind tunnel test results predicting pressure distribution over the toroidal surface are not available; hence, approximate calculations of the generated forces have been used. Several wind directions have been considered in the analysis. The most pertinent of these directions for the antenna at look angle is wind parallel to the ground plane, since this condition produces a higher combination of forces and torques on the structure. The wind load over each panel area is obtained by using

$$D = \frac{1}{2} C_D \rho A V^2$$

where

- D = drag force
- ρ = air density
- A = projected area of the panel
- V = wind velocity
- C_D = drag coefficient.

A drag coefficient value of 1.3, which is the shape factor for a parabola, has been used. The effects of side wind have been approximated by applying 20 percent of the front wind load to the structure.

The complexity of the structure makes it difficult to choose a representative temperature distribution. Numerous factors, such as wind, solar radiation, and gain or loss of heat by reflection and radiation, affect this distribution. A temperature differential of 5.6°C (10°F) between the front

and back of the antenna structure has been used in the analysis. This simple distribution may be representative of early morning conditions since the reflecting surface is oriented toward the east (looking at Atlantic satellites). As the day progresses, the front-to-back gradient should diminish. Since the structure is open, the wind will also contribute to a reduction in this "morning" gradient.

The loading conditions listed in Table 1 have been analyzed. The last two cases have been included to study the effects of constructing the antenna faceup and then mounting it at the look angle.

TABLE 1. LOADING CONDITIONS

Case No.	Loading Condition
1	gravity (g)
2	operational wind load
3	survival wind load
4	side wind (operational and survival)
5	temperature differential
6	g + case 2 (front side)
7	g + case 2 (back side)
8	g + case 4
9	g + case 3 (front side)
10	g + case 3 (back side)
11	g (antenna face up)
12	g (antenna horizontal)

Analysis of the structural model

The NASTRAN basic static analysis and normal mode analysis rigid formats are used for the static and dynamic analyses, respectively. The displacement method approach is specified. These analyses entail the solution of the matrix equations

$$[K] \{u\} = \{p\}$$

and

$$[K - \lambda M] \{u\} = 0$$

where

- $[K]$ = stiffness matrix
- $[M]$ = mass matrix
- $\{u\}$ = displacement vector
- $\{p\}$ = load vector
- λ = square of the natural frequency.

The outputs of the basic static analysis include the following:

- a. plots of the structural model,
- b. weight and balance information,
- c. displacements of grid points,
- d. foundation point reactions,
- e. forces in elastic elements,
- f. stresses in elastic elements.

The NASTRAN plots of the undeformed structure were obtained to verify the coordinates of the grid points, the transformation of coordinates, and the members of connection. Figure 8 is an orthographic front view projection of the final model. Figure 9 is a stereoscopic projection including the viewing method. The surface accuracy of the reflector

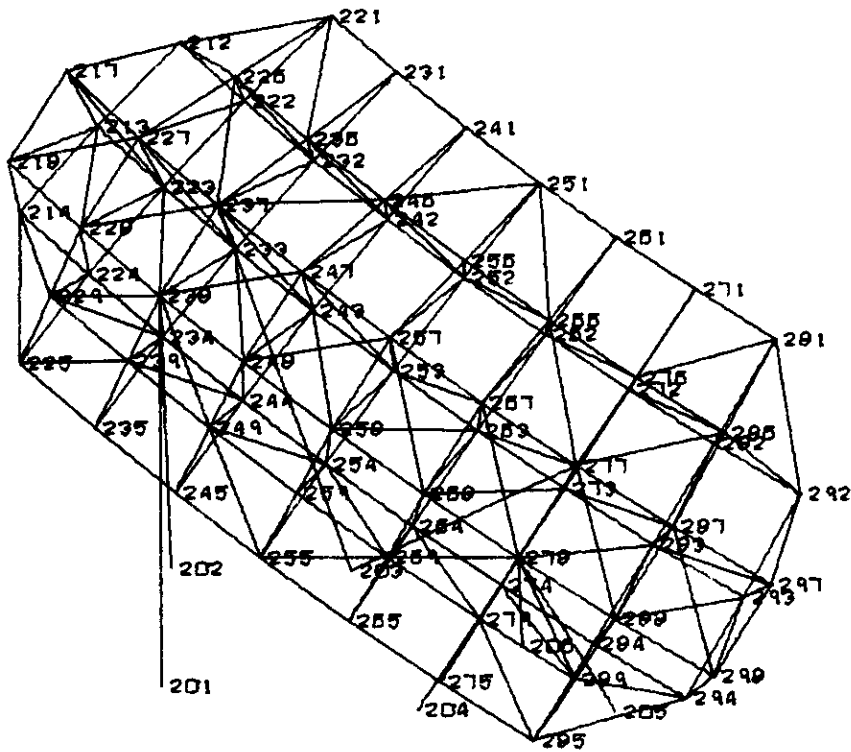
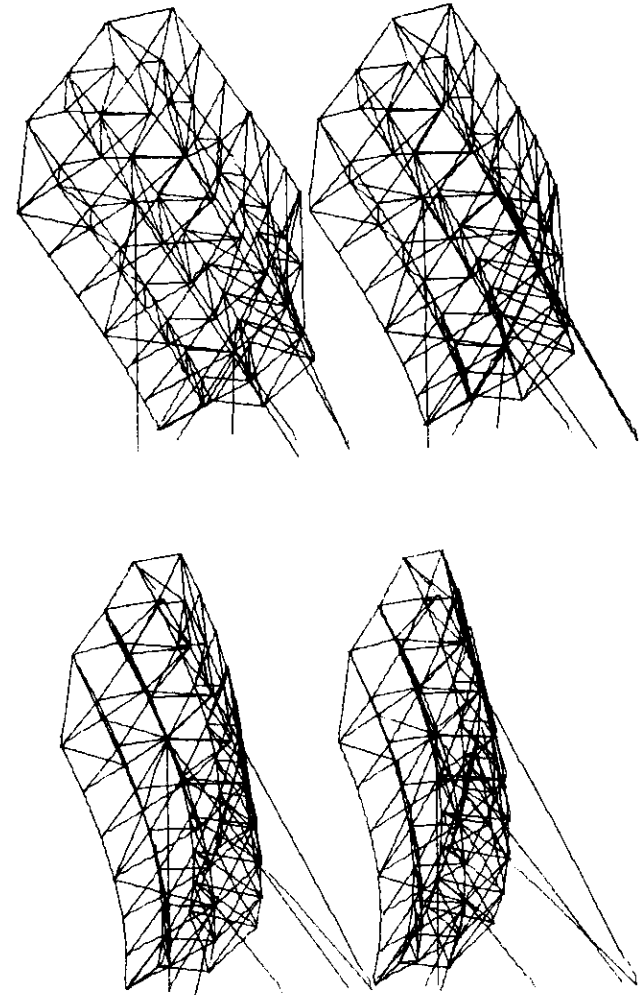


Figure 8. Orthographic Front View Projection



A three-dimensional effect may be achieved without the aid of a special viewer by holding a long envelope or piece of cardboard vertically out from the nose as a divider between the lines of sight so that each eye can see only one image of the stereo pair. By relaxing the eyes as if daydreaming the two retinal images can be made to merge into one. With practice the same effect can be achieved without the divider.

Figure 9. Stereoscopic Projection

under operational loading conditions and the safety factors for structural members under survival loading conditions were calculated by using the NASTRAN outputs.

rms surface deviations

The displacement vector obtained from the NASTRAN static analysis for each of the loading cases analyzed has specified a distorted position of the reflecting surface relative to the undistorted (zero deflection) position. The surface deflections consist of rigid body translations and/or rotations in addition to surface distortions. The rms surface error can be minimized if the average rigid body motions are applied to the structure in reverse and only the surface distortion component of the displacement is used in the calculations. The average rigid body translation and rotation of the surface are calculated and applied to the undistorted surface, hence defining a mean surface.

The rms surface error is defined by

$$\text{rms} = \left(\frac{\sum \delta_i^2}{n} \right)^{1/2}$$

where δ_i = displacement of joint from distorted surface to mean surface
 n = number of joints.

The displacements of the panel's supporting joints (backup structure joints) have been assumed to be identical to those of the reflecting surface. The X component (wind direction) of the displacement vector is the major contributor to surface distortions. Only this component is used in the surface rms calculations.

The surface accuracy results for pertinent loading cases are given in Table 2. These values take into account the distortions of the backup and support structures. The rms values are those calculated for the total reflecting surface. It should be noted that a given beam will illuminate only a portion of the total reflecting surface. The local rms values calculated for such regions are, on the average, 10 percent better than the values tabulated.

TABLE 2. REFLECTING SURFACE RMS AND POINTING ACCURACY

Loading Case	rms		Elevation (deg)	Azimuth (deg)
	cm	in.		
1	0.033	0.013	0.016	0.004
2	0.041	0.016	-0.012	-0.004
5	0.036	0.014	0.000	-0.002
6	0.025	0.010	0.004	-0.002
7	0.071	0.028	0.028	0.008
8	0.038	0.015	0.014	0.005
11	0.010	0.004	0.002	0.000

Stress in structural members

Elements having only extensional properties have been used to represent the structural members of the backup and support structures. The backup structure members have been divided by function into two categories, main and secondary members. The support structure consists of a tripod, a bipod (semi A-frame), and a yoke (V) frame connected to the backup structure spine as shown in Figure 7. The combined gravity and survival wind loadings produce the highest stresses in these members. The stresses are either tensile or compressive, depending on the orientation of the elements and the direction of the applied loads.

The stresses obtained from the NASTRAN analysis are examined to ensure that the various members have sufficient safety factors without overdesigning. The safety factor, SF, of each member is based on its actual maximum stress, σ_m , and its allowable stress, σ_a ; i.e.,

$$\text{SF} = \frac{\sigma_a}{\sigma_m}$$

Simple material failure (yielding) of members in tension and instability failures of members in compression govern the magnitude of the allowable stresses. Yielding is a material property, and the yield stress used is specified in the American Institute of Steel Construction (AISC) manual [2]. However, the allowable compressive stresses must be calculated for the various members that have different slenderness ratio values by using the modified Euler's formula specified in the AISC manual; i.e.,

$$\sigma_a = \frac{12\pi^2 E}{23(Kl/r)^2}$$

$$\sigma_{as} = \frac{\sigma_a}{1.6 - (l/200r)}$$

where

σ_a = allowable compressive stress for main members

σ_{as} = allowable compressive stress for secondary members

E = Young's modulus of elasticity

l = length of structural member

r = radius of gyration

K = effective length factor

Kl/r = length-slenderness ratio.

An effective length factor, K , of 1.0 has been used for truss members. The lengths of the members have been obtained from the generated mathematical model data, and the radii of gyration have been calculated from the member cross sections.

For the final model typical safety factors of 2.2 to 5.3 for the support structure members and 1.2 to 2.6 for the backup structure members have been obtained. These values do not take into account allowances permitted in the AISC manual and can be considered conservative. Several structural members experience low stresses under survival loading conditions. This is due to the surface accuracy requirements and the uniformity desired for manufacturing ease and economy.

Normal mode analysis

Structures designed for static loading only may still fail under oscillation excited by steady and/or gusty winds. Large deflections and stresses can result if the structure is to resonate, i.e., oscillate at a natural frequency.

The normal mode analysis was not included in the redesign process. This analysis was performed for the final model to verify the approximate hand calculation of the fundamental frequency (lowest natural frequency) of the structure. The approximate calculations had shown that the fundamental frequency of the structure was several octaves higher than that of wind gusts or vortices excited by steady wind frequencies. Here, the structure was idealized as a cantilever beam with an end mass.

The NASTRAN inverse power method [3], [4] with shifts was selected for the normal mode analysis, where the frequency range of interest and the estimated and desired number of natural frequencies were specified. The fundamental frequency of the antenna structure was found to be 7.9 Hz.

A particular deformation configuration is obtained at the instant when all the points in the structure reach an extremum as they execute harmonic motion about a position of static equilibrium. Each mode shape is associated with a natural frequency of the structure. The fundamental mode shape of the reflector surface is shown in Figure 10, in which only the X components of the normalized eigenvector displacements (normalized distance from equilibrium position to extreme position) obtained from the NASTRAN analysis are plotted. In this first mode, the reflector is exhibiting a cantilever motion about the tripod-supported region and a twisting motion about the approximate line of nodes (line of zero motion).

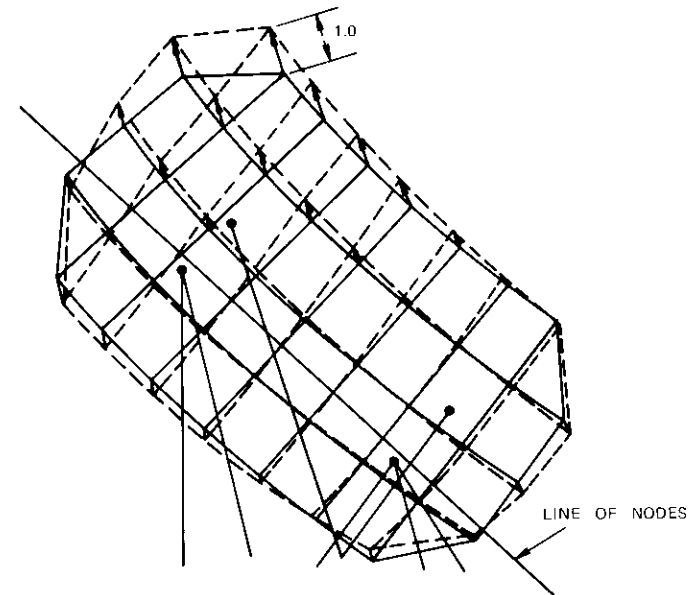


Figure 10. Fundamental Mode Shape

Redesign process

The structural model presented here is the final product of an iterative design cycle in which NASTRAN was used as the analysis tool. However, the effectiveness of the NASTRAN analysis was greatly hampered by time delays and errors occurring in the idealized model preparation stage and in the processing of the analysis results. This is particularly true of the preliminary design phase where alternatives were evaluated and changes were frequent. Hence, development of software is essential to improve the performance of the iterative process. The preprocessor and postprocessor used in concert with NASTRAN resulted in the semiautomated design procedure shown in Figure 11. The amount of data handling and the time-consuming repetitive calculations were reduced and a redesign cycle with a good turn-around time was obtained.

The iterative design process was divided into three stages: preliminary analysis, coarse analysis of the selected configuration, and refinement of the selected configuration. Alternatives were evaluated in the first stage and the general configuration shown in Figures 5-7 was selected. In the second stage, the selected configuration was analyzed further, and alternatives to this configuration were studied. The depth of the main spine truss was varied, 3- versus 4-point pickup supports were evaluated, and structural members were redistributed. The resulting 4-point pickup structure and 2.44-m (8.0-ft) spine truss model were then refined in the third stage by further redistributing members and by removing the corner points of the torus. Table 3 compares the resulting coarse model and the refined final model.

TABLE 3. COMPARISON OF COARSE AND REFINED MODELS

Description	Coarse Model	Final Model
Number of Joints	87	79
Number of Members	270	249
Number of Degrees of Freedom	243	219
Weight	13,200 kg (29,100 lb)	12,370 kg (27,280 lb)
rms Deviations, Gravity	0.056 cm (0.022 in.)	0.038 cm (0.015 in.)
Operational Wind	0.053 cm (0.021 in.)	0.033 cm (0.013 in.)

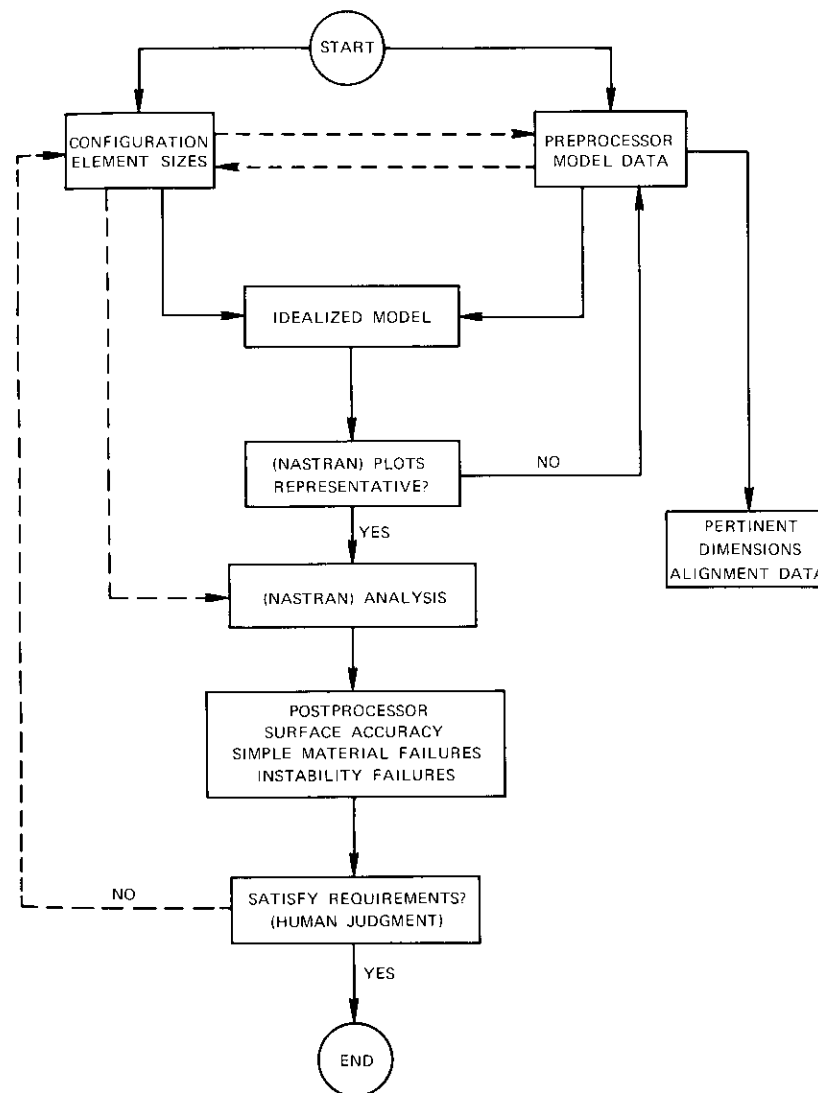


Figure 11. Flow Chart of Redesign Cycle

Conclusions

This paper has described the general structural analysis of the 10-m UET torus antenna. The redesign procedure utilizing the NASTRAN program and additional software produced a torus structure capable of meeting both operational and survival loading specifications. Further iterations would have resulted in only modest weight and performance improvements. The reflector and its backup structure can be used at any location with modification only to the support structure and feed mechanism so that the look angle at the site is obtained. Table 4 summarizes pertinent conclusions derived from the total data that pertain to the final model.

TABLE 4. PERTINENT DATA SUMMARY

Weight	
Reflecting Surface	2,430 kg (5,360 lb)
Backup Structure	4,920 kg (10,800 lb)
Support Structure	5,020 kg (11,060 lb)
Total	12,370 kg (27,280 lb)
Surface rms	
Gravity at Look Angle	0.033 cm (0.013 in.)
Operational Wind Load	0.041 cm (0.016 in.)
10°F ΔT	0.036 cm (0.014 in.)
Pointing Accuracy	
Elevation	
Gravity at Look Angle	0.014°
Operational Wind Load	0.012°
10°F ΔT	0.000°
Azimuth	
Gravity at Look Angle	0.004°
Operational Wind Load	-0.004°
10°F ΔT	-0.002°
Minimum Safety Factors	
Support Truss	2.2
Backup Structure	1.2
Fundamental Natural Frequency	7.9 Hz

Acknowledgments

The overall structural/mechanical design effort for the UET/MBTA has been directed by Mr. L. V. Smith of COMSAT. The structural analysis of his

selected configuration, as presented here, is only a small contribution toward the total effort of designing and installing a state-of-the-art antenna. The comments and directions of Mr. Smith and Mr. M. J. Vlissides, consultant, enhanced the convergence of the analysis. The helpful suggestions of Dr. W. Cook of COMSAT Labs permitted efficient use of NASTRAN. The author also wishes to acknowledge the guidance of Mr. P. R. Schrantz of COMSAT Labs throughout the analysis.

References

- [1] G. Hyde, "A Novel Multiple-Beam Earth Terminal Antenna for Satellite Communication," *IEEE 1970 International Conference on Communications*, San Francisco, California, June 8-10, 1970, IEEE Paper No. 70-CP-386-COM.
- [2] *Manual of Steel Construction*, American Institute of Steel Construction, Inc., 7th edition, 1970.
- [3] *The NASTRAN User's Manual*, NASA SP-222, edited by C. W. McCormick, October 1969.
- [4] *The NASTRAN Theoretical Manual*, edited by R. H. MacNeal, August 1969.
- [5] *Mechanical Engineering in Radar and Communications*, edited by C. J. Richards, Van Nostrand Reinhold Co., 1969.



Ali F. Abu-Taha joined COMSAT in 1969 as an assistant engineer. Upon obtaining his B.S.M.E. from George Washington University in 1972, he was made a member of the technical staff of the Structures/Mechanical Department. He has been involved in the design and structural analysis of various spacecraft and earth station components utilizing general-purpose and self-written programs.

Mr. Abu-Taha has performed extensive mass properties studies of INTELSTAT IV and other satellites. He is active in the design, stress analysis, and selection of lightweight components, and is responsible for the mechanical properties testing for the Spacecraft Laboratory.

High-performance corrugated feed horn for the unattended earth terminal

R. PRICE

(Manuscript received May 2, 1974)

Abstract

This paper describes a high-performance corrugated feed horn developed for the antenna of the unattended earth terminal (UET). The horn was designed to provide optimal illumination of a 32-ft offset-fed parabolic torus over the 3.7- to 4.2- and 5.9- to 6.4-GHz frequency bands and at the same time to be suitable for use in multiple-feed configurations in which sets of independently steered beams are generated by means of a fixed reflector and moveable feeds.

The horn is characterized by an axially symmetric beamwidth that is frequency independent over a broad band, a true phase center whose location is also independent of frequency, and negligible sidelobes. It is exceptionally small and compact for its type. Theory and design techniques are discussed and performance data are presented in the paper.

Introduction

For wideband satellite communications, radiating horns with circumferentially grooved walls possess important advantages: axially symmetric and frequency independent beams, negligible sidelobes, and true phase centers whose locations remain fixed with frequency. On the other hand, this type of horn is mechanically complex and generally exacts a penalty

in size and weight. Nonetheless, because of its superior RF performance, the corrugated horn was selected as the feed type to be developed for the unattended earth terminal (UET) antenna.*

Efficiency considerations

It was not initially obvious that the corrugated (scalar) horn would be the best choice for illuminating the torus reflector. Such horns had indeed been successfully used as feeds for circularly symmetric parabolic reflectors. The high performance obtained had been related to a close match between the horn's aperture fields and the reflector's focal region fields. It had also been demonstrated analytically that similar results would apply to spherical reflectors and to 2-reflector systems [1].

The UET parabolic torus is not circularly symmetric, and therefore it was not evident that previous results would apply. Nevertheless, certain gain and efficiency calculations performed with illumination function as a parameter did indicate that, for various torus antenna configurations, a corrugated horn would provide nearly optimum illumination [2]. These calculations showed that there was a range of reflector dimensions for which a $\cos^{3/2}(\theta)$ illumination taper, where θ is the angle formed between a ray from the phase center of the horns to the reflector vertex and a ray from the same origin to a field point on the reflector, maximizes both gain and efficiency. This taper is characteristic of many corrugated horns. Efficiency refers to the ratio of the actual gain obtained to that which would be obtained from a perfect paraboloid of the same area and with the same illumination.

Within this range of reflector dimensions, extending from around 150–250 wavelengths, aberration effects, while significant, are not dominant; therefore neither a uniform nor a highly tapered illumination function would be ideal. Uniform illumination places a high proportion of the available energy in wide-angle unfocused rays, while highly tapered illuminations make inefficient use of available reflector area. The dimensions of the UET torus antenna over its band of operations extend from 148 to 257 wavelengths.

An additional and important consideration in the choice of the corrugated horn as the UET feed was its extremely low sidelobe level of less

* See the papers entitled "The unattended earth terminal multibeam torus antenna" and "Antenna design studies for a U.S. domestic satellite," which also appear in this issue.

than 35 dB. This value is required for adequate beam isolation in certain multiple-beam applications and also ensures that there will be no significant antiphase components of current on the reflector.

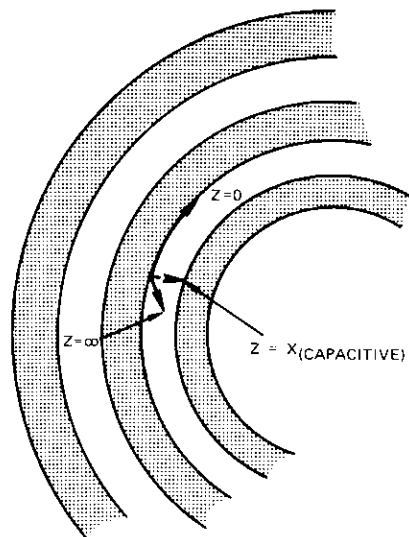
Hybrid modes and anisotropic surfaces

Antenna aperture efficiencies approaching 100 percent can be achieved by means of feeds whose aperture fields closely match the focal plane fields of the reflector [3]. It is not as yet known how to synthesize such feeds, although rather close approximations are possible. Conventional smooth wall horns do not provide a close approximation to the focal fields because smooth metallic walls cannot support the particular modes into which these focal fields may be resolved. Such modes are hybrid; that is, they have components of both electric and magnetic fields in the direction of propagation [4], [5]. They require for support anisotropic boundaries, i.e., boundaries having surface impedances that are varying functions of direction.

Smooth metal walls are obviously not anisotropic because they constitute short circuits in all directions. However, suppose that circumferential grooves a quarter wavelength deep were to be cut into the walls. These grooves would form quarter wavelength short-circuited radial transmission lines that would appear at their inputs as open circuits. The surface impedance would now be anisotropic. Consider a point along the outer rim of a groove, as shown in Figure 1. In the circumferential direction around the rim, the impedance would be zero; looking into the groove, it would be infinite; and across the groove, from rim to rim, it would be a capacitive reactance. Longitudinal grooves would produce a similar result.

The same hybrid modes which are required to match the focal region fields of a symmetrical reflector to realize efficiencies approaching 100 percent also yield circularly symmetric power patterns with low cross polarization [6]. Such power patterns are generated by antennas whose electric and magnetic fields have the same variation with a set of spatial coordinates; i.e., parallel components of the magnetic and electrical fields are described by identical functions.

Fields with this characteristic are made up of hybrid modes. While it is possible to decompose a hybrid mode into TE and TM components, each associated with one of the longitudinal fields, electric or magnetic, these component elements do not constitute independent propagating modes. As independent normal modes traveling in a conventional waveguide, they would have different cutoff wavelengths and velocities of



$Z = 0$ CIRCUMFERENTIALLY ALONG RIM OF GROOVE

$Z = \infty$ INTO OPEN END OF GROOVE

$Z = iX_C = \frac{1}{2\pi fC}$ ACROSS OPEN END OF GROOVE (RIM-TO-RIM)

Figure 1. Three Impedance Values as Functions of Direction on an Anisotropic Surface

propagation. However, the TE and TM components forming the hybrid mode are degenerate with respect to each other; that is, they have the same phase velocity and are linked in their travel along a transmission line. They are constituent parts of one and the same mode.

With this in mind, a hybrid mode field configuration will be synthesized by superpositioning a TM component on a TE component. First note that, within either of the constituent parts, TE or TM, parallel components of E and H do not have the same spatial variation; therefore, they do not individually meet the criteria for circularly symmetric power patterns with low cross polarization. However, it can be seen that, in the combination forming a hybrid mode, parallel components of E and H do indeed vary in the same manner as the spatial coordinates.

The vector components of the two contributing modes are shown in Figure 2. In the TE_{11} mode in circular waveguide,

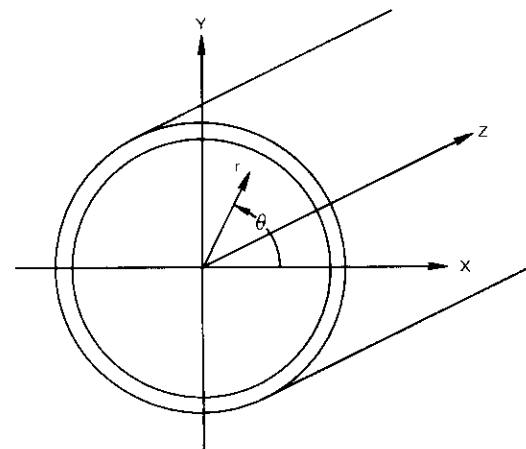


Figure 2. Coordinates for Equations (1)–(6)

$$E_{rh} = K_1 \frac{J_1(U)}{U} \sin \theta$$

and

$$H_{rn} = \frac{K_1}{Z} J_1'(U) \cos \theta$$

while

$$E_{\theta h} = K_1 J_1'(U) \cos \theta$$

and

$$H_{\theta h} = \frac{K_1 J_1(U)}{Z U} \sin \theta$$

In the TM_{11} mode

$$E_{re} = K_2 Z J_1'(U) \cos \theta$$

and

$$H_{re} = K_2 \frac{J_1(U)}{U} \sin \theta$$

while

$$E_{\theta e} = K_2 Z \frac{J_1(U)}{U} \sin \theta$$

and

$$H_{\theta e} = K_2 J_1'(U) \cos \theta$$

where the subscripts r and θ refer to the radial and circumferential components, respectively. The subscripts h and e refer respectively to the TE or H modes and TM or E modes,

$$U = \frac{2\pi r}{\lambda_{ch}} \text{ for the TE}_{11} \text{ mode}$$

and

$$U = \frac{2\pi r}{\lambda_{ce}} \text{ for the TM}_{11} \text{ mode}$$

where λ_{ce} and λ_{ch} are the cutoff wavelengths of the two modes. $J_1(U)$ is the 1st-order Bessel function of the first kind of argument U , and Z is the characteristic impedance of the waveguide.

Now the parallel components of the two modes will be combined to yield

$$E_r = K_1 \frac{J_1(U)}{U} \sin \theta + K_2 Z J_1'(U) \cos \theta \quad (1)$$

$$H_r = K_2 \frac{J_1(U)}{U} \sin \theta + \frac{K_1}{Z} J_1'(U) \cos \theta \quad (2)$$

$$E_\theta = K_1 J_1'(U) \cos \theta + K_2 Z \frac{J_1(U)}{U} \sin \theta \quad (3)$$

$$H_\theta = K_2 J_1'(U) \cos \theta + \frac{K_1}{Z} \frac{J_1(U)}{U} \sin \theta \quad (4)$$

$$E_z = K_3 J_1(U) \cos \theta \quad (5)$$

$$H_z = K_4 J_1(U) \cos \theta \quad (6)$$

It can be seen from equations (1)–(6) that the electric and magnetic field components parallel to each other (arranged above in pairs) have the same functional variation and, except for constants, satisfy Rumsey's criteria for identical power patterns with no cross polarization [7]. To permit this, the cutoff wavelengths of the two modes, λ_{ce} and λ_{ch} , and consequently the values of U_1 and U_2 , have been forced to be equal. This step would involve violating the boundary conditions imposed by any conventional surface. However, it is permissible for boundaries that are anisotropic, since the two

modes are not independent normal modes, but components of the same hybrid mode. In the special case in which the ratio of the longitudinal field components E_z and H_z equals the characteristic impedance of free space, i.e.,

$$\frac{E_z}{H_z} = \frac{K_3}{K_4} = Z_0 = 377\Omega$$

the mode is referred to as a balanced hybrid mode and its radiation pattern will have the polarization properties of a Huygens source.

Radiation patterns

Frequency-independent beamwidth is another interesting and remarkable characteristic of corrugated horns. The laws governing the radiation from apertures make no exceptions for corrugated horns. The characteristic derives from the horn's constant effective electric aperture that is essentially independent of the mechanical or physical aperture. If this condition does not hold, then the beamwidth will be an inverse function of frequency. The electrical aperture of a corrugated horn will be constant with frequency and independent of the mechanical aperture only if the size of the mechanical aperture is above a certain threshold. This threshold value is a function of flare angle. In an attempt to design for compact physical dimensions, the frequency independence of the beamwidth will be the first characteristic to be compromised.

The following expression for the aperture fields of a corrugated horn under balanced hybrid conditions has been derived [8] (see Figure 3):

$$E_a = K \frac{Z_0}{r} B_n(kr) J_0 \left[2.405 \frac{\theta}{\alpha} \right] e^{i\phi} [\pm \bar{a}_\theta + i \bar{a}_\phi] \quad (7)$$

where
$$B_n(kr) = H_n^2 + \frac{1}{2} \gamma = \frac{1}{2} \sqrt{nk r} H_n^2 + \frac{1}{2} [nk r]$$

and $H_m^2(X)$ = Hankel function of the second kind

α = horn half flare angle

θ = angle formed at the horn vertex by a ray to an aperture point and the horn axis

r = radial distance from the horn vertex to any point on the aperture

$\bar{a}_\theta, \bar{a}_\phi$ = unit vectors in the polar coordinate system.

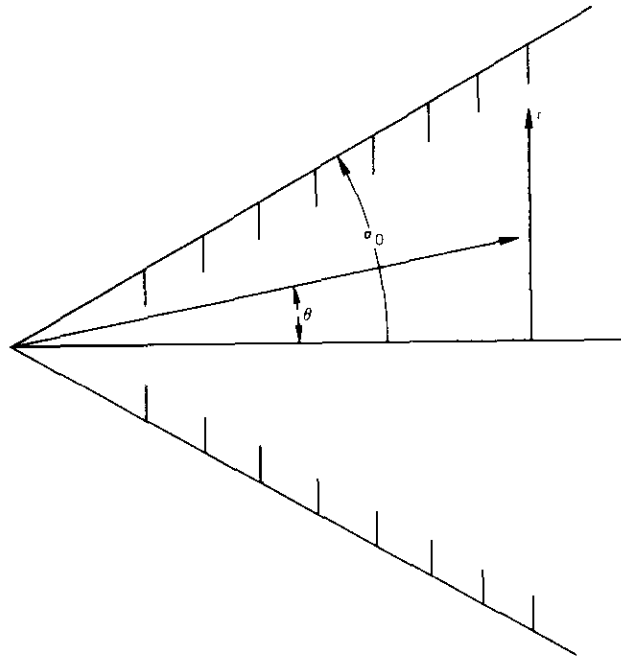


Figure 3. Geometry for Equation (7), Aperture Fields of a Corrugated Horn

The transverse field intensity is independent of ϕ as required for rotationally symmetric patterns. As a function of radial distance from the horn axis, the intensity is approximately Gaussian [9] with the aperture energy very largely concentrated in the region near the horn axis. This suggests a quick method of estimating the horn's radiation patterns and designing for a desired far-field beamwidth. If the self-transforming property of the Gaussian function is applied, the far-field intensity will be found to be proportional to $J_0[2.405(\theta/\alpha)]$; this indicates that beamwidth may be controlled by adjusting the parameter α . For example, to design for a 10-dB beamwidth, the following equation is solved for α :

$$J_0 \left[2.405 \frac{\theta_{10 \text{ dB}}}{\alpha} \right] = \sqrt{0.1} = 0.316 \quad (8)$$

where $\theta_{10 \text{ dB}}$ is the angle from the main beam axis out to the 10-dB point. Because the 10-dB beamwidth = $2\theta_{10 \text{ dB}}$,

$$\alpha = 0.65 BW_{10 \text{ dB}} \quad (9)$$

or

$$BW_{10 \text{ dB}} = 1.53\alpha \quad (10)$$

Corrugated horn design

Corrugated horns may be operated in a flare-angle-controlled mode or in an aperture-controlled mode. The former mode of operation yields frequency-independent patterns and is usually of greater interest. To design for angle-controlled operation, the horn flare angle is selected to yield a desired 10- or 3-dB beamwidth (BW) by using the following expression:

$$\alpha = 0.65 BW_{10 \text{ dB}} = 1.06 BW_{3 \text{ dB}}$$

The length of the horn is then set to yield the desired frequency-independent flare-angle-controlled beamwidth. This will result in an aperture considerably larger than that required for a conventional horn designed for the same beamwidth. While the exact size is a function of the flare angle, the following can be taken as a useful guide:

$$D = \frac{100\lambda}{BW_{3 \text{ dB}}}$$

where D is the aperture diameter and λ is the wavelength of the lowest frequency of interest.

Next, to excite and support the necessary balanced hybrid modes, the grooves are designed to form a capacitive surface reactance along the horn walls. The capacitive surface will suppress surface waves which, if allowed to propagate, would form a ring-type radiator at the aperture. Such a radiator would have a null on axis pattern and the intensified edge diffraction at the aperture would result in increased sidelobes and backlobes.

The grooves, which may be viewed as radial waveguides terminated in a short circuit, will be capacitive if they are between a quarter and a half wavelength deep. For wideband operation, their depth will be adjusted to $\lambda/4$ at the lowest operating frequency and the bandwidth will then extend up to the frequency at which the groove depth is $\lambda/2$. In practice, the groove is made somewhat deeper, typically 10 percent more than $\lambda/4$ at the lowest operating frequency, to avoid the appearance of mode

spikes at the lower end of the frequency band. The width of the grooves will be adjusted to less than $\lambda/2$ at the highest operating frequency to cut off any mode other than the fundamental radial waveguide mode. Unnecessarily high corrugation density will increase manufacturing costs without yielding a proportionate improvement in performance. Four corrugations per wavelength at the highest operating frequency has been found to be adequate.

Impedance matching

The match of a corrugated horn to the input transmission line is essentially determined by the geometry of the throat region. Beyond a half wavelength from the point at which the corrugations begin, the fields along the wall surface become very weak and detail changes in the groove design have little or no effect on the input VSWR. The horn is matched by correctly choosing the point at which the corrugations begin. This point is a function of the horn flare angle and can be most conveniently found experimentally with a scale model of the throat section only.

For matching purposes it is unnecessary to work with a model of the entire horn, since the geometry beyond the second or third corrugation has only a negligible effect on the input VSWR. Once the initial corrugation has been located, the match may be further improved by tapering the groove widths. Within limits, impedance matching may be accomplished without affecting the radiation patterns. It has been observed that locating the first groove further than $\lambda/2$ from the input waveguide junction degrades the patterns.

Sweep frequency data on the first generation UET feed horn are presented in Figure 4. The return loss averages 25 dB (equivalent to a VSWR of 1.21) over the receive 3.7- to 4.2-GHz band, rising above 20 dB only at the very bottom edge, i.e., at 3.7 GHz, where it reaches 17 dB (VSWR = 1.32). Over the transmit 5.925- to 6.425-GHz band, the return loss averages 32 dB (VSWR = 1.06) with a worst point of 29 dB (VSWR = 1.075). For the second version of the UET feed horn, the low-frequency level is improved to 22 dB (VSWR = 1.18) and the average return loss over the receive band is 29 dB (VSWR = 1.07).

Mechanical considerations

Beam steering with the UET torus antenna is accomplished by moving the feed rather than the entire reflector surface. Small compact feeds

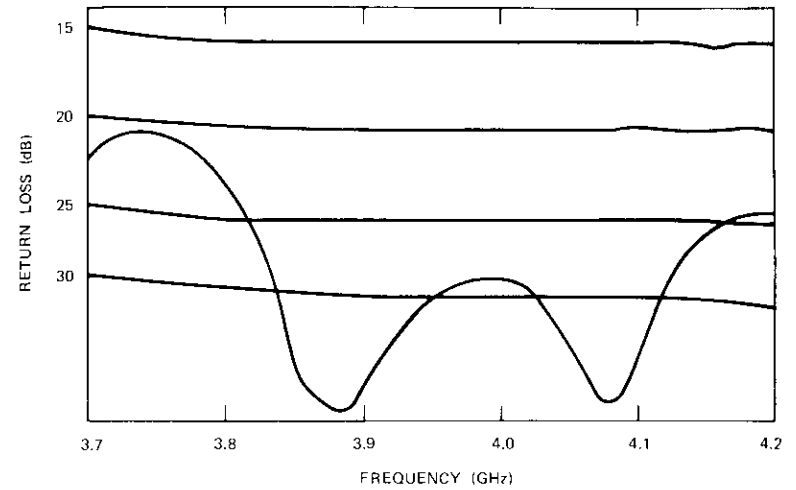


Figure 4a. Receive Band Return Loss of UET Feed Horn

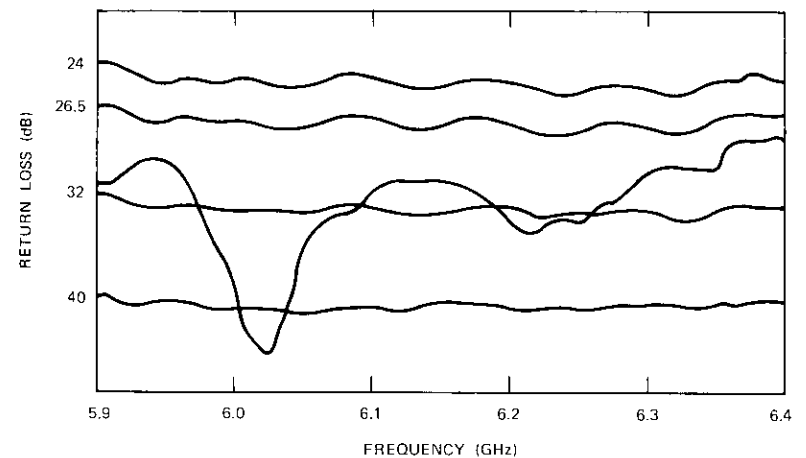


Figure 4b. Transmit Band Return Loss of UET Feed Horn

permit close spacing of beams along the orbital arc. However, in the past, corrugated horn feeds have typically been bulky and heavy. This has largely been due to both the low aperture efficiency and the necessity for horn wall to accommodate the corrugation depths.

Corrugated horns used in earth terminals of the global system have been as long as 14 feet and over 3 feet in diameter at the aperture. A design objective for the UET horn has been the achievement of a feed dimension that will accommodate satellite spacings of as little as 2° along the orbital arc without unacceptably compromising the performance. This has largely been accomplished. A tradeoff between dimensions and performance has resulted in a UET feed horn with an aperture of only 14 inches which, over the operating band, ranged from around 4.5 to 7 wavelengths (see Figure 5). The dimensions of the mechanical aperture were effectively allowed to approach those of the electrical aperture; the process was halted when edge diffraction effects were observed.

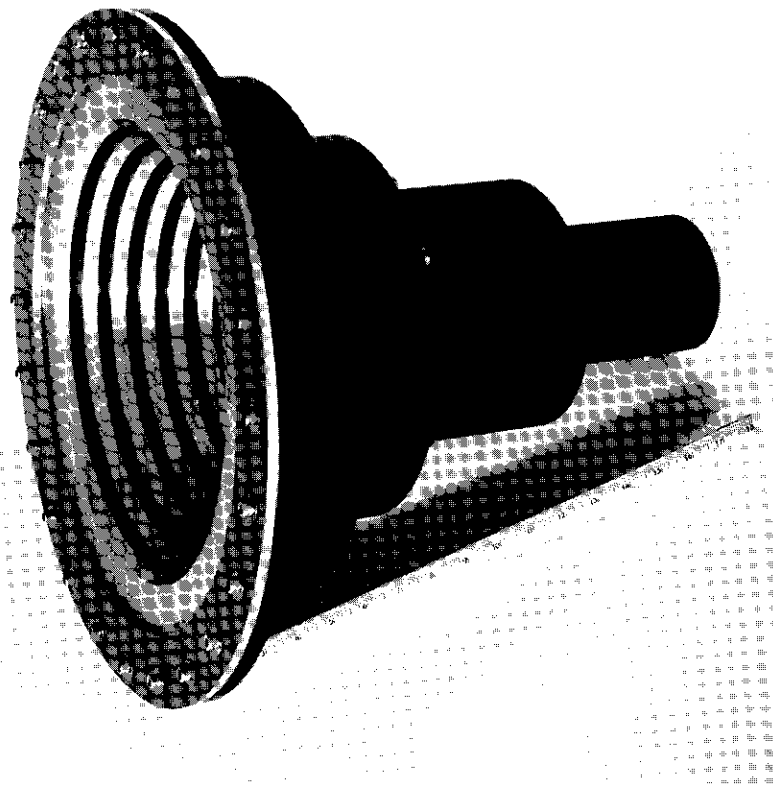


Figure 5. UET Feed Horn

Radiation patterns

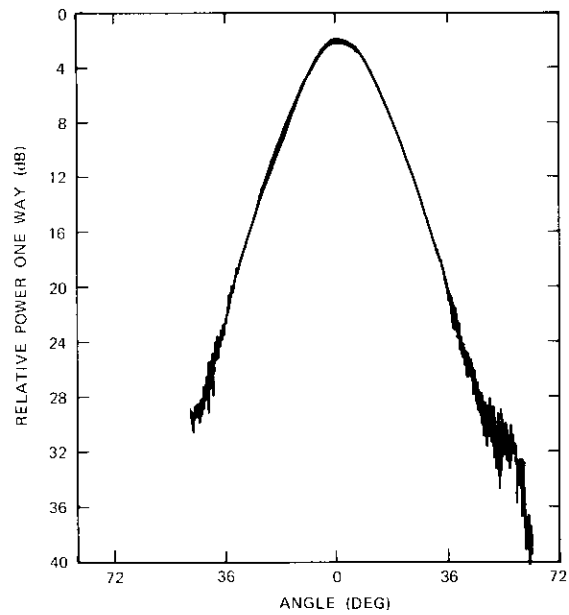
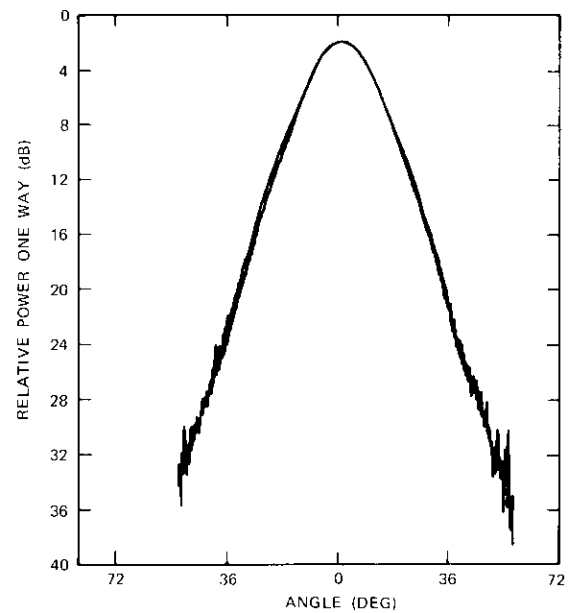
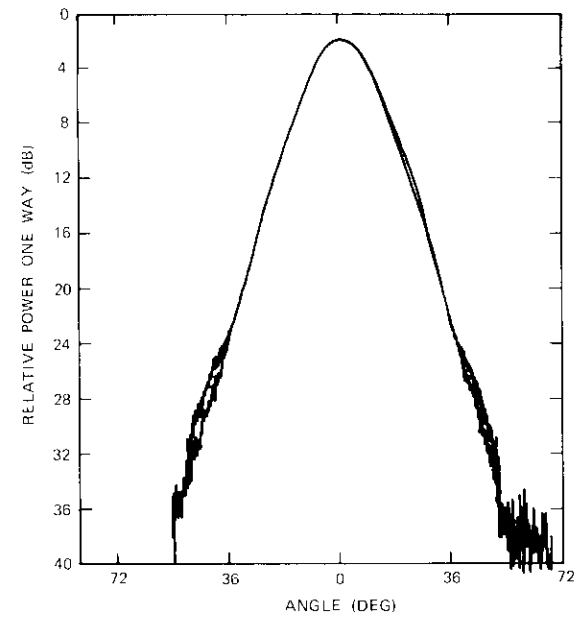
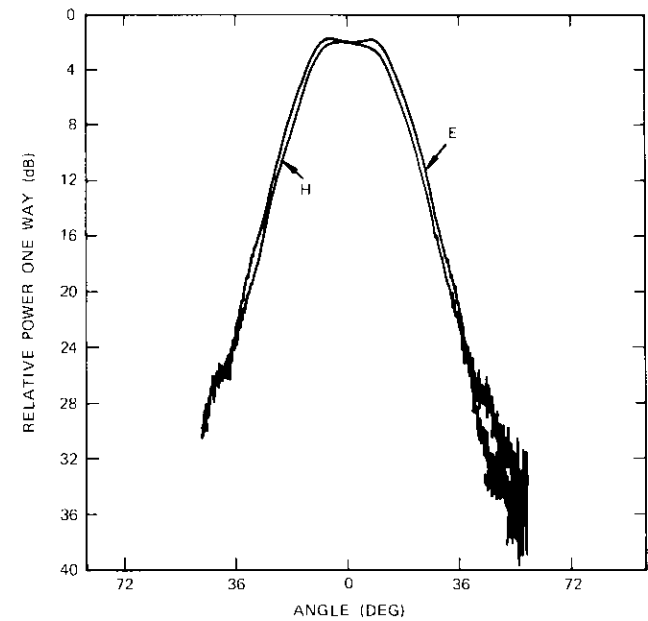
The results of an extensive set of measurements of the horn's radiation characteristics are presented in Figures 6 and 7. Figure 6 comprises E- and H-plane patterns taken at several frequencies. It can be observed that the receive band E- and H-plane patterns are almost perfectly congruent and that the beamwidths are constant with frequency.

These same characteristics are displayed on a sweep frequency basis in Figure 7. The sweep plots may be interpreted as follows. The solid 0-dB trace at the top of each figure represents the on-axis gain of the horn as a function of frequency. The other solid traces are calibration lines representing the indicated relative gain levels. The various dotted curves are the relative gain values of the horn measured at the indicated off-axis angles. The curves come in pairs in which each member is taken the same number of degrees off axis, but on opposite sides. The close overlay of the pair members is an indication of the absence of beam squint. Beamwidth stability is indicated by the slow frequency variation of the responses in relationship to the calibration lines.

Polarization characteristics

The polarization characteristics of the horn were investigated for possible future applications in which frequencies will be reused on orthogonal polarizations. It was significant that the E- and H-plane patterns were identical over a full 500-MHz band because it can be shown that, if these patterns are identical in a complex sense (i.e., if they have a common phase center, as well as congruent amplitude patterns), then the axial ratio of the antenna will be unity and the polarization isolation infinite.

The cross-polarized component of the horn was measured. This component typically has four lobes, one located in each of the four quadrants surrounding the main beam axis. The maxima of these lobes occur in the 45° planes. Patterns of the cross-polarized lobes in the planes of their maxima are shown in Figure 8. The worst case occurred at 4,200 MHz, where the peak of the cross-polarized component was more than 33 dB below that of the principally polarized component. At 9° off axis, which would be at the edge of earth of a spacecraft global horn, the cross-polarized component was 38 dB below the principally polarized components. At all other frequencies the results were even more favorable. At 3.7 GHz, the peak of the cross-polarized lobe was down 36.5 dB, and at the edge of earth angle, it was at the 45-dB level.

Figure 6a. *E- and H-Plane Patterns Taken at 3.7 GHz*Figure 6b. *E- and H-Plane Patterns Taken at 3.95 GHz*Figure 6c. *E- and H-Plane Patterns Taken at 4.2 GHz*Figure 6d. *E- and H-Plane Patterns Taken at 6.4 GHz*

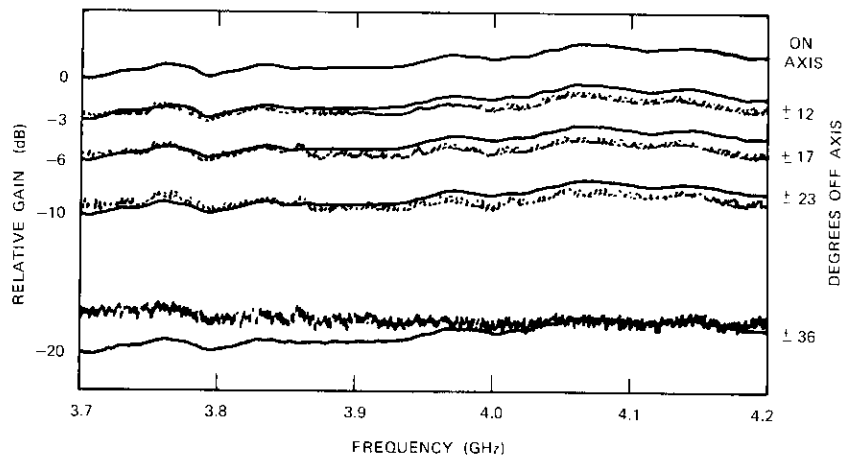


Figure 7a. *E-Plane Sweep Patterns Taken at 3.95 GHz*

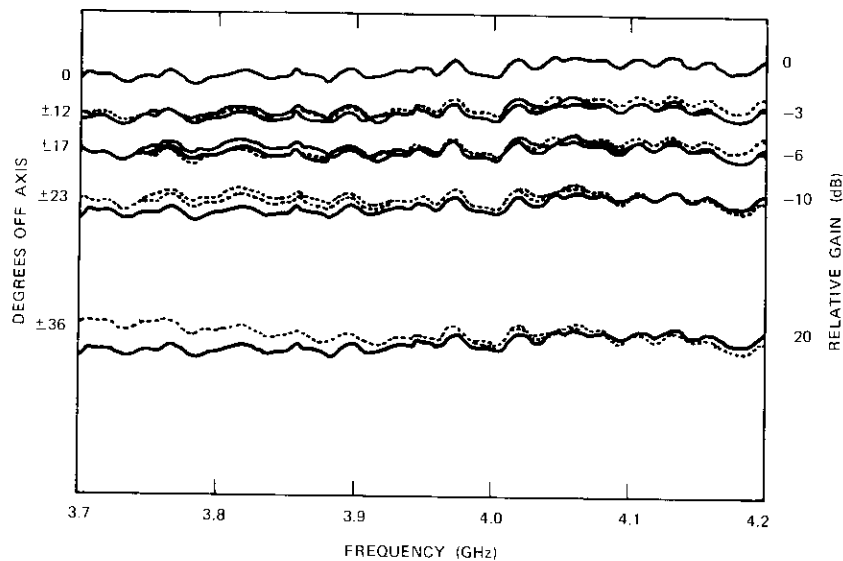


Figure 7b. *H-Plane Sweep Patterns Taken at 3.95 GHz*

These measurements were made with linear polarization and the figures directly give values of linearly polarized isolation as degraded by measurement chamber effects. To obtain circular polarization isolation, the linear

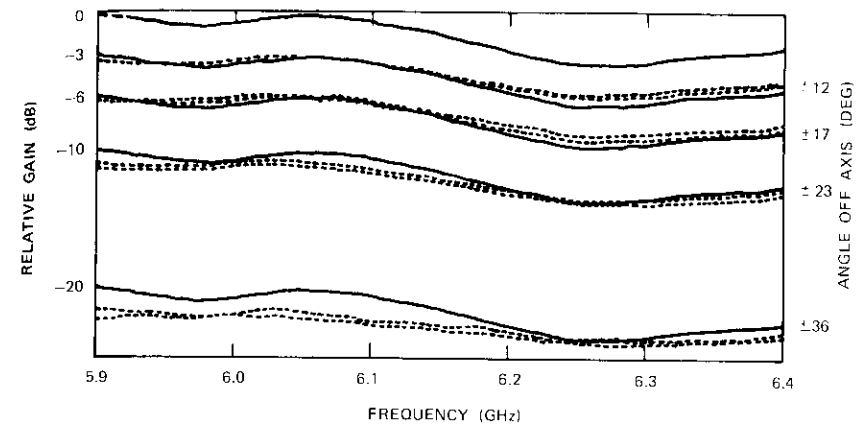


Figure 7c. *E-Plane Sweep Patterns Taken at 6.4 GHz*

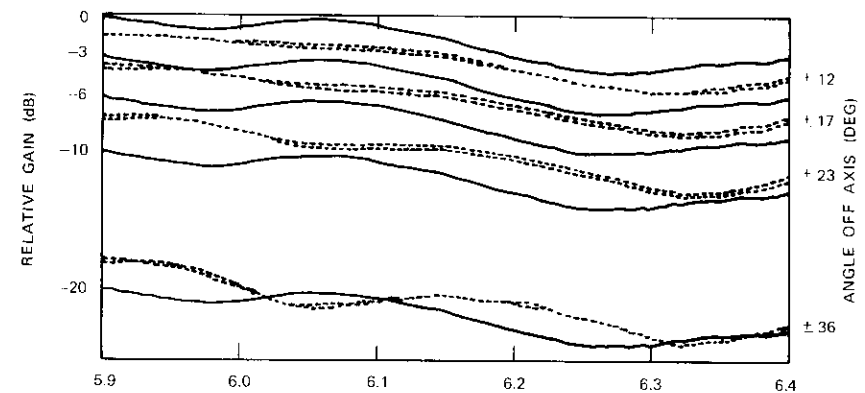


Figure 7d. *H-Plane Sweep Patterns Taken at 6.4 GHz*

isolation figure must be combined appropriately with that of the polarizer. In combination with a 0.1-dB axial ratio polarizer, the horn would yield a worst-case polarization isolation of 37.0 dB.

Conclusions

A high-performance, exceptionally compact, corrugated feed horn was designed for the UET. This type of horn radiates axially symmetric beams with negligible sidelobes and zero cross polarization. Horn phase

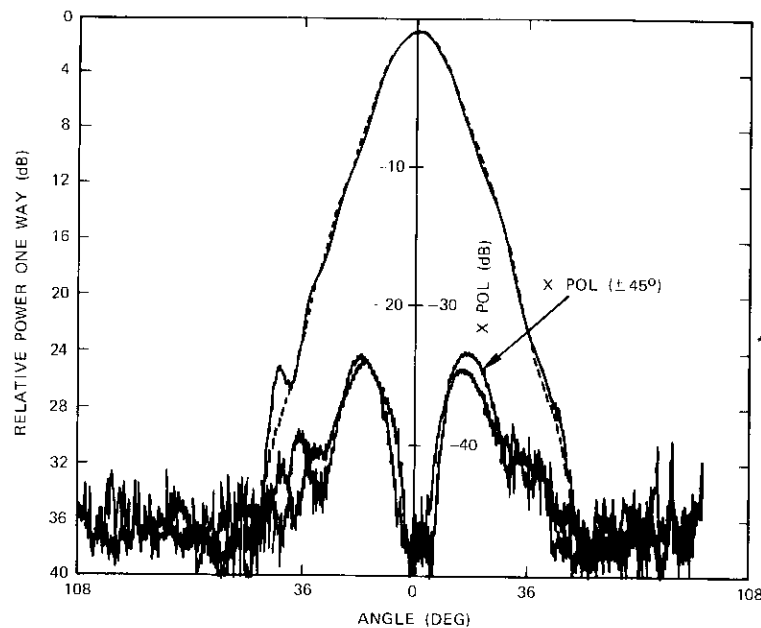


Figure 8. Patterns of Cross-Polarized Lobes in the Plane of Their Maxima

centers remain fixed in location with frequency, and the horn can be designed to maintain a constant beamwidth over nearly a 40-percent frequency band. These advantages derive from a multiple hybrid mode aperture field configuration that requires anisotropic boundaries to support.

The physical apertures of corrugated horns are large compared to their electrical apertures and the corrugation depths must be accommodated within their walls. As a result, corrugated horns have typically been large and heavy. However, the corrugated horn which has been developed for the UET is quite compact with little sacrifice in performance, demonstrating that the advantages of this type of antenna are available from structures with reasonable dimensions. It has been further demonstrated in the program that a reflector need not be circularly symmetric to be efficiently illuminated by a hybrid mode horn.

Acknowledgment

The author is happy to express his appreciation to Kenneth Pease and Henry Williams, the two senior technicians of the Antenna Department for

their extremely skillful work in performing the numerous measurements that were required in this program. He also wishes to thank Mr. Ronald Kessler and his Model Shop staff and Mr. Norman Miller and his colleagues in the Design Department for their efforts in converting the results of an R&D effort into an operating reality. Finally, he wishes to thank the members of the Antenna Department and Dr. G. Hyde for the interesting and useful discussions that occurred in the course of the program.

References

- [1] C. J. E. Phillips, "The Theoretical Performance of Spherical Reflectors with Gregorian Corrections and Scalar Feeds," Research Report 006/1969, Queen Mary College, University of London.
- [2] G. Hyde, Private Communication.
- [3] H. C. Minnett and B. Maca Thomas, "A Method of Synthesizing Radiation Patterns with Axial Symmetry," *IEEE Transactions on Antennas and Propagation*, AP-15, No. 5, September 1966, pp. 654-656.
- [4] C. H. Walter, *Travelling Wave Antennas*, New York: McGraw-Hill, 1965, pp. 213-230.
- [5] R. F. Harrington, *Time Harmonic Electro Magnetic Fields*, New York: McGraw-Hill, 1961, pp. 154-163.
- [6] L. E. Raburn, "The Calculation of Reflector Antenna Polarized Radiation," *IRE Transactions on Antennas and Propagation*, AP-8, pp. 43-49.
- [7] V. H. Rumsey, "Horn Antennas with Uniform Power Patterns Around Their Axes," *IEEE Transactions on Antennas and Propagation*, AP-15, No. 5, September 1966, pp. 656-658.
- [8] M. S. Narasimhan and Y. B. Malla, "Paraboloidal Reflector Illumination with Conical Scalar Horns," *Electronics Letters*, Vol. 8, No. 5, March 1972, pp. 111-112.
- [9] P. J. B. Clarricoats and P. K. Saha, "Propagation and Radiation Behavior of Corrugated Waveguide Feeds," *Proc. IEE*, Vol. 118, No. 9, September 1971, pp. 1167-1176.



Ronald Price received his B.E.E. degree in 1960 from the Polytechnic Institute of Brooklyn, where he also did his graduate work. He joined COMSAT in 1968 as a member of the technical staff of the RF Transmission Laboratory working on antennas and associated RF devices. More recently he has been a member of the Systems Engineering Department.

Before coming to COMSAT, Mr. Price was with the Sperry Gyroscope Company Radiation Division in Great Neck, N. Y., and subsequently with the General Electric Company Space and Re-entry Systems Division in Valley Forge, Pennsylvania.

Index: modems, unattended earth terminals

Design considerations for the unattended earth terminal wideband FM modem

M. GROSSMAN

(Manuscript received March 21, 1974)

Abstract

This paper discusses the design of the unattended earth terminal 855-MHz FM modulator-demodulator, analyzes modulator and demodulator operation, and describes possible tradeoffs. It also describes the implementation of a 612-channel modulator-demodulator and presents measured test results.

Introduction

The unattended earth terminal (UET) [1] must be capable of operating in the FM mode in a range of communications capacities from 24 to 1,872 telephone channels. To realize economic IF bandpass filters and operate with the smallest channel capacity, the upper IF limit is restricted to below 1 GHz. The modulator-demodulator designed for this system has been selected for its ability to handle the small capacities while simultaneously meeting the linearity and bandwidth requirements associated with the larger capacities. The modem specifications are as follows:

IF	855 MHz
IF bandwidth	605-1,105 MHz
modulator noise contribution	100 pW0p
demodulator noise contribution	100 pW0p

modulator deviation	26.5 MHz p-p max
modulator linearity	1 percent max
intelligible AM	<1 percent

855-MHz modulator

The maximum peak-to-peak deviation specified for the INTELSAT IV satellite system [2] is 26.5 MHz, yielding 972 channels in the global-beam mode. Although this represents the worst case in terms of linearity, it does not correspond to the largest capacity, since Δf_{rms} is specified as 4.417 MHz for 972 channels, while it is 3.181 MHz for 1,872 channels in the spot-beam mode.

Experience has shown that voltage-controlled oscillators (VCOs) can be made sufficiently linear over a 10-percent-deviation bandwidth, but 7 percent is considered a conservative upper limit. To achieve the required 1-percent modulator linearity, a push-pull design has been chosen.

The well-known theory of this device [3], [4] is included here to illustrate the cancellation of even-order distortion terms. The instantaneous frequency of a lossless circuit using a shunt varactor diode is given by

$$f_0 + \Delta f = f_0 \left(1 - \frac{\Delta C}{C_0} \right)^{-1/2} \tag{1}$$

where f_0 = resonant frequency
 ΔC = change in capacity
 C_0 = initial capacity.

A Taylor series expansion of equation (1) yields

$$f_0 \left(1 + \frac{\Delta f}{f_0} \right) = f_0 \left[1 + \frac{1}{2} \left(\frac{\Delta C}{C_0} \right) + \frac{3}{8} \left(\frac{\Delta C}{C_0} \right)^2 + \frac{5}{16} \left(\frac{\Delta C}{C_0} \right)^3 + \dots \right]$$

so that

$$\frac{\Delta f}{f_0} = + \frac{1}{2} \left(\frac{\Delta C}{C_0} \right) + \frac{3}{8} \left(\frac{\Delta C}{C_0} \right)^2 + \frac{5}{16} \left(\frac{\Delta C}{C_0} \right)^3 + \dots \tag{2}$$

The 1st-order term produces the desired modulation, while the higher order terms result in distortion. To minimize these distortion terms for a fixed value of inductance, L, $(\Delta C/C_0)$ must be minimized. With Δf fixed according to S/N requirements, $\Delta f/f_0$ can be minimized only by making f_0 as high as is practically possible.

The capacitance-voltage relationship of a varactor diode [4] is

$$C(V) = BV_1^{-1/2}$$

where B = diode coefficient
 V_1 = diode voltage.

Substitution into equation (1) yields

$$f_0 + \Delta f = f_0 \left[1 + \frac{\Delta V}{V_0} \right]^{1/4} \tag{3}$$

where $\frac{\Delta C}{C_0} = -\frac{\Delta V}{V}$

and $\Delta V = \frac{1}{2} \Delta V_1$

Expanding this expression as before yields

$$\frac{\Delta f}{f_0} = \frac{1}{4} \left(\frac{\Delta V}{V_0} \right) - \frac{3}{32} \left(\frac{\Delta V}{V_0} \right)^2 + \frac{21}{384} \left(\frac{\Delta V}{V_0} \right)^3 - \dots \tag{4}$$

The ideal relationship between the oscillator frequency and the bias voltage on a voltage-variable capacitor should be linear (line BC in Figure 1). Actually, the characteristic is nonlinear (curve BA) due to series expansion, and the difference is a measure of the nonlinearity. Only the first term of the equation is of interest, since the remaining terms of the series are distortion terms. Hence, it is then necessary to increase the sensitivity of the oscillator to reduce the ratio $\Delta V/V_0$ to the desired value.

Selecting $f_0 \gg f_{IF}$ and then down-converting to the desired IF alleviates the requirements on ΔC and ΔV , and also reduces the oscillator percentage deviation bandwidth. Since the beat-frequency oscillator operates in a push-pull configuration, cancellation of the even harmonics is theoretically possible.

Expanding $(1 \pm x)^{-1/2}$ and taking the difference,

$$A = (1 + x)^{-1/2} = 1 - \frac{1}{2}x + \frac{3}{8}x^2 - \frac{5}{16}x^3 + \dots$$

$$B = (1 - x)^{-1/2} = 1 + \frac{1}{2}x + \frac{3}{8}x^2 + \frac{5}{16}x^3 + \dots$$

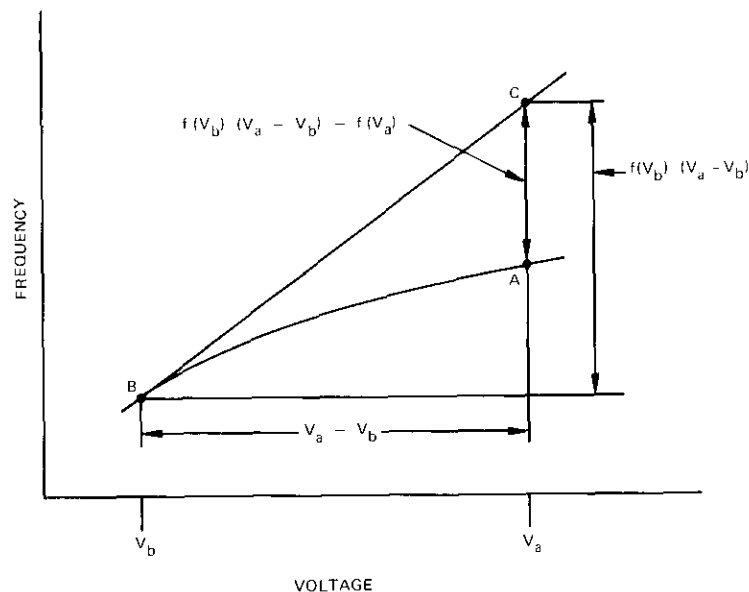


Figure 1. Frequency vs Voltage for Voltage-Variable Capacitor

eliminates all of the even harmonic terms. Choosing the second oscillator frequency so that the instantaneous frequencies are ordered, i.e.,

$$f_{02} > f_{01} > f_{0IF}$$

and letting

$$f_{02} - f_{01} = f_{0IF}$$

makes it possible to frequency modulate the oscillators generating f_{01} and f_{02} in opposite directions in a push-pull configuration, thus cancelling the even terms.

Let $\alpha = (\Delta C/C_{02})$ and $\beta = (\Delta C/C_{01})$ represent voltage-to-frequency transfer coefficients. Then,

$$f_2 = f_{02} \left(1 + \frac{\Delta f_{02}}{f_{02}} \right) = f_{02} \left(1 - \frac{1}{2} \alpha + \frac{3}{8} \alpha^2 - \frac{5}{16} \alpha^3 \right) \quad (5)$$

$$f_1 = f_{01} \left(1 - \frac{\Delta f_{01}}{f_{01}} \right) = f_{01} \left(1 + \frac{1}{2} \beta + \frac{3}{8} \beta^2 + \frac{5}{16} \beta^3 \right) \quad (6)$$

If the output of two such oscillators is applied to a mixer and all terms except the difference term $(f_2 - f_1)$ are filtered out, the mixer output will be

$$\cos 2\pi(f_2 - f_1)t = \cos 2\pi f_{IF}t \quad (7)$$

where

$$f_{IF} = f_{0IF} \left(1 + \frac{\Delta f}{f_{0IF}} \right) = f_{0IF} - \frac{1}{2} (\alpha f_{02} + \beta f_{01}) + \frac{3}{8} (\alpha^2 f_{02} - \beta^2 f_{01}) - \frac{5}{16} (\alpha^3 f_{02} + \beta^3 f_{01}) \quad (8)$$

From equation (8), it can be seen that setting $\alpha^2 f_{02} = \beta^2 f_{01}$ minimizes the quadratic term. Since α and $\beta < 1$, α^3 and $\beta^3 \ll 1$ and the contribution of the 3rd-order term is minimal.

Modulator design

The choice of frequencies used in the dual oscillator modulator was governed by several factors:

- a. $f_2 - f_1 = 855$ MHz (the specified IF).
- b. $f_2 > f_1 > f_{IF}$.
- c. All unwanted products must fall outside the frequency interval between 605–1,105 MHz to permit carrier wave operation for wide-band digital modulation utilizing the entire 500-MHz bandwidth at IF.

Two frequencies satisfying these constraints and obtainable with reliable devices are $f_2 = 2,255$ MHz and $f_1 = 1,400$ MHz. The nearest interference products are $2f_1 - f_2 = 545$ MHz and $2f_2 - f_1 = 1,705$ MHz. For these two frequencies, the ratio of α and β is

$$\frac{\alpha}{\beta} = \frac{f_{01}}{f_{02}} = 0.81$$

Now that the center frequency has been established, the second problem is to obtain the required modulator sensitivity.

At these frequencies, transmission line techniques are easily employed. A transmission line section inserted between the varactor and the transis-

tor makes it possible to use the transistor shunt capacitance to achieve an increased tuning range for the oscillator. The transmission line section transforms the varactor capacitive reactance into an inductive reactance at the transistor, as shown in Figure 2. The capacitance of the tank circuit, C_{tot} , is the sum of the transistor output capacitance and the package shunt capacitance, while the tank inductance is the transformed varactor capacitance. This circuit has been designed according to the method outlined in References 5-7.

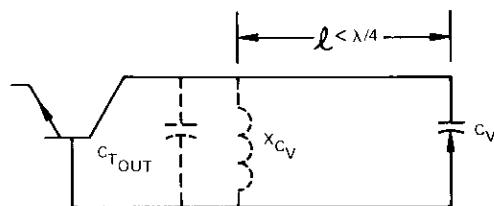


Figure 2. Oscillator Circuit with Transmission Time Section Between the Varactor and the Transistor

855-MHz demodulator

The demodulator specification required a system noise contribution no greater than 100 pW0p. Because the UET was proposed to operate at C/N ratios above 10 dB, a requirement for threshold extension was unnecessary. Demodulators capable of the required linearity at this IF were the phase discriminator, frequency feedback (FMFB), and phase-lock loop (PLL) threshold extension demodulators. Because it represented the simplest approach, the phase discriminator was investigated first. However, the critical matching, component selection, temperature considerations, fabrication tolerances, and the requirement for a limiter with little AM/PM conversion at 855 MHz made its implementation impractical. The phase-lock loop discriminator was examined next.

Phase-lock loop demodulator

The theory of operation of a PLL demodulator has been well developed [8]-[10]. The advantage of this demodulator over the FMFB scheme stems from the fact that it requires neither a linear discriminator nor a limiter, both of which would present major design problems at 855 MHz.* Spe-

*The loop filter for the FMFB is at IF, while that of the PLL is at baseband.

cific design procedures for a 2nd-order loop have been given in References 8 and 10.

VCO distortion

A major source of PLL distortion [10] is the VCO nonlinearities. In general, the dynamic modulation equation is of the form

$$\Delta\omega(t) = a_1V(t) + a_2V^2(t) + a_3V^3(t) \dots \tag{9}$$

where $\Delta\omega(t)$ = VCO radian frequency deviation about a quiescent center frequency

$V(t)$ = VCO input control voltage

a_1, a_2, a_3, \dots = voltage/frequency transfer coefficients.

Since, as shown previously, the distortion in a varactor-controlled oscillator is principally due to the voltage squared term, a push-pull distortion cancellation technique, similar to that used in the modulator, was employed. For low-distortion conditions, equation (9) may be reduced to

$$\Delta\omega(t) = a_1 \left\{ V(t) + \frac{a_2}{a_1} [V(t)]^2 \right\} \tag{10}$$

from which the 2nd-order distortion component is

$$V_d = \frac{a_2}{a_1} [V(t)]^2 \tag{11}$$

For FDM, the modulating voltage $V(t)$ may be represented by Gaussian noise with 2-sided power spectral density $G(f)$ which has a constant value η_2 over the baseband range from frequency f_1 to f_2 and is zero elsewhere [11]. The power spectral density, $G(f)$, of $V^2(t)$ is [12] then

$$G_2(f) = 2 \int_{-\infty}^{\infty} G_1(u) G_1(f - u) du + [\overline{V^2(t)}]^2 \delta(f) \tag{12}$$

where $G_1(u)$ is the 2-sided power spectral density of the modulating voltage and $\delta(f)$ is the dirac delta function. The second term of equation (12)

represents a DC component and can be omitted for this analysis. Thus, the noise-power ratio (NPR) is

$$\text{NPR} = \left(\frac{a_1}{a_2}\right)^2 \left[\frac{G(f)}{G_d(f)} \right] \tag{13}$$

where $G_d(f)$ is the power spectral density of $V^2(f)$.

Equation (13) assumes narrowband FDM channels over which both the signal and the distortion power spectral densities are essentially flat. Therefore, the NPR in a channel is proportional to the ratio of the power spectral densities. It is convenient to define a normalized distortion spectrum [10] as

$$G_{dn}(f) = G_d(f) [4\eta_2^2(f_2 - f_1)] \tag{14}$$

Since

$$(\Delta\omega_{rms})^2 = 2\eta_2^2(f_2 - f_1)$$

is the mean square frequency deviation in rad/s², equation (13) becomes

$$\text{NPR} = \left(\frac{a_1}{a_2}\right)^2 \frac{1}{2(\Delta\omega_{rms})^2 G_{dn}(f)} \tag{14}$$

The ratio $(a_1/a_2)^2$ is related to the percentage linearity of the VCO. If V_p causes the oscillator to reach peak deviation, the frequency error at the deviation peak is $(a_1/a_2) V_p$ and the percentage error is

$$\Delta = 100 \left(\frac{a_2}{a_1}\right) V_p \tag{15}$$

Assuming a 10-dB peak-to-rms ratio for the input modulation and substituting into equation (14) yields

$$\text{NPR} = \frac{10^5}{2\Delta^2 G_{ch}(f)} \tag{15}$$

where $G_{ch}(f)$ is a normalization factor whose value depends on the specific channel of interest.

Figure 3 indicates that the greatest distortion resides in the low-frequency portion of the baseband. Therefore, setting $G_{ch}(f) \simeq 1$ and solving equation (15) for Δ yields

$$\Delta = \left[\frac{10^5}{2\text{NPR}} \right]^{1/2} \text{ percent} \tag{16}$$

The NPR equivalent to 100 pW0p for 612-channel FDM operation is 51.25 dB, for example. Substituting into equation (16) gives $\Delta = 0.614$ percent. This indicates that the VCO must be within ± 0.614 percent of linear deviation over the required peak-to-peak deviation of 12.6 MHz.

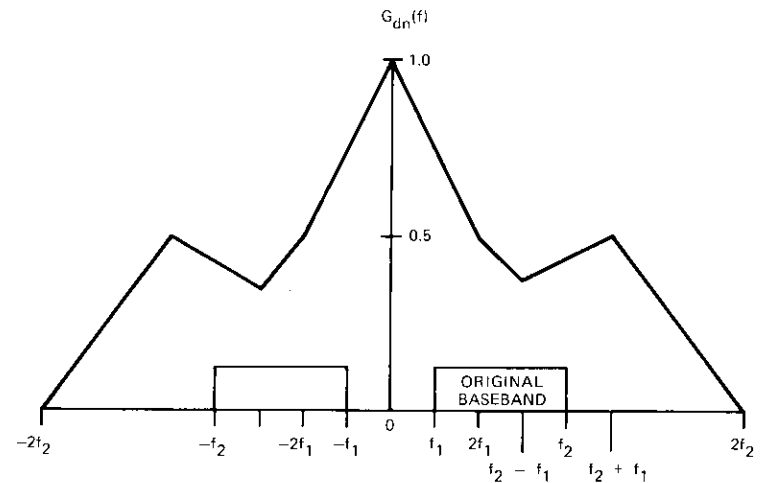


Figure 3. Normalized Spectrum for Square Law Distortion

Design implementation and test results

Modulator implementation and tests

Figure 4 is a block diagram of the modulator. An IF filter ($BW_{1\text{ dB}} = 85$ MHz) has been inserted in the output line to reduce spurious outputs.

The modulator sensitivity test results shown in Figure 5 indicate a sensitivity of 226 MHz/V. The amount of intelligible AM measured with a test tone deviation of 454 kHz rms (612-channel equivalent) is 0.8 percent.

Demodulator implementation and tests

Figure 6 is a block diagram of the demodulator. The VCO sensitivity (Figure 7) is 226 MHz/V. The other important parameter which must be measured before the PLL design can be implemented is the phase detector sensitivity. A Merrimac DMM-2-500A double-balanced mixer has been used as a phase detector, with a sensitivity of 0.0505 V/rad.

NPR measurements

A 612-channel modem was implemented to demonstrate the performance of the design and to provide a useful modulator-demodulator over carriers with a large amount of traffic.

The INTELSAT IV specification for 612 channels at 8,000 pW0p is C/T = 134.2 dBW/K. The noise bandwidth used to reference the C/T is 20 MHz. As can be seen from Figure 8, which is a plot of S/N vs C/T, the top slot is within 0.25 dB of the specified theoretical operating point. In the case of no additive IF noise, the unit performed as shown in Table 1.

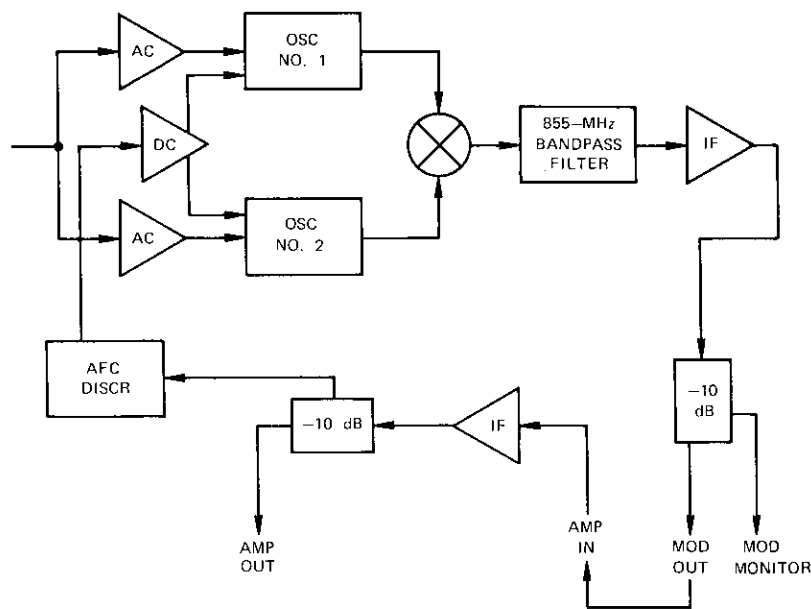


Figure 4. 855-MHz FM Modulator

TABLE 1. PERFORMANCE OF A 612-CHANNEL MODEM WITH NO ADDITIVE IF NOISE

Slot	pW0p
14 kHz	210
1,002 kHz	120
2,438 kHz	60

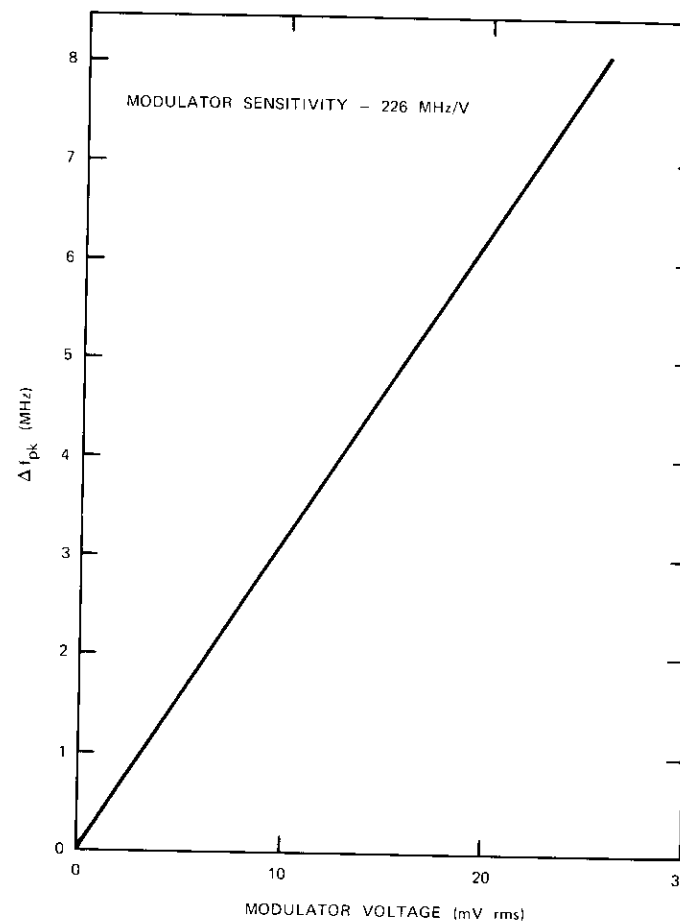


Figure 5. 855-MHz Modulator Deviation vs Modulating Voltage ($f_m = 200$ kHz, modulator sensitivity = 226 MHz/V)

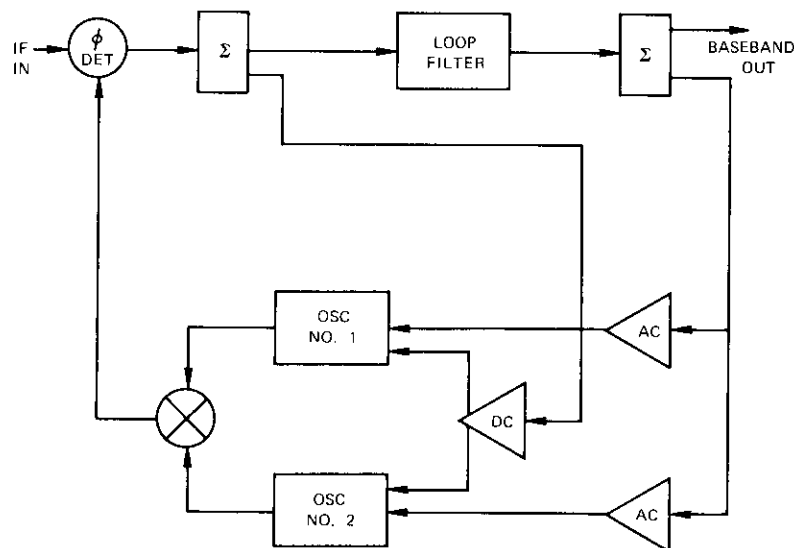


Figure 6. Phase-Lock Loop Demodulator

Figure 9 is a plot of S/N vs deviation at the operating point of C/T = -134.2 dBW/K. The curves indicate that the unit is aligned at the optimum point for operation in the lowest slot (14 kHz).

The modem baseband response is flat within 0.2 dB from 10 Hz to 2.5 MHz and rises to a 1-dB peak at 4 MHz. Since the modem has been designed for 612 channels (12 kHz to 2.54 MHz), the unit is optimized for this bandwidth. Changing the loop filters makes it possible to optimize the modem for other channel capacities.

Conclusions

It has been demonstrated that an 855-MHz FDM/FM modem can perform in the context of the UET overall configuration and is capable of meeting the INTELSAT IV system operating specifications. Operation with 612 channels has been demonstrated and data indicate that, for wider band operation (e.g., up to 1,872 channels), PLL receivers can be realized.

Acknowledgment

The author would like to acknowledge Dr. W. K. Sones for numerous enlightening discussions, and Messrs. L. F. Gray and A. F. Standing for their many helpful suggestions.

References

- [1] L. Pollack and W. Sones, "An Unattended Earth Terminal for Satellite Communications," *COMSAT Technical Review*, Vol. 4, No. 2, Fall 1974.
- [2] "The INTELSAT IV Communications System," edited by P. Bargellini, *COMSAT Technical Review*, Vol. 2, No. 2, Fall 1972, pp. 437-572.
- [3] R. K. Altenbach, "Notes on FM Distortion in Varactor-Modulated Oscillators," *General Radio Experimenter*, September/October 1969.

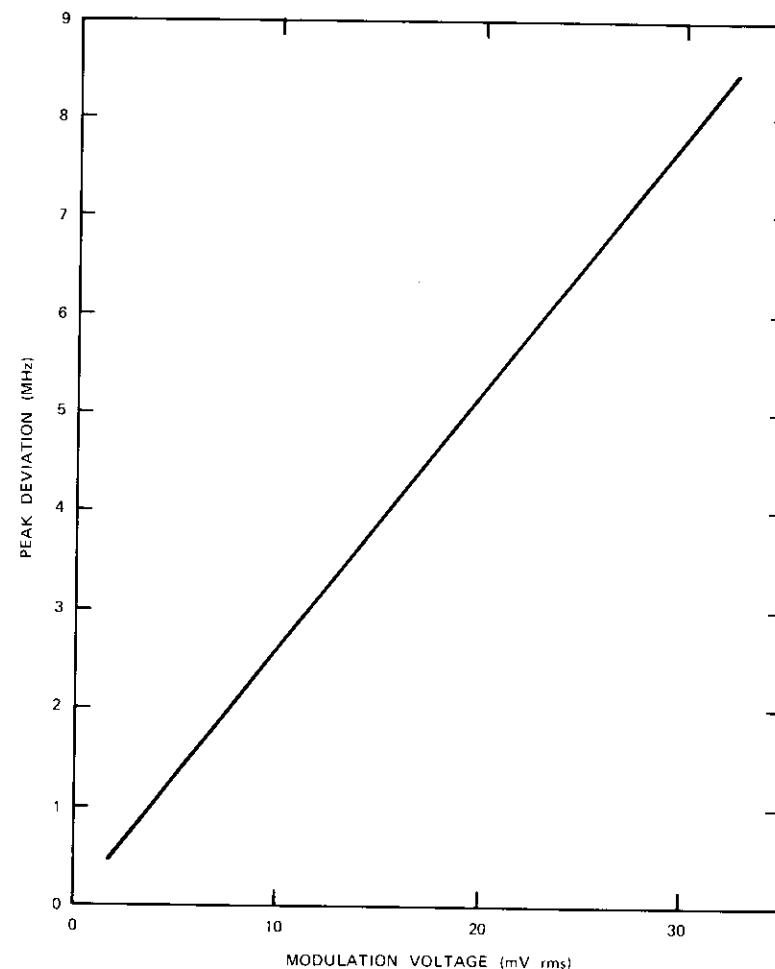


Figure 7. 855-MHz Voltage-Controlled Oscillator Deviation vs Modulating Voltage ($f_m = 200$ kHz, VCO sensitivity = 184 MHz/V)

- [4] H. B. Mead, "Linearity and Stability in Voltage-Controlled Oscillators," *Electro-Technology*, November 1966.
- [5] C. N. Herbert and S. Chernega, "Broadband Varactor Tuning of Transistor Oscillators," *Microwaves*, March 1967.

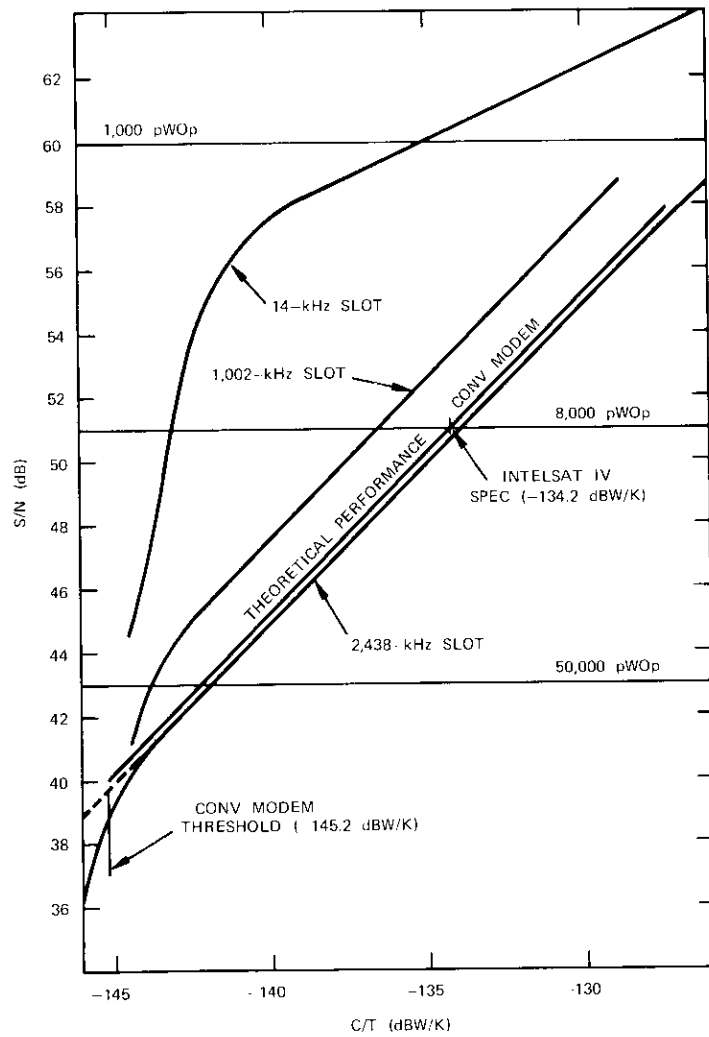


Figure 8. S/N vs C/T

- [6] W. H. Froehner, "Quick Amplifier Design with Scattering Parameters," and "S-Parameters—, Circuit Analysis and Design," Hewlett-Packard Application Note 95, September 1968.
- [7] G. J. Palladino and K. A. Richter, "End Guessing in Oscillator Design," *Microwaves*, October 1970.
- [8] W. C. Lindsey, *Synchronization Systems in Communication and Control*, Englewood Cliffs, New Jersey: Prentice-Hall, Inc., 1972, Chapter 15.
- [9] A. J. Viterbi, *Principles of Coherent Communication*, New York: McGraw-Hill Book Co., 1966.

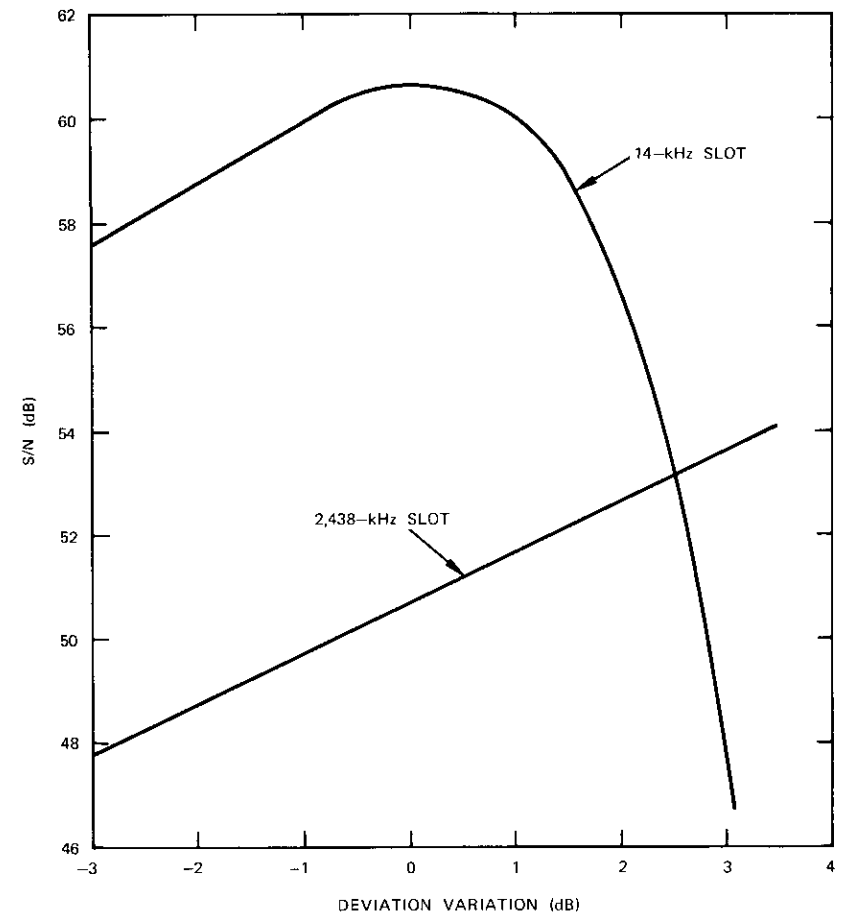


Figure 9. S/N vs Deviation at $C/T = -134.2 \text{ dBW/K}$
(nominal deviation = 1,996 kHz rms)

- [10] J. Klapper and J. Frankle, *Phase-Locked and Frequency-Feedback Systems, Principles and Techniques*, New York: Academic Press, 1972, Chapter 6.
- [11] *Transmission Systems for Communications*, Murray Hill, New Jersey: Bell Telephone Laboratories, 1964, p. 534.
- [12] Davenport and Root, *An Introduction to the Theory of Random Signals and Noise*, New York: McGraw-Hill Book Co., 1958, Section 12-2.



Melvyn Grossman received a B.E.E. from the City College of New York in 1961 and an M.S. from George Washington University in 1974. Prior to joining COMSAT, he was a design engineer with the Space Communications Laboratory, ITT Defense Communications Division, Nutley New Jersey, where he engaged in PLL and FMFB receiver design. He joined the RF Transmission Laboratory of COMSAT Laboratories in 1969. He is presently engaged

in the design of wideband FDM/FM modulators, phase-locked loop receivers, and elliptic function filters for earth terminal use. He is a member of the IEEE.

Index: transponders, repeaters, intermodulation, amplifiers

The Butler matrix transponder

W. A. SANDRIN

(Manuscript received February 11, 1974)

Abstract

This paper describes the Butler matrix transponder, a new design for a multiple-channel repeater. The design consists of a pair of complementary $N \times N$ Butler matrix networks that precede and follow a set of N amplifying devices, and a set of filters that follow the output matrix network. The linearizing property of this configuration permits it to suppress a substantial fraction of the intermodulation product power formed by the amplifier nonlinearities. Therefore, satellite transponder high-level amplifiers can be operated at a higher output power level for a given carrier-to-intermodulation noise ratio and thereby realize a greater overall DC-to-RF efficiency. For example, it is possible to double the overall DC-to-RF efficiency with a 12-channel Butler matrix transponder operating with multiple carriers in each channel. Another advantage of this network is that the output power can be conveniently reapportioned among the channels.

Introduction

In commercial communications satellites separate amplifiers (transponders) are used for each channel. Most channels are occupied by signals

This paper is based upon work performed in COMSAT Laboratories under the sponsorship of the International Telecommunications Satellite Organization (INTELSAT). Views expressed in this paper are not necessarily those of INTELSAT.

whose envelopes are not constant, such as, for example, multicarrier FDM/FM/FDMA telephony signals. In such cases the channel amplifiers must operate at a level where the amount of intermodulation product (IMP) noise generated by the amplifier nonlinearities is acceptable [1].

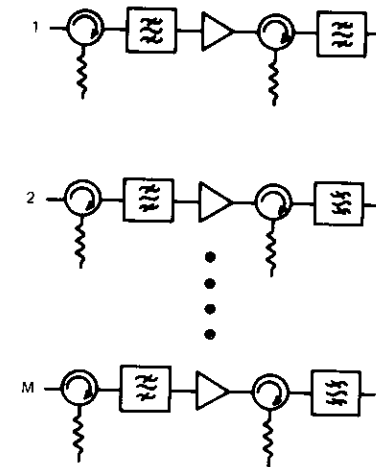
The purpose of this paper is to describe and calculate the performance of a new transponder configuration, the Butler matrix transponder (BMT), suggested by G. R. Welti [2]. This multichannel transponder amplifies signals with less IMP distortion than is possible with conventional multichannel amplifier configurations. Conversely, a BMT is able to operate at higher output levels and higher DC-to-RF efficiencies for a given output carrier-to-intermodulation noise (C/I) ratio.

Figure 1 shows both the conventional and BMT amplifier networks. The BMT consists of two complementary Butler matrix networks [3]-[4] which precede and follow a set of amplifiers. These networks distribute and collect each signal to and from each amplifier. Linearized performance is achieved by separating a number of interfering IMPs from the desired signals. This separation is achieved by a special phase shifting process performed by the Butler matrix networks, which causes a substantial fraction of the IMPs to appear at output ports that are tuned to frequencies different from the IMP frequencies. These IMPs are attenuated by the output port filters and do not appear as interference. With a portion of the IMPs removed from the output signals, the amplifiers can be operated closer to saturation for a specified output C/I ratio.

The BMT described in this paper is intended for application to a multichannel system in which the channels occupy contiguous frequency bands and each channel is occupied by multiple-carrier signals. Note that, in this paper, the term "channel" refers to the frequency band occupied by the signals that are amplified by a single transponder. *It does not refer to one-half of a voice circuit.*

Optimum BMT performance is achieved when the signal power in all bands is equal, although the BMT configuration offers a flexible power-sharing capability not offered by conventional transponders. A noteworthy characteristic for practical application is that the BMT network contains no active components other than the amplifying devices.

The following sections describe the theory of BMT operation and briefly discuss the advantages and disadvantages of such a design over a conventional transponder arrangement. As an example, it is demonstrated that a 100-percent increase in overall DC-to-RF efficiency is possible for a 12-channel BMT using 16×16 matrices. A 4-channel BMT demonstration experiment is also described.



a. CONVENTIONAL M-CHANNEL TRANSPONDER

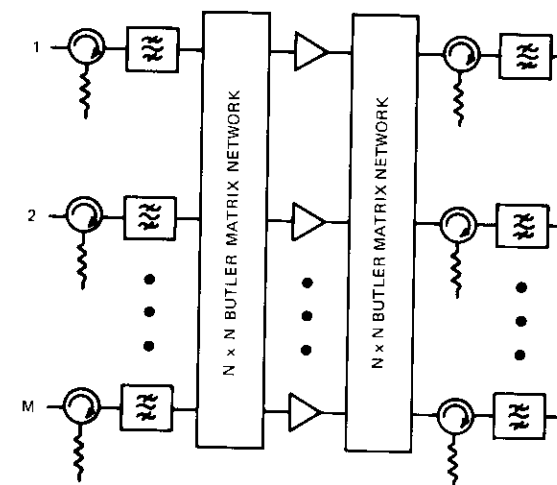
b. M-CHANNEL $N \times N$ BMT

Figure 1. Conventional and BMT Configurations

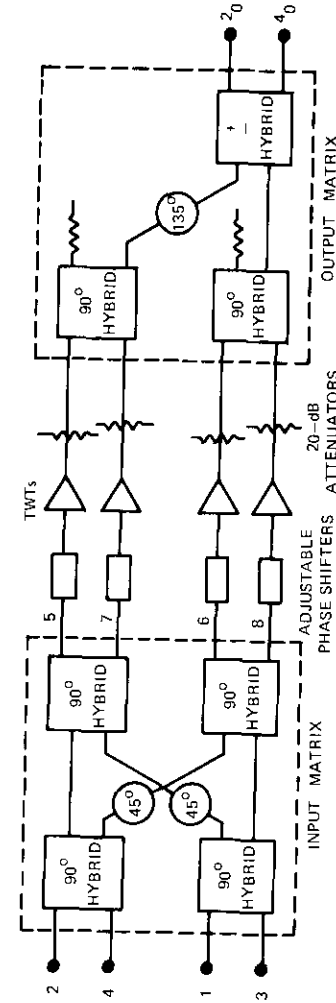
Butler matrix transponder principle of operation

This section summarizes, in physical terms, the mathematical description of BMT operation given in Appendix A. Figure 1 shows the BMT configuration in which M distinct (multicarrier) signals are amplified by N amplifiers ($M \leq N$). As shown, the N nonlinear amplifiers are sandwiched between two $N \times N$ Butler matrices. These matrices, while identical, are connected by the amplifiers in mirror image fashion.

The Butler matrix, which was developed as a multiple-beam feed network for a phased array antenna, is a linear passive and ideally lossless network consisting of hybrid couplers and phase shifters [3], [4]. Figure 2 is an example of a 4×4 Butler matrix circuit. A signal applied to the l th input port by an $N \times N$ Butler matrix appears at each of the output ports attenuated by a factor of $1/N$ and having port-to-port phase shifts equal to $2\pi l/N$.

The Butler matrix network is reciprocal. Hence, if two identical Butler matrices are connected back-to-back, a signal applied at an input port will appear at the corresponding output port (ideally with no attenuation), and no component of this signal will appear at any other port if all ports are terminated with matching impedances. Thus, when N identical nonlinear amplifiers are inserted between two identical Butler matrices to form a BMT, signals applied at the input ports will appear amplified at the corresponding output ports.

Note that each amplifier's input consists of the sum of all signals divided by N . However, because of the different relative phase shifts of each signal at the input to the BMT amplifiers, each IMP at the amplifiers' output will also have amplifier-to-amplifier phase shifts that cause the IMP to be directed to a single output port. The particular output port to which an IMP is directed depends on the input ports of the signal components which generate the IMP and on the order of the IMP. It is this property of a BMT which permits the reduction of IMP interference. As shown in the following sections, if signal frequency bands are judiciously assigned to BMT ports, a large number of IMPs can be routed to ports that are tuned to frequencies different from the IMP frequencies for suppression by the output port bandpass filters. When the number of signals, M , is less than the number of ports, N , the unused BMT input and output ports are terminated with matching impedances.



PARTS LIST

- 90° HYBRIDS: NARDA MODEL 3034
- HYBRID: ALFORD MODEL 7199
- ADJUSTABLE PHASE SHIFTERS: GENERAL RADIO MODEL 874
- TWT's: HUGHES MODEL 215H
- ATTENUATORS: NARDA MODEL 792 FM
- 45° AND 135° FIXED PHASE SHIFTERS: SPECIALLY CUT LENGTHS OF SEMIRIGID COAX

Figure 2. Experimental 4×4 BMT

Port-frequency assignments

To design a BMT for use in an FDM system with M contiguous frequency bands, judicious selection of port-frequency assignments is necessary for maximum IMP power rejection. The specific problem discussed here is that of assigning the M contiguous frequency bands to the ports of an $N \times N$ ($M \leq N$) BMT so that every 3rd-order IMP (formed by the amplifiers) is directed to an output port tuned to a frequency band different from the IMP frequency. It is assumed that the BMT is operating with one carrier per port.

As an example, consider a 4×4 BMT with ports numbered 1, 2, 3, and 4, which amplifies four contiguous frequency bands, also numbered 1, 2, 3, and 4. Figures 3 and 4 illustrate the 3rd-order IMP frequencies and output ports for both of these port-frequency assignment plans. From Figure 3 it can be seen that the port-frequency assignment 1, 2, 4, 3 is ideal since no 3rd-order IMPs appear at an output port with a signal frequency assignment which is the same as the IMP frequency. (In this particular case it can be shown that all 5th-order IMPs also have this

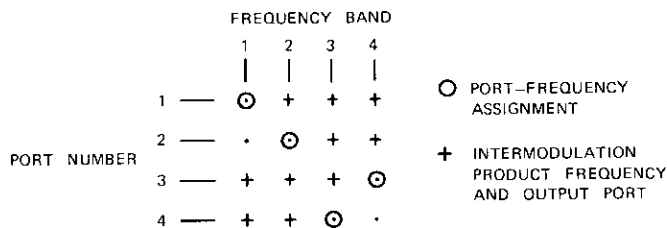


Figure 3. Optimum Port-Frequency Assignment Plan for a 4×4 BMT

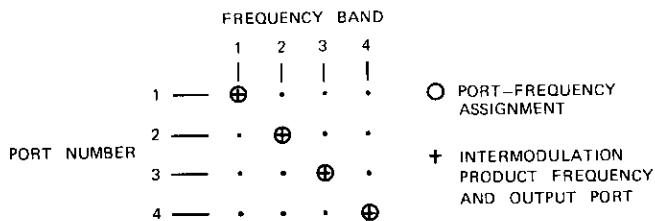


Figure 4. Nonideal Port-Frequency Assignment Plan for a 4×4 BMT

property.) Correspondingly, Figure 4 shows that port-frequency assignment 1, 2, 3, 4 is not optimum, since IMPs appear at ports with signal frequency assignments which are the same as the IMP frequencies.

Exhaustive examination has shown that there are eight valid port-frequency assignments of the 24 possible permutations for a 4×4 BMT and four contiguous frequency bands ($M = 4$). Similarly, with $M = 6$ and $N = 6$, there are 12 valid port-frequency assignment plans of 720 possible permutations. Exhaustive computation has also shown that, for $M = 8$ and $N = 8$, there are no valid port-frequency permutations. In this case either noncontiguous frequency bands must be used, or M must be equal to or less than 7. However, a valid port-frequency plan has been found for the case in which $M = 10$ and $N = 10$. Table 1 gives examples of port-frequency plans for various values of M and N .

There is no known procedure for direct calculation of ideal port-frequency assignments. However, an algorithm which permits very rapid evaluation of candidate plans by a trial and error procedure has been developed. This algorithm has been used to find the $M = 12$, $N = 16$ port-frequency assignment given in Table 1.

BMT multicarrier performance

The preceding section described optimum port-frequency assignment plans which permit the BMT to suppress all 3rd-order IMPs when one unmodulated carrier per port is used. However, a BMT application is not practical in this situation, since signals with constant envelopes permit distortion-free use of separate fully saturated amplifiers. A BMT becomes useful for signals which do not have a constant envelope, such as FDM/FM or AM signals. The IMPs formed in BMT amplifiers with this type of signal structure fall into two classes. The first class consists of IMPs formed by components of signals from different ports. If it is assumed that the port-frequency assignments are optimum, as discussed previously, these IMPs are suppressed. The second class of IMPs consist of those which are formed by the components of the same signal. These IMPs have the same amplifier-to-amplifier phase differences as the signal components from which they are formed; hence, they are directed to that signal's output port where they appear as interference.

To calculate BMT performance, the signal at each port is assumed to be the number, I , of equal-amplitude carriers. The division between the two classes of IMPs is calculated and the resulting output C/I ratio is compared with that of a conventional transponder.

TABLE 1. EXAMPLES OF VALID PORT-FREQUENCY ASSIGNMENT PLANS FOR A BUTLER MATRIX TRANSPONDER

[M = number of channels (contiguous), N = number of ports, $M \leq N$]

a. $M = 4, N = 4$												
Frequency	1	2	3	4								
Port	1	2	4	3								
b. $M = 6, N = 6$												
Frequency	1	2	3	4	5	6						
Port	1	3	2	5	6	4						
c. $M = 8, N = 8$												
No Valid Plan												
d. $M = 10, N = 10$												
Frequency	1	2	3	4	5	6	7	8	9	10		
Port	1	2	9	3	5	10	8	4	7	6		
e. $M = 12, N = 16$												
Frequency	1	2	3	4	5	6	7	8	9	10	11	12
Port	1	8	11	16	12	6	5	8	3	7	14	4

For example, assume that the input to the l th port of the BMT is

$$f_l = \sum_{i=1}^I \cos(\omega_m^i t) \quad , \quad 1 \leq m \leq M \quad (1)$$

where ω_m^i is the radian frequency of the i th carrier in the m th frequency band. Also assume that signals of this type are applied to M ports of an $N \times N$ BMT ($M \leq N$). At the r th output port of the input Butler matrix the signal, F_r , from equation (A2) in Appendix A is

$$F_r = \frac{1}{N} \sum_{m=1}^M \sum_{i=1}^I \cos\left(\omega_m^i t - \frac{2\pi l_m r}{N}\right)$$

$$= \frac{1}{N} \sum_{m=1}^M \sum_{i=1}^I \cos \phi_{im} \quad (2)$$

where $\phi_{im} = \omega_m^i t - (2\pi l_m r)/N$

l_m = port assignment of the m th frequency band.

The ϕ_{im} terms form the matrix

$$\begin{matrix} \phi_{11} & \phi_{12} & \cdot & \cdot & \cdot & \phi_{1M} \\ \phi_{21} & \cdot & \cdot & \cdot & \cdot & \phi_{2M} \\ \cdot & \cdot & \cdot & \cdot & \cdot & \cdot \\ \cdot & \cdot & \cdot & \cdot & \cdot & \cdot \\ \phi_{I1} & \phi_{I2} & \cdot & \cdot & \cdot & \phi_{IM} \end{matrix} \quad (3)$$

At the r th input port of the second Butler matrix, after nonlinear amplification, the signal, F'_r , is

$$F'_r = \frac{c}{N} \sum_{m=1}^M \sum_{i=1}^I \cos \phi_{im} + \text{IMPs} \quad (4)$$

where c is the amplifier's gain constant and where the IMPs can generally be represented as in equation (A9) of Appendix A, or, as shown in the following, divided into classes of suppressed and nonsuppressed IMPs.

It can be shown [5] that, as the number of carriers in a nonlinear amplifier is increased to a large number while a constant input power is maintained, the ratio of the carrier to the IMPs falling on the carrier's frequency approaches a constant. Thus, if the number of carriers per channel (port) is large, the C/I ratio at the output of each of the BMT amplifiers is the same as that at the output of a single amplifier operating at the same input power with only the signal from one channel. However, as discussed previously, those IMPs in a BMT which are produced by signal components from different channels are suppressed. Hence, an overall improvement in output C/I is realized.

The phase and frequency of each of the IMPs present at the output of the r th amplifier are determined by linear combinations of the $I \times M$ terms of the matrix given in equation (3). Table 2 summarizes all of the 3rd-order IMPs and indicates whether or not they are suppressed when

The phase shifters used in the matrix networks were made from coaxial cables cut to different electrical lengths. For the experiment this design was adequate over the entire 160-MHz bandwidth. The adjustable phase shifters which preceded each TWT were used to compensate for slight tube-to-tube phase differences.

A frequency plan of four contiguous 40-MHz channels, centered at 3,765, 3,805, 3,845, and 3,885 MHz, respectively, was used, and the input and output matrices were designed for a 3,825-MHz mid-band frequency. The input and output port numbers given in Figure 2 correspond to contiguous assignments in the "port domain." For example, a carrier input at port 2 is amplified and appears at output port 2₀; the 3rd-order IMPs produced by a carrier from port 2 and a carrier from port 3 will ideally appear only at output ports 4₀ and, if the complete output matrix is built, at 1₀. The port-frequency assignment plan was 1, 2, 4, 3.

Tests of the experimental BMT were performed with different types of signals, including single, dual, and multiple (4, 5, and 6) unmodulated carriers applied in varying combinations to the four ports, and slotted noise bands. Tests made with single- and dual-carrier signals provided port isolation and transmission data. For example, with the input and output matrices connected back-to-back, transmission losses of 0.25 to 1.25 dB were measured for the paths from ports 2-2₀ and 4-4₀ over the operating bands, while isolation greater than 20 dB was measured in the six remaining paths.

Figure 5 shows the results of a test with two carriers in one port and one carrier in each of the remaining three ports. It also shows computed results, based on the analysis of the preceding sections, and the measured and computed 2-carrier performance for a single TWT amplifier. Discrepancies between the experimental and computed results in this figure are attributed to measurement errors in the spectrum analyzer used for this test, and to an imprecise definition of the single-carrier TWT amplifier saturation point.

Figure 6 shows the results of a slotted noise band experiment. In this test each of four channels was loaded with equal-power noise bands with bandwidths of 2.25 to 16 MHz. A narrow slot was inserted at the midpoint of one of the bands (channel 2) so that the power measured in the slot (1 kHz) in the output signal represented the IMP power level in that band. Figure 6 includes plots of measured and computed C/I ratios versus input power for a single noise band amplified by a single TWT (curve a), and four noise bands amplified by a BMT (curve b). It also includes a plot of C/I ratio measured at the output of one of the TWTs operating in the

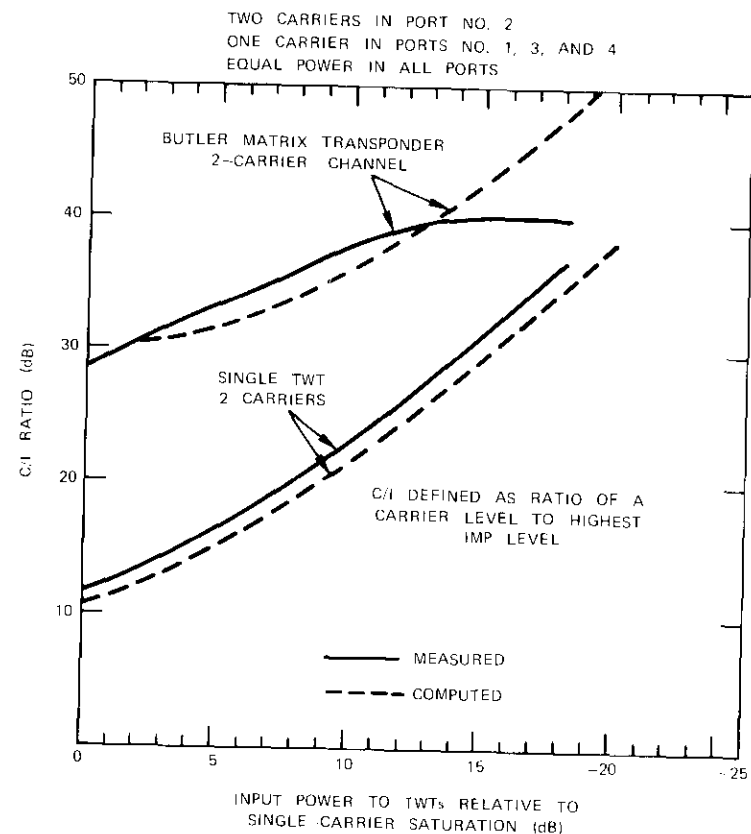


Figure 5. Comparison of Experimental and Calculated Results for a 4×4 BMT and a Single TWT

BMT (curve c). The test setup used for this experiment had a limiting C/I ratio of 31.5 dB. This limitation is attributed to nonlinearities in the mixer and low-level amplifier which were used in the test circuit.

In Figure 6 the improved C/I ratio for the BMT channel can be attributed to two phenomena. The first improvement is simply a consequence of loading the TWT with a sparse spectrum. This effect, which is indicated by the difference between curves a and c, diminishes as the transponder bands are filled. The second is the improvement resulting from BMT operation on selected classes of IMPs. This improvement, Q , described by equation (6), equals 3.58 dB for four channels, and corresponds

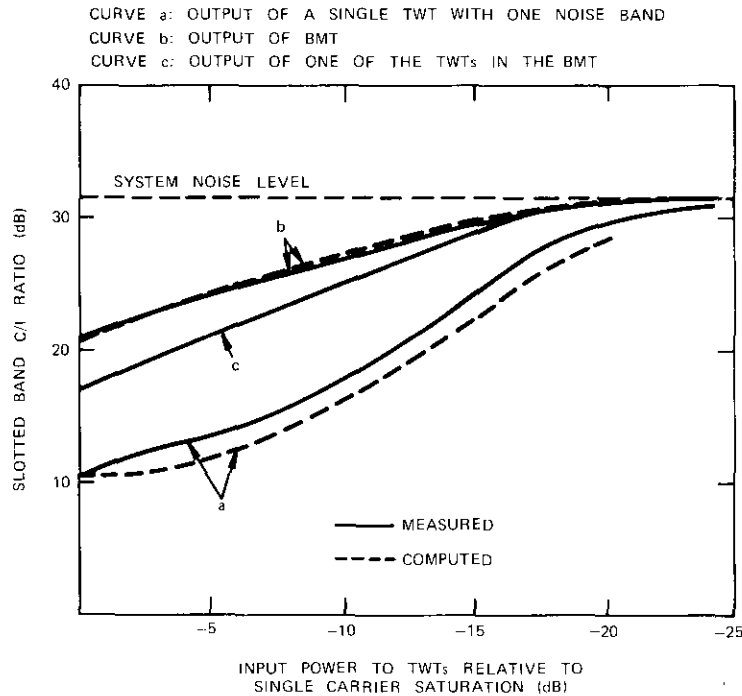


Figure 6. Slotted Band C/I Measurements for a 4×4 BMT with Four Bands of Noise (one per port)

to the measured difference (at low C/I ratios at which the test circuit noise was negligible) between curves b and c.

Performance comparison

The performance of a BMT relative to a single-amplifier-per-transponder arrangement is plotted in Figure 7 for 4 and 12 channels. As indicated previously, if it is assumed that the signals occupy contiguous bands, a 4×4 BMT is used for $M = 4$ and a 16×16 BMT is required for $M = 12$. Each channel in Figure 7 is assumed to contain a large number of equi-level carriers that occupy the major portion of each band. The data for the single amplifier in this figure were computed [6] by using the complex characteristics of an INTELSAT IV high-level TWT (Hughes model

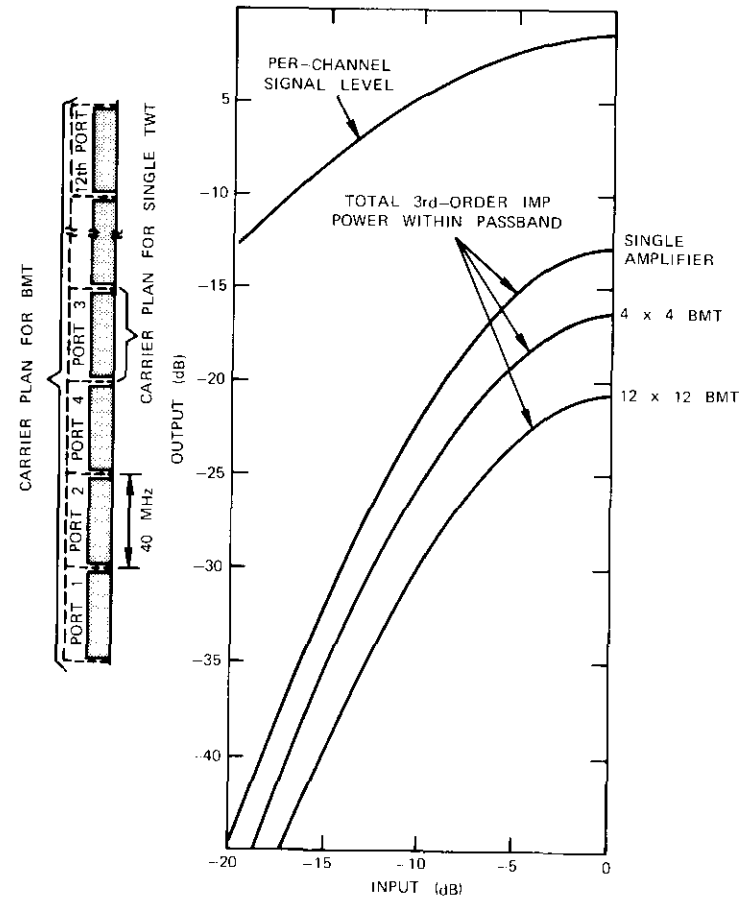


Figure 7. BMT vs Single-Amplifier Performance for Infinite Carriers per Channel

261H), while the performance of the BMT using amplifiers with the characteristics of the single amplifier was obtained from equation (6). The single-carrier saturation power of the amplifiers in the $M = 12$ ($N = 16$) BMT was assumed to be three-fourths that of the amplifiers in the single-amplifier-per-signal configuration so that the comparison was made on the basis of equal operating points.

Figure 7 demonstrates the relationship between C/I improvement and output power increase. For example, Figure 7 shows that, at relatively

low input levels (high backoffs), the 12-channel BMT gives a 4.4-dB output power improvement over a single-amplifier-per-channel configuration for a given C/I value, excluding implementation losses. Conversely, for a given output power per channel, the output C/I ratio for the 12-channel BMT is 7.9 dB higher than that of a conventional amplifier.

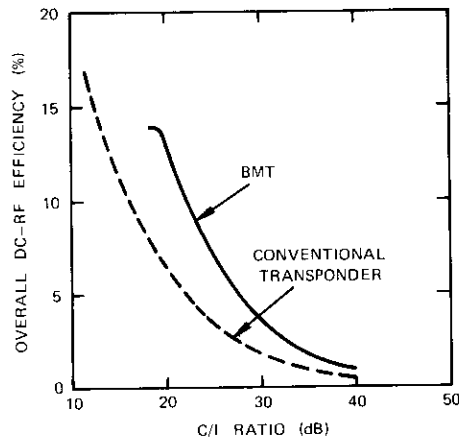


Figure 8. Overall DC-to-RF Efficiency vs C/I Ratio for a 12-Channel BMT

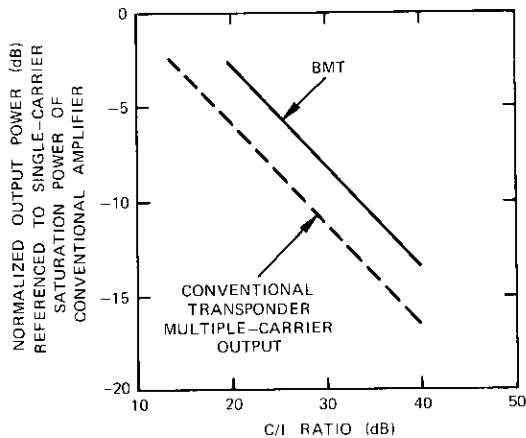


Figure 9. Output Power vs C/I Ratio for a 12-Channel BMT

If it is assumed that the DC power required by the amplifiers is independent of drive level and that the implementation loss (i.e., combined output matrix and amplifier imbalance losses) is 1.4 dB, this power improvement is equivalent to a 100-percent increase in overall DC-to-RF efficiency, as shown in Figures 8 and 9. These figures are derived directly from Figure 7, with an amplifier single-carrier saturation efficiency of 27.6 percent assumed.

The BMT performance shown in Figure 7 is representative of a system in which all carrier levels are equal, under fully loaded conditions. If some of the M channels do not fully occupy their bands, the in-band IMP levels are lowered because of the spectral periodicity of the signal being amplified. Also, as the power in some of the channels is lowered, the IMP level in all channels is lowered. Hence, it is possible, under partially loaded conditions,

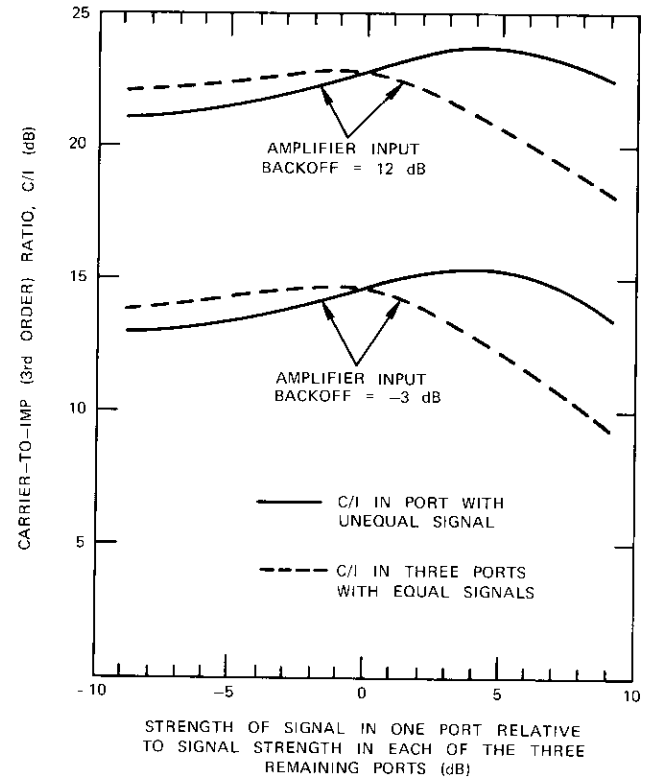


Figure 10. Performance of a 4×4 BMT with Four Carriers per Port as the Level of the Signal into One Port is Varied

to boost the output of one or more channels to levels greater than the nominal fully loaded output levels.

Figure 10 indicates the computed performance of a 4×4 BMT with four carriers per channel in terms of a variation in the level of one port relative to the power in the remaining ports. In this example, the operating point of the amplifiers, and hence the BMT total output power, is kept constant as the level of one channel is increased (or decreased) while the remaining channels are all decreased (or increased) slightly. Because the BMT remains fully loaded in this example, the C/I is degraded in some channels and enhanced in others.

Implementation losses and considerations

Deviations from the ideal performance described in the preceding sections can be expected from an operational BMT. The major sources of these losses are input and output Butler matrix insertion losses, and random and systematic amplitude and phase errors in the matrix networks and amplifying devices.

If the matrix networks are constructed of stripline building blocks (consisting of 3-dB hybrids and phase shifters) connected by coaxial cables, a loss of between 0.2 to 0.3 dB per stage can be expected depending on weight/size and performance tradeoffs. If the matrix networks have $N = 2^n$ input/output ports, each network has n stages. Hence, a BMT using 16×16 Butler matrices can be expected to have an insertion loss of approximately 1 dB in the input and output matrix networks.

Systematic errors will occur in BMT matrix networks and amplifiers because of small performance variations of these components with frequency. However, analysis has shown that the effect of these errors can be expected to be negligible because their magnitude can be made very small over the bandwidths of interest (500 MHz at 4 GHz, for example), and because the input/output matrices are complementary so that these errors are largely self-compensating.

The effects of random errors have been analyzed using an approach similar to those employed in References 7 and 8. In this analysis it has been assumed that the major contributor to these errors is the amplifiers. The results are summarized in Table 3, which shows that, with single-carrier output mean gain and phase deviations of the order of ± 0.5 dB and $\pm 7^\circ$, respectively, for amplifiers operating in a 12-channel 16×16 BMT, the probability that the C/I will not be degraded by more than 1 dB is 0.99. These gain and phase deviations are well within the variations

TABLE 3. TUBE-TO-TUBE AMPLITUDE AND PHASE VARIATION SPECIFICATION FOR A 12-CHANNEL 16×16 BMT

C/I Degradation (dB)	Probability of C/I Degradation Not Being Exceeded	Mean Value of Allowable Individual Carrier Output Deviation	
		Amplitude (dB)	Phase (deg)
1	0.99	± 0.5	± 7
2	0.8	± 1	+21
3	0.63	± 2.6	± 38

that can be expected during the lifetime of a spaceborne TWT, provided, however, that the TWTs are closely matched initially.

A BMT and a single-channel amplifier are affected differently by tube failures. The failure of an amplifier in a conventional multichannel transponder results in catastrophic failure of one channel with no impairment to the other channels. On the other hand, the failure of a single amplifier in a BMT results in partial power and C/I degradation; hence, the system operator may select the channel(s) that must be turned off so that the remaining channels will not be impaired and/or reapportion the channel power to exploit the excess system margins so that the number of operating channels can be maximized.

Table 4 shows the calculated output power reduction and C/I degradation caused by a single tube failure for BMTs of various sizes and a large number of carriers per BMT channel when the tube fails without changing its input/output impedance. Failure of a tube with a high input VSWR

TABLE 4. C/I DEGRADATION AND OUTPUT POWER REDUCTION IN A BMT DUE TO A SINGLE TUBE FAILURE

Number of BMT Channels, M	Number of BMT Tubes, N	C/I Degradation (dB)	Output Power Reduction (dB)
4	4	0.58	2.5
8*	8	0.28	1.16
10	10	0.22	0.92
12	16	0.10	0.56

* Noncontiguous frequencies assumed.

may cause some performance degradation, depending on the structure of the signal networks preceding the BMT. However, this degradation can be remedied by using circulators preceding the input Butler matrix.

Discussion

The BMT is a multichannel amplifier which suppresses the IMP noise generated by individual amplifier nonlinearities. The amount of IMP suppression increases with the number of channels used.

The advantages of a BMT over a conventional arrangement of separate amplifiers for each channel are as follows. First, for a given C/I ratio and DC power, the output RF power is increased. Hence, the BMT offers a means of boosting output power without increasing individual amplifier output ratings. Also, of significant importance for space application, the overall DC-to-RF efficiency is increased. The corollary is also true; i.e., for a given output power and efficiency, the C/I ratio is improved by using a BMT.

Another advantage of the BMT is that, if the number of channels is less than the number of BMT ports, the output power per channel is fractionally greater than that of the amplifying devices. For example, a 12-channel 16×16 BMT would have a per-channel output power of $4/3$ of the individual amplifier power. Hence, the BMT provides a means of efficiently paralleling power-limited amplifiers. A further advantage is that the BMT, under non-peak loading conditions, has a flexible power-sharing capability which permits some channels to operate with a greater output power than others without C/I degradation in any channel.

Disadvantages of the BMT are as follows. First, the bandwidth of the amplifiers in an M -channel BMT must be M times as wide as that of a single-channel transponder. Second, under fully loaded conditions, the power in each channel must be equal if it is assumed that all channels are subject to the same minimum C/I specification. Also, analysis indicates that, when one or more of the channels are operated in a single-carrier (constant envelope) mode, the BMT rapidly loses its power saving qualities and distortion is added to the single-carrier signal. Finally a BMT, when compared to other linearization techniques [10], [11], has the obvious disadvantage of requiring multichannel operation.

Conclusion

The concept of the BMT has been introduced by describing the theory of operation, giving the results of an experimental demonstration, and

briefly discussing the advantages and disadvantages of such a design over a conventional multichannel transponder configuration. It has been demonstrated that the IMP noise is reduced by special phase processing of the signals amplified in the BMT. Although specific system parameters must be known before the utility of a BMT application can be fully assessed, the analysis provided in this paper indicates that the overall DC-RF efficiency can be doubled by a 12-channel BMT.

Acknowledgment

The author is grateful for the helpful suggestions and contributions provided by George R. Welti.

References

- [1] "The INTELSAT IV Communications System," edited by P. L. Bargellini, *COMSAT Technical Review*, Vol. 2, No. 2, Fall 1972, pp. 437-572.
- [2] "Butler Matrix Transponder Improvements" (G. R. Welti), U.S. Patent Application, Serial No. 412399, filed November 2, 1972.
- [3] J. L. Butler, "Digital Matrix and Intermediate Frequency Scanning," *Scanning Antennas*, edited by R. C. Hansen, Chapter 3, Vol. III, New York: Academic Press, 1966.
- [4] J. P. Shelton and K. S. Kelleher, "Multiple Beams from Linear Arrays," *IRE Transactions on Antennas and Propagation*, March 1961, pp. 154-161.
- [5] R. J. Westcott, "Investigation of Multiple FM/FDM Carriers Through a Satellite TWT Operating Near Saturation," *Proceedings of the IEE*, Vol. 114, No. 6, June 1967, pp. 726-740.
- [6] J. C. Fuenzalida, O. Shimbo, and W. L. Cook, "Time-Domain Analysis of Intermodulation Effects Caused by Nonlinear Amplifiers," *COMSAT Technical Review*, Vol. 3, No. 1, Spring 1973.
- [7] L. A. Rondinelli, "Effects of Random Errors on the Performance of Antenna Arrays of Many Elements," *IRE Convention Record*, Pt. 1, 1959, pp. 174-189.
- [8] J. Ruze, "Physical Limitations on Antennas," Technical Report 248, M.I.T. Research Laboratory of Electronics AD No. 62351, October 30, 1952.
- [9] A. F. Standing, "An Active Phase and Amplitude Correction Device for Reducing Intermodulation Produced by TWTs and Klystrons," *IEE Conference on Earth Station Technology*, London, England, October 14-16, 1970, IEE Publication No. 72, pp. 274-279.
- [10] H. Seidel, "A Microwave Feed Forward Experiment," *Bell System Technical Journal*, Vol. 50, No. 9, November 1971, pp. 2879-2916.

Appendix A. Butler matrix transponder operation

The configuration of the Butler matrix transponder (BMT), in which M distinct (multicarrier) signals are amplified by N nonlinear amplifiers ($M \leq N$) "sandwiched" between two $N \times N$ Butler matrices, has been shown in Figure 1 of the paper. These matrices, while identical, are connected by the amplifiers in mirror image fashion. This appendix explains the operation of the BMT by describing a single Butler matrix, the operation of two Butler matrices back-to-back, the generation of intermodulation products (IMPs) in nonlinear amplifiers, and the effect of a BMT on IMPs.

Butler matrix network

The Butler matrix, which was developed as a multiple-beam feed network for a phased array antenna, is a network consisting of hybrid couplers and phase shifters [A1], [A2]. The total number of ports in such a network is usually 2×2^p , although networks with $2 \times q^p$ (where q and p are integers > 1) total ports are possible. Figure 2 of the paper is an example of a 4×4 Butler matrix circuit. The normalized input/output port relationships for the Butler matrix network are

$$F_r = \frac{1}{\sqrt{N}} \sum_{i=0}^{N-1} f_i \exp \left[-j \frac{2\pi lr}{N} \right] \quad (\text{A1})$$

$$f_i = \frac{1}{\sqrt{N}} \sum_{r=0}^{N-1} F_r \exp \left[j \frac{2\pi lr}{N} \right] \quad (\text{A2})$$

where

f_i = signal at the i th input port

F_r = signal at the r th output port.

Equations (A1) and (A2) are a discrete Fourier transform pair [3].

It can be shown from equations (A1) and (A2) that, if two identical ideal Butler matrix networks are connected back-to-back so that the second network is a mirror image of the first, a signal applied to an input matrix port will appear unattenuated at the corresponding output matrix port. No component of that signal will be present at any other port if all ports are terminated with matching impedances. Thus, in the absence of amplifier nonlinearities, each signal (by superposition) in an ideal BMT is amplified independently of the signals applied to other input ports.

The nonlinear amplifier model

The transfer characteristic of a nonlinear amplifier can be expressed as

$$e_{\text{out}} = g(e_{\text{in}}) \exp[jf(e_{\text{in}})] \quad (\text{A3})$$

where $g(e_{\text{in}})$ represents the amplitude distortion characteristic, and $f(e_{\text{in}})$ represents the amplifier's phase shift caused by input amplitude variations, i.e., the AM-PM conversion characteristic. Several forms of $g(e_{\text{in}})$ and $f(e_{\text{in}})$ have been used to characterize nonlinear amplifiers [A4]–[A11]. Reference A12 provides a unified description of amplitude distortion and AM-PM conversion, with examples of power series and Fourier series expansions which include both effects. Reference A13 discusses the effect of using nonlinear amplifiers in the radiating elements of a phased array antenna.

When the input signals are multiple carriers, the calculation of the amplifier's output can be separated into two steps: the combinatorial problem of determining the frequency and relative phase (i.e., relative to the phases of the input signals) of each of the IMPs of the classes of interest, and the problem of finding the magnitude and absolute phase of each class of IMPs. In this appendix, only the former calculation is performed; thus, the results presented are independent of the specific forms of $g(e_{\text{in}})$ and $f(e_{\text{in}})$.

If a multiple-carrier input to a nonlinear amplifier is expressed as

$$e_{\text{in}} = \sum_{m=1}^M a_m \sin(\phi_m) \quad (\text{A4})$$

where

$$\phi_m = \omega_m t + \alpha_m$$

then the output of the amplifier can be expressed as

$$e_{\text{out}} = c \sum_{m=1}^M a_m \sin(\phi_m) + \text{Re} \left\{ \sum_{k_1=-\infty}^{\infty} \sum_{k_2=-\infty}^{\infty} \cdots \sum_{k_M=-\infty}^{\infty} \right. \\ \left. \cdots \sum_{k_M=-\infty}^{\infty} A, k_1, k_2, \dots, k_m, \dots, k_M \right. \\ \left. \cdot \exp[j(k_1\phi_1 + k_2\phi_2 + \dots + k_m\phi_m + \dots + k_M\phi_M)] \right\} \quad (\text{A5})$$

where c is the amplifier's gain constant; $A, k_1, k_2, \dots, k_m, \dots, k_M$ is a complex quantity representing the amplitude and phase of a single IMP determined by $g(e_{\text{in}})$ and $f(e_{\text{in}})$; and the k_m coefficients are any integer including zero, subject to the following constraint:

$$\sum_{m=1}^M k_m = 1 \quad (\text{A6})$$

if only in-band products are to be considered.

Transponder operation

This section analyzes signal and IMP flow in a BMT. Let

- f'_l = input to the l th port of the first (input) Butler matrix
 F_r = output from the r th port of the first Butler matrix
 F'_l = input to the r th port of the second (output) Butler matrix
 f_l = output from the l th port of the second Butler matrix.

Also let

$$f'_l = \operatorname{Re} \left\{ \sum_{m=1}^{M_l} A_{m,l} \exp[j\omega_{m,l} t] \right\} \quad (\text{A7})$$

where M_l = number of carriers at the l th input port
 $A_{m,l}, \omega_{m,l}$ = amplitude and radian frequency of the m th carrier at the l th input port, respectively.

Substituting equation (A7) into equation (A1) yields

$$F'_r = \operatorname{Re} \left\{ \frac{1}{\sqrt{N}} \sum_{l=0}^{N-1} \sum_{m=1}^{M_l} A_{m,l} \exp \left[j \left(\omega_{m,l} t - \frac{2\pi l r}{N} \right) \right] \right\} \quad (\text{A8})$$

F'_r and F_r represent the input and output, respectively, of the r th amplifier in the BMT if the transmission line phase shift constants are omitted. Note that equation (A8), similar to equation (A4), represents a multicarrier amplifier input signal. The exponential and double subscript notation in equation (A8) is compatible with the notation of equations (A1) and (A2), and permits a variable number of carriers (M_l) at each of the input ports. Using this notation and a form similar to that of equation (A5) makes it possible to express the output of the r th nonlinear amplifier, F_r , as follows:

$$\begin{aligned} F_r = & \operatorname{Re} \left\{ \frac{c}{\sqrt{N}} \sum_{l=0}^{N-1} \sum_{m=1}^{M_l} A_{m,l} \exp \left[j \left(\omega_{m,l} t - \frac{2\pi l r}{N} \right) \right] \right\} \\ & + \operatorname{Re} \left\{ \frac{1}{\sqrt{N}} \sum_{k_{1,0}=-\infty}^{\infty} \sum_{k_{2,0}=-\infty}^{\infty} \sum_{k_{3,0}=-\infty}^{\infty} \dots \sum_{k_{M_0,0}=-\infty}^{\infty} \dots \right. \\ & \quad \dots \sum_{k_{M_{N-1},N-1}=-\infty}^{\infty} A, k_{1,0}, k_{2,0}, k_{3,0}, \dots \\ & \quad \dots, k_{M_0,0}, \dots, k_{M_{N-1},N-1} \\ & \quad \left. \cdot \exp [j(k_{1,0}\phi_{1,0} + k_{2,0}\phi_{2,0} + k_{3,0}\phi_{3,0} \dots \right. \\ & \quad \left. + k_{M_0,0}\phi_{M_0,0} \dots + k_{M_{N-1},N-1}\phi_{M_{N-1},N-1})] \right\}, \\ & 1 \leq m < M_l, \quad 0 \leq l \leq N-1 \end{aligned} \quad (\text{A9})$$

$$\text{where} \quad \phi_{m,l} = \omega_{m,l} t - (2\pi l r / N) \quad (\text{A10})$$

The coefficients $k_{m,l}$ in equation (A9) are any integer including zero, subject to the constraint that

$$\sum_{l=0}^{N-1} \sum_{m=1}^{M_l} k_{m,l} = 1 \quad (\text{A11})$$

where the subscripts m,l refer to the m th carrier of the l th output port. [Note that both equations (A9) and (A5) represent the output of a nonlinear amplifier with a multiple-carrier input; the only difference between the two is the notation.] The phase term $2\pi l r / N$ in equations (A8) and (A9) represents relative phases. The absolute phase shift through the system, assumed to be equal for all transmission paths and amplifiers, is not included in these expressions. Note that the amplifier-to-amplifier phase difference for a signal directed to the l th output port is $2\pi l / N$.

Substitution of the first part of equation (A9), i.e., the signal components of the inputs to the second Butler matrix, into equation (A2), i.e., the input/output equation for the second matrix, yields the BMT's signal component outputs. For an arbitrary output port, p , let f_p (signal) represent the signal component of the output at this port. Then,

$$\begin{aligned} f_p(\text{signal}) = & \operatorname{Re} \left[\frac{1}{\sqrt{N}} \sum_{r=0}^{N-1} \left\{ \frac{c}{\sqrt{N}} \sum_{l=0}^{N-1} \sum_{m=1}^{M_l} A_{m,l} \exp \left[j \left(\omega_{m,l} t - \frac{2\pi l r}{N} \right) \right] \right\} \right. \\ & \left. \cdot \exp \left(j \frac{2\pi p r}{N} \right) \right] \\ = & \operatorname{Re} \left\{ \frac{c}{N} \sum_{r=0}^{N-1} \sum_{l=0}^{N-1} \sum_{m=1}^{M_l} A_{m,l} \exp [j(\omega_{m,l} t)] \right. \\ & \left. \cdot \exp \left[j \frac{2\pi r}{N} (p - l) \right] \right\} \\ = & \operatorname{Re} \left\{ c \sum_{m=1}^{M_l} A_{m,l} \exp [j(\omega_{m,l} t)] \right\} \delta(p - l) \end{aligned} \quad (\text{A12})$$

where $\delta(p - l)$ is the Kronecker delta. Equation (A12) indicates that the signal component at the p th output port of a BMT is an amplified replica of the signal at the p th input port, with no signal components at other input ports.

From equations (A9) and (A10), the i th IMP frequency, ω_i , of the amplifier outputs, F_r , is

$$\omega_i = \sum_{l=0}^{N-1} \sum_{m=1}^{M_l} k_{m,l} \omega_{m,l} \quad (\text{A13})$$

where the coefficients $k_{m,i}$ must satisfy the condition of equation (A11). Similarly, from equations (A9) and (A10), the amplifier-to-adjacent-amplifier phase difference for the i th IMP, defined as α_i , at the amplifier outputs is

$$\alpha_i = \frac{2\pi}{N} \sum_{l=0}^{N-1} \sum_{m=1}^{M_l} lk_{m,l} \quad (A14)$$

Equations (A13) and (A14) show that, when a specific IMP (i.e., one set of $k_{m,i}$) has a frequency ω_i equal to the frequency of a specific signal (e.g., the m th carrier of the p th port, $\omega_{m,p}$), the IMP phase difference term, α_i , will not generally be the same as the signal's amplifier-to-amplifier phase difference, $2\pi p/N$. Thus, if

$$\sum_{l=0}^{N-1} \sum_{m=1}^{M_l} lk_{m,l} \neq p \quad \text{modulo } N, \quad 0 < p \leq N-1 \quad (A15)$$

this IMP will appear at an output port [as can be seen by substitution into equation (A2)] different from the port p at which the signal at $\omega_{m,p}$ appears. It is this property of a BMT, i.e., the routing of a large portion of the IMPs to output ports that are tuned to frequencies different from the IMP frequencies, which permits the intermodulation interference to be reduced. As discussed previously, if the BMT port-frequency assignments are judiciously selected, the IMPs which are routed to output ports tuned to frequencies not equal to the IMP frequency are those which are produced by combinations of carriers that originate from different input ports.

To summarize, the BMT adds an orthogonal dimension to each of the signals and IMPs. That is, each signal has both a frequency and a port assignment, and each IMP also has both a frequency and a port assignment that are uniquely determined by the signal components which generate the IMP. If the output port to which an IMP is directed is tuned to a frequency different from the IMP's frequency, the IMP is suppressed by the port's bandpass filter.

References

- [A1] J. L. Butler, "Digital Matrix and Intermediate Frequency Scanning," *Scanning Antennas*, edited by R. C. Hansen, Chapter 3, Vol. III, New York: Academic Press, 1966.
- [A2] J. P. Shelton and K. S. Kelleher, "Multiple Beams from Linear Arrays," *IRE Transactions on Antennas and Propagation*, March 1961, pp. 154-161.
- [A3] W. H. Nester, "The Fast-Fourier Transform and the Butler Matrix," *IEEE Transactions on Antennas and Propagation*, May 1968, p. 360.
- [A4] R. J. Westcott, "Investigation of Multiple FM/FDM Carriers Through a Satellite TWT Operating Near Saturation," *Proceedings of the IEE*, Vol. 114, No. 6, June 1967, pp. 726-740.

- [A5] *Transmission Systems for Communications*, Bell Telephone Laboratories, Third Edition, 1964, p. 220.
- [A6] A. L. Berman and E. J. Podraczky, "Experimental Determination of Intermodulation Distortion Produced in a Wideband Communications Repeater," *1967 IEEE International Convention Record*, Vol. 15, Pt. 2, pp. 69-88.
- [A7] C. R. Cahn, "Crosstalk Due to Finite Limiting of Frequency-Multiplexed Signals," *Proceedings of the IRE*, Vol. 48, January 1960, pp. 53-59.
- [A8] P. D. Shaft, "Limiting of Several Signals and Its Effect On Communication System Performance," *IEEE Transactions on Communications Technology*, COM-13, No. 4, December 1965, pp. 504-512.
- [A9] A. L. Berman and C. E. Mahle, "Nonlinear Phase Shift in Traveling Wave Tubes as Applied to Multiple Access Communication Satellites," *IEEE Transactions on Communications Technology*, COM-18, No. 1, February 1970, pp. 37-48.
- [A10] A. R. Kaye, D. A. George, and M. J. Eric, "Analysis and Compensation of Bandpass Nonlinearities for Communications," *IEEE Transactions on Communications*, October 1972, pp. 965-972.
- [A11] J. C. Fuenzalida, O. Shimbo, and W. L. Cook, "Time-Domain Analysis of Intermodulation Effects Caused by Nonlinear Amplifiers," *COMSAT Technical Review*, Vol. 3, No. 1, Spring 1973, pp. 89-143.
- [A12] O. Shimbo, "Effects of Intermodulation, AM-PM Conversion, and Additive Noise in Multicarrier TWT Systems," *Proceedings of the IEEE*, Vol. 59, February 1971, pp. 230-238.
- [A13] W. A. Sandrin, "Spatial Distribution of Intermodulation Products in Active Phase Array Antennas," *IEEE Transactions on Antennas and Propagation*, November 1973, pp. 864-868.



William A. Sandrin received a B.S.E.E. degree from the University of Vermont in 1963 and an M.E.E. degree from Rensselaer Polytechnic Institute in 1966. From 1966 to 1971 he worked for the Boeing Company, Aerospace Group, where he was involved in space communications system design and in the development of phased array antennas. In 1971 he joined COMSAT Laboratories, where he has been engaged in multibeam antenna studies, transponder linearizer development, and systems analysis. He is presently a member of the Communications Network Studies Group of the Transmission Systems Laboratory. He is a member of IEEE, Tau Beta Pi, and Eta Kappa Nu.

An experimental investigation of 8-phase CPSK signal transmission in band-limited satellite channels

D. CHAKRABORTY AND G. A. ROBERTSON

(Manuscript received April 5, 1974)

Abstract

An experimental investigation has been performed to assess the potential applications of 8-phase CPSK signal transmission through a band-limited satellite channel. This paper describes certain measurements through an INTELSAT IV satellite spot-beam transponder simulator. These measurements permit a comparison of linear and nonlinear channel performance of a carrier modulated by a pseudonoise sequence, a study of adjacent channel and cochannel interference, and a study of interburst interference.

Introduction

The ever-increasing demand for satellite communications capacity suggests the possible introduction of more sophisticated modulation and multiple-access techniques. For example, the current FDM/FM/FDMA technique allows an INTELSAT IV spot-beam transponder to yield a maximum communications capacity of about 1,000 telephone channels; ap-

This paper is based upon work performed at COMSAT Laboratories under the sponsorship of the International Telecommunications Satellite Organization (INTELSAT). Views expressed in this paper are not necessarily those of INTELSAT.

proximately the same capacity can be achieved by using PCM 4-phase CPSK/TDMA technique. However, as a result of the power available from a spot-beam transponder (carrier-to-noise ratio, C/N , $\cong 30$ dB when operating through a standard earth station), 4-phase CPSK becomes inefficient, while 16-phase CPSK is only marginal. Therefore, high-speed 8-phase CPSK modems have been procured, and a feasibility study of their possible application to INTELSAT IV spot-beam transponders has been undertaken. One of the objectives of this study is to increase the bit rate while keeping the transponder bandwidth fixed at the nominal 36-MHz value.

The study was directed toward advancing the state of the art of practical, near-term hardware for satellite communications while carefully assessing the performance of the 8-phase CPSK modulation system, especially in the case of the INTELSAT IV transponder operating at or near saturation. The satellite simulation studies included analysis of linear and nonlinear channel performance and adjacent channel interference when the adjacent channel was loaded with FDM/FM carriers of various sizes. A bit rate of 108 Mbps was used.

Satellite simulation study

8-phase CPSK modem description

Figure 1 is a simplified block diagram of the 8-phase CPSK modem [1]. The modulator accepts three channels of parallel PCM data, the clock, and a 70-MHz carrier on-off signal. The PCM data are differentially encoded and converted into multilevel baseband signals to simplify the feed-forward predistortion technique used to reduce intersymbol interference. After passing through low-pass filters and delay equalizers, these signals amplitude modulate quadrature carriers which have been switched by the carrier on-off signal; thus, a 70-MHz 8-phase PSK wave is obtained.

In the demodulator, the input PSK wave is divided into three channels which are fed into the carrier recovery, bit-timing recovery, and demodulator circuits. The PSK signal entering the carrier recovery circuit is frequency multiplied by eight, using three stages of frequency doubling, and the extracted carrier component is sampled by the recovered clock. It is then heterodyned down to 40 MHz by an 8x local oscillator signal, and the 40-MHz signal is fed to a bandpass filter to reduce the noise components. After amplitude limiting, the signal is divided by eight to bring it down to 5 MHz and then heterodyned up to 70 MHz by a 65-MHz local

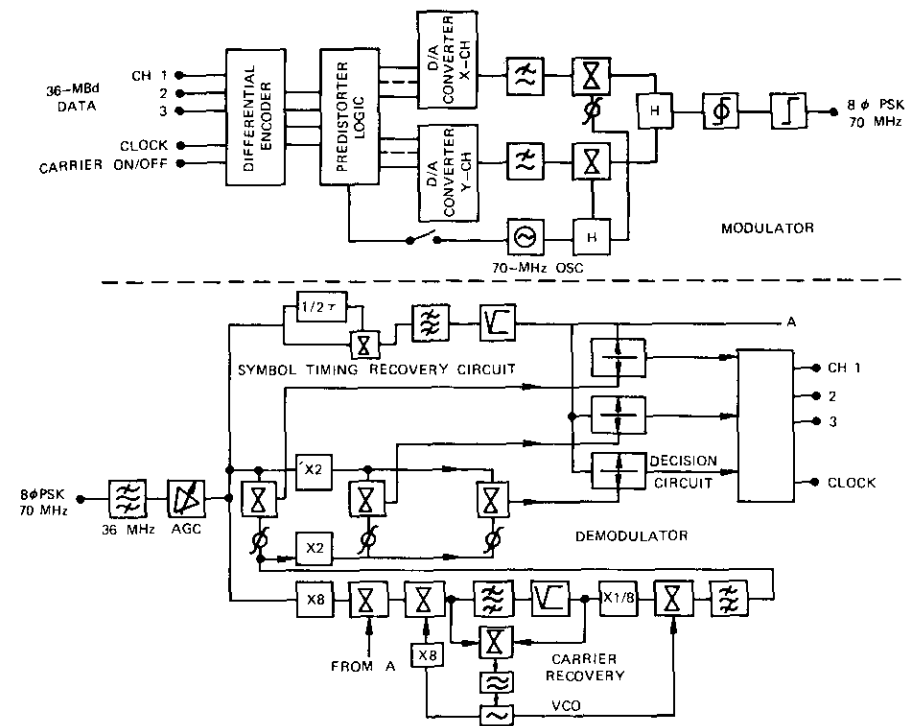


Figure 1. Simplified Block Diagram of High-Speed 8-Phase CPSK Modems

oscillator. The bit timing signal is extracted by half-bit delay detection followed by a bandpass filter.

The multiplication method used in the demodulator reduces the number of phase detectors and samplers and also simplifies demodulator alignment. The three baseband signals from the demodulator are sampled by the recovered clock and differentially decoded to yield three channels of PCM data and the clock.

The modem back-to-back error rate performance and the 8-phase CPSK theoretical performance are shown in Figure 2.

Satellite simulator description

Figure 3 is a simplified block diagram of the INTELSAT IV simulator, including the up- and down-links. The 40-MHz bandpass filter used after the up-converter is well equalized and introduces very little group-delay distortion. The simulator represents a complete satellite channel with

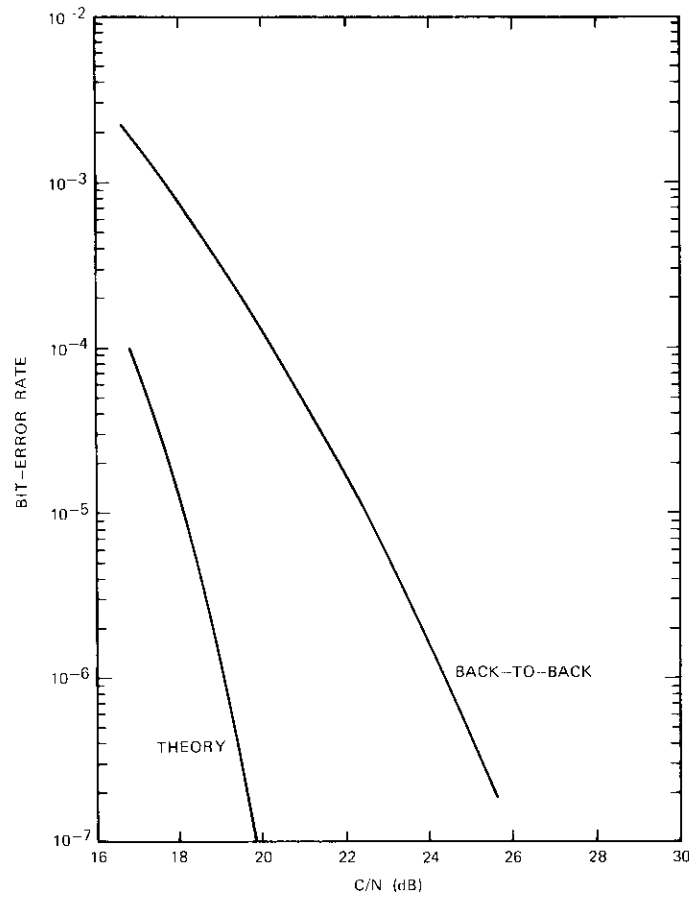


Figure 2. 8-Phase PSK Modem Back-to-Back Performance, BER vs C/N

the exception of the earth station high-power amplifier and the low-noise receiver. Since the high-power amplifier is normally operated in the linear region to avoid out-of-band emission, its contribution to signal distortion is expected to be small.

Linear translator channel performance

To isolate the degradation caused by the satellite, it is necessary to estimate the degradation introduced by the up- and down-links. This may be

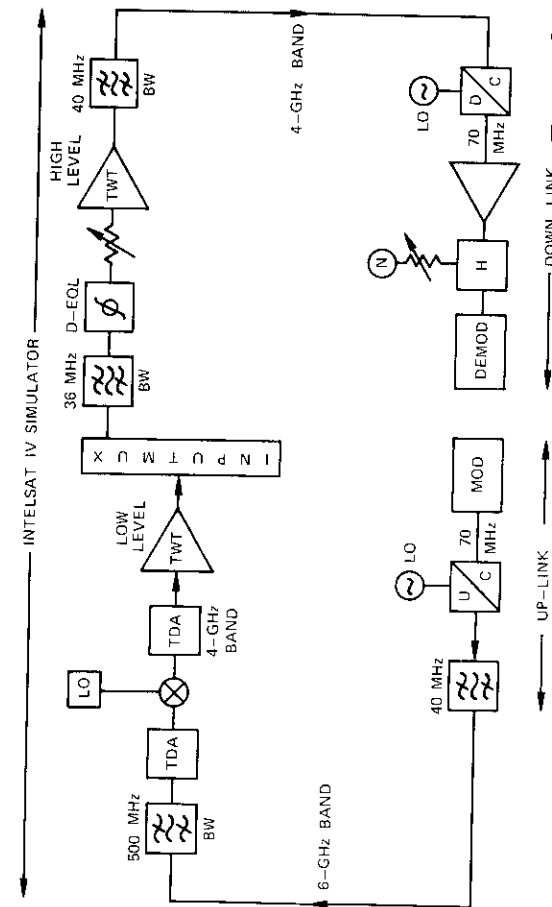


Figure 3. Basic Block Diagram of the INTELSAT IV Simulator Including the Up- and Down-Links

accomplished by replacing the satellite with a linear translator, as shown in Figure 4.

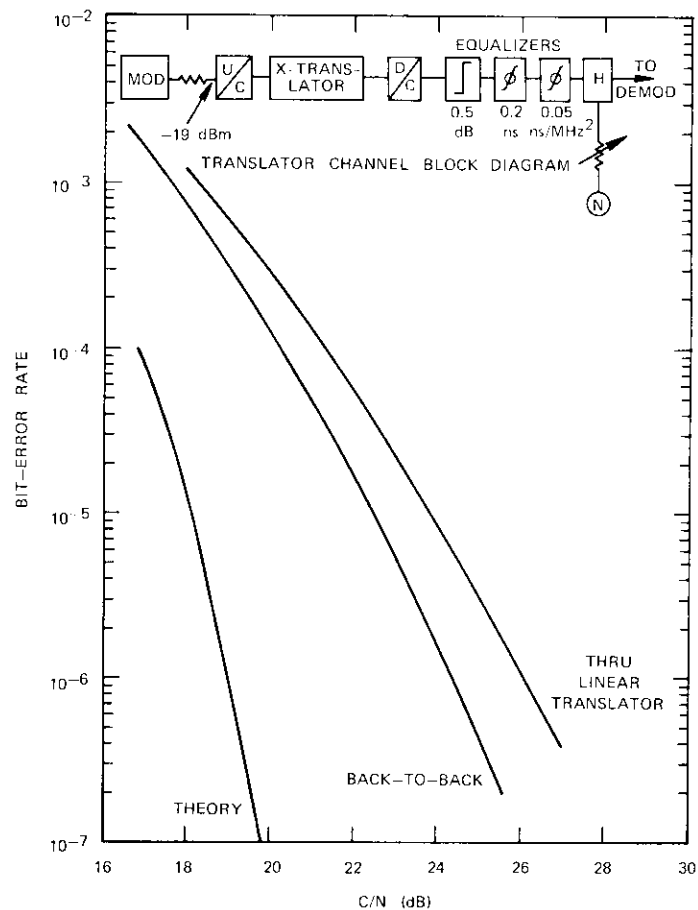


Figure 4. 8-Phase PSK Modem Linear Translator Channel Performance

Critical amplitude and group-delay equalization are necessary to maintain low loss relative to the modem back-to-back performance. The up-converter operating level is extremely important. High-level (-10 - to $+10$ -dBm) up-conversion is normally used in satellite links and, at this level, the AM-PM loss introduced by the up-converter mixer was found to be excessive (~ 4 -dB loss in C/N at 10^{-4} error rate compared to the back-to-

back channel performance). Experimentally, the optimum level of operation at the input of the up-converter was found to be -19 dBm. With this operating level, the bit-error rate versus C/N was measured with noise injected prior to demodulation. The linear translator channel bit-error rate performance curve is shown in Figure 4, which also includes the modem back-to-back performance curve and the theoretical performance curve for comparison.

Satellite channel performance

The equalized amplitude and group-delay response of the complete satellite channel is shown in Figure 5. The satellite channel bit-error rate

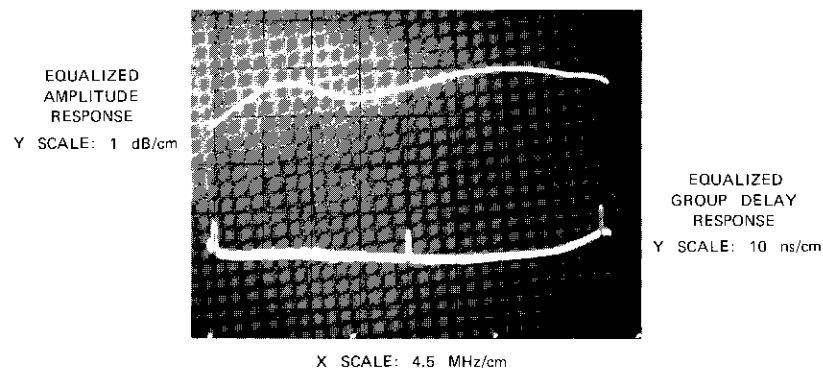


Figure 5. Equalized Amplitude and Group-Delay Response of the Satellite Channel

versus C/N performance has been measured at various operating points from saturation to 14-dB input backoff, beyond which point the TWT operates in an essentially linear manner. The measured input-output power transfer curve of the final TWT is shown in Figure 6. For a fixed input backoff, the bit-error rate versus C/N has been measured with noise injected prior to demodulation as before. The measured bit-error rate versus C/N curves at various input backoff points is shown in Figure 7, which also includes the linear translator channel curve and the modem back-to-back performance curves for comparison.

System application considerations

The space link C/N available from an INTELSAT IV spot-beam transponder operated in conjunction with a standard earth station ($G/T = 40.7$

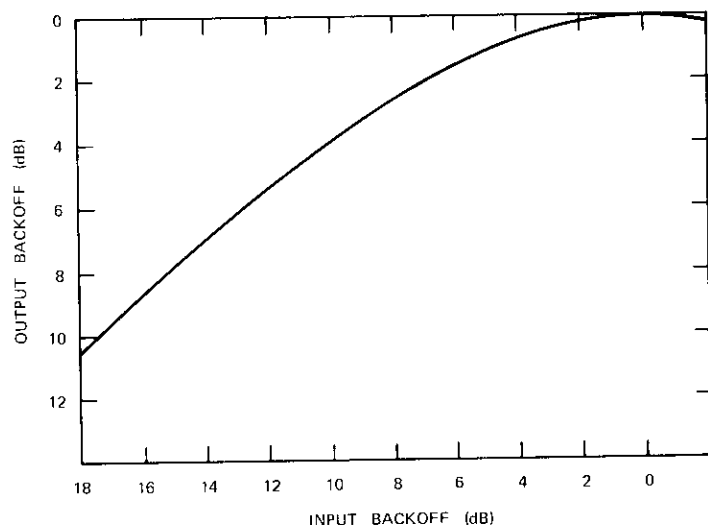


Figure 6. Satellite TWT Power Transfer Curve

dB/K) has been calculated as a function of the transponder input backoff for gain steps 4-8 of the transponder gain step attenuator (prior to the high-level TWT, as shown in Figure 3). Each gain step corresponds to about 3.5-dB attenuation. The calculated results are shown in Figure 8 and the parameters used for the computation are shown in Table 1.

TABLE 1. INTELSAT IV F-3 PRELAUNCH DATA

Single-Carrier Saturated e.i.r.p. at Beam Edge	35 dBW
Down-Link Loss at 10° Elevation	196.7 dB
Receive Antenna Gain-to-Noise Temperature Ratio	40.7 dB/K
Saturated Flux Density at Gain Setting 4	-68 dBW/m ²
Satellite Antenna Gain-to-Noise Temperature Ratio at Beam Edge	-17 dB/K
Gain of a 1-m ² Antenna in the Up-Link (6 GHz)	37 dB

From the C/N versus backoff curves in Figure 8, the error rate versus backoff curves shown in Figure 9 are generated by using Figure 7. Hence, the locus of the optimum operating points (input backoff) of the 8-phase

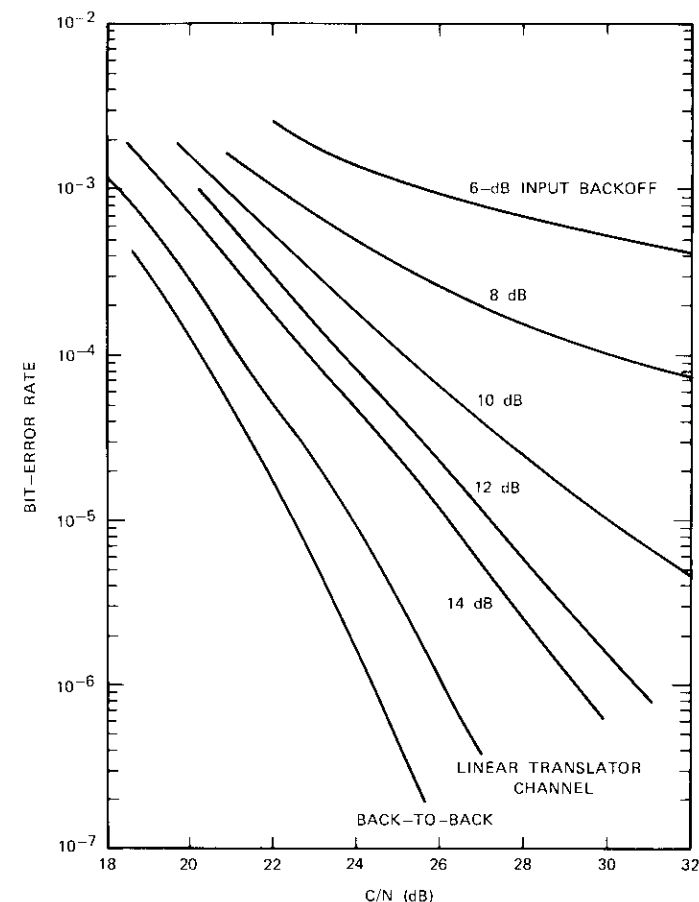


Figure 7. 8-Phase PSK Modem Satellite Channel Performance

PSK transmission through an INTELSAT IV spot-beam transponder is determined.

Interference considerations

When a band-limited PSK spectrum is transmitted through an active device operating at or near saturation, spectrum regeneration occurs and the sidelobe energy reappears. The extent of this sidelobe power depends on the filtering used after the active device and the operating point of the device. The case in point is illustrated in Figure 10. Figure 10a is the spec-

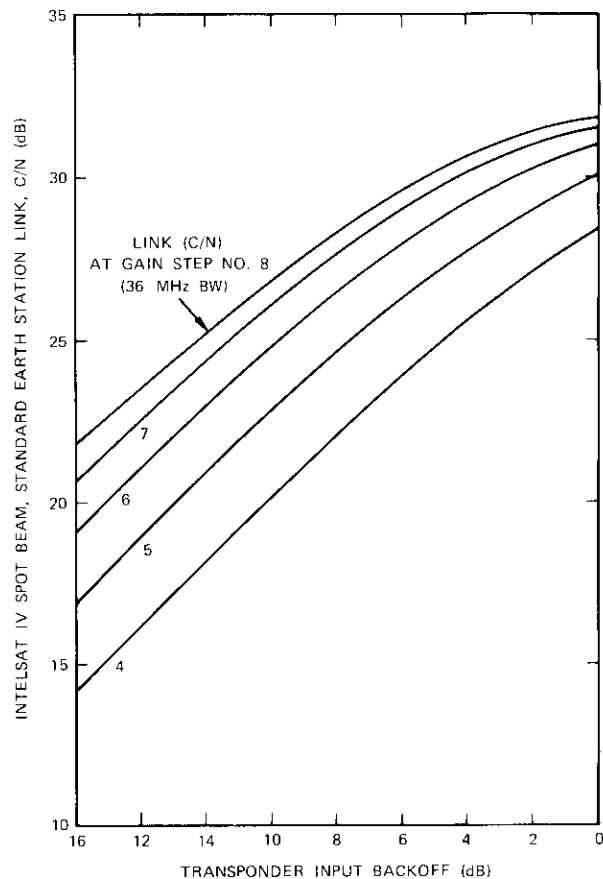


Figure 8. INTELSAT IV *Spot-Beam Link C/N vs Input Backoff*

trum at the output of the modulator and Figures 10b and 10c are the spectra at the output of the transponder TWT output filter at 0- and 6-dB input backoff, respectively. Figures 10d and 10e are the spectra at the output of the transponder TWT (before output filtering) at 0- and 6-dB backoff, respectively. The energy in the sidelobes arising from the spectrum regeneration interferes with carriers transmitted through the adjacent transponder; the interference is comparatively strong if the adjacent transponder contains a small carrier at the band edge. The interference model which has been used in these experiments is shown in Figure 11.

The following cases of interference have been studied:

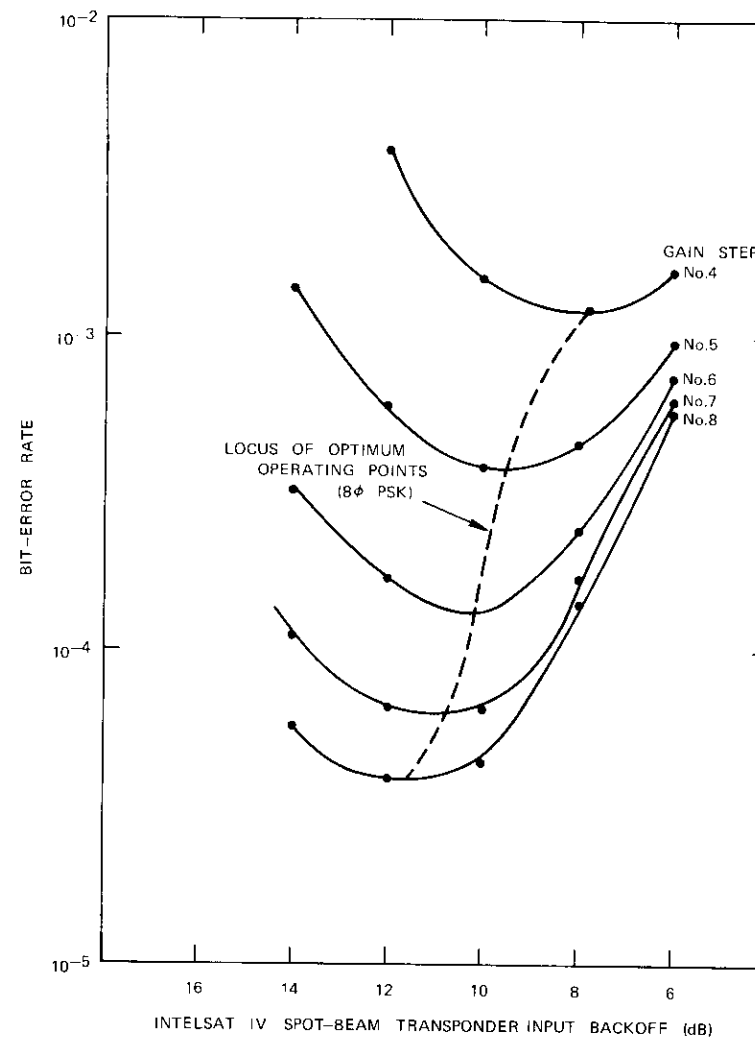


Figure 9. INTELSAT IV *Spot-Beam and 8-Phase PSK Application, BER vs Backoff (gain step as a parameter)*

ADJACENT CHANNEL INTERFERENCE

8-phase PSK carrier operated at different input backoffs interfering with an 1,800-channel FDM/FM carrier in the adjacent transponder (see Figure 12). (Beyond 6-dB input backoff, the degradation is negligible.)

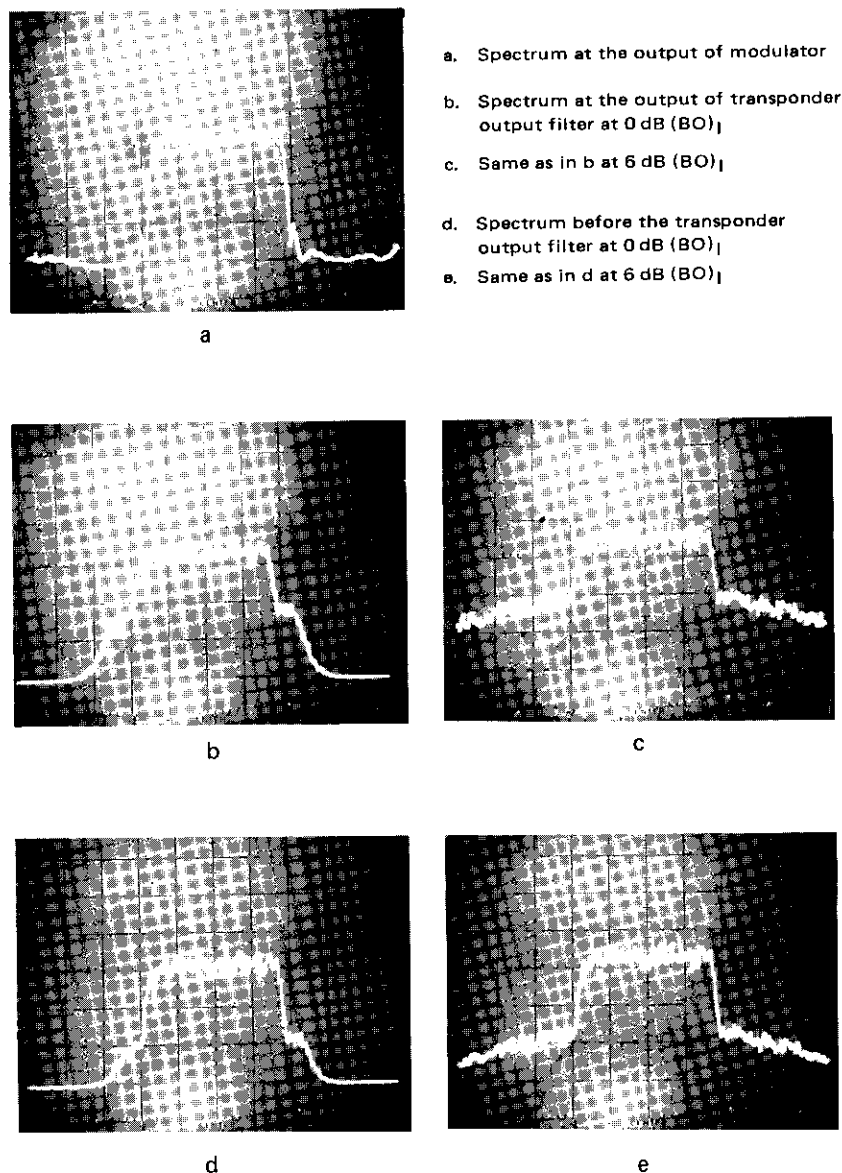


Figure 10. 8-Phase PSK Spectra (scale X: 10 MHz/cm, scale Y: 10 dB/cm)

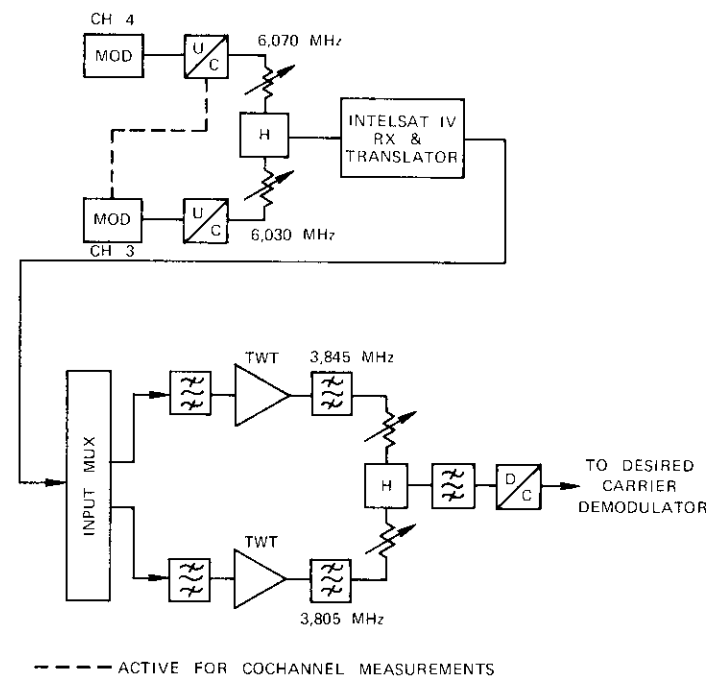


Figure 11. Interference Measurement Model

1,800-channel FDM/FM carrier interfering with an 8-phase PSK carrier operated at 12-dB input backoff, corresponding to a spot-beam transponder C/N of 25 dB, in the adjacent transponder (see Figure 13).

8-phase PSK carrier interfering with a 24-channel FDM/FM carrier located at the band edge of the adjacent transponder (see Figure 14).

8-phase PSK carrier interfering with a 252-channel FDM/FM carrier located at the band edge of the adjacent transponder (see Figure 15).

COCHANNEL INTERFERENCE

8-phase PSK carrier operated at 12-dB input backoff interfering with an 1,800-channel FDM/FM carrier (see Figure 16).

1,800-channel FDM/FM carrier interfering with an 8-phase PSK carrier operated at 12-dB input backoff (see Figures 17 and 18).

In the cochannel interference measurements, the interfering carrier was injected in both the up-link, as shown by the dotted line in Figure 11, and

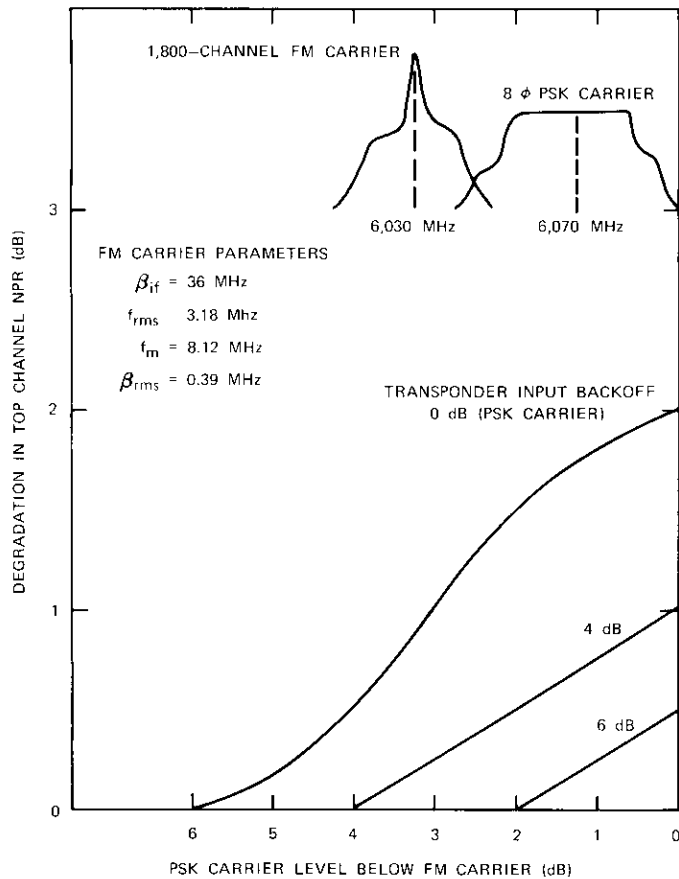


Figure 12. 8-Phase PSK Carrier Interfering with an 1,800-Channel Adjacent FM Carrier

the down-link. The effects of these links have been studied independently, as shown in Figures 16-18.

For a PSK carrier input backoff of 12 dB, the adjacent channel interference on an FDM/FM carrier of any size is insignificant. The worst interference case is that of the 24-channel FDM/FM carrier located at the band edge of the adjacent transponder (see Figure 14). The 24-channel FDM/FM carrier utilizes 6 dBW of satellite e.i.r.p. and the maximum e.i.r.p. of the PSK carrier is about 29 dBW. The relative level difference is

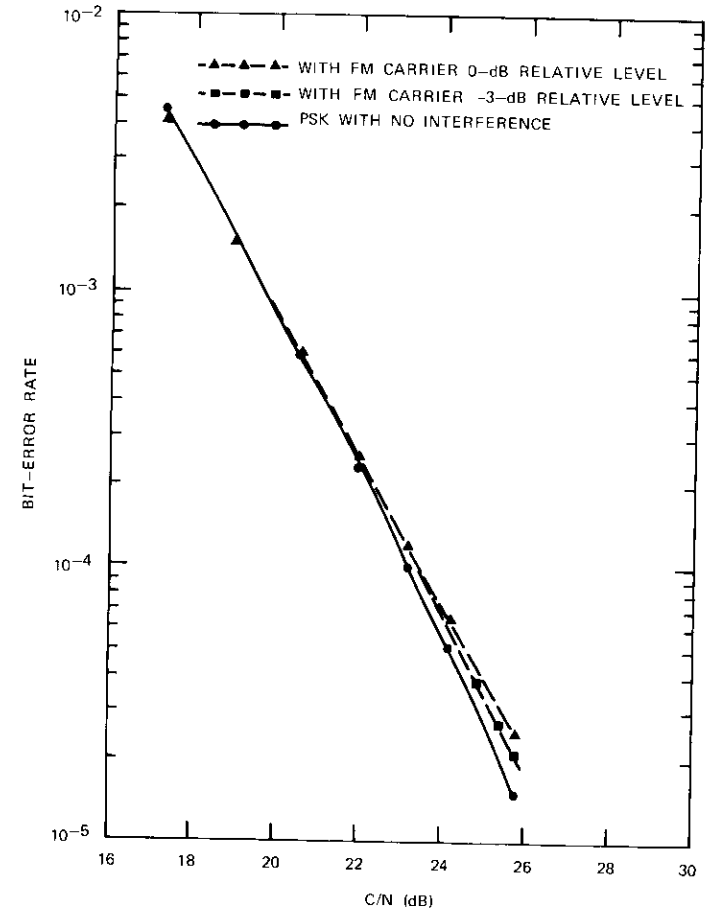


Figure 13. 1,800-Channel FM Carrier Interfering with an Adjacent Transponder 8-Phase PSK Carrier

approximately 23 dB and, at 12-dB input backoff for the PSK carrier, the loss in the top channel NPR of the 24-channel FDM/FM carrier is about 4 dB. To compensate for this loss, the e.i.r.p. of the 24-channel carrier can be increased.

The cochannel interference effects are shown in Figures 16-18. The tolerable carrier-to-interference (C/I) ratio must be maintained in excess of 30 dB for efficient operation in the 10^{-4} to 10^{-5} bit-error rate region.

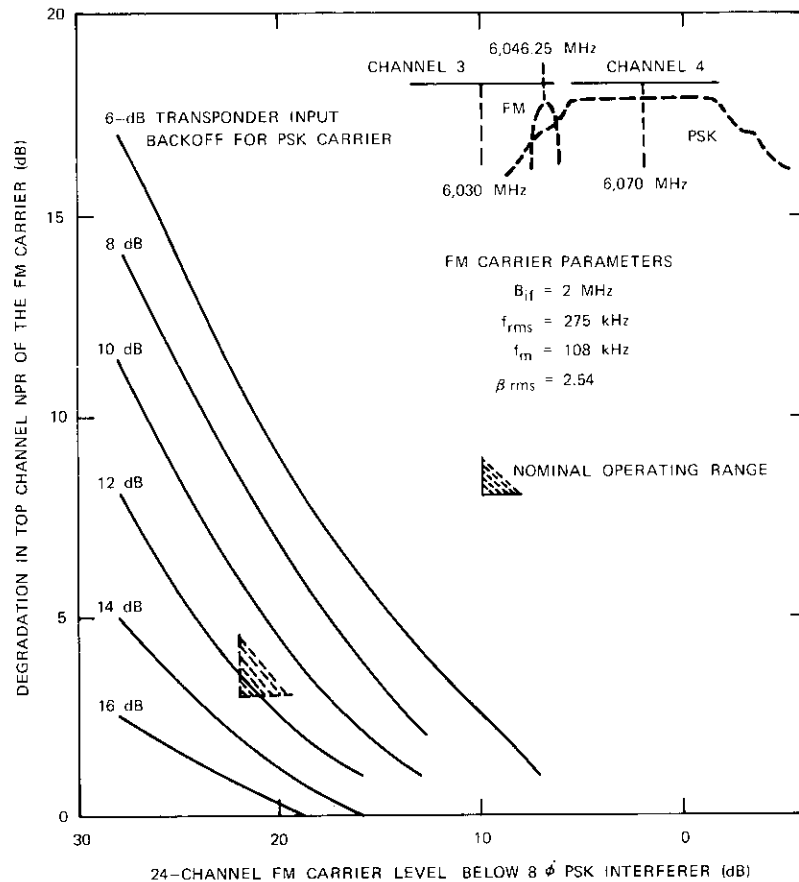


Figure 14. 8-Phase PSK Carrier Interfering with a 24-Channel FM Carrier Located at the Band Edge of the Adjacent Transponder

TDMA application considerations

For efficient TDMA modems, the carrier recovery circuit design is a compromise. To make the system more efficient, the recovery time should be as short as possible, which calls for a wide bandwidth. However, as the loop bandwidth becomes wider, the phase jitter, and hence the C/N degradation, increases. Therefore, the selection of loop bandwidth is a compromise between these two factors.

The energy storing elements used in the relatively narrowband carrier recovery loop filter (200 kHz for the 8-phase modem) give rise to ex-

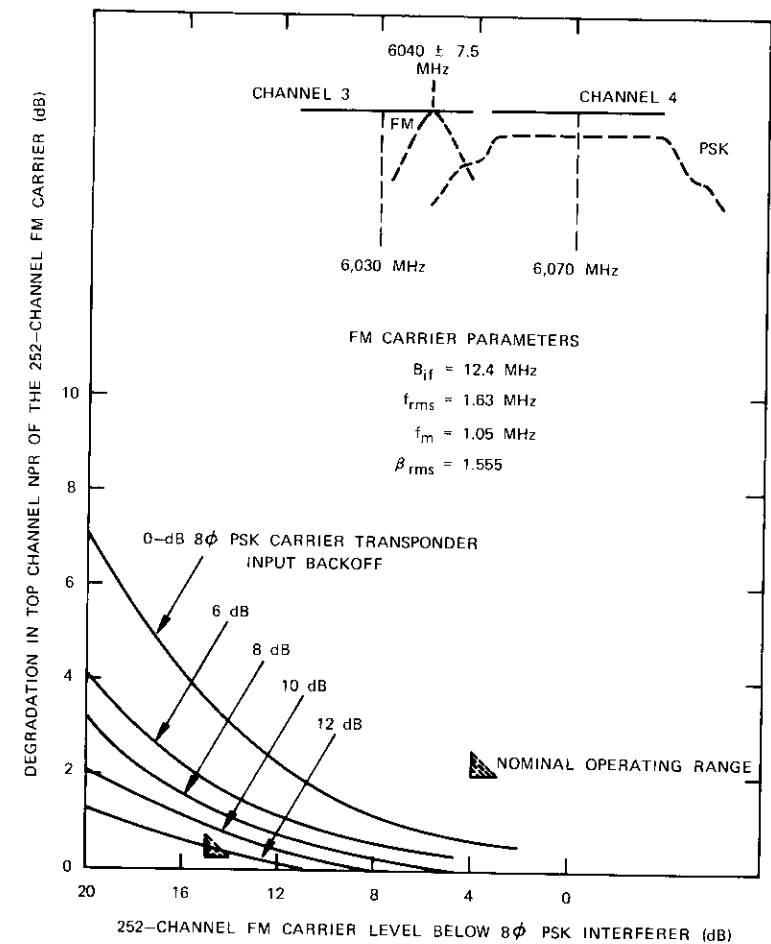


Figure 15. 8-Phase PSK Carrier Interfering with a 252-Channel FM Carrier Located at the Band Edge of the Adjacent Transponder

ponential growth and decay of energy from a received burst. Hence, the tail end of the previous burst is superimposed on the growing end of the existing burst, causing interburst interference, which represents an additional source of degradation in coherent carrier recovery. The interburst interference effect in the 8-phase modem over a simulated satellite link has been examined with a guard time of 100 ns. Figure 19 is a schematic of the 2-burst test setup. The test results are shown in the bit-error rate versus C/N curves of Figures 20 and 21, where the error is measured on specific

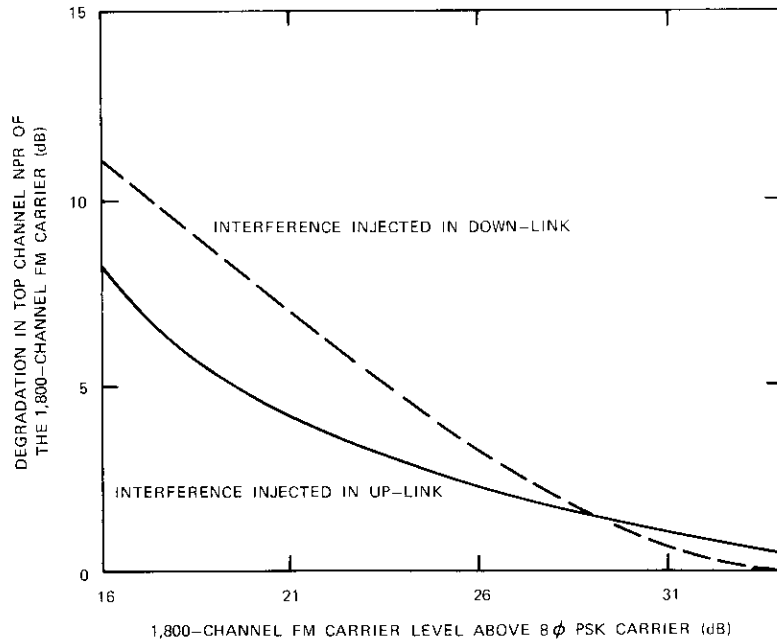


Figure 16. *Cochannel Interference, 8-Phase PSK Carrier Interfering with an 1,800-Channel FM Carrier*

symbols of the burst, namely, the 1st, 4th, 12th, 15th, 64th, and 256th symbols. The solid curves show the performance without interburst interference and the dashed curves show the performance with interburst interference.

Comments on the experimental results

The linear channel and back-to-back performance shown in Figure 4 are within expectations. The modem implementation loss is of the order of 3 dB above the theoretical value at an error rate of 10^{-4} , and an additional loss of 1 dB through the linear translator is considered reasonable. The equalization of the satellite channel, as shown in Figure 5, appears to be the best available using the available equalizing networks.

The nonlinear channel performance shown in Figure 7 is below expectations. The excessive loss of the nonlinear channel can be attributed to the following factors:

a. As the bandwidth-to-symbol-period product tends to unity (36 megasymbols/second in 36 MHz for 8-phase modems), the AM-PM transfer loss becomes asymptotic, even for a nominal value of $K_p = 1^\circ/\text{dB}$.

b. As the operating point reaches saturation, the spectrum spreading becomes severe (see Figure 10), giving rise to spectrum truncation. However, the system application of the 8-phase modem has been examined further, as shown in Figures 8 and 9. Figure 9 shows that the optimum

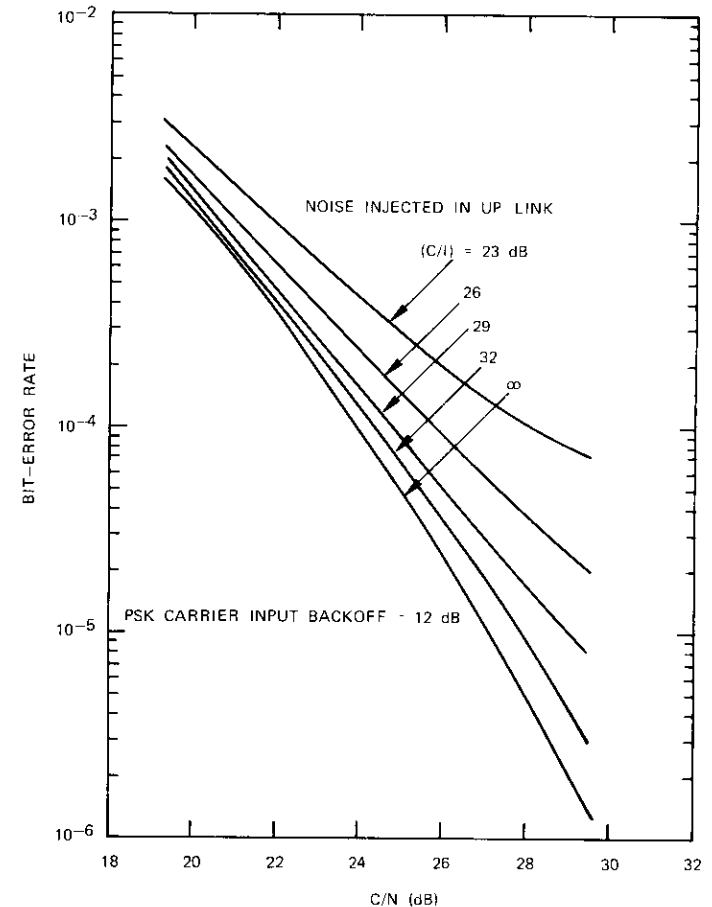


Figure 17. *Cochannel Interference, 1,800-Channel FM Carrier Interfering with an 8-Phase PSK Carrier*

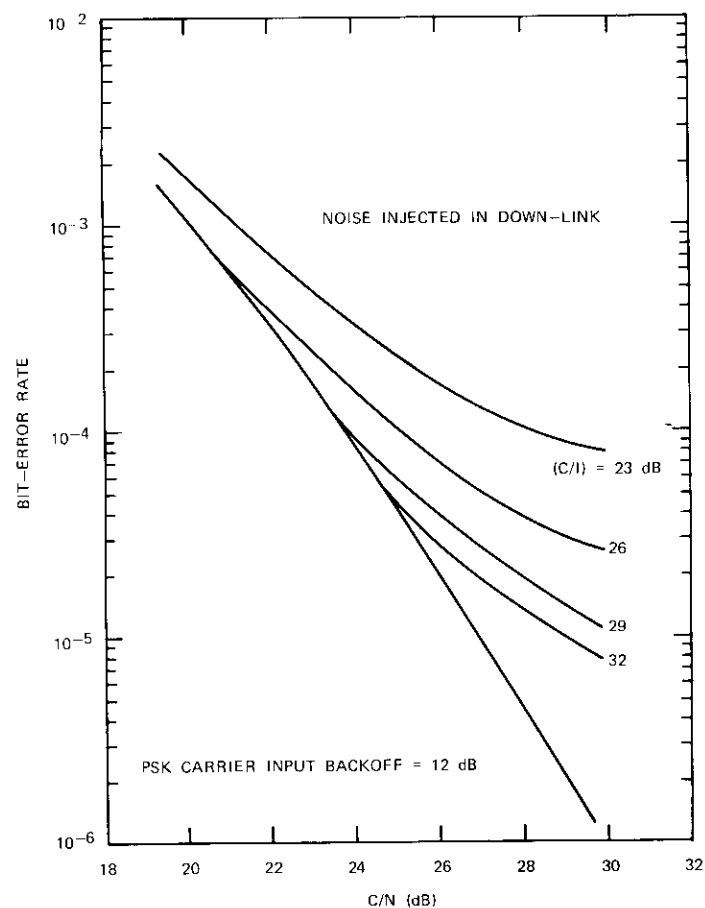


Figure 18. *Cochannel Interference, 1,800-Channel FM Carrier Interfering with an 8-Phase PSK Carrier*

operating point (input backoff) for the 8-phase modem is about 12 dB, yielding an error rate of 4×10^{-5} . At this backoff point, the maximum available link C/N is 25 dB when spot-beam transponder gain setting 8 is used. The earth station e.i.r.p. for this gain setting is of the order of 97 dBW (~ 3 kW for 63-dB antenna gain). For an operating C/N of about 25 dB, the bit-by-bit error rate beyond and including the 15th symbol is below 10^{-4} , as shown in the 2-burst test results (Figure 21).

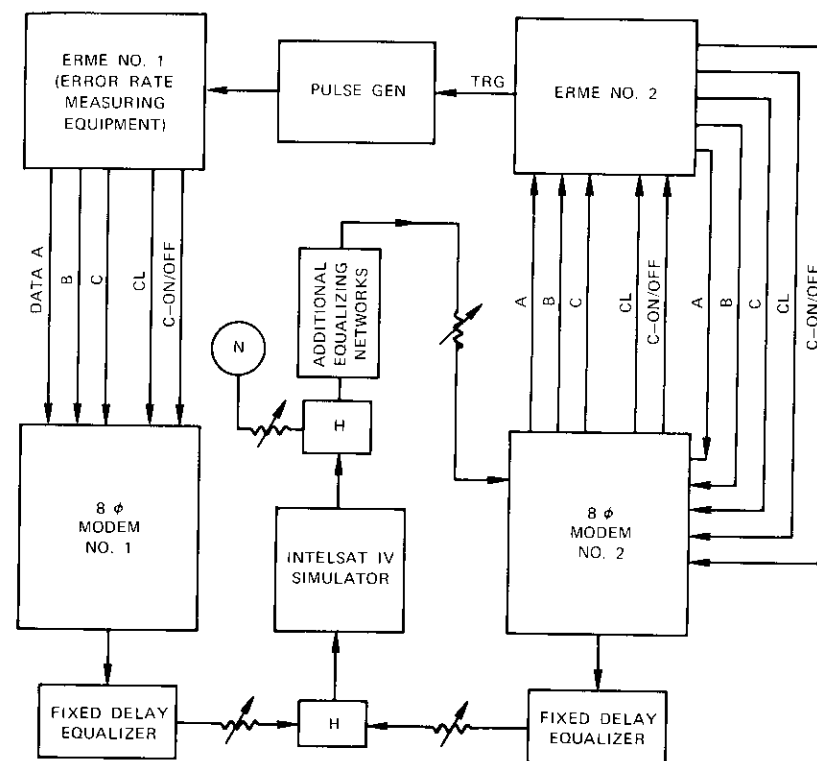


Figure 19. *2-Burst Test Block Schematic*

Conclusions

Transmission characteristics of the 8-phase CPSK modem have been experimentally verified. Severe band restriction by the satellite filters, coupled with the AM-PM transfer effect of the TWT, preclude the utilization of the full power of the transponder. Modifications of the modem to improve its performance are now under consideration.

Reference

- [1] M. Asahara, H. Nakamura, and T. Sugiura, "8-Phase and 16-Phase High Speed PSK Modems for PCM-TDMA Satellite Communications," *Fujitsu Scientific and Technical Journal*, Vol. 8, No. 4, December 1972.

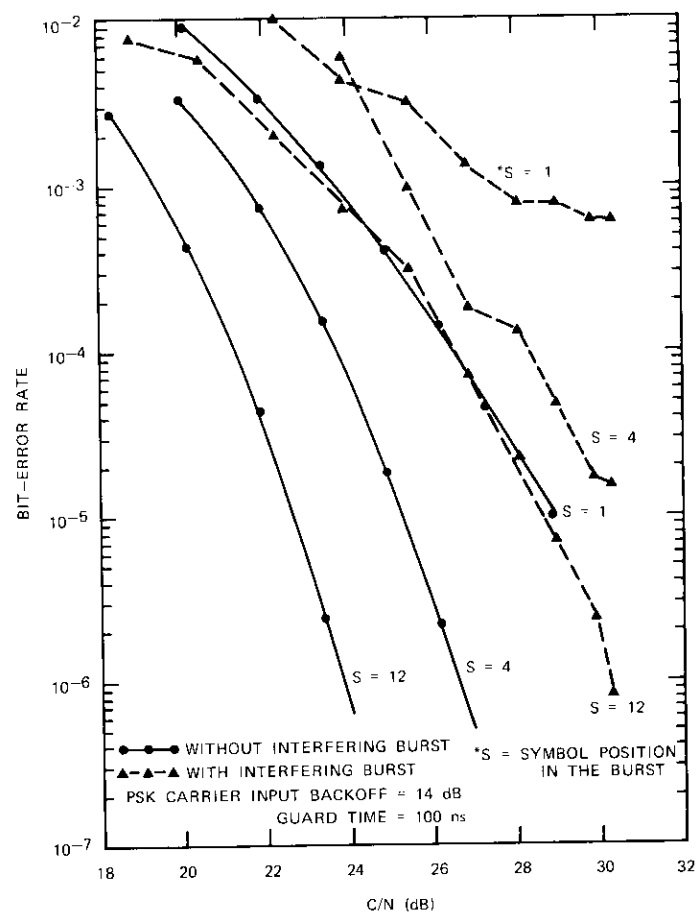


Figure 20. 8-Phase PSK Modem 2-Burst Test Results, BER vs C/N with Symbol Position in the Burst as a Parameter (symbol position, S , = 1, 4, and 12)

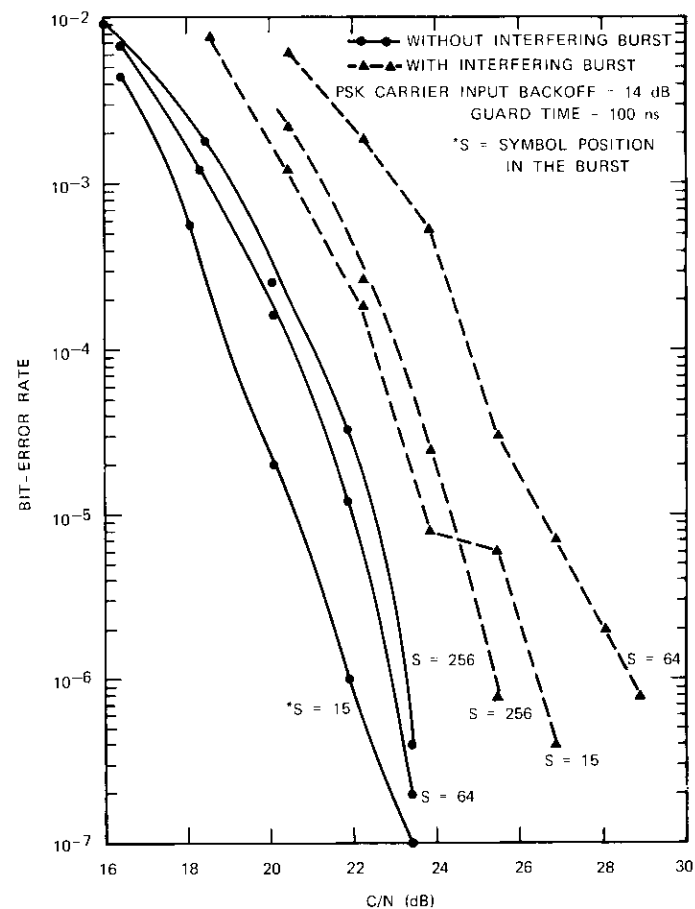


Figure 21. 8-Phase PSK Modem 2-Burst Test Results, BER vs C/N with Symbol Position in the Burst as a Parameter (symbol position, S , = 15, 64, and 256)



Dayamoy Chakraborty was graduated in Natural Science from Calcutta University, served with the Indian Overseas Communications Service, and trained in radio engineering at Marconi College in England, he was employed by Elliott Bros., Ltd. Completing graduate studies in Microwave Physics at Battersea College of Advanced Technology, London (1957-1959), he was employed by Decca Radar Development Laboratory (1959-1961), and by

the British Post Office Research Department (1961-1968) as a Senior Scientific Officer becoming responsible for design and development of low-noise amplifiers for satellite communications.

In 1965 Dr. Chakraborty was awarded a postgraduate studentship at the University of Surrey, where he obtained his Ph.D. in Physics. Since 1968, he has been employed by COMSAT; his assignments include implementation of high-speed digital techniques through INTELSAT systems. He is a member of IEEE and a corporate member of IEE (London).

George A. Robertson was born in Dundee, Scotland, in 1940. In 1946 he emigrated to South Africa, where he matriculated at Dameelin College, Johannesburg, in 1958. Returning to Scotland in 1959, he joined the Royal Air Force in Ground Electronics, serving in England on early warning radar systems and in the Far East on guided missile radar systems. In 1969 he emigrated to the U.S.A. and joined the Systems Laboratory of COMSAT Laboratories. In 1974, he transferred to Operations, where he is currently employed in the M&S Service Center.



Index: voice communications, digital techniques, speech compression, digital speech interpolation systems, multichannel communications systems statistics, adaptive communications.

Results and analysis of the speech predictive encoding communications system field trial

H. G. SUYDERHOUD, J. A. JANKOWSKI, AND R. P. RIDINGS

(Manuscript received April 1, 1974)

Abstract

A field trial of the speech predictive encoding communications (SPEC) system has established confidence in the technical feasibility of this type of digital multichannel compression system. During the field trial two operational SPEC terminals provided 64 toll-quality voice circuits via satellite at the same power and bandwidth normally required to accommodate 24 circuits using conventional FDM/FM. An extensive technical evaluation of the SPEC system was conducted under these conditions. This paper presents results and analysis of the operational performance of the SPEC system during the field trial and describes the testing procedures employed.

Introduction

The speech predictive encoding communications (SPEC) system is a digital multichannel speech compression system incorporating an adaptive zero-order predictor. The system processes the digitally encoded samples from each of 64 input speech channels, and, using the predictor, decides which samples require transmission. Reference 1 provides a detailed description of the SPEC system, including the theoretical aspects. The

present paper is concerned primarily with the analysis of the results obtained from an extensive field trial of two complete terminals operating on a link between two COMSAT earth stations.

The performance of the SPEC system is analyzed in terms of the following two conditions:

- a. the variation in the number of input channels containing active speech,
- b. the variation of the bit-error rate introduced in the space-segment transmission path.

As the number of channels containing active speech increases beyond the available SPEC system transmission capacity (overload), a linear increase in total noise power, evenly distributed over all channels, occurs. This type of noise power is significantly minimized by the adaptation algorithm of the adaptive zero-order predictor described in Appendix A. This algorithm causes a gradual increase in quantization noise which is hardly distinguishable from ordinary PCM quantizing noise.

Bit errors introduced in the digital bit stream of speech compression systems may affect the synchronization information, which is critical to system performance. Errors occurring in the synchronization information are detected in the SPEC system receiver to prevent received TDM stacked PCM samples from being directed to improper channels. Appendix B describes the processing of synchronization information. Errors occurring in the PCM samples affect the voice channels as expected in PCM transmission.

The field trial was conducted to evaluate the performance of the SPEC system under the two conditions described previously. Two SPEC terminals with a capacity of 64 two-way channels were put into operation over a satellite link between earth stations located at Brewster, Washington, and Paumalu, Hawaii. COMSAT Laboratories' personnel conducted the field trial for three weeks beginning on August 10, 1973, and the earth station personnel kept the system in operation for additional data collection until November 6, 1973.

Data were collected and recorded, through the use of a minicomputer, to provide statistical information essential for analyzing SPEC system performance. Specifically, results were analyzed in terms of the signal-to-distortion ratio and in terms of a subjective evaluation by both experienced and "naive" talkers. Distortion was interpreted in a broad sense to include the contributions of quantization granularity and bit errors in both synchronization and PCM sample information.

System operation

The SPEC system is designed to accommodate the traffic of N PCM telephone trunks in a TDM capacity of $N/2$ PCM channels. Specifically, it operates at the transmitter by removing redundant samples of active speech and utilizing the silent intervals between speech segments. Every PCM sample from each incoming channel is examined for redundancy since only nonredundant samples are to be transmitted. The algorithm used is based on a simple difference criterion between the present sample and its most recent predecessor. Redundancy of a new sample means that its immediate predecessor contains all the necessary information. Since the receiver stores the most recently received sample of each channel, redundancy at the transmitter simply means that the receiver repeats the stored sample until it is replaced by a new nonredundant sample.

The SPEC system processes 64 channels, as described above, every 125 μ s. As speech and call activity* increase beyond the processing capacity, the degradation is manifested as an increase in quantization noise without any of the annoying effects of speech segment clipping. Since this type of degradation is virtually imperceptible to the user, it is called "graceful" degradation.

Figure 1 is a simplified block diagram of the SPEC encoder. The input consists of the digitally encoded samples from each of the N analog input channels. These samples are multiplexed into a TDM bit stream and fed to a time-shared digital voice switch which continuously scans all input samples and distinguishes between active speech and silence to prevent the transmission of noise during silence intervals.

The zero-order predictor examines each sample from the input channels and sends only unpredictable samples along with a channel sample assignment word (SAW) to the output multiplexer. The aperture[†] of the zero-order predictor is adaptively adjusted depending on the instantaneous ensemble speech activity of the input trunks.

An error control unit protects the SAW by generating a simple parity check. The assignment recirculation unit rotates the priority of service to the input channels, thereby equalizing the quality of all channels. Frame and assignment-sequence synchronization codes are also multiplexed into the output TDM frame.

* Call activity is the number of SPEC channels that are in use.

† The aperture is the threshold which, when exceeded by the difference between the present sample and its immediate predecessor, renders the present sample unpredictable.

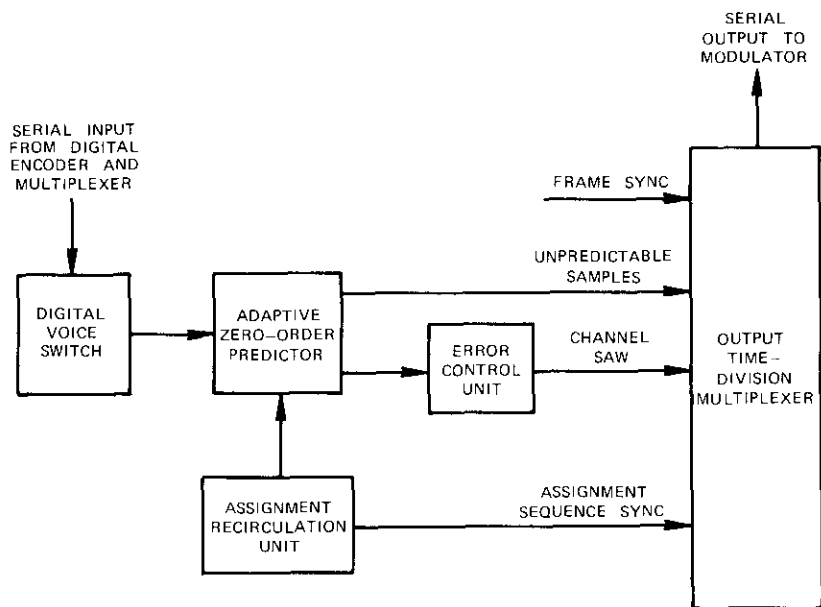


Figure 1. SPEC Encoder

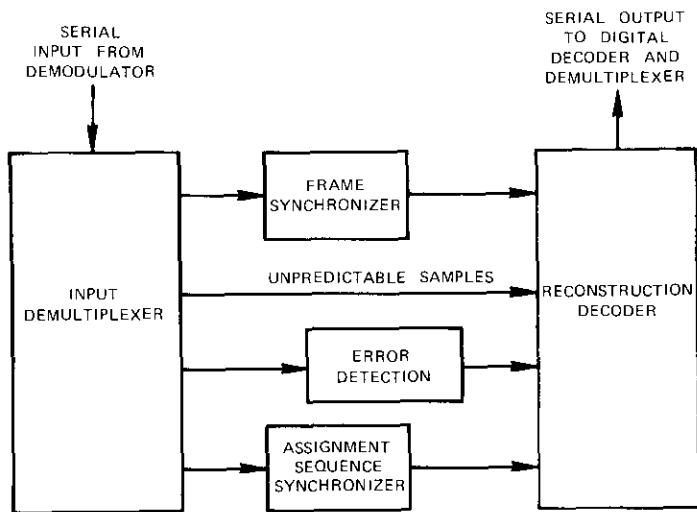


Figure 2. SPEC Decoder

The SPEC decoder, shown in Figure 2, demultiplexes the received TDM frame and performs frame and sequence synchronization. Following a parity check, the SAW is used to direct unpredictable PCM samples to the correct output channels. Predictable samples are regenerated by the reconstruction decoder.

Field trial system configuration

The general arrangement of the equipment used in the field trial is shown in Figure 3. The 64 input channels of the SPEC system were loaded in the following manner:

- a. the alternate output of a hybrid coil following the supergroup demodulator, normally used for patching or measurement, provided 60 channels of live traffic, demultiplexed into individual voice signal sources for loading the SPEC system*;
- b. one channel was provided for a 1,100-Hz, 0-dBm0 sine wave test tone to measure the signal-to-distortion ratio;
- c. two channels were provided for test personnel as order wires;
- d. one channel served as a demonstration channel.

Each of the analog signal sources was interfaced with the SPEC channel unit at a nominal +7-dB transmission level point and low-pass filtered at 3,500 Hz. Each channel was sampled at 8 kHz and subsequently A-law companded using 8-bit encoding (C.C.I.T.T.) to result in a noise floor of -70 dBm0 referenced to a clipping level of +2 dBm0. The PCM samples were multiplexed into a 4.096-Mbps TDM/PCM serial bit stream which constitutes the basic input to the SPEC system. The SPEC encoder processed the samples as described in the previous section to result in a 2.048-Mbps TDM/PCM/SPEC bit stream at the output of the encoder. This signal was transmitted utilizing 2-phase differentially encoded PSK at a 70-MHz modulating frequency and a 2.56-MHz noise bandwidth. The carrier-to-noise ratio was varied to achieve bit-error rates ranging from 10^{-4} to 10^{-8} [2]. The remaining equipment used in the communications link was supplied by the earth stations.

To record system performance, an HP 3960 4-channel tape recorder was employed at each of the earth stations. Some demonstration conversations were recorded on the two "direct recording" channels, while the output of the distortion analyzer was recorded on one of the FM mode

* Service for these channels was carried in parallel by the FDM/FM normally provided between earth stations.

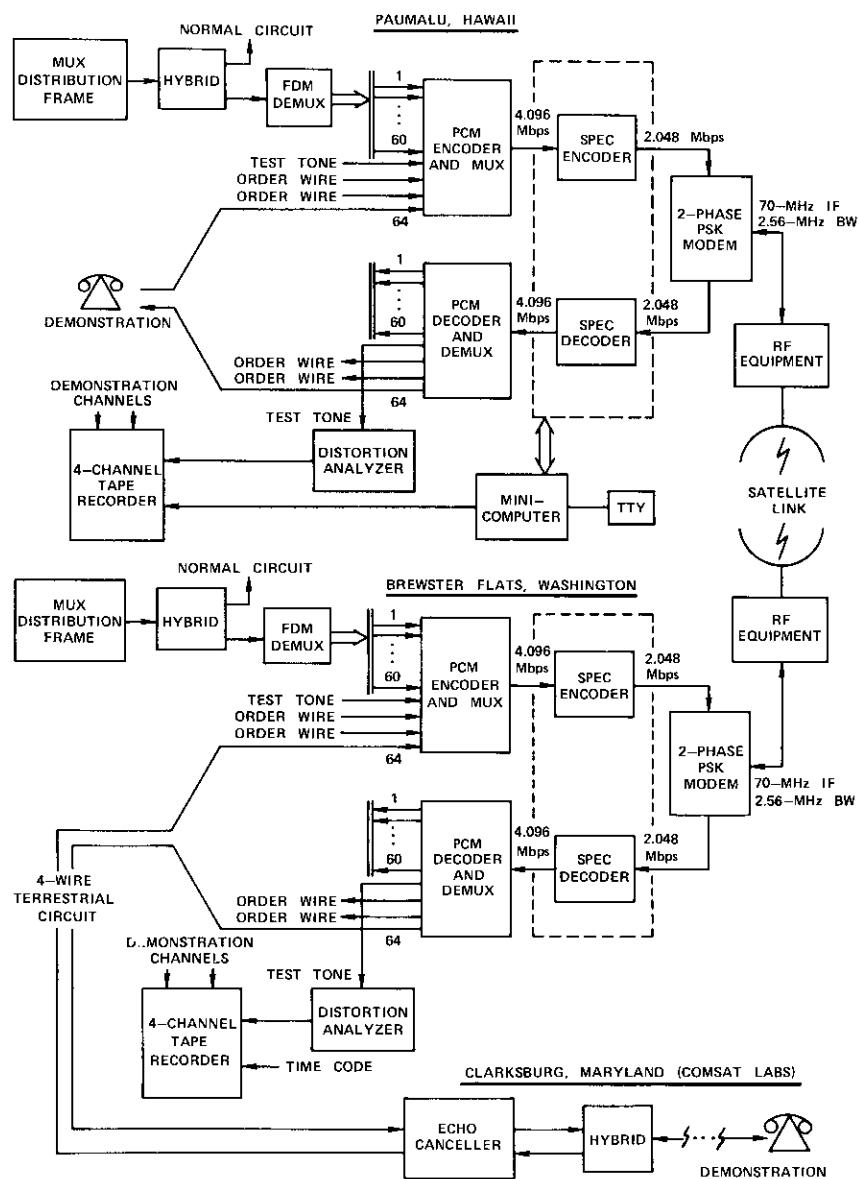


Figure 3. Field Trial Configuration

channels. At Brewster, a time code was recorded on the remaining FM mode channel.

The Paumalu terminal employed a minicomputer to compute real-time performance data. Every $125 \mu\text{s}$ the data were fed to the computer, where they were averaged over 10-s intervals, i.e., over 80,000 samples. These averages were then recorded on the fourth channel of the tape recorder and fed to a teletype machine enabling the test personnel to monitor the system operation. The following information was recorded:

- ensemble speech activity*, expressed as the percentage of the 64 input channels containing active speech as determined by the voice switch;
- system activity*, expressed in terms of the number of channels requiring transmission after prediction (see Appendix A);
- system overload*, expressed as the percentage of SPEC frames for which the system activity exceeds the SPEC processing capacity;
- predictor aperture*, expressed in terms of the allowed threshold between two successive PCM samples, which defines the range of prediction;
- time*, expressed in hours, minutes, and seconds.

Quantitative system performance

The quantitative performance of the SPEC system will be analyzed from various recorded signal-to-distortion ratio (S/D) data under different conditions of ensemble speech activity and bit-error rate.* Figure 4a shows a recording of S/D during two hours of peak telephone traffic. The variations in ensemble speech activity over this period are shown in Figure 4b. These data were recorded at a bit-error rate of 10^{-8} , which compares with error-free transmission.

The maximum S/D of 41 dB (Figure 4a) is due to the practical limitation of the PCM encoder/decoder. In Figures 4a and 4b, note that the S/D decreases from this maximum value only when the ensemble speech activity exceeds 38 percent. The minimum S/D is 30 dB, which corresponds approximately to 50- to 55-percent ensemble speech activity. As will be shown in the section on performance analysis, such high ensemble speech activity occurs only five percent of the time or less.

* Different bit-error rates were introduced in the transmission path by varying the signal power output of the modulator.

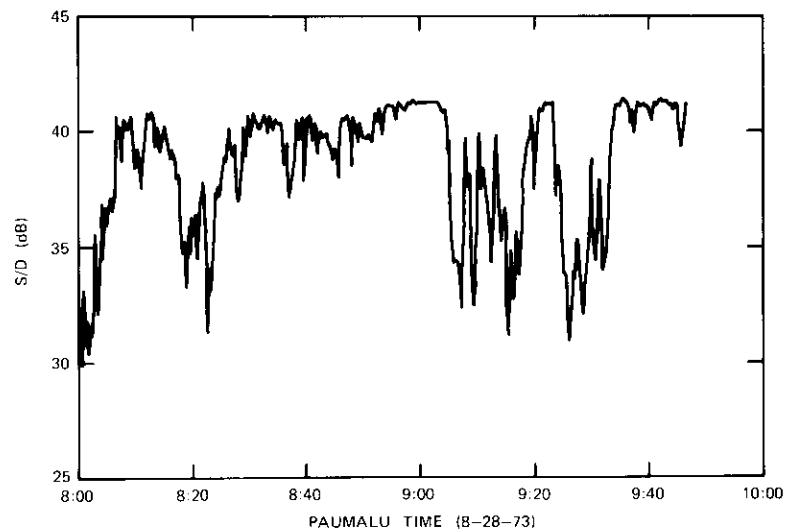
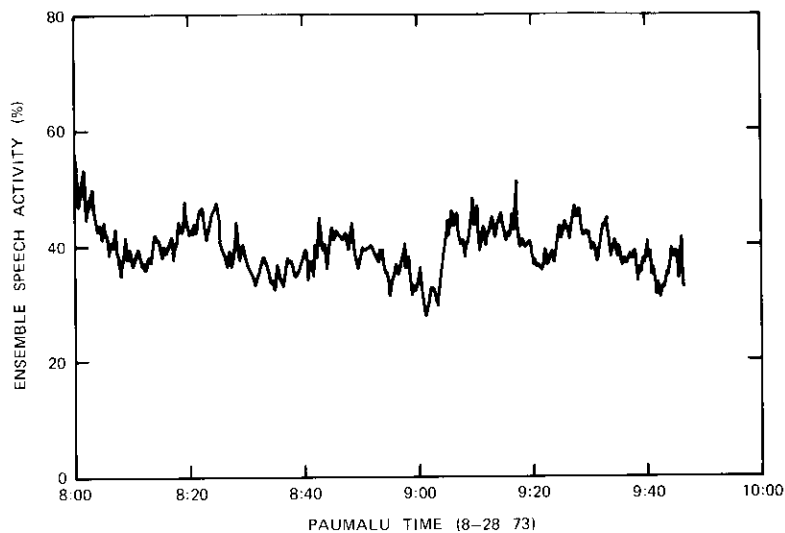
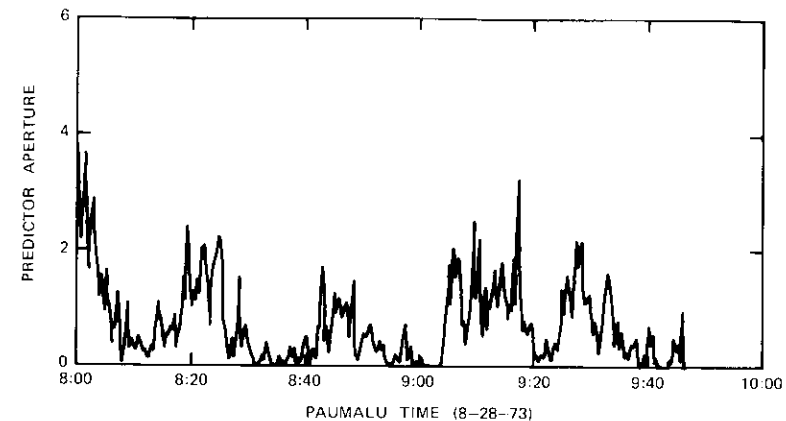
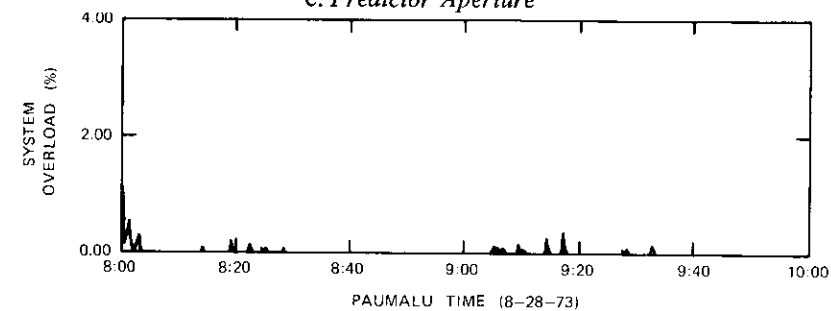
a. *S/D*b. *Ensemble Speech Activity*

Figure 4. SPEC Performance Parameters Measured During 2 Hours of Peak Telephone Traffic Averaged over 10-Second Intervals

c. *Predictor Aperture*d. *System Overload*

The average S/D as a function of ensemble speech activity is shown in Figure 5. After reaching approximately 38-percent ensemble speech activity, the total noise power starts to increase, resulting in a gradual decrease in the S/D. At this point the average number of input channels with unpredictable speech samples is exceeding the capacity of the SPEC predictor to operate at zero aperture. This forces the aperture to increase, causing an increase in quantizing noise.

The relationship between S/D and call activity for different values of average speech activity* is shown in Figure 6. Note that call activity has no effect on the system performance until the average speech activity exceeds 38 percent.

Figure 4c shows the aperture of the predictor during this 2-hour period.

* Defined as the ratio of the number of channels containing active speech to the total number of channels in use, expressed in percent.

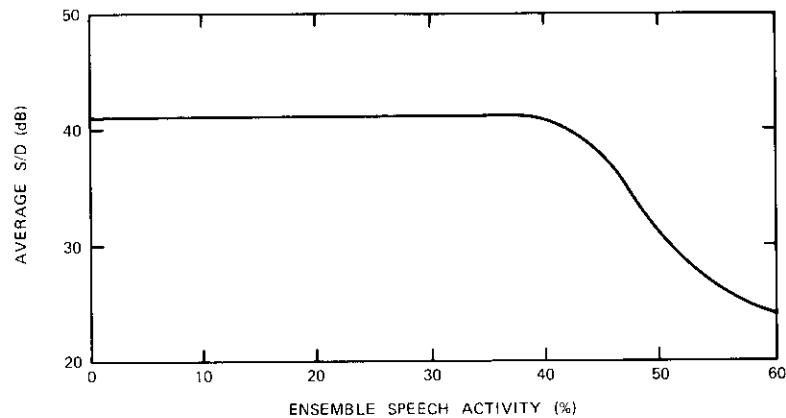


Figure 5. Average S/D vs Ensemble Speech Activity

As expected, there is virtually perfect correlation between these data and the S/D data shown in Figure 4a. The gradual increase in distortion power is due to the adaptation algorithm of the predictor, which prevents the manifestation of the higher distortion power which would result from system overload.

The occurrence of system overload is shown in Figure 4d. Note that overload rarely occurred during this 2-hour period, which included brief portions of 50- to 55-percent ensemble speech activity (Figure 4b at 8:00 AM). Even at such high values of speech activity, overload reached a worst value of only one percent.

On a per-channel basis this worst overload is negligible because the recirculation scheme of the SPEC system evenly distributes the penalty of freeze-out over all active channels (likely to be at least 50), and because

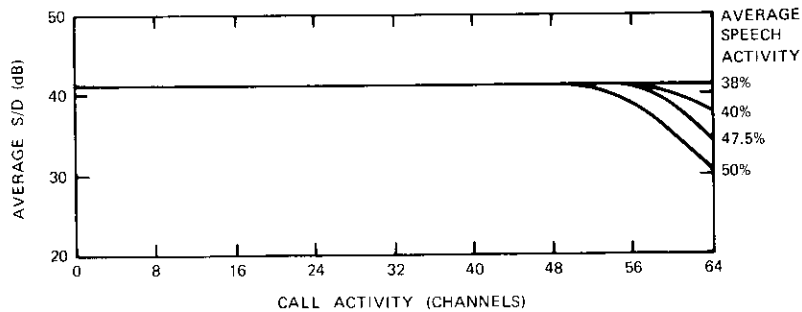


Figure 6. Average S/D vs Call Activity

freeze-out does not imply the loss of a sample, but, due to the prediction algorithm, merely amounts to a slight increase in quantization noise.

To study the effect of transmission channel bit-error rate, the output level of the SPEC modulator was attenuated until the carrier-to-noise ratio was reduced to cause a bit-error rate of 10^{-4} . Figure 7a indicates the S/D of the SPEC system for a 4-hour period at this bit-error rate. Figure 7b shows the predictor aperture for this same period.

Note that there was a general decrease of about 2 dB in S/D during the first 2-hour period when the system aperture remained virtually at zero. This indicates that the decrease in S/D during that period is due to the increase in bit-error rate. During the remaining two hours of operation the S/D followed the predictor aperture as expected. Therefore, it can be concluded that the observed S/D performance is due to both the higher bit-error rate and system loading (speech activity).

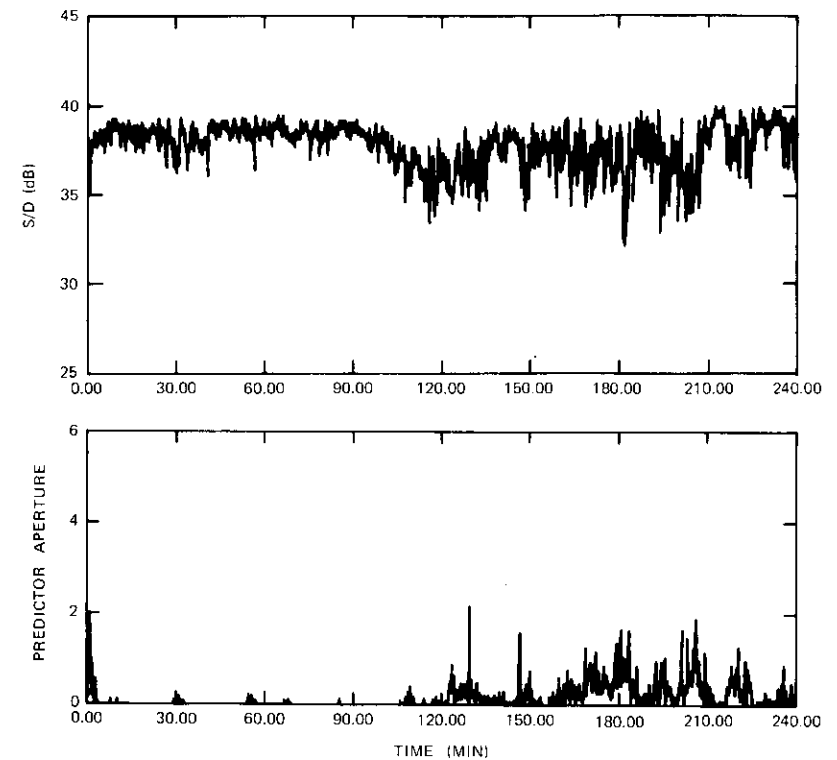


Figure 7. S/D and Predictor Aperture for 4 Hours at a Bit-Error Rate of 10^{-4}

Qualitative system performance

One channel of the SPEC system was used for demonstration. For that purpose a 4-wire voice grade circuit was leased between COMSAT Laboratories in Clarksburg, Maryland, and the earth station in Brewster, Washington. This circuit was patched directly into the SPEC system at Brewster, thus enabling telephone communications between Paumalu and the Laboratories. At the Laboratories, the circuit terminated in an artificial line to simulate a local loop and a standard telephone hand set (500 type). The circuit composition is shown in Figure 3. For echo protection, an experimental echo canceller developed by COMSAT Laboratories [3] was installed at the Clarksburg end. In Paumalu a 4-wire telephone instrument was used.

During the field trial, over 100 demonstration calls were made to interested persons. The calls were made during periods of peak telephone traffic, as indicated in Figure 4. The bit-error rate was maintained at 10^{-8} for all calls. The results obtained from these calls indicated that the SPEC system introduced no perceptible degradation. The participating callers rated the quality of the demonstration circuit equal to or better than that of a good long-distance telephone circuit.

The system was also subjectively assessed at a bit-error rate of 10^{-4} by both the field trial personnel and the earth station personnel during the four hours shown in the S/D plot of Figure 7a. A parity error indicator for the SAW and a frame synchronization indicator were both monitored on an oscilloscope.

The results of these objective indications agreed with the subjective performance of the voice channels in that there was no evidence of loss of frame synchronization. Neither speech clipping nor crosstalk between channels was experienced. The only perceptible degradation was the instantaneous increase in noise power which occurred when a bit error was detected in the SAW (see Appendix B) or when a bit error occurred in the PCM sample corresponding to the channel under test. Both the field trial personnel and the earth station personnel agreed that a bit-error rate of 10^{-4} was no deterrent to the quality of communications.

Analysis of SPEC system performance

The SPEC system is a combined PCM transmission and digital speech interpolation (bit rate compression) system. Hence, it is unique and, to the authors' knowledge, no performance requirements have been formally documented.

Reference 1 has pointed out that the effect of freeze-out during overload is entirely different from that produced in TASI-like systems although SPEC also utilizes the intersyllabic pauses of speech. Speech clipping, which does not occur in the SPEC system, is "replaced" by an increase in quantizing noise.

Reference 1 also provides calculated system performance curves for various conditions of loading (speech activity) and other parameters such as E_b/N_o and bit-error probability. The intention of this paper is to relate the actually measured performance statistics discussed previously to known criteria developed for similar systems.

The C.C.I.T.T. has established requirements for conventional PCM systems in Recommendation G.712 [4]. Under Section 9, the requirement for total distortion, which includes quantizing distortion, is a sine-wave-to-distortion ratio of 33 dB for a sine wave in the range of -30 to 0 dBm0. Below -30 dBm0, this requirement relaxes linearly.

Under heavy load conditions, the SPEC system produces a rapidly varying S/D, as may be seen in Figure 8. Fluctuations between a value as poor as 23 dB and one as good as 39 dB may often occur.

To link such data with the known and better understood performance of conventional PCM systems, a limited subjective evaluation was conducted to compare SPEC and conventional PCM. The subjective test was executed as follows. A 2-track tape loop with identical speech segments was played back simultaneously through the SPEC system and through a conventional PCM (8-bit, A-law companded) system. The SPEC system under five different loading conditions from moderate to heavy loading (in terms of ensemble speech activity) was compared with the conventional PCM channel in which the S/D could be varied over a known set of levels. For each condition, listeners were asked to equate the quality of the two systems by varying the S/D of the PCM channel. Twelve listeners participated, each performing the test under the five different conditions.

For each of the SPEC system conditions tested, the long-term average S/D was also calculated from recorded data similar to those collected during the field trial. Calculated and subjectively equivalent averages are compared in Figure 9, which shows that the calculated S/D values contain a margin of 1-2 dB compared to subjectively equivalent values for conventional PCM systems.

To interpret Figure 9 correctly, it should be noted that an average measured S/D as low as 33 dB for SPEC corresponds to an ensemble speech activity of 48 percent. Figure 10 shows that this occurs only 5 percent of the time. Thus, it may be concluded that the SPEC system meets the C.C.I.T.T.

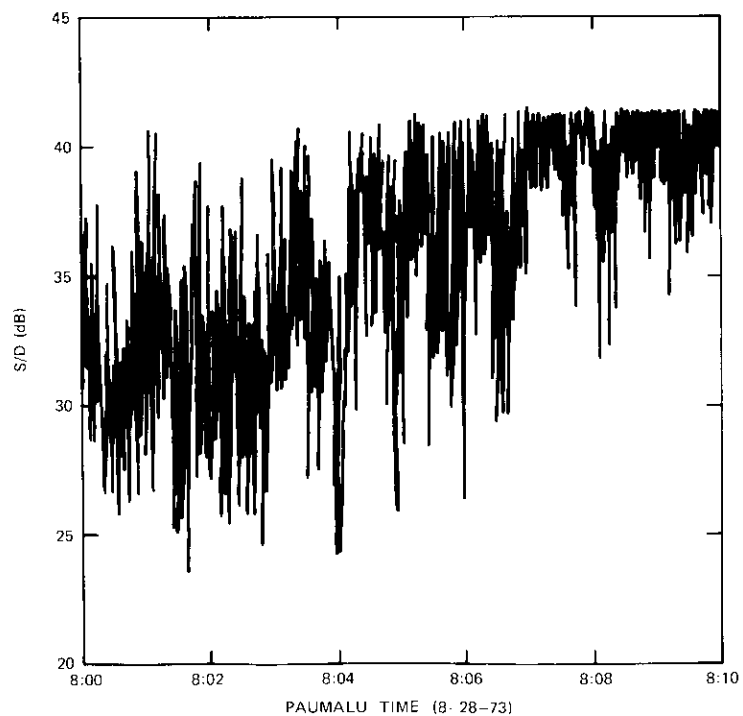


Figure 8. Fluctuations in S/D (averaged over 0.1 s) as the Speech Activity Decreases from 50 to 40 Percent

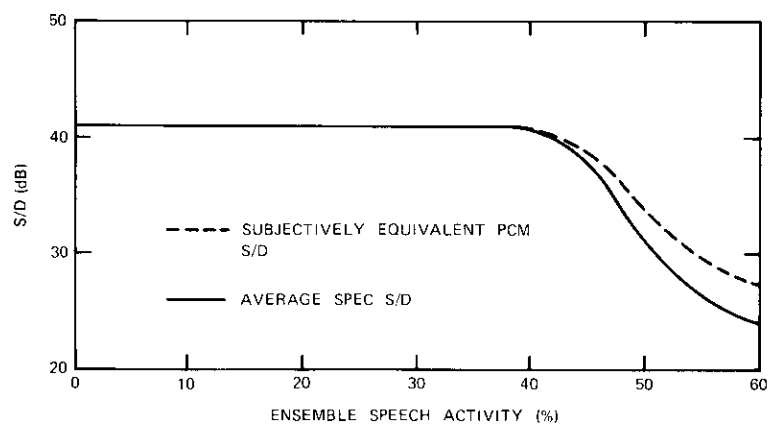


Figure 9. Measured and Subjectively Equivalent S/D as Functions of Ensemble Speech Activity

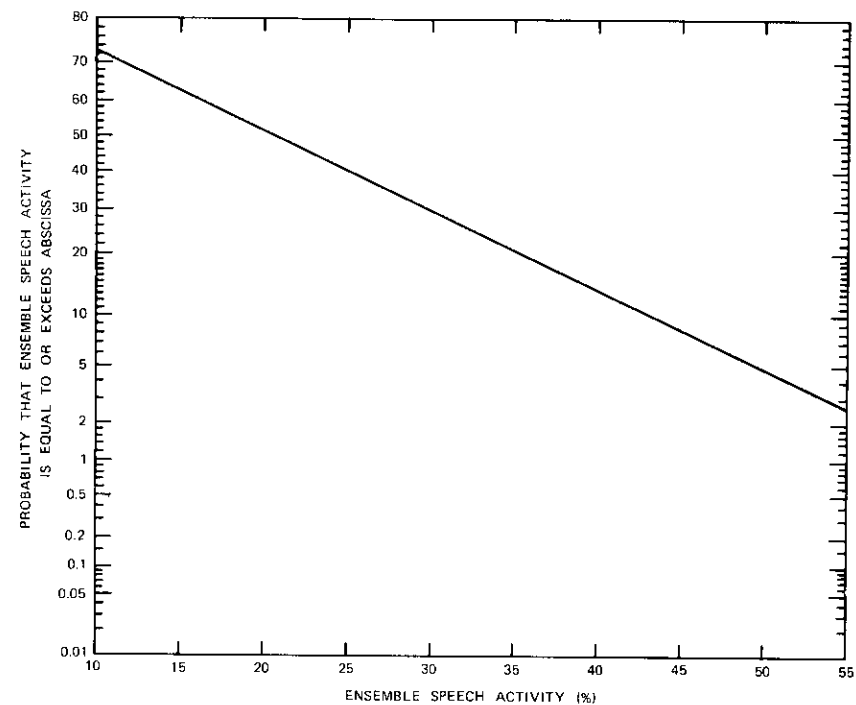


Figure 10. Ensemble Speech Activity Measured over a 24-Hour Period During SPEC Field Trial

requirement 95 percent of the time, and that this performance is based on the measured value of the average S/D , which is directly comparable to the S/D value recommended by the C.C.I.T.T. for conventional PCM systems. This is a remarkable conclusion, since SPEC has twice the capacity of a conventional PCM system.

In terms of the crosstalk performance of SPEC, the following argument applies. Intelligible crosstalk can occur only during a coherent loss of synchronization of the SAW. Such an occurrence has virtually zero probability as a result of a parity error check on the SAW to safeguard its synchronization. Thus it can be argued that intelligible crosstalk is non-existent.

In terms of its sensitivity to transmission channel bit-error rate, the SPEC system experienced the same effect normally experienced by PCM/2-phase PSK. At the highest introduced error rate of 10^{-4} , no loss of synchronization was experienced.

In terms of SPEC system overload performance, the section on quantitative system performance has already shown that the per-channel effect is insignificant.

Conclusions

The characteristics of the SPEC system demonstrated by the field trial can be summarized as follows:

- a. it meets or exceeds C.C.I.T.T. S/D requirements 95 percent of the time;
- b. it has an insignificantly small probability of crosstalk occurrence;
- c. it performs similarly to any other PCM system with respect to bit errors when speech is present (of course, bit errors do not contribute to idle channel noise, since during pauses [silent intervals] no information is transmitted);
- d. the average system overload is considerably less than 0.5 percent;
- e. subjective evaluations of its quality indicate that it is as good as or better than existing good long-distance telephone quality.

Acknowledgment

The SPEC development from its conception to the end of the field trial involved many individuals. Dr. S. J. Campanella and J. A. Sciulli were the originators of the SPEC idea. Both worked on the theoretical aspects and organized the program for implementation. The following individuals subsequently contributed significantly to the development of the system: R. H. Lanier was responsible for designing and building most of the hardware; F. L. Corcoran built the PSK modems and provided general technical assistance; R. Costales was responsible for computer analysis to determine the effects of overload and channel error rate; P. A. Lutz was responsible for computer-aided data collection; L. DaCosta designed the synchronization circuits; and many individuals at the Paumalu and Brewster earth stations provided valuable assistance during the field trial.

References

- [1] J. A. Sciulli and S. J. Campanella, "A Speech Predictive Encoding Communications System for Multichannel Telephony," *IEEE Transactions on Communications Technology*, COM-21, No. 7, July 1973, pp. 827-835.
- [2] S. Stein and J. J. Jones, *Modern Communications Principles*, New York: McGraw-Hill, 1967, p. 241.

- [3] S. J. Campanella, H. G. Suyderhoud, and M. Onufry, "Analysis of an Adaptive Impulse Response Echo Canceller," *COMSAT Technical Review*, Vol. 2, No. 1, Spring 1972.
- [4] The International Telegraph and Telephone Consultative Committee (C.C.I.T.T.), Recommendation G. 712, *Vth Plenary Assembly, Green Book*, Vol. III-2, Geneva: International Telecommunications Union, 1973.

Appendix A. SPEC system adaptive zero-order predictor

The objective of the predictor is to adapt its aperture to the instantaneous ensemble speech activity (α) of each frame by choosing the smallest aperture value which prevents system overload.

The minimum amplitude difference required for predictability increases as the aperture increases, thereby reducing the need for transmitting unpredictable samples. Figure A-1 shows the percentage reduction in unpredictable samples

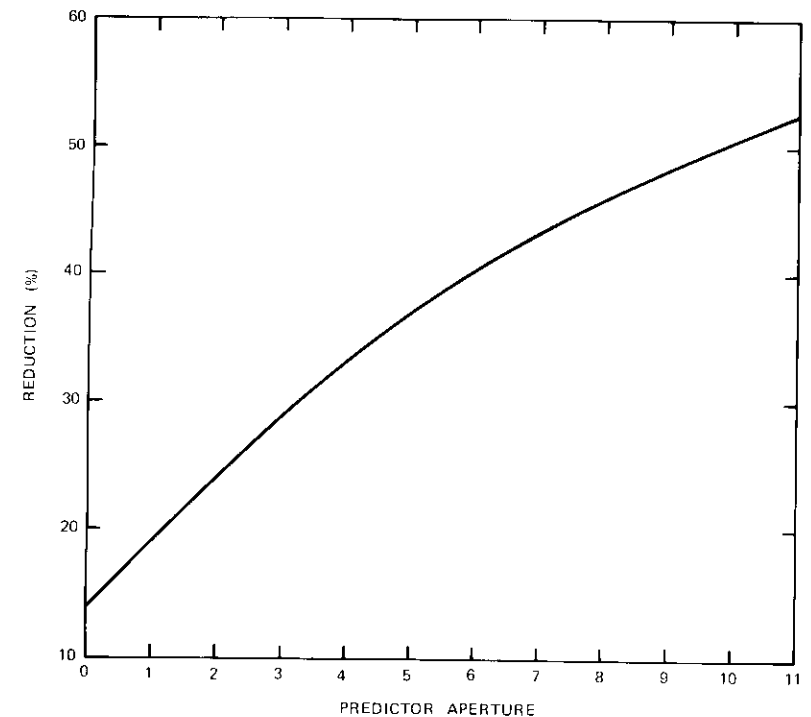


Figure A-1. Reduction in Unpredictable Samples vs Predictor Aperture

for aperture values ranging from 0 to 11.* As the aperture increases the quantization noise increases because of the reduced resolution of the reconstructed sample value. The maximum allowable aperture value of 11 has been subjectively determined so that the increased quantization noise introduced is slightly less objectionable than overload noise.

To determine the optimum aperture for a given ensemble speech activity, the signal-to-quantization noise ratios due to the aperture and the overload, S/N_Q and S/N_o , respectively, can be determined for different aperture values [A-1]. In Figure A-2 S/N_Q and S/N_o are shown for aperture values ranging from 0 to 11 and for ensemble speech activities ranging from 30 to 60 percent. (Note

* This curve was determined from the average difference between ensemble speech activity and system activity at each aperture value.

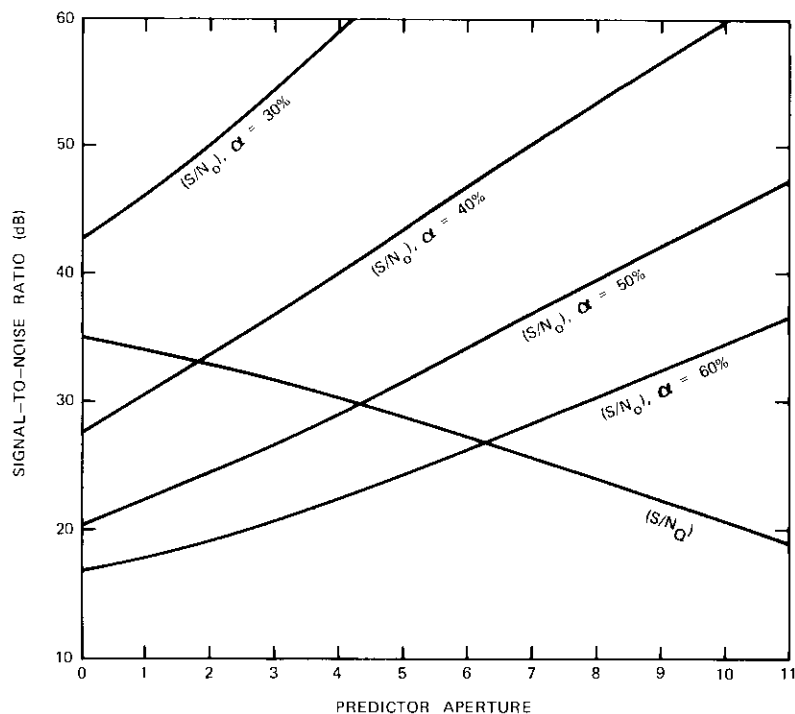


Figure A-2. Signal-to-Overload Noise Ratio and Signal-to-Quantizing Noise Ratio vs Predictor Aperture

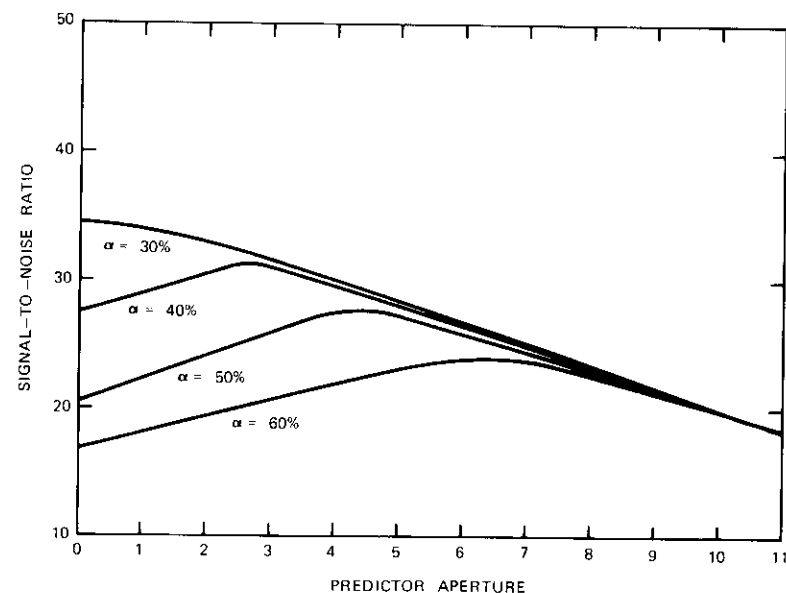


Figure A-3. Total Signal-to-Noise Ratio vs Predictor Aperture

that S/N_Q is independent of the ensemble speech activity.) Figure A-3 shows the sum of the two noise sources for the conditions in Figure A-2. The optimum apertures, determined by the integers following the peak values of signal-to-noise ratio are respectively 0, 3, 5, and 7 for the four values of ensemble speech activity given in Figure A-3.

References

- [A-1] J. A. Sculli and S. J. Campanella, "A Speech Predictive Encoding Communications System for Multichannel Telephony," *IEEE Transactions on Communications Technology*, COM-21, No. 7, July 1973, pp. 827-835.

Appendix B. Synchronization information in the SPEC system

The SPEC system contains three different types of synchronization information:

- a 64-bit channel sample assignment word (SAW),
- a 8-bit sequence word,
- an 8-bit frame synchronization word.

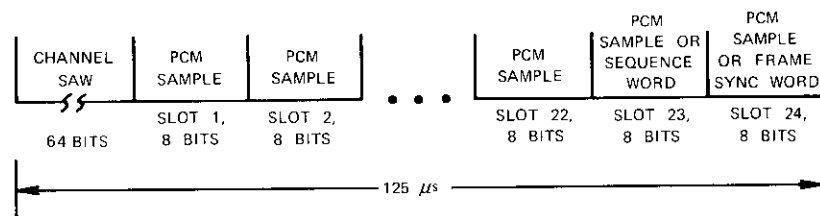


Figure B-1. Format of the SPEC Frame

Figure B-1 shows the format of the SPEC frame, indicating the location of these three synchronization words.

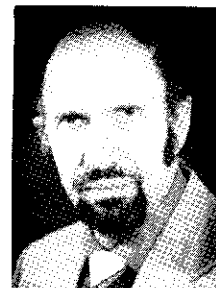
The SAW assigns the incoming PCM samples to their proper channels. This word is protected by a single parity bit. When a parity error occurs in the SAW portion of the frame, the receiver ignores the incoming PCM samples for that frame and repeats its stored samples for all 64 channels. This causes an instantaneous increase in quantization noise, but eliminates the more objectionable quantization noise resulting from unintelligible crosstalk between channels.

The sequence word gives the bit address (0 to 63) in the SAW where the parity bit is located. The parity bit rotates position through the 64 SAW bits, thereby eliminating the need for a 65th bit. When the parity bit is located at a given address n ($0 \leq n \leq 63$), the PCM sample for channel n will always be transmitted if the system activity permits. Hence, the receiver can determine whether or not a PCM sample was transmitted for channel n simply by counting the total number of samples transmitted and determining the system activity.

The sequence word is transmitted in the 23rd sample slot (Figure B-1) provided that no more than 22 PCM samples require transmission. Otherwise the sequence word will not be transmitted. Since the parity bit address rotates in a predetermined manner, its absence does not present any problem for the system. A counter is located in both the SPEC encoder and decoder and each is programmed to count in the same pattern. Therefore, once they are synchronized at the same address, any additional synchronization information (sequence word) will be used for redundant checking of the synchronization between counters.

The frame synchronization word is used to synchronize the SPEC decoder timing control with the incoming SPEC frame. This word is located in sample slot 24 and is transmitted only when no more than 23 PCM samples require transmission. For frame synchronization to occur, eight consecutive bits must be comparable to the bit pattern of the frame synchronization word, with no more than K allowed errors accumulated over N frames. The synchronization circuit will search all possible groups of eight adjacent bits and will send a synchronization pulse to the decoder timing control only when this condition

is satisfied. Once frame synchronization has been established, the synchronization word is continually rechecked provided that the number of PCM samples is 23 or less.

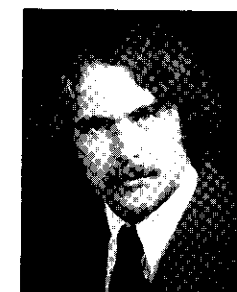


H. G. Suyderhoud was born in Borneo, Indonesia. He received the Ingenieur degree from Delft Technological University in The Netherlands in 1955, and the M.S. degree in Applied Mathematical Statistics from Rutgers in 1966.

He is presently Manager of the Signal Processing Department of the Communications Processing Laboratory, COMSAT Laboratories, where he is responsible for communications signal processing research and development. He is a member of

the IEEE and the American Statistical Association.

Joseph A. Jankowski, Jr. received a B.S. degree in Electrical Engineering from Northeastern University in 1973. In July 1973 he joined COMSAT Laboratories, where he is presently a member of the technical staff of the Communications Processing Laboratory. He is a member of Tau Beta Pi.



Robert P. Ridings received a B.S.E.T. from Capitol Institute of Technology in 1969. He joined COMSAT Laboratories as a Senior Technician in 1970 and participated in the development and field trial of the SPEC system. After receiving a B.S.E.E. from George Washington University in 1973, he became a member of the technical staff of the Communications Processing Laboratory and is now Project Manager of the SPEC system. He is a member of Sigma Tau.

Index: pulse code modulation, quantization, computerized simulation

Quantization noise and distortion power spectra of PCM systems

J. C. SU AND S. J. CAMPANELLA

(Manuscript received March 15, 1974)

Abstract

Computer simulation is used to obtain the signal-to-quantization noise ratios for speech and sinusoidal signals and the intermodulation distortion power spectra for sinusoidal signals processed by PCM. Both uniform and nonuniform (μ -law with $\mu = 255$ and A-law with $A = 87.6$) amplitude quantization processes are studied.

The simulation is based on speech and sinusoidal signals processed by a computer programmed to execute the PCM algorithms and eventually determine the resulting quantization noise, distortion, and power spectra. Hence, the limitations resulting from certain assumptions regarding the probability density function of the input signals are avoided. This method requires processing of long speech segments involving different talkers to avoid dependence on language and talker characteristics. Signal-to-noise ratios are presented for speech inputs at 32, 64, 128, and 256 levels of amplitude quantization. Harmonic and intermodulation distortion are obtained for 1- and 2-tone inputs with 128 and 256 levels of amplitude quantization. Finally, certain computer-generated results are compared with the theoretical results.

Introduction

This paper examines quantization noise, harmonic and intermodulation distortion, and related power spectra encountered in PCM systems

currently utilized in commercial telephony. Performance is evaluated as a function of quantization resolution for a number of bit rates, with emphasis on 7- and 8-bit PCM with sampling of speech and sinusoidal inputs at 8,000 Hz. Both uniform and nonuniform quantization are considered. In the nonuniform case, both μ -law ($\mu = 255$) and A-law ($A = 87.6$) companding characteristics are applied. The 13-linear-segment approximation of the A-law is also considered for speech. These laws are of particular importance because of well-known C.C.I.T.T. recommendations [1].

The principal results, the signal-to-quantization noise (S/N_q) ratio and the distortion power spectra for sampled speech and sinusoidal inputs, are determined by computer simulation. This approach is advantageous because it does not require knowledge of the amplitude probability density function of the input signal. Thus, limitations imposed by assumptions regarding this function are avoided and it is possible to determine results over the full range of input signal levels, including the overload region.

Estimates of the S/N_q ratio have been produced by previous investigators [2]-[5]. However, these estimates are usually based on the assumption of either a Gaussian or an exponential amplitude probability density function for the speech input; consequently, they are subject to the limitations inherent to these approximations.

Since PCM terminals are expected to accept multifrequency tones, harmonic distortion has been calculated for single tones and intermodulation distortion for tone pairs. The distortion power spectrum and S/N_q ratio have been computed for the uniform μ - and A-law cases. The results show that linear quantization produces less harmonic and intermodulation distortion than nonuniform quantization; however, there is little difference in the amounts of harmonic and intermodulation distortion produced by μ - and A-law companders.

System model and methods of calculation

The PCM codec consists of a digital compressor on the transmit side that quantizes and encodes the input signal, and a digital expander on the receive side that decodes the received signal and ultimately produces a replica of the original input signal. The sampling rate is set at 8 kHz to accommodate 4-kHz baseband inputs. Low-pass filters which eliminate aliasing components are included in the transmit and receive processors.

The function of the compander (compressor/expander) has been discussed in detail elsewhere [6]. In PCM voice transmission it is desirable to

obtain an essentially constant S/N_q over a wide dynamic range of input signal amplitudes. Hence, the quantization noise power must be made proportional to the signal amplitude. The compander accomplishes this by making the quantizing error small for low signal amplitudes and permitting larger quantizing errors to occur at high signal amplitudes. Two important companding laws, known as the μ -law [5] and the A-law [7], have been considered. The μ -law characteristic is given by

$$F_\mu(x) = y_{\max} \operatorname{sgn}(x) \frac{\ln[1 + \mu|x|/x_{\max}]}{\ln(1 + \mu)}, \quad -x_{\max} \leq x \leq x_{\max} \quad (1)$$

where x_{\max} and y_{\max} are the maximum values of the input and output of the compressor, respectively. The parameter μ determines the dynamic range of the input for a relatively constant S/N_q . The A-law characteristic is given by

$$F_A(x) = \begin{cases} y_{\max} \operatorname{sgn}(x) \frac{1 + \ln(A|x|/x_{\max})}{1 + \ln A}, & \frac{x_{\max}}{A} < |x| \leq x_{\max} \\ y_{\max} \operatorname{sgn}(x) \frac{A|x|/x_{\max}}{1 + \ln A}, & 0 \leq |x| \leq \frac{x_{\max}}{A} \end{cases} \quad (2)$$

In this case, the parameter A determines the dynamic range of the input for a relatively constant S/N_q .

The S/N_q ratio for PCM systems is of the form [8], [9]

$$S/N_q = Cf(\sigma_x) 2^{2\eta} \quad (3)$$

where η is the number of bits per sample, C is a constant which depends on the probability density function of the input signal, and $f(\sigma_x)$ is a function which accounts for the variation in S/N_q with input signal level. For uniform quantization, $f(\sigma_x) = \sigma_x/\sigma_{\max}$, where σ_x is the rms value of the signal, and σ_{\max} is the maximum value of σ_x set by the peak-to-peak range of the codec and the acceptable clipping distortion level. It has been shown that [6]

$$f(\sigma_x) \doteq \left[\frac{\sigma_{\max}}{\sigma_x} \int_x \frac{p(x)}{|F'(x)|^2} dx \right]^{-1} \quad (4)$$

where $F'(x)$ is the first derivative of the compressor characteristic and $p(x)$ is the probability density function of the input signal. It should be noted that equation (4) is not valid in the overload region.

For speech inputs, $p(x)$ is often assumed to be Laplacian; i.e.,

$$p(x) = \frac{1}{\sqrt{2}\sigma} \exp\left(-\sqrt{2}\frac{|x|}{\sigma}\right) \quad (5)$$

Since the function of the compressor part of a compander is to flatten the probability density function of speech, the S/N_q ratio after compression may be assumed to be that of a uniformly distributed signal. This implies that the value of C in equation (3) is approximately unity for speech inputs. For sinusoidal signals, $p(x)$ is

$$p_s(x) = \frac{1}{\pi\sqrt{A_p^2 - x^2}} \quad (6)$$

where A_p is the peak value of the sine wave. The value of C in equation (3) is 1.5 for such inputs. Equations (1) through (6) can be used to compute the theoretical S/N_q ratio for both companded and un-companded PCM with either speech or sinusoidal inputs at various levels.

An alternate method utilizing computer simulation techniques can also be employed to determine S/N_q as a function of input signal level. Provided that the Nyquist sampling criterion is satisfied, the average of the squared sample values of the signal equals the time average of the squared signal. Thus,

$$\overline{x^2(kT_s)} \doteq \overline{x^2(t)} \quad (7)$$

where k is an integer designating the sample number and T_s is the sample epoch. Therefore, the signal power may be obtained by averaging the squares of the instantaneous samples of $f(t)$ over a sufficiently large number of samples.

The mean-squared error, i.e., the quantization noise resulting from the difference between the input signal and the reconstructed output signal, can be calculated in this manner. Therefore, S/N_q may be obtained for PCM codecs with arbitrary characteristics and various input signals in a manner which is particularly suited to computer simulation techniques.

The direct determination of the distortion power spectrum is also of particular interest. Through the application of the discrete fast Fourier

transform (DFFT) [10], [11] to the error values, computer-generated distortion power spectra can be easily obtained. This method is particularly convenient for evaluating harmonic and intermodulation distortion for single- and multiple-frequency sinusoidal inputs.

Discussion of results

S/N_q versus input level

This subsection compares theoretical and computer-generated results of S/N_q versus input signal level under various conditions for PCM codecs currently in use. In all cases, the upper limit of the dynamic range is specified by defining $\sigma_{\max} = +2$ dBm0 for a sinusoidal signal. This definition, which implies that a sine wave occupying the full peak-to-peak input signal range will be at a level of +2 dBm at a zero test level, is commonly used to determine the overload point for PCM codecs [1], [2]. Sinusoidal levels higher than σ_{\max} suffer peak clipping; thus the range of input sinusoidal signal levels above +2 dBm0 is called the overload range. During a typical telephone conversation the average level is -9 dBm0, which is 11 dB below the upper limit of the PCM codec. Because of the higher value of the peak-to-rms ratio encountered in speech, a speech signal may sometimes result in overloading.

Figure 1 shows the performance of uniformly quantized PCM obtained by computer simulation for speech input signals using 5, 6, 7, and 8 bits per sample. The input speech sample lasts about 15 seconds and consists of test sentences spoken in turn by a male and female talker. To calibrate the speech power relative to σ_{\max} , the rms level of the entire sample has been calculated. Figures 2 and 3 show the theoretical and computer-calculated results for speech using 8 bits per sample and μ -law ($\mu = 255$) and A-law ($A = 87.6$) companding, respectively. Figure 3 also shows the computer-simulated results obtained with the 13-segment A-law described in C.C.I.T.T. Rec. G.711.

In all of these cases the values of S/N_q obtained from the computer calculations using the input speech sample are slightly better than the theoretical results at high signal levels, but slightly poorer at low signal levels. The effect of changing the number of bits per sample for the μ - and A-law cases, both theoretical and computer simulated, is shown in Figure 4. The curves are separated by 6 dB per bit in terms of the S/N_q ratio over the range of 5 to 8 bits, as implied by the theoretical model. It is also apparent that μ -law ($\mu = 255$) companding provides better performance

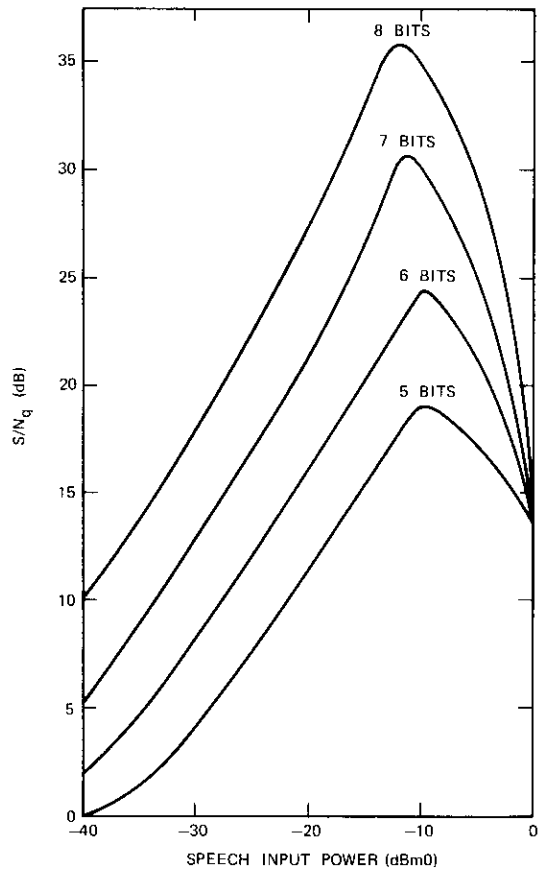


Figure 1. S/N_q vs Speech Level for Linear Codec with Speech Input

than A-law ($A = 87.6$) companding at low signal levels, with a small sacrifice in performance at high signal levels.

Performance for a 1,100-Hz sinusoidal input with μ -law ($\mu = 255$) and A-law ($A = 87.6$) companding using the computer-simulated and theoretical approaches is presented in Figures 5 and 6, respectively. The undulations appearing in the computer-simulated curves are attributed to the combined effect of the quantizing levels and the preciseness of the sinusoidal pattern. Such undulations do not appear for speech inputs because of the randomness of speech. Note that the theoretical results exceed the simulated results by about 2 dB in terms of S/N_q .

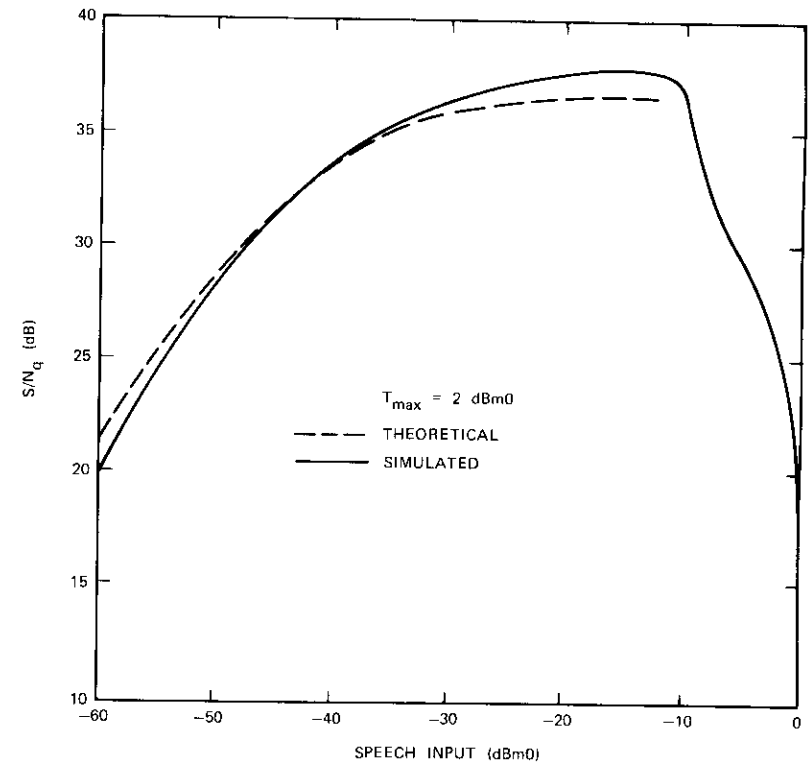


Figure 2. Theoretical and Simulated S/N_q vs Speech Level for 8-Bit PCM with $\mu = 255$

Distortion power spectra

The output distortion power spectra for single- and multiple-frequency sinusoidal (tone) inputs were obtained by using a 2,000-point DFFT yielding a spectral resolution of 4 Hz. The single-frequency input was a full load (+2-dBm0) sinusoid at 1,100 Hz. The multifrequency input consisted of two sinusoids of equal power at 1,100 and 1,700 Hz with a composite level of -7 dBm0. These parameters were chosen in accordance with the general considerations outlined by the C.C.I.T.T. [1].

Results obtained for both 7- and 8-bit uniform and nonuniform quantization with μ -law ($\mu = 255$) and A-law ($A = 87.6$) companding characteristics are shown in Table 1. Figure 7 shows a computer-produced spectrum for the single-tone case using 8-bit quantization and μ -law com-

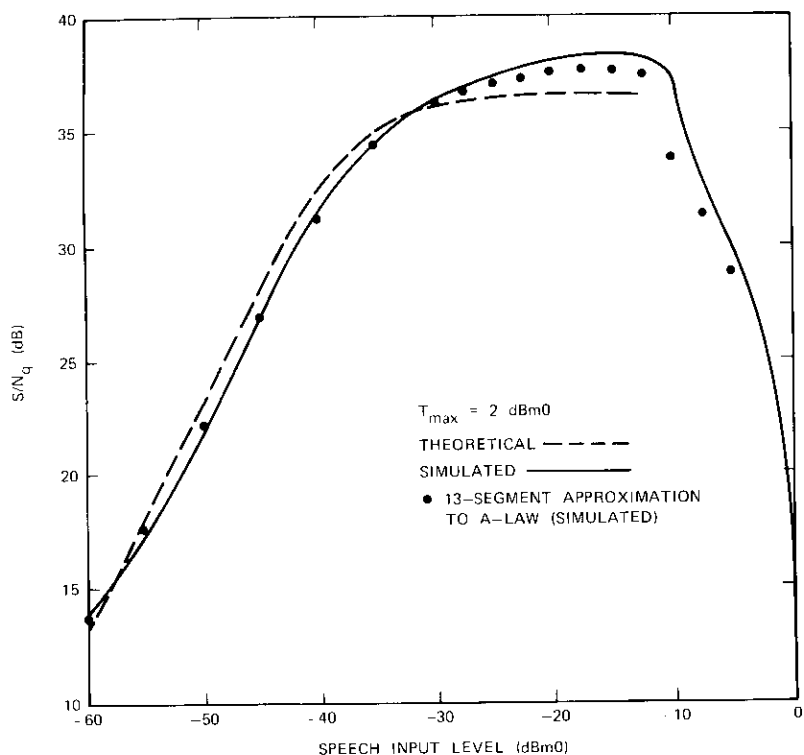


Figure 3. Theoretical and Simulated S/N_q vs Speech Level for 8-Bit PCM with $A = 87.6$

panding. It should be noted that the distortion terms occur at odd harmonics of 100 Hz because the period of a periodically sampled periodic function inherently contains the lowest possible integer number of periods of each constituent. For the case analyzed here, in which a sinusoid of 1,100 Hz is sampled at 8,000 Hz, an interval of 0.01 s contains 11 periods of 1,100-Hz sinusoid and 80 periods of the sampling function. Hence, the quantization distortion terms fall at multiples of 100 Hz and, since the distortion is symmetrical, only odd-order components are observed. The same situation prevails in the 2-tone case.

A review of the data shown in Table 1 yields the following observations concerning the single-frequency (1,100-Hz) input. For 7- and 8-bit linear quantization, the S/N_q ratios are 44.6 and 50.2 dB, respectively, and the

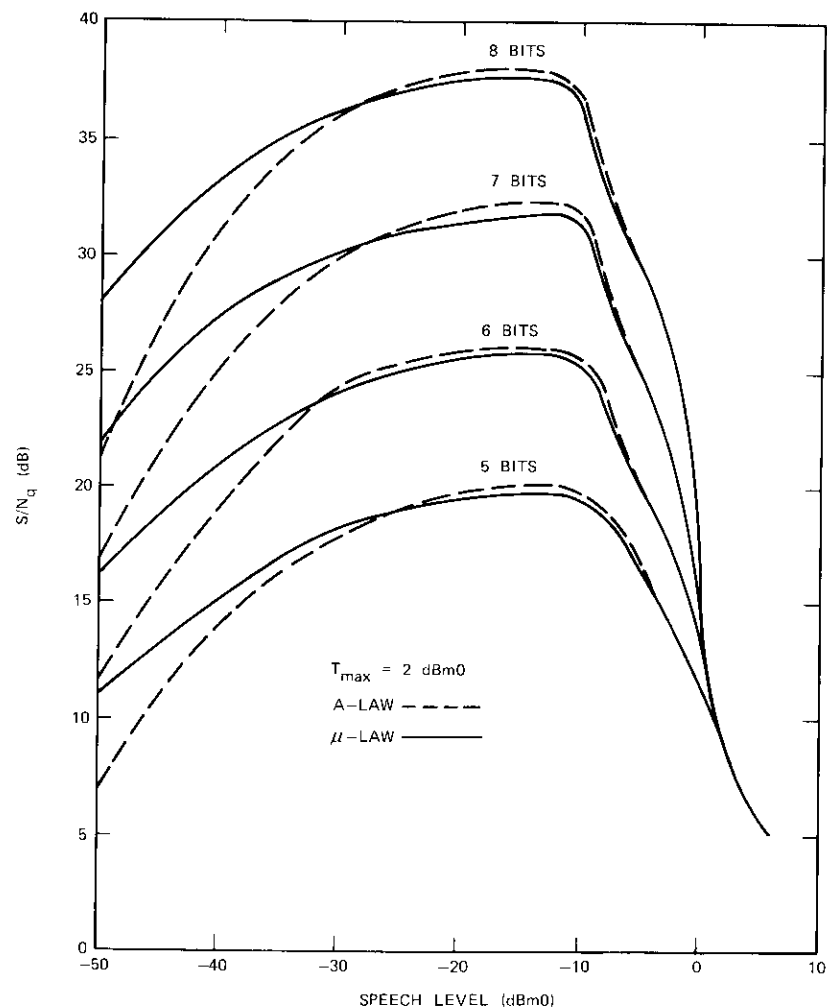


Figure 4. S/N_q vs Speech Level for 5-, 6-, 7-, and 8-Bit PCM with $\mu = 255$ and $A = 87.6$

highest level distortion components are down by 52 dB (2,100 Hz) and 58 dB (2,300 Hz), respectively. For 7- and 8-bit A-law quantization, the S/N_q ratios are 33.1 and 39.2 dB, respectively, and the highest level distortion components are down by 39 dB (3,200 Hz) and 48 dB (300 and

TABLE 1. DISTORTION COMPONENT LEVELS BELOW TONE LEVEL IN dB

Distortion Component Frequency (Hz)	Tone Frequency,* f (Hz)	Case											
		7-Bit Linear		8-Bit Linear		7-Bit A-Law		8-Bit A-Law		7-Bit μ -Law		8-Bit μ -Law	
		S/N_q Level Below (dB)	Distortion Component Tone Level (dB)	S/N_q Level Below (dB)	Distortion Component Tone Level (dB)	S/N_q Level Below (dB)	Distortion Component Tone Level (dB)	S/N_q Level Below (dB)	Distortion Component Tone Level (dB)	S/N_q Level Below (dB)	Distortion Component Tone Level (dB)	S/N_q Level Below (dB)	Distortion Component Tone Level (dB)
100	1,100	44.6	75	50.2	67	33.1	40	39.2	51	33.2	41	40.1	51
	1,100 1,700	35.2	45	40.6	51	35.9	73	36.5	49	31.9	44	39.0	48
300	1,100	44.6	71	50.2	71	33.1	56	39.2	48	33.2	54	40.1	49
	1,100 1,700	35.2	45	40.6	52	35.9	56	36.5	64	31.9	49	39.0	54
500	1,100	44.6	60	50.2	64	33.1	48	39.2	64	33.2	44	40.1	52
	1,100 1,700	35.2	56	40.6	59	35.9	51	36.5	48	31.9	54	39.0	47
700	1,100	44.6	62	50.2	68	33.1	45	39.2	56	33.2	49	40.1	53
	1,100 1,700	35.2	45	40.6	63	35.9	38	36.5	64	31.9	43	39.0	63
900	1,100	44.6	63	50.2	65	33.1	52	39.2	64	33.2	46	40.1	57
	1,100 1,700	35.2	42	40.6	62	35.9	49	36.5	56	31.9	59	39.0	47
1,100	1,100	44.6	0	50.2	0	33.1	0	39.2	0	33.2	0	40.1	0
	1,100 1,700	35.2	0	40.6	0	35.9	0	36.5	0	31.9	0	39.0	0
1,300	1,100	44.6	70	50.2	70	33.1	48	39.2	50	33.2	44	40.1	51
	1,100 1,700	35.2	57	40.6	60	35.9	39	36.5	45	31.9	37	39.0	66
1,500	1,100	44.6	55	50.2	59	33.1	44	39.2	52	33.2	47	40.1	53
	1,100 1,700	35.2	56	40.6	53	35.9	46	36.5	68	31.9	40	39.0	45

1,700	1,100	44.6	62	50.2	77	33.1	50	39.2	52	33.2	66	40.1	54
	1,100 1,700	35.2	0	40.6	0	35.9	0	36.5	0	31.9	0	39.0	0
1,900	1,100	44.6	55	50.2	63	33.1	46	39.2	60	33.2	53	40.1	53
	1,100 1,700	35.2	60	40.6	55	35.9	40	36.5	78	31.9	38	39.0	49
2,100	1,100	44.6	52	50.2	77	33.1	58	39.2	61	33.2	42	40.1	49
	1,100 1,700	35.2	54	40.6	47	35.9	41	36.5	58	31.9	46	39.0	51
2,300	1,100	44.6	75	50.2	58	33.1	39	39.2	63	33.2	44	40.1	65
	1,100 1,700	35.2	43	40.6	53	35.9	52	36.5	39	31.9	51	39.0	55
2,500	1,100	44.6	56	50.2	70	33.1	48	39.2	50	33.2	70	40.1	50
	1,100 1,700	35.2	57	40.6	52	35.9	51	36.5	51	31.9	44	39.0	66
2,700	1,100	44.6	55.5	50.2	71	33.1	47	39.2	54	33.2	45	40.1	55
	1,100 1,700	35.2	39	40.6	69	35.9	61	36.5	48	31.9	50	39.0	44
2,900	1,100	44.6	65	50.2	63	33.1	54	39.2	50	33.2	62.5	40.1	51
	1,100 1,700	35.2	43	40.6	65	35.9	50	36.5	45	31.9	45	39.0	55
3,100	1,100	44.6	60	50.2	60	33.1	45	39.2	56	33.2	54	40.1	53
	1,100 1,700	35.2	55	40.6	65	35.9	50	36.5	52	31.9	48	39.0	56
3,300	1,100	44.6	62	50.2	69	33.1	67	39.2	48	33.2	50	40.1	65
	1,100 1,700	35.2	51	40.6	58	35.9	48	36.5	65	31.9	41	39.0	47
3,500	1,100	44.6	60	50.2	78	33.1	52	39.2	52	33.2	48	40.1	50
	1,100 1,700	35.2	56	40.6	59	35.9	68	36.5	44	31.9	45	39.0	55
3,700	1,100	44.6	62	50.2	60	33.1	64	39.2	75	33.2	45	40.1	67
	1,100 1,700	35.2	60	40.6	62	35.9	72	36.5	56	31.9	46	39.0	46
3,900	1,100	44.6	78	50.2	62	33.1	47	39.2	69	33.2	46	40.1	57
	1,100 1,700	35.2	43	40.6	42	35.9	39	36.5	43	31.9	55	39.0	55

*For a single tone, the level is +2 dBm0; for two tones, each tone has a level of -10 dBm0.

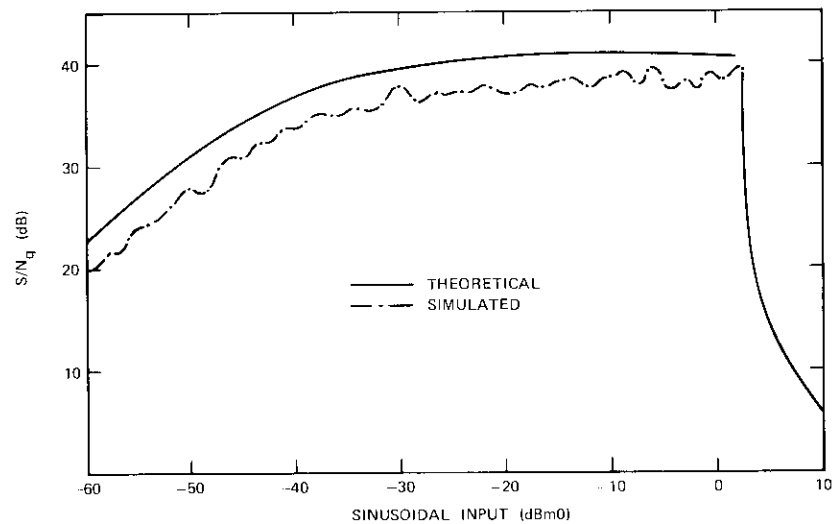


Figure 5. Theoretical and Simulated S/N_q vs Input Level for a 1,100-Hz Sinusoidal Input Using 8-Bit μ -Law-Companded PCM ($\mu = 255$)

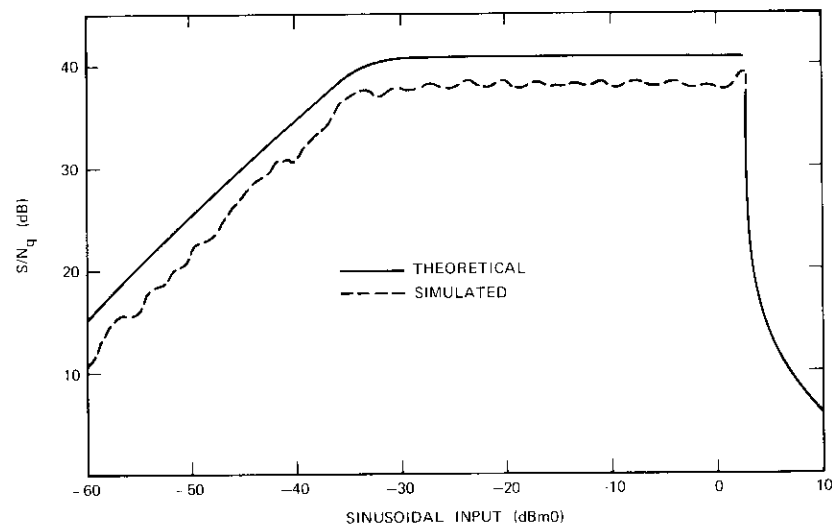


Figure 6. Theoretical and Simulated S/N_q vs Input Level for a 1,100-Hz Sinusoidal Input Using 8-Bit A-Law-Companded PCM ($A = 87.6$)

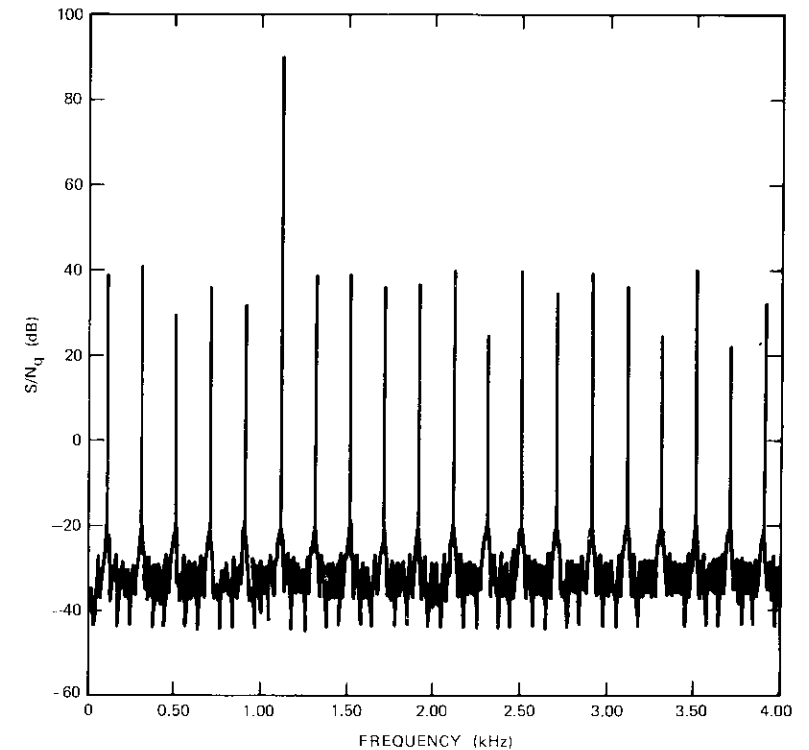


Figure 7. Power Spectrum of the Output of an 8-Bit μ -Law Codec (single-tone full load input $S/N_q = 40.08$, $f_1 = 1,100$ Hz)

3,300 Hz), respectively. For 7- and 8-bit μ -law quantization, the S/N_q ratios are 33.2 and 40.1 dB, respectively, and the highest level distortion components are down by 41 (100 Hz) and 42 dB (2,100 Hz) and by 49 dB (300 and 2,100 Hz), respectively.

In general, for the other distortion components of the single-frequency case, the results of μ -law ($\mu = 255$) companding are only slightly better than those of A-law ($A = 87.6$) companding. Uniform quantization yields distortion components that are on the average 10 dB less than those of either of the companded quantizers. This result must be tempered by the -2-dBm0 signal level; i.e., for lower signal levels the difference margin will diminish. The most intense distortion products occur at 2,100 or 2,300 Hz (i.e., near but not precisely at the second harmonic) and at 100 and

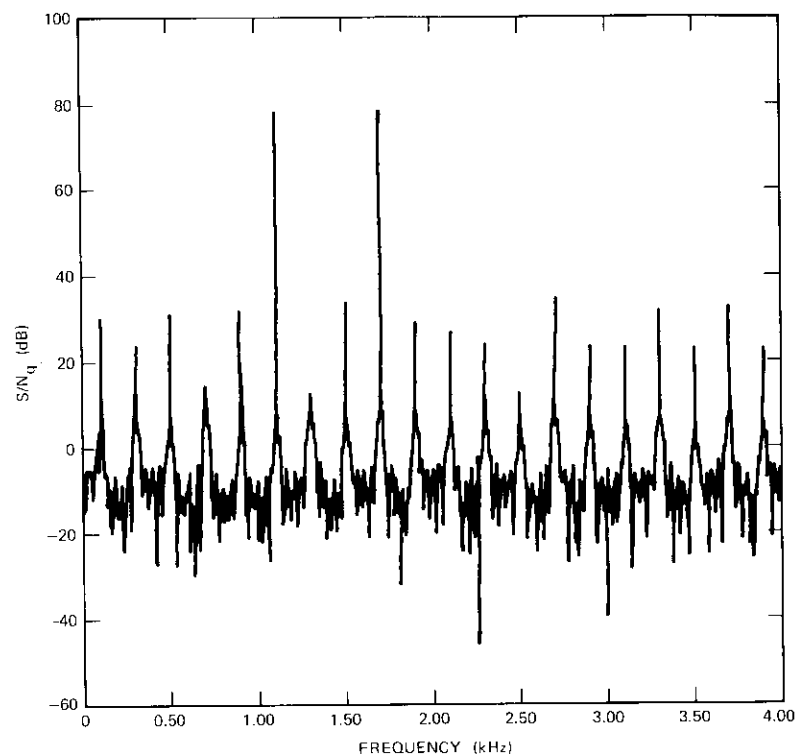


Figure 8. Power Spectrum of the Output of an 8-Bit μ -Law Codec with -7 -dBm0 2-Tone Input ($S/N_q = 38.38$ dB, $\mu = 255$, $f_1 = 1,100$ Hz, $f_2 = 1,700$ Hz)

300 Hz for uniform quantization; the next most intense occur at 2,100 or 2,300 Hz for companded quantization.

For 2-frequency inputs a typical spectrum is shown in Figure 8. The results summarized in Table 1 suggest the following observations. Since the levels of the combined tones are adjusted to -7 or -10 dBm0 for each tone alone, the values cited in Table 1 were measured relative to the level of a single tone. For 7- and 8-bit uniform quantizations, the S/N_q ratios were 35.2 and 40.6 dB, respectively, and the highest level distortion components were down by 42 (900 Hz) and 43 dB (2,300, 2,900 and 3,900 Hz) and by 42 (3,900 Hz), 51 (100 Hz), and 52 dB (300 and 2,500 Hz), respectively. For 7- and 8-bit A-law quantizations, the S/N_q ratios were 35.9 and 36.5 dB, respectively, and the highest level distortion components

were down by 39 (1,300 and 3,900 Hz) and 40 dB (1,900 Hz) and by 39 dB (2,300 Hz), respectively. For the 7- and 8-bit μ -law quantizations, the S/N_q ratios were 31.9 and 39.0 dB, respectively, and the highest level distortion components were down by 37 (1,300 Hz), 38 (1,900 Hz), and 44 dB (2,700 Hz) and by 44 (2,700 Hz) and 45 dB (1,500 Hz), respectively.

For 2-tone signals, the S/N_q ratios and the level of the highest level distortion terms were greater for uniform quantization for either form of companded quantization. The behavior of the spectral composition of the distortion terms as a function of both the type of companding and the number of bits used for quantization was rather complex and did not seem to follow a consistent pattern. For the companded quantizations there was a tendency for the most intense distortion terms to occur at 1,300 or 1,500 Hz, i.e., between the frequencies of the two input signal tones. Intense terms were also found in the vicinity of 2,100 or 2,300 Hz for all forms of quantization. The distortion spectral variance was about the same for both the 2-tone and the 1-tone cases.

Finally, the manner in which the total S/N_q varied as a function of the number of quantizing bits was quite interesting. This behavior is illustrated in Table 2, where the S/N_q ratio and its first differences are tabulated ver-

TABLE 2. SIGNAL-TO-QUANTIZATION NOISE RATIO VERSUS NUMBER OF BITS PER SAMPLE, 2-TONE SIGNAL

Companding Law	Bits/Sample	S/N_q (dB)	Differences in S/N_q (dB)
A = 87.6	6	26.3	
	7	35.9	9.6
	8	36.5	0.6
	9	43.1	6.6
$\mu = 255$	6	26.4	
	7	31.9	5.5
	8	39.0	7.1
	9	43.3	4.3

sus the number of quantizing bits for the 2-tone input signal using 6, 7, 8, and 9 bits per sample and μ - and A-law companding. This table shows that, although there is a general slope of 6 dB per bit for both cases, the actual observed values can differ significantly from this trend. For example, in the A-law case, the S/N_q increased by only 0.6 dB in going from 7 to 8 bits per sample, whereas it increased by 9.6 dB when going from 6 to 7 bits per sample. This effect is attributed to the relationship between the quantizing levels and the pattern of signal values and should be expected to vary significantly as this relationship is modified. It appears to be more pronounced in the A-law case than in the μ -law case.

Conclusions

A computer simulation technique has been used to analyze the performance of PCM codecs designed for 5, 6, 7, and 8 bits per sample and employing uniform or nonuniform [μ -law ($\mu = 255$) and A-law ($A = 87.6$)] quantization. For both speech and single-tone input signals, the S/N_q ratios have been calculated over a dynamic range of 50 to 60 dB inclusive of the overload range. The results are unique in that they are representative of the performance of ideally fabricated PCM codecs.

Comparisons with the results obtained by using theoretical models and 8-bit-per-sample quantization show that, for speech inputs, the theoretical model was slightly optimistic at low levels and slightly pessimistic at high levels in the case of companders using the A-law ($A = 87.6$) as well as the C.C.I.T.T. 13-linear-segment approximation to the A-law. The difference between the C.C.I.T.T. 13-linear-segment approximation and the actual A-law was found to be very small. For a single-tone input signal, the theoretical model was found to be optimistic by several decibels over the entire dynamic range for both the μ - and A-law cases. Comparisons between the μ - and A-law cases with 5, 6, 7, and 8 bits per sample showed that μ -law companding consistently provided better performance at low speech signal levels, with only a small sacrifice in performance at high levels.

Discrete Fourier spectrum analyses were also performed on a single-tone (1,100-Hz) input signal applied at a level of 2 dBm0 and a pair of equal amplitude tones (1,100 and 1,700 Hz) applied at a combined level of -7 dBm0 to assess the spectral nature of the distortion products. In both cases, as a consequence of the periodicity resulting from the relationship between the sampling rate and the frequency of the single-tone input, the distortion terms appeared at odd multiples of 100 Hz. For a single-tone

input at 1,100 Hz in both the uniform quantization and companded cases, some of the highest level distortion components occurred in the vicinity of 2,100 and 2,300 Hz, but none at 2,200 Hz. The distortion terms were weaker in the uniform case than in either companded case, while the companded cases did not differ significantly from one another. Varying the number of bits per sample had a very small effect on these results.

For the 2-tone input (1,100 and 1,700 Hz), in the companded cases some of the stronger distortion terms occurred between 1,300 and 1,500 Hz; however, in the linear case the components at these same frequencies were among the lowest. Otherwise, the distortion component distributions for the 2-tone input, especially for the companded cases, were rather complex and did not adhere to any particularly distinct pattern. It is especially interesting to note that the manner in which the total S/N_q ratio varied as a function of the number of bits per sample (as shown in Table 2) was quite erratic, especially in the A-law case. The distribution of distortion components and the total S/N_q ratio is attributed to the relationship between the signal pattern and the quantizing levels as influenced by the companding law.

Acknowledgment

The authors would like to acknowledge the work of Joseph Sciulli, who assisted in developing the simulation algorithms and performing the theoretical comparisons which appear in this paper.

References

- [1] The International Telegraph and Telephone Consultative Committee (C.C.I.T.T.), *Green Book, V Plenary Assembly*, Vol. III, Rec. G.711 and G.712.
- [2] D. L. Richards, "Transmission Performance of Telephone Networks Containing PCM links," *Proceedings of IEE*, Vol. 115, No. 9, September 1968.
- [3] W. R. Bennett, "Spectra of Quantized Signals," *Bell System Technical Journal*, Vol. 27, July 1948, p. 446.
- [4] H. S. Black, *Modulation Theory*, New York: Van Nostrand, 1953.
- [5] B. Smith, "Instantaneous Companding of Quantized Signals," *Bell System Technical Journal*, Vol. 36, May 1957, pp. 653-709.
- [6] Members of the Technical Staff, Bell Laboratories, Inc., *Transmission Systems for Communications*, fourth edition, Winston-Salem: Western Electric Co., 1970.

- [7] R. F. Purton, "Survey of Telephone Speech Signal Statistics and Their Significance in the Choice of a PCM Companding Law," *Proceedings of IEE*, Vol. B109, June 1962, pp. 60-66.
- [8] S. Stein and J. Jones, *Modern Communication Principles*, New York: McGraw-Hill Book Company, 1967.
- [9] H. Taub and D. Shilling, *Principles of Communication Systems*, New York: McGraw-Hill Book Company, 1970.
- [10] J. W. Cooley and J. Tukey, "An Algorithm for the Machine Calculation of Complex Fourier Series," *Mathematics of Computation*, Vol. 19, April 1965, pp. 297-301.
- [11] R. C. Singleton, "An Algorithm for Computing the Mixed Radex Fast Fourier Transform," *IEEE Transactions on Audio and Electroacoustics*, AU-17, No. 2, June 1969, pp. 93-103.

James C. Su received his B.S.E.E. from Taiwan University and his Ph.D. in electrical engineering from the University of Pennsylvania. From 1963 to 1967, while at the Moore School of Electrical Engineering, he worked on functional series representation of time-varying nonlinear systems with arbitrary input.

As a member of the technical staff at COMSAT Laboratories since 1967, Dr. Su has been engaged in signal and speech processing techniques. He has developed a system for regenerating the pointing data of synchronous satellites and a nonlinear phase-locked loop for fast acquisition of the signal.



S. J. Campanella received a B.S.E.E. from the Catholic University of America, a M.S.E.E. from the University of Maryland, and a Ph.D. in electrical engineering from the Catholic University of America. Before joining COMSAT, he was Manager of the Electronics Research Center at Melpar, Inc.

He is presently Director of the Communications Laboratory of COMSAT Laboratories, where he is responsible for the technical orientation of the efforts pursued in the Signal Processing, Digital Control, and Modulation Techniques Departments.

Dr. Campanella is a member of AIAA, IEEE, Sigma Xi, Phi Eta Sigma, and the Acoustical Society of America. He is also a member of the board of directors of EASCON.

Index: polarization (waves), antenna design, communications satellites.

Antenna design studies for a U.S. domestic satellite

R. W. GRUNER AND W. J. ENGLISH

(Manuscript received April 1, 1974)

Abstract

This paper describes antenna design studies for application to U.S. domestic communications satellite systems using orthogonal linear polarization to achieve frequency reuse. Antennas with polarization-selective reflection or transmission surfaces can achieve the highest beam polarization isolations (35–50 dB), but have the greatest mechanical design complexity. Antennas with dual-polarized feed systems generate orthogonally polarized coincident beams from a single reflector in mechanically simple configurations. Worst-case polarization isolations achieved over the coverage region(s) range from 30–35 dB. The necessity of swept frequency measurement techniques to completely and accurately characterize the polarization isolation, gain, and frequency-sensitive beam squint of the antenna system is demonstrated.

Introduction

U.S. domestic communications satellite antennas [1] capable of providing frequency reuse by means of two orthogonal linearly polarized beams require 30- to 50-dB polarization isolations over the entire beam coverage area. Gain over the required coverage area is also an important design consideration. In addition, the antenna system configurations must be dimensionally, mechanically, and thermally compatible with the spacecraft environment.

Two basic design approaches are considered. The first approach uses polarization-selective reflecting or transmitting surfaces consisting of either a parallel grid of wires or grating strips. Antennas with polarization gratings or grids are potentially capable of yielding the highest polarization isolations (35–50 dB). However, this approach involves greater mechanical and thermal design complexity. Launch vehicle shroud dimensions or weight limitations often require a wide-bandwidth feed design (spanning both the up- and down-link frequencies) for antennas which are limited to a single linear polarization. As a result, gain and coverage contours may not be optimized for each individual frequency band. Antenna configurations combining both polarization-selective

transmission and reflecting surfaces can also be used to minimize the required launch vehicle shroud dimensions.

The second design approach uses a dual-polarized narrowband feed (spanning either up- or down-link frequencies) to generate coincident orthogonally polarized beams from a single reflector surface. Although this approach yields a lower polarization isolation (30–35 dB) than the polarization filtered antennas, it is lightweight with a simplified mechanical and thermal design.

When the design studies for the COMSAT system began in the fall of 1970, initial requirements called for up-link (5,925–6,425 MHz) and down-link (3,700–4,200 MHz) coincident continental U.S. coverage beams (nominally $3.5^\circ \times 7.0^\circ$ elliptical or equivalent shaped beams) on orthogonal linear polarizations. Offshore spot-beam coverage to Alaska, Hawaii, and Puerto Rico was also required. Offshore beams were to be directly connected to a dedicated satellite transponder or coupled to a continental U.S. beam (coupled mode service).

An important aspect of the design studies has been the formulation of measurement techniques which fully characterize the antennas in a dual-polarized satellite communications system. Swept frequency measurements across the up- and down-link bands are required to identify the worst-case polarization isolations at each coverage angle. Several distinct antenna depolarization sources contribute to the polarization isolation; hence, measurement data at a specific coverage angle can show considerable frequency variation. However, polarization isolation contours based on worst-case swept frequency data are shown to be well defined.

Discussion of design approaches

Polarization-selective transmission filters

A polarization-selective filter is placed in front of a reflector to create a linearly polarized aperture plane field. The filter may be constructed of wires, printed circuit lines, or grating elements. Typical filter configurations designed to transmit a vertically polarized signal and reflect a horizontally polarized signal are shown in Figure 1.

The wire and printed circuit grids block a measurable percentage of the vertically polarized signal. The blockage is proportional to the metal's diameter, d , or width, w , relative to the spacing, S . The grating operates as a waveguide beyond cutoff for the signal polarized parallel to the grating elements. It uses much wider spacings and depth, D , in the direction of propagation to provide attenuation. The signal polarized perpendicular

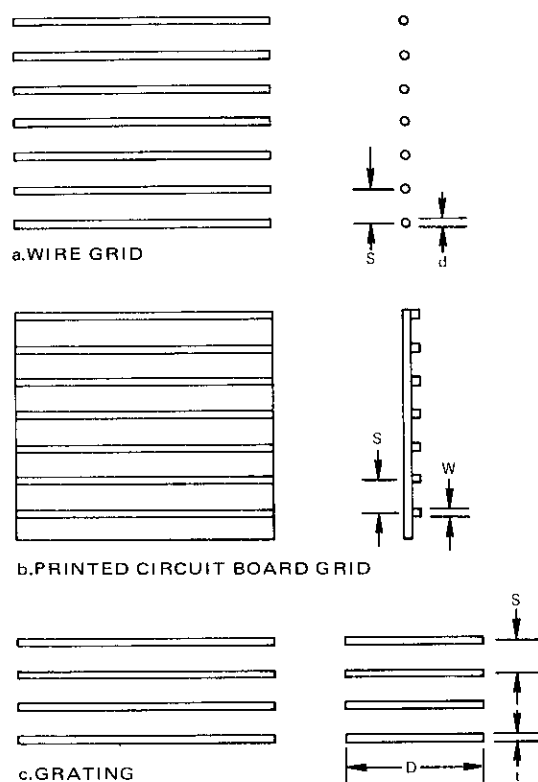


Figure 1. Polarization-Selective Filters

to the grating elements is transmitted through the thin grating elements with negligible loss. The transmission and reflection characteristics of grids and gratings are summarized in Appendix A.

Figure 2a shows a grating in front of both the feed and the reflector. This configuration ensures low cross polarization in the secondary beam of the antenna since all depolarization sources are shielded by the grating. Scattering and diffraction from the edge of the grating may limit the

performance achieved. In Figure 2b the grating is placed between the feed and the reflector in a more advantageous mechanical position. Performance is then limited by scattering from the feed and feed support mechanism and reflection of the incident cross-polarized feed energy by the grating. Also, cross-polarized energy between the reflector and grating may resonate and cause serious degradation of the isolation performance. This effect will be discussed further in the section on measured results.

Figure 2c shows an offset reflector configuration which is mechanically advantageous for spacecraft applications and also eliminates the depolarization caused by feed scattering. Offset reflector configurations increase the amount of cross-polarized energy incident upon the grating and the possibility of a resonance.

"Dual-mode" [2] or wide-bandwidth feed designs (spanning both the up- and down-link frequencies) permit the generation of multiple coincident beams from a single reflector. These options will generally compromise the gain or angular coverage performance of the antenna system.

Polarization-selective reflecting surfaces

Figure 3 shows antenna configurations using polarization-selective reflecting surfaces. This design technique uses the grid or grating as the reflecting surface for the desired polarization. The cross-polarized component is transmitted through the surface.

The polarization isolation achieved with reflecting surfaces is less than that attained when the same surface is used as a transmission filter. This is particularly true of the gridded reflector shown in Figure 3a, where the finite wire diameter reflects cross-polarized energy as a focused beam. The improvement in polarization isolation for a polarization-selective reflecting surface relative to a solid metal surface reflector is equal to the return loss of the surface to the cross-polarized signals [return loss = $-20 \log_{10}$ (reflection coefficient)]. The backup structure and the dielectric constant of the substrate that hold the wires contribute to the return loss.

The return loss of the grating reflector shown in Figure 3b is substantially higher than that of the gridded reflector shown in Figure 3a. This results in improved polarization isolation.

Polarization-selective transmission filters and reflecting surfaces

Antenna configurations using both polarization-selective transmission filters and reflecting surfaces permit in-line stacking of two reflector systems and hence minimize the required launch vehicle shroud dimensions.

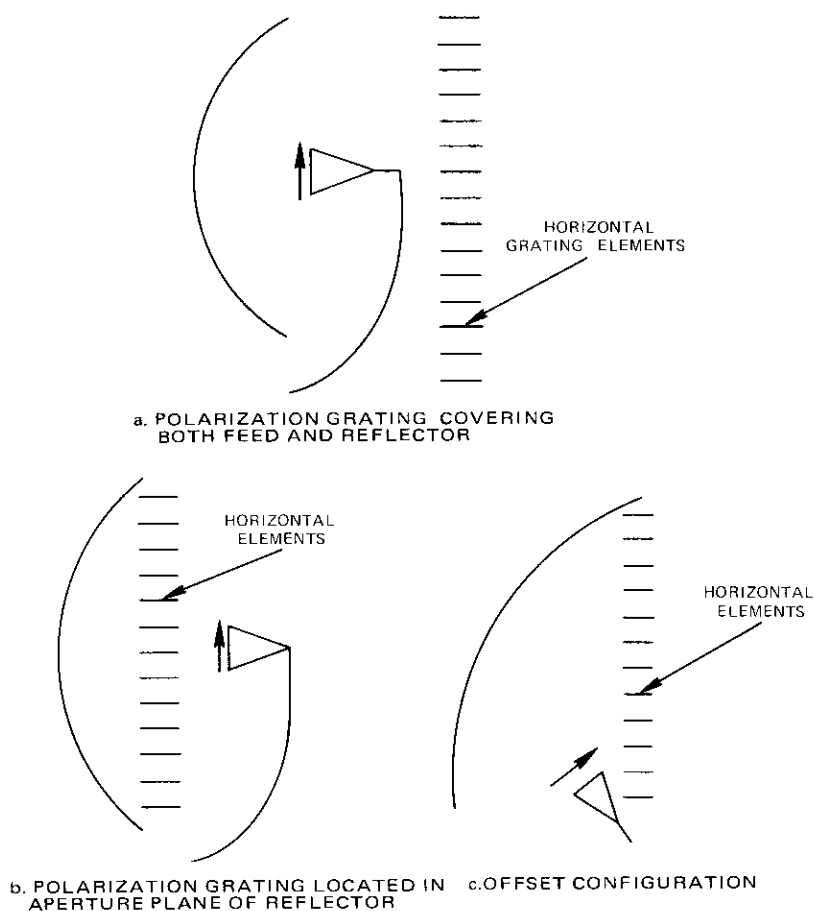


Figure 2. Transmission Filter Configurations

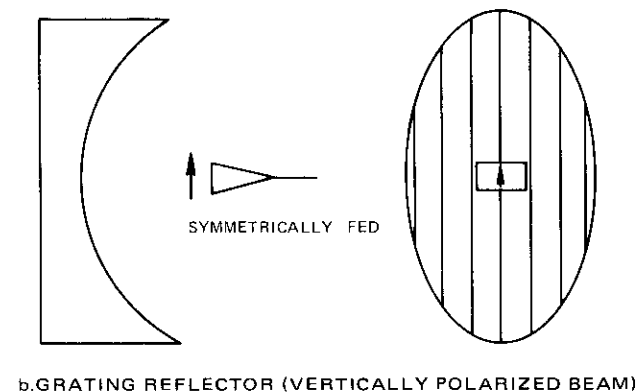
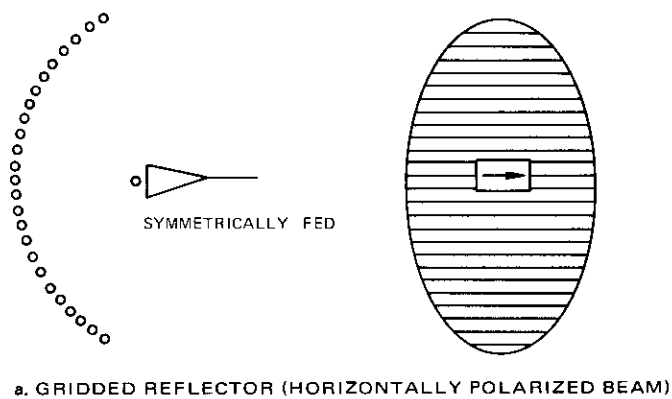


Figure 3. Polarization-Selective Reflecting Surfaces

In Figure 4a the front reflector surface is formed by a grid which acts as both a polarization-selective reflecting surface for the horizontally polarized signal, and as a polarization-selective transmission filter for the vertically polarized back reflector system. The back antenna can be a solid or polarization-selective surface. The polarization isolations achieved for each beam in this reflector arrangement are lower than those of the equivalent individual reflector systems because of increased scattering and blockage effects.

These effects are minimized in the offset reflector system shown in Figure 4b. However, a portion of the feed energy intended for the back

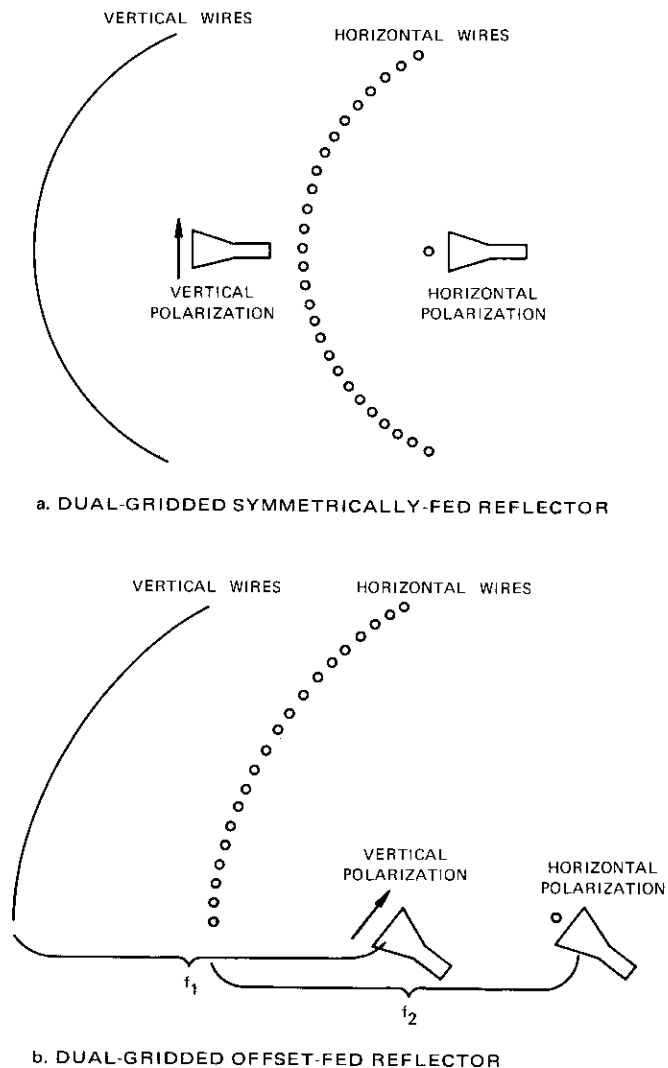


Figure 4. Dual Gridded Reflectors

reflector is intercepted by the front reflector. This intercepted energy appears as a squinted and defocused beam which combines with the beam from the back reflector to result in frequency-sensitive beam squint. The

amount of beam squint depends upon the focal point displacements of the two reflector systems and the return loss of the front reflecting surface.

Cylindrical parabolic reflector with line source feeds

A cylindrical parabola fed by a vertically or horizontally polarized line source feed theoretically generates no cross polarization. This design approach has been evaluated in a separate COMSAT study [3]. Independent controls of two reflector dimensions permit an arbitrary principal plane beamwidth ratio. A design difficulty is the realization of the required line source feed characteristics.

Parabolic reflectors with Huygens source feeds

A parabolic reflector provides an aperture plane stereographic projection of feed system polarization characteristics [4]. Since angular relationships between polarization components incident upon the parabola from the feed are preserved upon reflection, the desired aperture plane polarization characteristics are determined by the feed properties. The feed element with the specific polarization character required to yield good secondary beam polarization isolation characteristics from a parabola is a Huygens source [5], which will be discussed in Appendix B.

Coincident beams on orthogonal linear polarizations are generated from a single reflector with Huygens source feeds. Electrically small, open-ended, circular waveguides provide the required feed characteristics over an up- or down-link 500-MHz bandwidth. These small-diameter feeds provide several unique design capabilities. Arrays of Huygens source feeds with independent amplitude and phase excitations may be utilized to form shaped-beam contours or offshore spot-beam coverages with high polarization isolation.

Polarization orthogonality is established in the feed system; therefore, secondary beam polarization isolation characteristics are relatively insensitive to reflector-feed misalignments or mechanical distortion of the reflector surface. This design approach, which is used with symmetrical reflectors, results in a mechanically simple and lightweight spacecraft antenna system. However, the feed and feed support blockage limit the antenna system polarization isolation.

Measurement techniques

An important consideration in the COMSAT design study has been the establishment of measuring techniques which fully characterize an orthog-

onally polarized communications satellite antenna system. Figure 5 shows a polarization ellipse at a given angular coordinate in the beam contour. The polarization characteristics of a wave may be specified by several equivalent methods [6]. Specifically, the polarization ellipse may be measured by rotating a linearly polarized antenna to determine the ratio of the major axis voltage amplitude to the minor axis voltage amplitude (axial ratio $\equiv E_{max}/E_{min}$) and noting the angle of the voltage maximum relative to a reference axis (ellipse orientation angle $\equiv \tau$). Equivalently, the relative amplitude and phase of two orthogonal signal components, i.e., $g \equiv |\tilde{E}_x|/|\tilde{E}_y|$ and $\epsilon = \angle \tilde{E}_x - \angle \tilde{E}_y$, can be measured to establish the polarization ellipse.

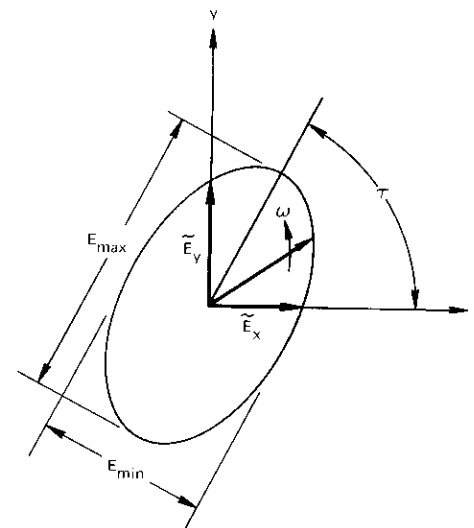


Figure 5. Polarization Ellipse Parameters

Information channels at the same frequency in a dual-polarized system remain independent at a given angular coordinate in the beam as long as the signals are orthogonally polarized. Antenna depolarization effects do not necessarily imply deorthogonalization of the signals [7], [8]. As an extreme example, the conversion of orthogonal linear polarizations to orthogonal circular polarizations (right- and left-hand circular polarizations) can be viewed as a depolarizing effect, yet the signals are still orthogonally polarized.

In a linearly polarized communications satellite system in which the earth station receiving (or transmitting) terminal is a pair of orthogonal linear probes, the polarization isolation between signals at the same frequency is related to their axial ratios and relative ellipse orientations. It is important to note that the axial ratio is a measure of polarization isolation only in the special case in which the difference between the orientation angles of the polarization ellipses is precisely 90° . The orthogonal linear probes of the earth station antenna are represented in the measuring setup by an orthogonal mode transducer (OMT) used as a transmit or receive boresight.

The polarization characteristics of antenna systems with coincident beams are measured most directly by specifying the antenna's carrier-to-interference power (C/I) ratio at a given angular coordinate in the beam. This representation includes the pattern factor for the principally polarized beam. One port of the satellite antenna system is excited to produce the carrier power response at the earth station OMT port, and the orthogonal satellite antenna system port is excited to produce the interference power response. The procedure is then repeated for the orthogonal earth station OMT port. It is important to note that the earth station OMT ports should not be rotated to individually optimize the C/I ratio which appears at a single port. This will generally result in a degradation of the C/I ratio in the orthogonal port. In practice the earth station OMT port orientations at a given point in the satellite antenna coverage contour are chosen to minimize a balanced C/I ratio in the two ports.

Swept frequency measuring techniques are used to evaluate polarization characteristics. Antenna systems typically have several distinct depolarization sources. Depolarizing test range reflections and boresight source characteristics can also affect the measured polarization characteristics. The effect of these multiple sources can be extremely frequency sensitive over the up- and down-link bands.

In conventional antenna test procedures, the frequency is fixed and radiation patterns are taken in principal planes and other planes which allow accurate construction of the copolarized and cross-polarized beam contours. Pattern measurements are generally performed at several discrete frequencies within a 500-MHz bandwidth. This results in a complete spatial but limited frequency representation of the radiating characteristics of the antenna. Interpolation between measured frequency points is then required.

Throughout the design studies the polarization response has been measured at discrete spatial positions with the frequency swept across a

500-MHz band. The response of the antenna is then known for every frequency in the band at given angular coordinates in the beam contour. Measurements at successive angular coordinates will accurately establish the copolarized and cross-polarized contour patterns. Interpolation between angular coordinates is then required. The antenna C/I response varies smoothly with angular coordinates when worst-case swept frequency data are used.

Polarization characteristics are more accurately determined by interpolating between spatial intervals rather than frequency intervals, as demonstrated by actual measured data shown in Figures 6 and 7. Of particular interest to the system designer is the worst-case C/I in the frequency band for the satellite antenna(s) at various points in the beam contour. Figure 6 is a swept frequency display of the carrier and interference power of the antenna under test at an angular location in the beam contour specified by θ_{N-S} and θ_{E-W} . The worst-case C/I ratio (35 dB) in the 500-MHz frequency interval is plotted at the appropriate angular location in the beam contour referenced in Figure 7. The average C/I ratio across the bandwidth may be considerably higher than this worst-case value. Figure 7 shows that the contours of worst-case C/I ratios measured at 1° intervals in the beam coverage area are systematic and smoothly varying. Swept frequency C/I data (Figure 6) can be displayed

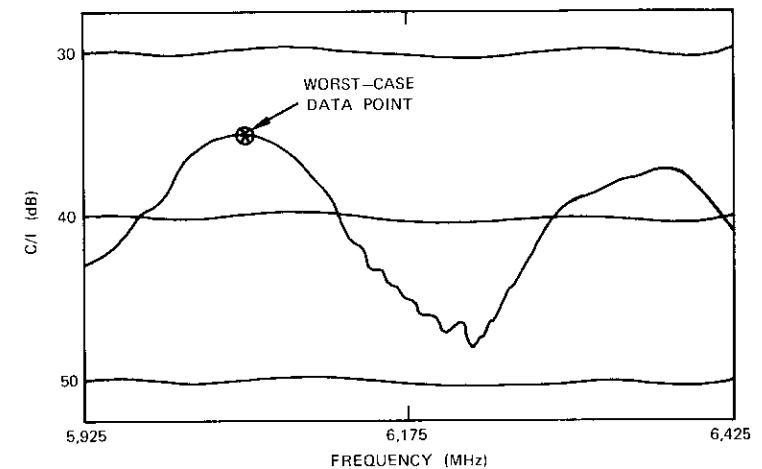


Figure 6. Swept Frequency Carrier-to-Interference Level at $\theta_{N-S} = 1^\circ$, $\theta_{E-W} = -3.0^\circ$

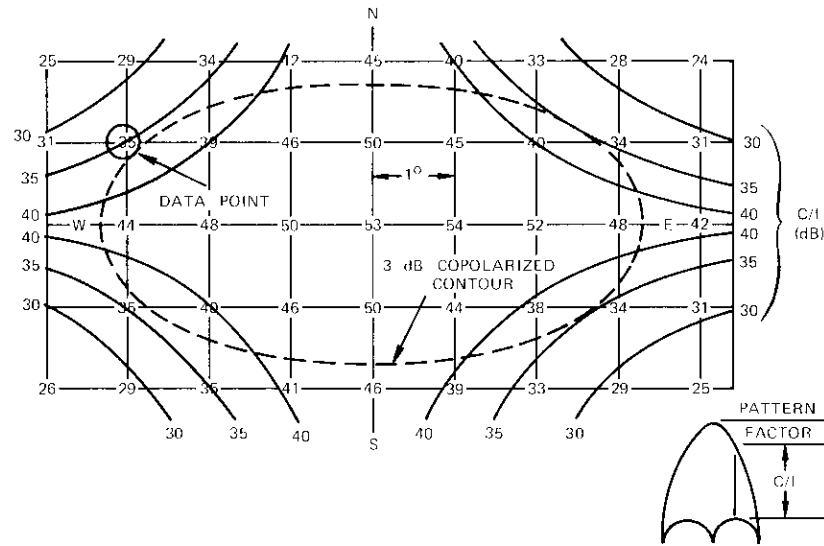


Figure 7. Carrier-to-Interference Contour (worst-case swept frequency)

on an oscilloscope or network analyzer and the worst-case value plotted on the contour. This test setup is shown in Figure 8.

Figure 6 also shows the necessity for swept frequency measurements. The standard technique of measuring low-, mid-, and high-frequency performance yields C/I levels of 43, 45, and 41 dB, respectively. However, the worst-case value (35 dB) is considerably lower. Worst-case C/I data presented in Figure 7 represent the lower bound on antenna system performance.

The peak and edge-of-beam gain and input VSWR are also measured by using swept frequency techniques. Frequency-sensitive beam squint must be evaluated when multi-element feeds, offset reflectors, feeds capable of supporting higher order electrical modes, and polarization grids or gratings are used. Frequency-sensitive beam motion may significantly reduce the gain to prescribed coverage areas.

Frequency-sensitive beam squint is measured by comparing the received power at symmetrically displaced off-axis angles (or coverage contour points). As the frequency is swept across a 500-MHz band, received power variations of alternate sign indicate beam squinting. The power

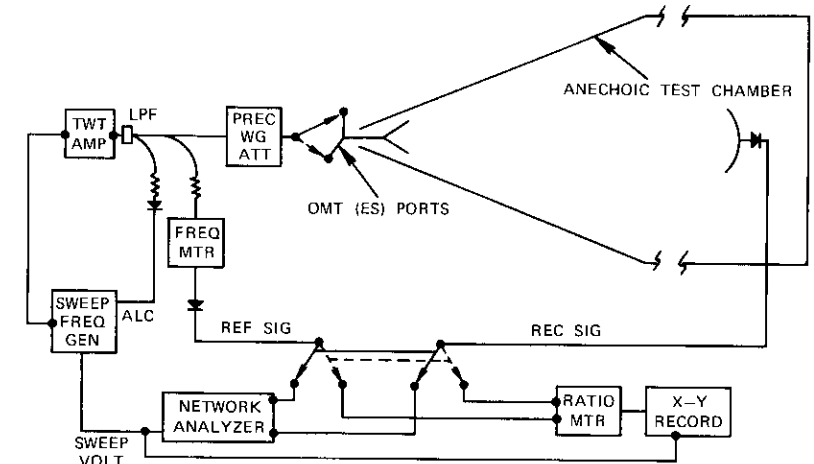


Figure 8. Test Setup for Measuring Swept Frequency Carrier-to-Interference Ratio, Gain, and Beam Squint

received relative to that of a calibrated standard-gain horn is used to determine the edge-of-beam gain.

Measured results

Polarization-selective transmission filters

A 21- × 42-in. (53- × 106-cm) solid surface parabolic reflector with a 16.4-in. (42-cm) focal length was fabricated as a baseline antenna. Two rectangular-aperture sectoral horn feeds were designed to orient the feed polarization along the major and minor axis of the elliptical reflector, respectively. The secondary half-power beamwidths at 6 GHz were nominally $3.5^\circ \times 7.0^\circ$, approximating coverage of the contiguous U.S. The measured results were essentially the same for either feed polarization.

All measurements were conducted in the anechoic test chamber at COMSAT Laboratories. Swept frequency cross-polarized field probe measurements of the anechoic chamber test zone established a 50-dB polarization measurement limit. Worst-case C/I contours for the baseline antenna measured over a swept frequency 500-MHz bandwidth are presented in Figure 9. The contours show high isolation in the principal planes and four balanced lobes, as expected for a reflector with quadrant

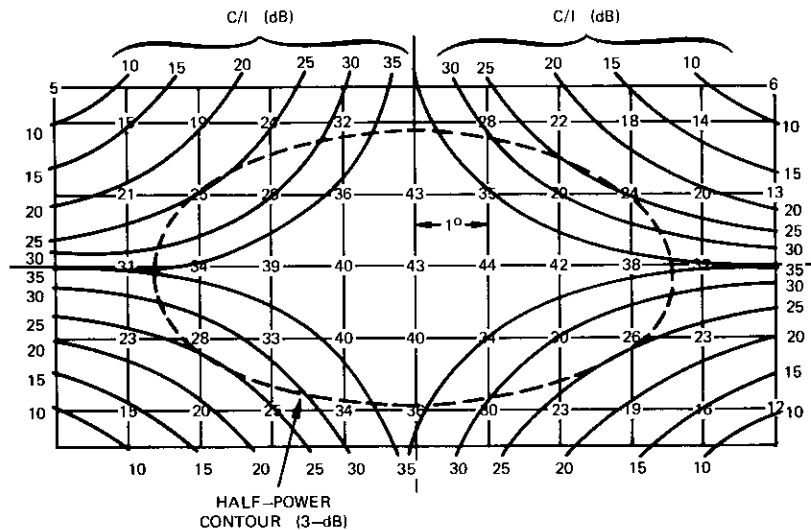


Figure 9. Carrier-to-Interference Contour (worst-case swept frequency) for Solid Metal Reflector (baseline design)

symmetry. The worst-case C/I is 25 dB at the edge of the half-power beam contour (-3 dB). The measured interference power is -28 dB and the carrier power is -3 dB relative to beam peak, yielding a net C/I of 25 dB. These data are used to determine the improvement obtained by placing a polarization-selective transmission filter in front of the antenna.

The measured polarization characteristics of the baseline antenna design are in excellent agreement with calculated values obtained by using measured feed data and the analysis presented in Appendix B. Antenna analysis programs which integrate vector surface currents on the reflector surface, obtained from calculated feed properties, also give excellent agreement with measured results [8].

A polarization grating was placed in front of the antenna to cover both the feed and the reflector, as shown schematically in Figure 2a. A bread-board grating was constructed by interleaving 16-mil aluminum strips and 0.5-inch (1.27-cm) styrofoam strips. The depth in the direction of propagation was 1 inch (2.54 cm). Figure 10 shows that the C/I ratio was in excess of 43 dB everywhere within the -3 -dB coverage contour. The reduction of C/I away from beam center was primarily a result of the carrier signal pattern factor. The interference levels obtained were near the measurement limit of the anechoic test chamber. Similar results

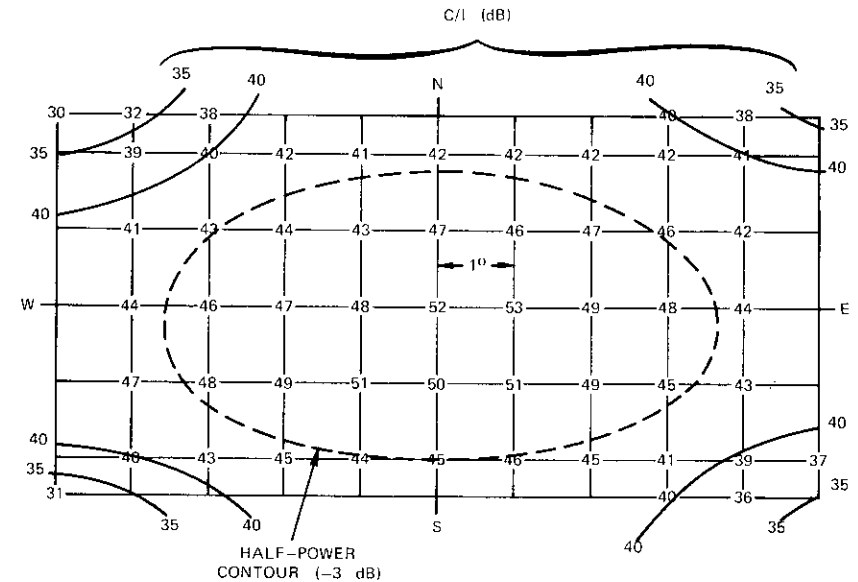


Figure 10. Carrier-to-Interference Contour (worst-case swept frequency) for Baseline Antenna Covered with Grating

were obtained when a grid ($w = 10$ mils, $S = 50$ mils) was used in front of the antenna. Tests were made in both polarizations using grids and gratings to cover the entire reflector-feed system. Worst-case C/I values were in excess of 43 dB over the entire coverage contour for all configurations tested.

Figure 11 shows the principal plane patterns of a continental U.S. beam at 5,925, 6,175, and 6,425 MHz with the grating covering the entire feed-reflector system. Radiation patterns show no change when the grid or grating is added to this antenna system.

A swept frequency power response at the peak and symmetrically disposed off-axis angles is shown in Figure 12 for the antenna configuration with a grating. A standard-gain horn calibration allows the absolute gain to be determined on a swept frequency basis. The nearly identical sweep data measured at the two off-axis angles (0° , $\pm 3.5^\circ$) indicate virtually no frequency-sensitive beam motion. The peak and edge-of-beam gains are plotted in Figure 13. Aperture and beam efficiencies for the symmetrically fed, electrically-small apertures (10λ – 25λ) tested range from 50–60 percent.

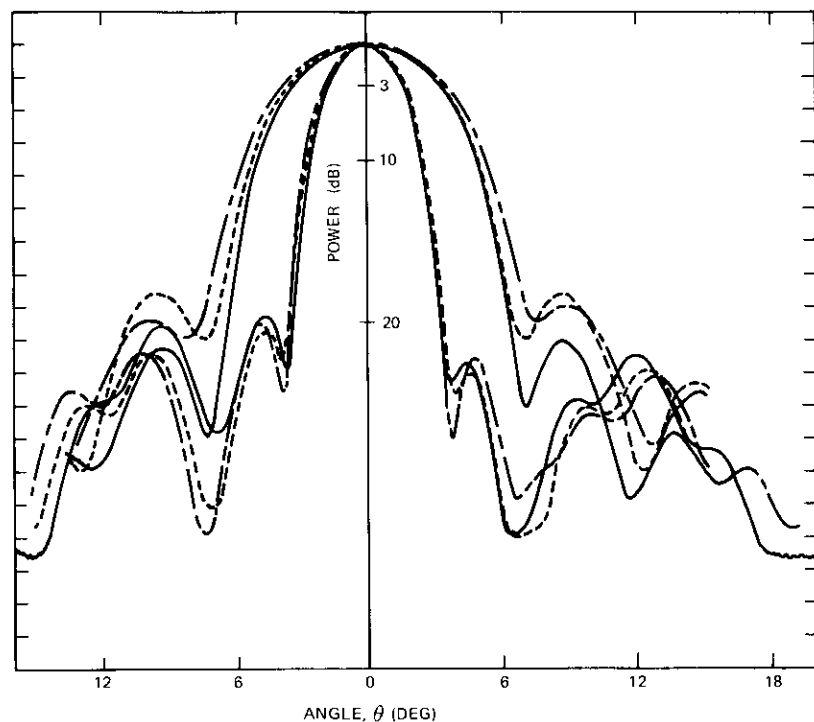


Figure 11. North-South and East-West Patterns for Baseline Antenna Covered with Grating (low, mid, and high frequencies)

The gain loss contributions of the grids or gratings were also measured on a swept frequency basis. The grating gain loss was less than 0.1 dB. The grid gain loss was 0.5 dB, which confirms a 10-percent blockage loss prediction (Appendix A). Grids or gratings used as transmission filters yield equivalent polarization performance; however, superior gain performance is obtained with gratings.

A simpler mechanical implementation and a more compact antenna configuration were obtained by moving the grating into the aperture plane of the reflector, as shown in Figure 2b. However, a serious electrical problem was observed during the swept frequency measurements. Cross-polarized energy caused a "cavity" resonance condition between the reflector and screen.

Figure 14a shows a swept frequency C/I measurement at a point in the contour. At the resonant frequencies, serious degradation of the C/I char-

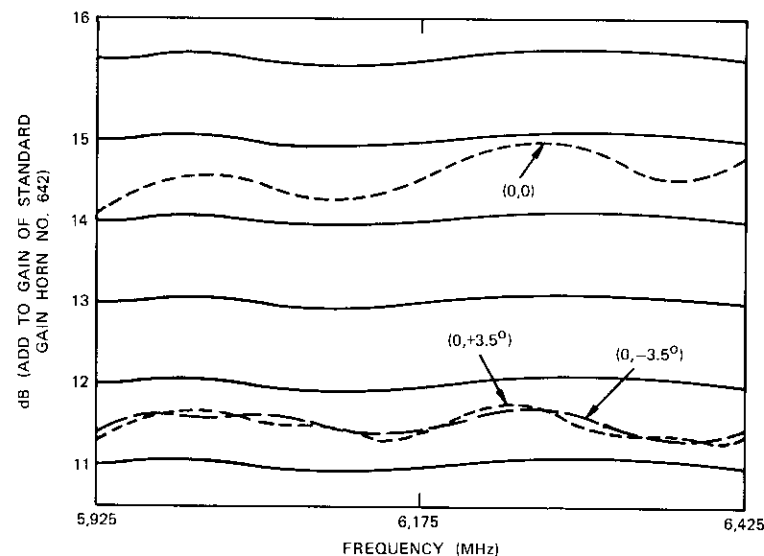


Figure 12. Swept Frequency Peak and Edge-of-Beam Gain Measured Data

acteristics of the screened antenna was observed. To check this theory of resonance, a small amount of RF absorbing material was placed on the reflector surface in areas with high cross-polarization current and the swept frequency measurements repeated. Figure 14b shows that the resonant spikes have essentially disappeared. The absorbing material was used as a diagnostic aid and is not suggested as a solution to the problem. However, the same damping effect could be achieved by designing the reflector as a polarization-selective surface. Measurements of the configuration shown in Figure 2b indicated that its performance was poorer than that of the configuration shown in Figure 2a due to resonances and scattered energy from the feed.

The same resonance condition can appear in the configuration shown in Figure 2a. However, the larger physical spacing between the reflector surface and polarization grating permits a portion of the trapped energy to leak out as wide-angle scatter, thus effectively lowering the "Q" of the resonant cavity. Grating misalignment with the principal polarization of the feed can also give rise to resonance effects. The offset configuration shown in Figure 2c circumvents feed scattering and blockage, but may also support grating-reflector resonances.

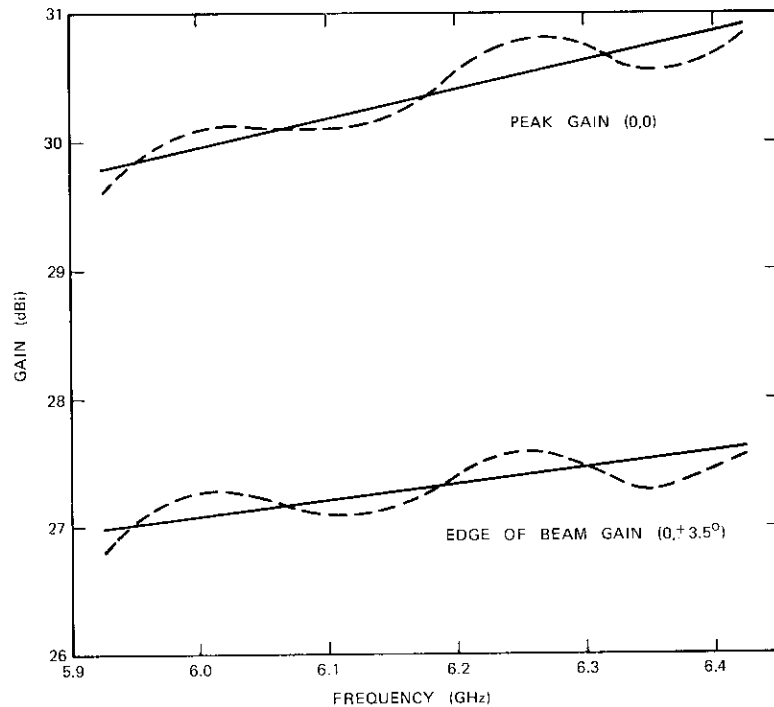


Figure 13. Measured Gain for 21- x 42-Inch Parabolic Reflector with Polarization Grating

Polarization-selective reflecting surfaces

Three different reflectors were constructed to measure the effect of polarization-selective reflecting surfaces. Two 21- x 42-in. elliptically shaped gridded reflectors with a 16.4-in. focal length were fabricated, one with the wires parallel to the major axis and the other with the wires parallel to the minor axis of the reflector. The grid pattern consisted of 17-mil-diameter wires spaced 100 mils apart on a 25-mil-thick fiberglass board. A foam spacer was used to position a second identical fiberglass surface one quarter of a wavelength from the front surface, partially canceling the fiberglass-to-air dielectric mismatch. A grating reflector was also fabricated. The reflector was first cast in urethane foam which was subsequently sliced into 0.5-in. (1.27-cm) strips. The curved arc from each strip was then traced onto a 3-mil-thick piece of copper sheet.

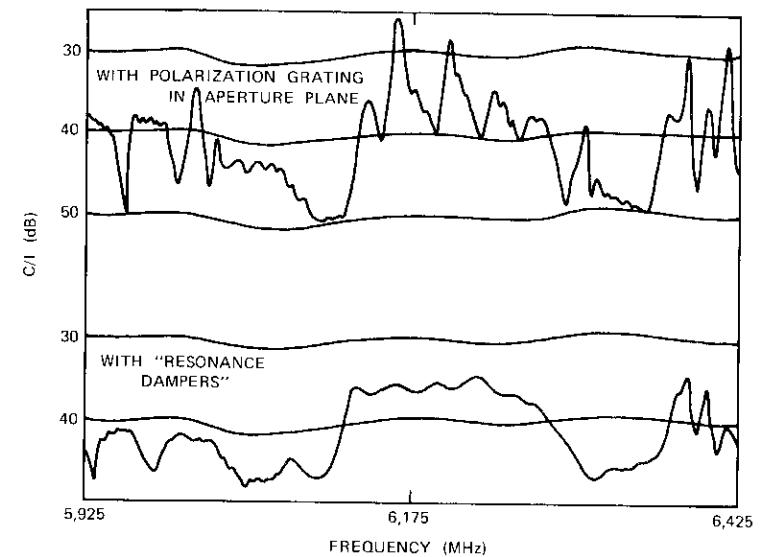


Figure 14. Swept Frequency Carrier-to-Interference for Grating in Aperture Plane with and without "Resonance Damper," $\theta_{N-S} = 1.0^\circ$, $\theta_{E-W} = 3.0^\circ$

Finally, the alternating foam and copper strips were bonded together to form the reflector. The grating depth in the direction of propagation was 1 in. (2.54 cm).

Measured data for the gridded reflector surface indicated a return loss, consisting of both grid blockage and fiberglass reflections, of 9 dB. This return loss represents the maximum polarization improvement for a gridded reflector relative to a solid reflector. The worst-case C/I for the solid reflector was 25 dB at the -3-dB contour. Measurements of the two gridded reflectors indicated worst-case C/I values of 33 dB. The polarization improvement was 8 dB, approximately equal to the return loss of the gridded reflector surface.

The measured return loss of the grating reflector shown in Figure 3b is 18 dB. Measured polarization data indicate a worst-case C/I of 36 dB at the edge of the contour, or an 11-dB improvement over the solid reflector data shown in Figure 9. This improvement is less than the full grating return loss of 18 dB. Feed and feed support scattering limit the performance of this configuration near the 36-dB level. Reflecting objects behind the polarization-reflective surface also tend to degrade performance.

An offset gridded reflector eliminates depolarization due to feed scatter-

ing; however, the inherent cross polarization of the offset reflector is worse than that of a symmetric reflector with the same f/D ratio [9]. An offset reflector constructed with grating elements has the potential of providing excellent polarization isolation for this class of antenna.

The arrangement of reflectors shown in Figure 4 permits in-line stacking of two reflectors to minimize antenna system dimensions. Cross polarization was measured on each of two gridded reflectors arranged as shown in Figure 4a. For the front horizontally polarized reflector, a worst-case C/I of 30 dB over the coverage contour was measured as opposed to a 32-dB C/I when the antenna was tested by itself. The back reflector C/I degraded to 27 dB as a result of the additional scattering from in-line stacking. The offset configuration shown in Figure 4b eliminates a portion of this scattering, but may have increased cross polarization due to other factors described previously.

Antenna systems using polarization-selective surfaces necessarily place orthogonal linear signals on separate antennas. Therefore, careful alignment of the polarizations of these antennas must be established and maintained over in-orbit environmental conditions.

Parabolic reflector with Huygens source feed

A theoretical discussion of the Huygens source feed for symmetrical parabolas is given in Appendix B. The required Huygens source feeds are open-ended circular waveguides with a diameter of 1.375 in. (3.55 cm) in the 6-GHz band. Figure 15 is a schematic representation of the feed assembly. The major and minor axis reflector illumination functions of the arrayed feeds are virtually identical because the E- and H-plane beamwidths of the individual feed elements are the same. Although the feed is operated close to cutoff, the input VSWR is less than 1.3 in both ports, and feed isolation between orthogonal ports is in excess of 47 dB across the band. The parabolic reflector has an elliptic aperture of 21×42 in.

Figure 16 shows the measured east-west and north-south continental U.S. coverage patterns, which are identical for both polarizations. The beams obtained with this approach are narrower than those obtained previously with sectoral horn feeds. However, for normal Gaussian shaped beams, analysis shows that a -4.3 -dB pattern factor maximizes the edge-of-coverage gain. Peak and edge-of-coverage gains at the mid-band frequency are respectively 30.8 and 26.8 dB.

As shown in Figure 17, for the minor axis polarization, the worst-case C/I over the beam contour is 33 dB. Data for the major axis polarization are identical.

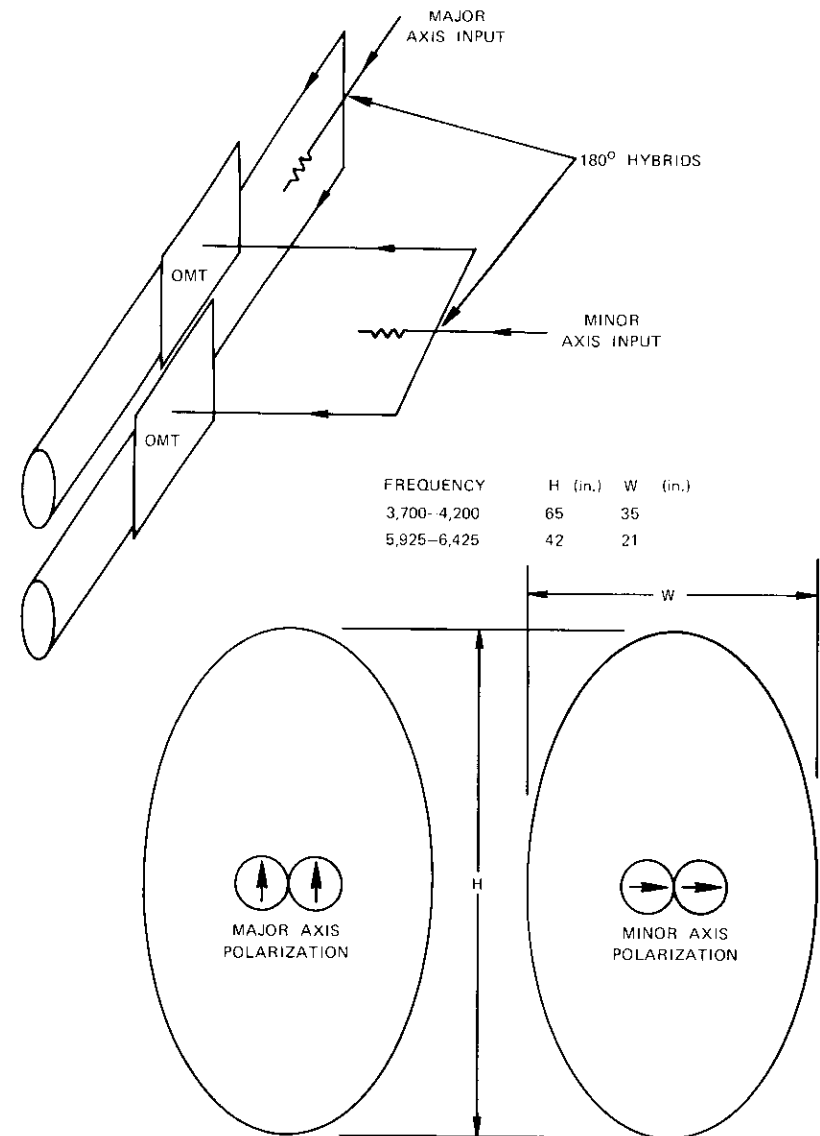


Figure 15. Huygens Source Feed Array

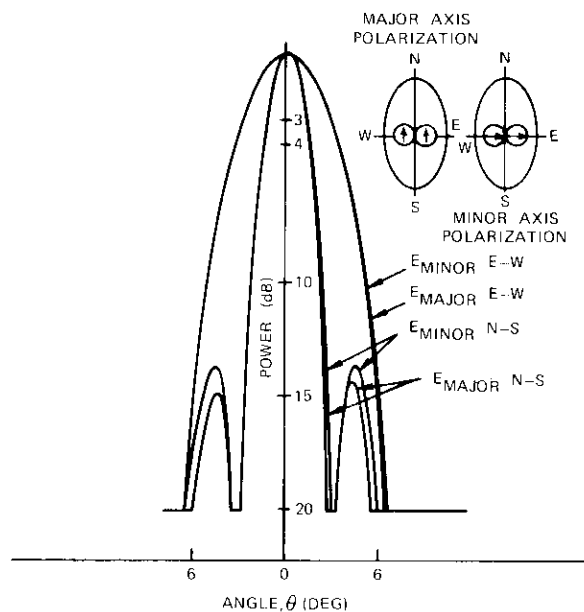


Figure 16. Principal Plane Patterns of 21- x 42-Inch Elliptic Reflector with Huygens Source Feed Array

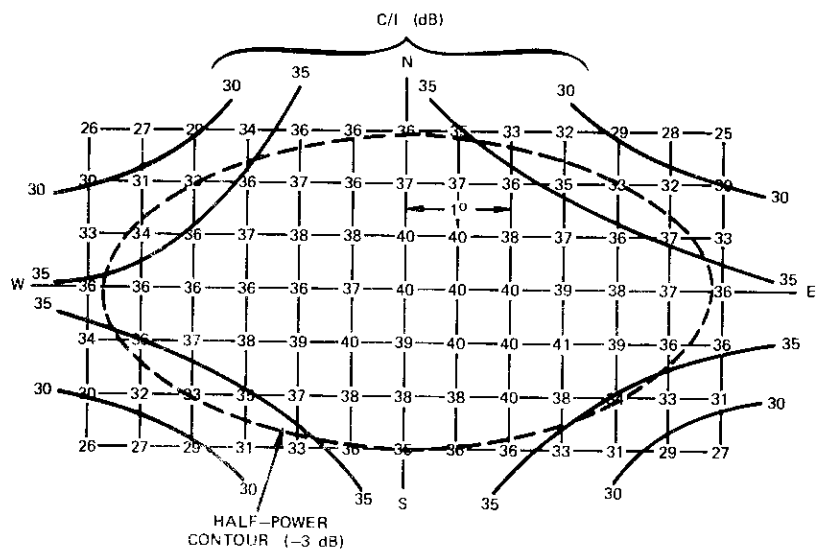


Figure 17. Carrier-to-Interference Contour (worst-case swept frequency) for 21- x 42-Inch Elliptic Reflector with Huygens Source Feed Array

As opposed to conventional antenna designs which provide elliptic contours, parabolic reflectors and arrayed Huygens source feeds are amenable to further beam shaping to provide a nearly rectangular coverage contour which improves the gain coverage characteristic over the continental U.S. Increased aperture area is necessary for this beam shaping and the 21- x 42-in. elliptic reflector is replaced with a 42-in.-diameter circular reflector. A circular reflector fed with two Huygens source feeds is shown in Figure 18a. Each offset feed element launches a squinted secondary constituent beam with low cross polarization, as shown in Figures 18b and 18c. The constituent beams may be added to form a shaped coverage contour with high polarization isolation between shaped beams. In addition, off-shore spot-beam coverage may then be formed on the same circular reflector.

Figure 19 compares a $3.5^\circ \times 7.0^\circ$ elliptic contour beam and the shaped-beam contour over the continental U.S. East-west coast edge-of-beam gains increase, and a gain of 29 dB is realized over the major part of the continental U.S. Figure 19 also shows the offshore beams that may be formed with a single 42-in.-diameter circular reflector at 6 GHz. Additional Huygens source feeds have been located in the focal region to launch the offshore coverage beams. These offset feeds produce beams with wide-angle cross polarization in excess of 30 dB over the continental U.S. Figure 20 shows a worst-case swept frequency cross-polarization contour for the Hawaii spot beam. The cross-polarization levels are relative to the peak copolarized spot-beam gain of 33 dB.

Worst-case data for the continental U.S. shaped-beam system indicate a C/I in excess of 33 dB for both polarizations. When the three additional feeds are added to provide offshore coverage, the worst-case C/I degrades to 28 dB because of the increased scattering of the additional feeds located in the focal region. Integration of the offshore spot-beam feeds onto the same reflector with continental U.S. coverage beam feeds has the advantage of minimizing beam source array effects when the off-shore beam(s) are coupled to the U.S. beam (coupled mode service).

As a practical communications satellite system requirement, four coincident continental U.S. beams (two in each polarization) must be provided in the down-link 4-GHz band. This requirement allows alternate transponder outputs in the satellite to be placed on separate beams, hence greatly simplifying the satellite down-link multiplexing requirement. A single-aperture antenna system suitable for frequency reuse applications can provide four coincident continental U.S. beams and three offshore coverage beams. This system uses two Huygens source feed elements with

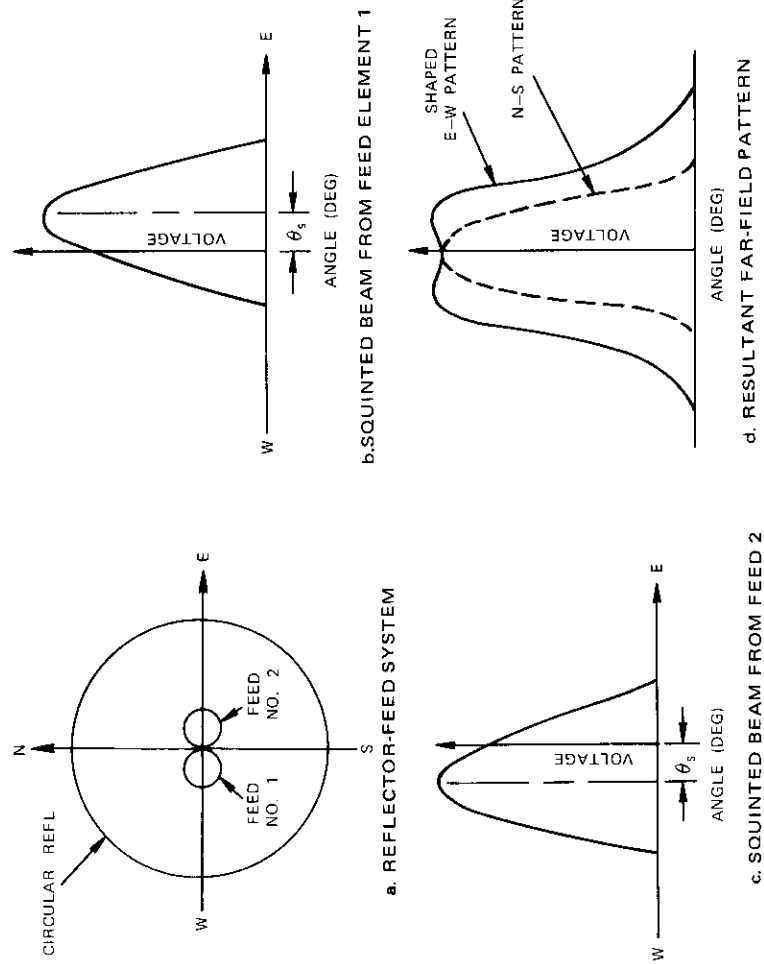


Figure 18. Beam Shaping Using Addition of Squinted Far-Field Beams

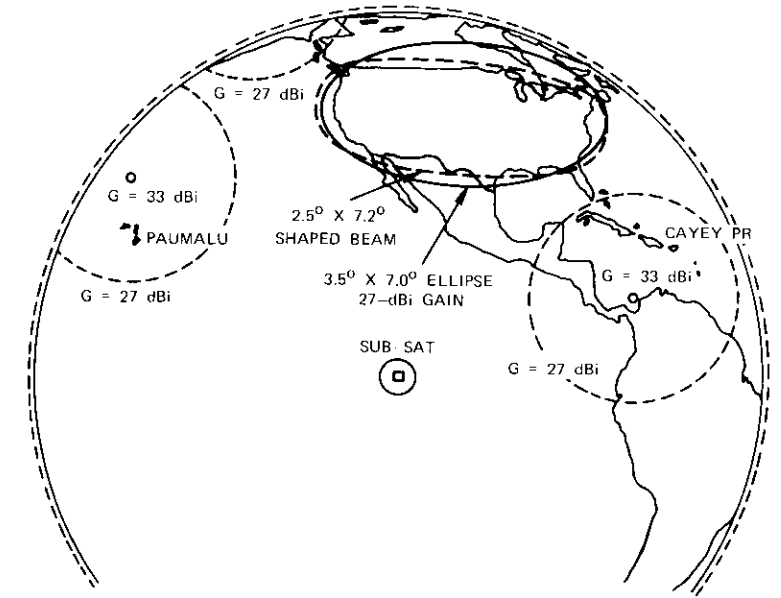


Figure 19. Continental U.S. Shaped and Elliptic Beams and Spot-Beam Locations

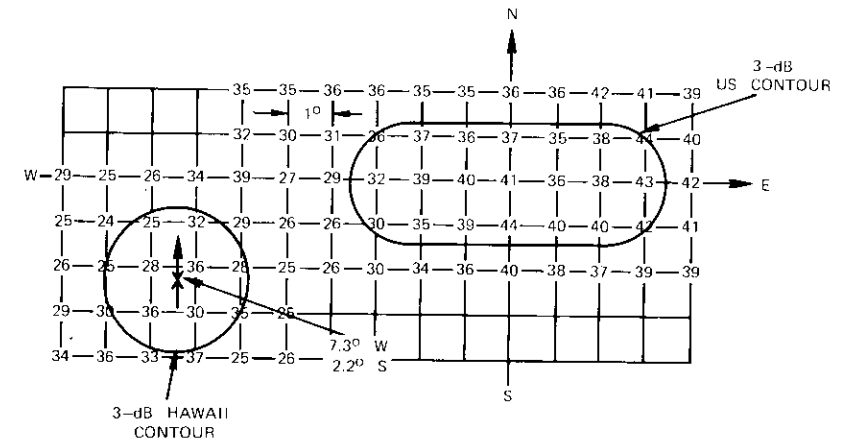


Figure 20. Hawaii Spot-Beam Cross-Polarized Isolation (worst-case swept frequency)

dual polarization and quadrature excitation. The ability to form coincident beams from the same reflector and feed by varying the element phase is referred to as "dual-mode" excitation [2]. A 64-in.-diameter parabolic reflector would be required for the down-link 4-GHz band.

Figure 21 shows the continental U.S. gain contour for all four input ports. The beam contour is derived from measured far-field constituent beam patterns. Improved east-west coast gain is obtained at the expense of reduced gain in the north-south plane at the center of the continental U.S. An additional feed element which provides a beam to the center of the continental U.S. could be used to restore a more rectangular beam contour. Dual-mode beam formation is also possible with a 3-element feed.

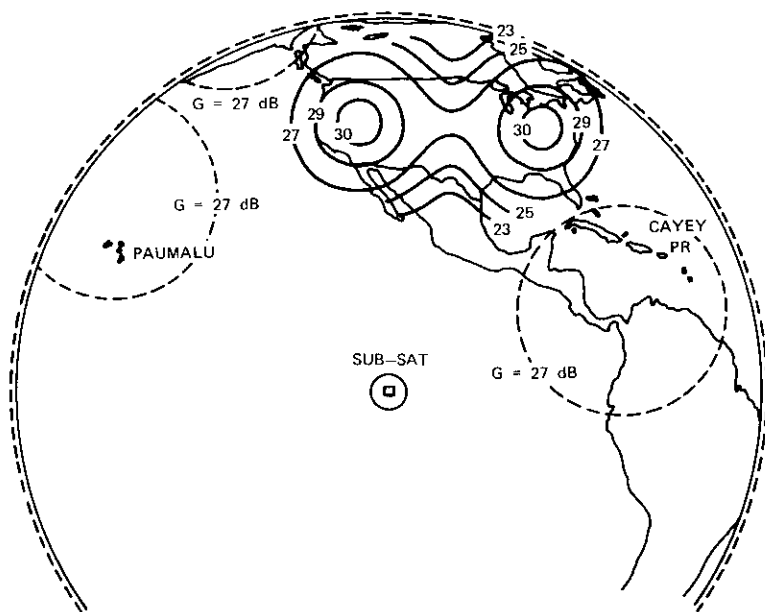


Figure 21. Gain Contour for Quadrature Fed Huygens Source Feed Array in 65-Inch-Diameter Circular Reflector

Conclusion

This paper has described antenna design studies performed at COMSAT Laboratories to provide performance and specification guidelines for a

U.S. domestic satellite. The achievement of 30- to 50-dB antenna system polarization isolations between orthogonal linear polarizations over the entire satellite beam coverage areas permits reuse of the allocated 4/6-GHz frequency spectrum, hence significantly increasing the channel capacity of the satellite.

It has been shown that swept frequency measurement techniques are necessary to completely and accurately characterize the polarization isolation, gain, and frequency-sensitive beam squint properties of the antenna systems. The presence of polarization isolation resonances in antenna designs which use polarization-selective transmission screens can best be ascertained with swept frequency measurement techniques. The polarization isolation performance presented in this report is based on worst-case data and represents a lower bound on antenna system performance.

Two distinctly different design approaches for orthogonal linearly polarized satellite antenna systems have been considered. The first approach uses grid or grating polarization-selective reflection or transmission surfaces and is potentially capable of achieving the higher polarization isolations (35–50 dB). However, because the required spatial orthogonality of the grid or grating elements must be maintained under in-orbit thermal and mechanical loads, the mechanical design is more complex.

Grating surfaces have less electrical blockage than grid surfaces and therefore provide better electrical performance. However, mechanical design considerations are also an important factor in the choice of a particular polarization-selective surface. Feed system blockage which limits the polarization performance achieved in front-fed symmetrical reflector systems may be eliminated by utilizing offset reflector configurations. Broad-bandwidth feed networks and in-line stacking of separate reflector systems are used to increase the number of coincident coverage beams available from limited launch vehicle shroud dimensions.

The second design approach forms coincident orthogonally polarized beams from a single solid surface reflector. Because polarization orthogonality is established in the feed, the thermal and mechanical design of the antenna system is simplified. Worst-case swept frequency polarization isolations achieved over the entire beam coverage areas range from 30–35 dB. The required quadrant reflector symmetry with a Huygens source feed results in feed blockage and depolarization in front-fed configurations. However, the use of separate reflectors for the satellite up- and down-link bands permits optimization of the feed system on a narrowband (500-MHz) basis.

Three interrelated considerations determine a spacecraft antenna

system design: electrical performance requirements, weight and mechanical complexity, and available launch vehicle shroud dimensions. The risk factor associated with various design approaches must be considered. The in-orbit electrical performance ultimately achieved is strongly related to the mechanical and thermal design aspects of the spacecraft antenna system.

References

- [1] R. Briskman, "A Domestic Satellite Design," *IEEE Transactions on Aerospace and Electronic Systems*, AES-7, No. 2, March 1971, pp. 263-268.
- [2] J. A. Janken, W. J. English, and D. F. DiFonzo, "Radiation from Multi-Mode Antennas," *G-AP International Symposium Digest*, 1973, pp. 306-309.
- [3] E. J. Wilkinson, "A Dual-Polarized Cylindrical-Reflector Antenna for Communication Satellites," *Microwave Journal*, Vol. 16, No. 12, December 1973.
- [4] J. Hanfling, "Aperture Fields of Parabolic Reflectors by Stereographic Mapping of Feed Polarization," *IEEE Transactions on Antennas and Propagation*, AP-18, No. 3, May 1970, pp. 392-396.
- [5] I. Koffman, "Feed Polarization for Parallel Currents on Reflectors Generated by Conic Sections," *IEEE Transactions on Antennas and Propagation*, AP-14, No. 1, January 1966, pp. 37-40.
- [6] M. Born and E. Wolf, *Principles of Optics*, New York: Pergamon Press, 1964, pp. 26-28.
- [7] R. W. Kreutel, "The Orthogonalization of Polarized Fields in Dual-Polarized Radio Transmission Systems," *COMSAT Technical Review*, Vol. 3, No. 2, Fall 1973, pp. 375-386.
- [8] V. H. Rumsey et al., "Techniques for Handling Elliptically Polarized Waves with Special Reference to Antennas," *Proc. IRE*, May 1951, p. 533.
- [9] D. F. DiFonzo, W. J. English, and J. A. Janken, "Polarization Characteristics of Offset Reflectors with Multiple Element Feeds," *G-AP International Symposium Digest*, 1973, pp. 302-305.

Appendix A. Polarization characteristics of grids and gratings

Grid and grating configurations act as polarization-selective transmission filters or reflecting surfaces [A1]-[A4]. A grid is designed by establishing conductor widths and spacings to achieve specified values of rejection for one polarization within the electrical blockage constraints of the orthogonal polarization. The measured polarization rejection characteristic of a printed circuit grid configuration in the 5,925- to 6,425-MHz band as a function of the grid electrical blockage

is shown in Figure A-1. Equivalent results for the 3,700- to 4,200-MHz band are established by scaling the dimensional parameters given by the wavelength ratio (≈ 1.5).

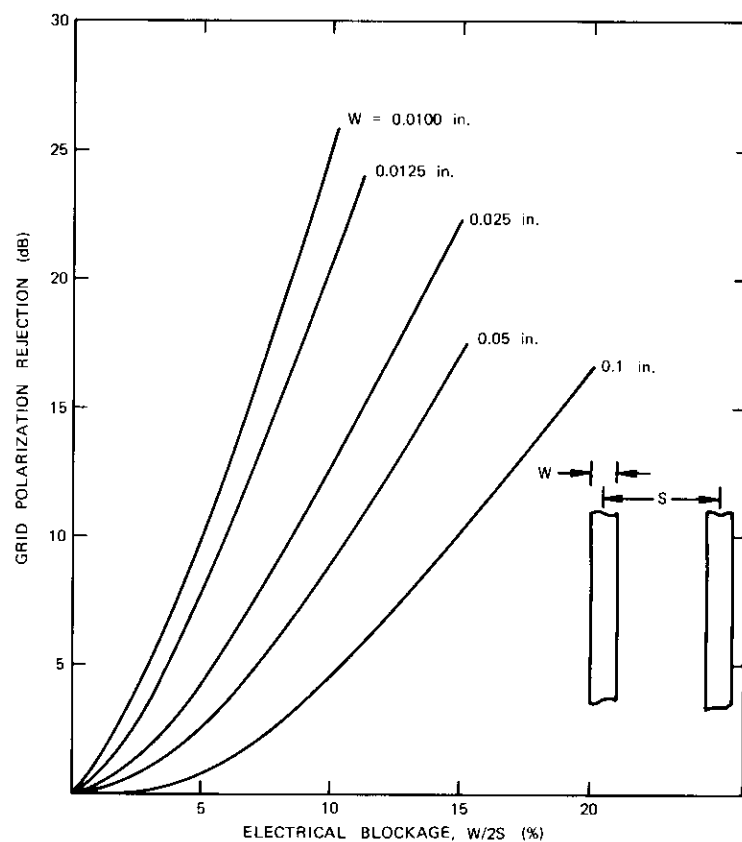


Figure A-1. 6-GHz Grid Polarization Rejection

The attenuation properties of planar polarization gratings have been calculated from a cutoff waveguide analysis. Attenuation versus grating strip spacings, S , and frequency is shown for a fixed grating strip depth, D , of 1.0 in. in Figure A-2, where attenuation in dB increases linearly with D . The attenuation is given by

$$ATT \text{ (dB)} = -8.7 \beta D \quad (\text{A1})$$

where the cutoff waveguide propagation factor is

$$\beta = \sqrt{(\pi/S)^2 - (2\pi/\lambda)^2} \quad (\text{A2})$$

D is the grating depth in the direction of propagation, and λ is the free space wavelength. These attenuation values have been confirmed by experiment. Scattering and diffraction from the edge of a grating or grating-reflector interactions often limit the performance achieved in grated antenna configurations.

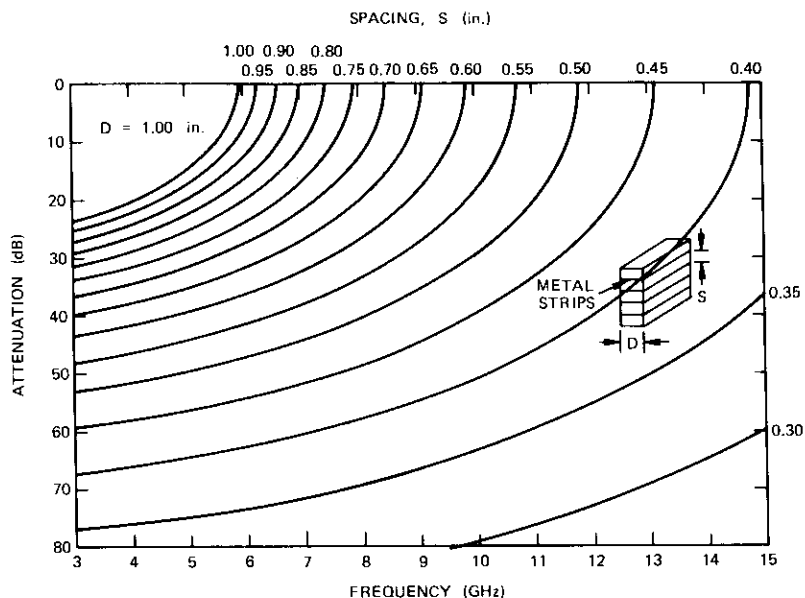


Figure A-2. Attenuation vs Grating Strip Spacing, S , and Frequency ($D = 1.0$ inch)

References

- [A1] T. F. Carlson and A. E. Heins, "The Reflection of an Electromagnetic Plane Wave by an Infinite Set of Plates, Part I," *Quarterly of Applied Mathematics*, Vol. 4, 1947, pp. 313-329.
- [A2] T. F. Carlson and A. E. Heins, "The Reflection of an Electromagnetic Plane Wave by an Infinite Set of Plates, Part II," *Quarterly of Applied Mathematics*, Vol. 5, 1947, pp. 82-88.
- [A3] S. Silver, *Microwave Antenna Theory and Design*, New York: McGraw-Hill Book Company, Inc., 1949, pp. 449-450.
- [A4] R. Collin, *Field Theory of Guided Waves*, New York: McGraw-Hill Book Company, Inc., 1960, pp. 430-438.

Appendix B. Theoretical discussion of parabolic reflectors with Huygens source feeds

The polarization characteristics of reflector antennas have been the subject of considerable study [B1]-[B5]. Reference B5, which provides a simple quantitative representation of the polarization quality required of the feed to eliminate secondary beam cross polarization from a symmetric parabola, is particularly useful.

Figure B-1 shows the basic coordinate system and quantities used to calculate the principal and cross-polarized aperture plane fields of the reflector antenna. Because the *tilde* (or bar) spherical coordinate system designated by $\tilde{\theta}$ and $\tilde{\phi}$ facilitates the wide-angle characterization of the feed polarization on a contour basis, it has replaced the conventional θ, ϕ spherical coordinate system. The measurement coordinate system is easy to implement with either an elevation-over-azimuth or an azimuth-over-elevation test mount.

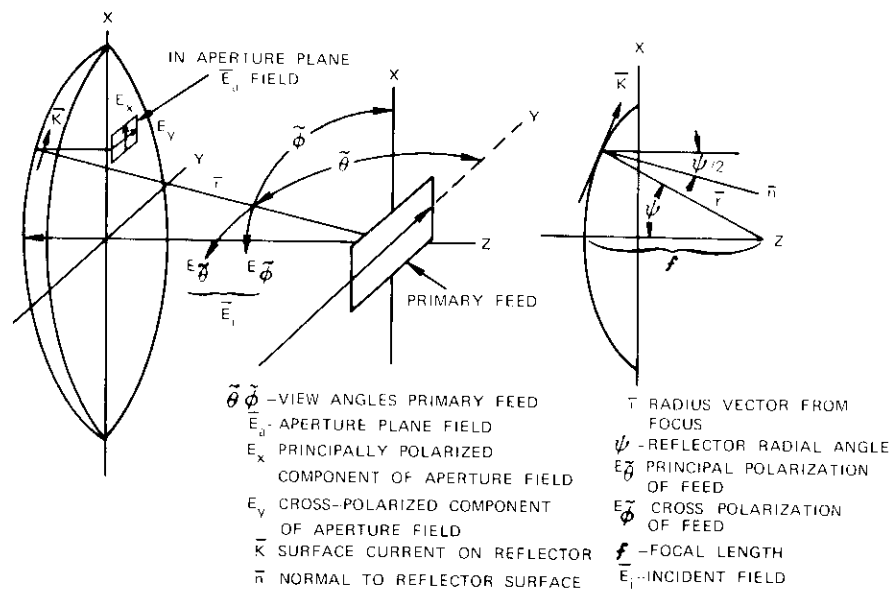


Figure B-1. Coordinate System and Quantities

If a large gently curved reflector surface with an outward normal \hat{n} is illuminated by an incident magnetic field \vec{H}_i propagating in the direction \vec{r} from a point source, a surface current \vec{K} flows on the reflector such that

$$\vec{K} = 2\vec{n} \times \vec{H}_i \quad (B1)$$

Therefore,

$$\bar{K} = \frac{2}{Z_0} (\bar{n} \times \bar{r} \times \bar{E}_i) \quad (B2)$$

For a collimated beam (all rays parallel), the projected electric field in the aperture plane is

$$\bar{E}_a = \frac{\bar{K} Z_0}{2 \cos(\psi/2)} \quad (B3)$$

Therefore,

$$\bar{E}_a = \frac{\bar{n} \times \bar{r} \times \bar{E}_i}{\cos(\psi/2)} \quad (B4)$$

Expressing the incident radiation field \bar{E}_i in terms of primary feed components $E_{\tilde{\theta}}$ and $E_{\tilde{\phi}}$ and writing the unit vector for the reflector normal and radius vector to the reflector results in the following expressions:

$$\bar{E}_y = \frac{\bar{E}_{\tilde{\theta}} (\sin \tilde{\theta} + \sin \tilde{\phi}) + \bar{E}_{\tilde{\phi}} (\cos \tilde{\theta} \cos \tilde{\phi})}{1 + \sin \tilde{\theta} \sin \tilde{\phi}} \left(\frac{f}{r} \right) \quad (B5)$$

$$\bar{E}_x = \frac{\bar{E}_{\tilde{\theta}} (\cos \tilde{\theta} \cos \tilde{\phi}) - \bar{E}_{\tilde{\phi}} (\sin \tilde{\theta} + \sin \tilde{\phi})}{1 + \sin \tilde{\theta} \sin \tilde{\phi}} \left(\frac{f}{r} \right) \quad (B6)$$

For a parabolic reflector,

$$\left(\frac{f}{r} \right) \cdot \frac{1}{1 + \sin \tilde{\theta} \sin \tilde{\phi}} = 1 \quad (B7)$$

Thus, the equations can be simplified to yield

$$\bar{E}_y = \bar{E}_{\tilde{\theta}} (\sin \tilde{\theta} + \sin \tilde{\phi}) + \bar{E}_{\tilde{\phi}} (\cos \tilde{\theta} \cos \tilde{\phi}) \quad (B8)$$

$$\bar{E}_x = \bar{E}_{\tilde{\theta}} (\cos \tilde{\theta} \cos \tilde{\phi}) - \bar{E}_{\tilde{\phi}} (\sin \tilde{\theta} + \sin \tilde{\phi}) \quad (B9)$$

The principally polarized radiation pattern may be calculated by taking the Fourier transform of the reflector aperture \bar{E}_y distribution. This distribution may be approximated by resolving the aperture into a number of small squares and using array theory to calculate the secondary beam. The amplitude of each element in the array is the calculated E_y voltage in a particular square. Similarly, the

cross-polarization radiation pattern may be determined by using the calculated E_x aperture plane voltages.

For a narrow-beam antenna with a feed polarization which yields $E_x = 0$ over the entire aperture plane of the reflector, there will be no cross polarization ($E_{\tilde{\phi}} \approx E_x$) in the secondary beam. Therefore, if $\bar{E}_{\tilde{\theta}}$ and $\bar{E}_{\tilde{\phi}}$ are in time phase and given by

$$\frac{\bar{E}_{\tilde{\phi}}}{\bar{E}_{\tilde{\theta}}} = \frac{\cos \tilde{\theta} \cos \tilde{\phi}}{\sin \tilde{\theta} + \sin \tilde{\phi}} \quad (B10)$$

there will be no secondary beam cross polarization. This is equivalent to requiring an infinite axial ratio and a polarization orientation given by

$$\tau = \tan^{-1} \frac{\cos \tilde{\theta} \cos \tilde{\phi}}{\sin \tilde{\theta} + \sin \tilde{\phi}} \quad (B11)$$

at a given point $\tilde{\theta}, \tilde{\phi}$ in the feed pattern. The infinite axial ratio implies that $\bar{E}_{\tilde{\theta}}$ and $\bar{E}_{\tilde{\phi}}$ are in time phase, which requires coincident E - and H - plane phase centers for the feed [B6]. For a circularly symmetric feed aperture this is equivalent to requiring equal E - and H -plane amplitude and phase patterns.

Complex circular pattern symmetry can be realized with a scalar or corrugated horn, a dual-mode (Potter) horn, flanged or choked circular horns, and electrically-small circular waveguide apertures. The scalar or corrugated horn exhibits excellent performance with respect to equal E - and H -plane beamwidths and coincident phase centers [B7]; however, the necessity of providing many high-order waveguide modes requires the use of electrically large (inefficient) apertures. The large physical size of the corrugated horn results in increased feed blockage and depolarization.

The dual-mode horn [B8]-[B10] also produces equal E - and H -plane beamwidths and coexistent phase centers; however, the bandwidth in which the complex pattern symmetry can be maintained is quite limited.

Choked flanged circular apertures may be thought of as degenerate cases of the corrugated or Potter horn. The patterns approach circular symmetry and the phase centers are coincident over the required 12-percent bandwidth. Choked horns attenuate the currents induced along the outside of the guide which would otherwise reradiate as cross-polarized energy.

Measurements and calculations show that an electrically small ($D \approx 0.7\lambda$) circular waveguide yields equal E - and H -plane beamwidths and coincident phase centers. This is particularly useful, since the wide-angle radiation of the small aperture makes an efficient feed for low- f/D systems. The small aperture size allows close placement of the feeds for multi-element feed arrays used in beam shaping. Feed blockage and subsequent depolarization due to scattering are minimized in the low- f/D systems.

In the absence of interelement coupling, the arraying of Huygens source feeds is a scalar process and permits the generation of multiple beams or shaped beams with low cross polarization. For COMSAT applications, two circular apertures are arrayed side by side to efficiently feed a 2-to-1 aspect elliptic reflector. This provides an elliptic secondary beam with low cross polarization. Each of the two circular apertures is fed by an orthogonal mode transducer (OMT) and a 3-dB power divider to provide polarizations perpendicular and parallel to the major axis of the elliptic reflector. Since the *E*- and *H*-plane beamwidths of the individual array elements are identical, the same reflector amplitude illumination function is obtained for both polarizations when the circular waveguide elements are arrayed. This is a unique aspect of the circularly symmetric Huygens source feed design approach.

References

- [B1] V. Kerdelmelidis, "A Study of Cross-Polarization Effects in Parabolic Antennas," California Institute of Technology, Antenna Laboratory, Technical Report 36, May 1966.
- [B2] E. M. T. Jones, "Parabolic Reflector and Hyperbolic Lens Antenna," *IRE Transactions on Antennas and Propagation*, AP-2, July 1954, pp. 119-127.
- [B3] I. Koffman, "Feed Polarization for Parallel Currents on Reflectors Generated by Conic Sections," *IEEE Transactions on Antennas and Propagation*, AP-14, No. 1, January 1966, pp. 37-40.
- [B4] D. F. DiFonzo, "Offset and Symmetrical Reflector Antennas—Polarization and Pattern Effects," M. S. Thesis, California State University, Northridge, California, 1972.
- [B5] L. E. Raburn, "The Calculation of Reflector Antenna Polarized Radiation," *IRE Transactions on Antennas and Propagation*, AP-8, January 1960, pp. 43-49.
- [B6] E. Muehldorf, "The Phase Center of Horn Antennas," *IEEE Transactions on Antennas and Propagation*, AP-18, No. 6, November 1970, pp. 753-760.
- [B7] H. C. Minnett and B. Maca Thomas, "A Method of Synthesizing Radiation Patterns with Axial Symmetry," *IEEE Transactions on Antennas and Propagation*, AP-14, 1966, pp. 654-656.
- [B8] P. D. Potter, "A New Horn Antenna with Suppressed Sidelobes and Equal Beamwidths," *Microwave Journal*, Vol. 5, June 1963, pp. 71-78.
- [B9] R. H. Turrin, "Dual Mode Small-Aperture Antennas," *IEEE Transactions on Antennas and Propagation*, March 1967, pp. 307-308.
- [B10] T. Satoh, "Dielectric-Loaded Horn Antenna," *IEEE Transactions on Antennas and Propagation*, AP-20, No. 2, 1972, pp. 199-201.

Robert Gruner received his B.S. degree in electrical engineering from Northeastern University in 1962. From 1962 to 1969 he was employed by General Telephone and Electronics working on radar antennas, satellite antennas, and earth station microwave and antenna design. In 1969 he came to COMSAT, where he is presently a member of the Antennas Department of the Microwave Laboratory, working primarily in the area of dual-polarized antennas and associated microwave components. He is a member of Tau Beta Pi and Eta Kappa Nu.



Washington University.

Dr. English is a member of the GMTT and APS sections of the IEEE and also plans to be a charter member of the over-moded waveguide society when it is formed.

William J. English is a member of the Antennas Department at COMSAT Laboratories. Born in Oil City, Pennsylvania, he received mathematics and electrical engineering degrees with honors in 1964. In 1969 he earned the Ph.D. degree in Applied Space Sciences at Carnegie-Mellon University, where he was a Teaching Fellow. He is presently on the professional staff at the Department of Electrical Engineering and Computer Sciences at George

Index: tunnel diodes, standards, stress analysis, creep properties.

Prescreening techniques for flight Germanium tunnel diodes

P. L. FLEMING

(Manuscript received March 15, 1974)

Abstract

This paper presents the results of an investigation to develop, test, and verify screening criteria for flight tunnel diodes. Diodes of various types were subjected to step stress (time and temperature) testing. The failure mode in diodes with contact mesh supports was found to be characteristic of the creep failure mode investigated previously at COMSAT Laboratories.

The results of a special life test confirm the usefulness of prescreening. The screening procedure has been incorporated in the INTELSAT IV-A program as well as the ATS-F transponder program at COMSAT Laboratories.

Introduction

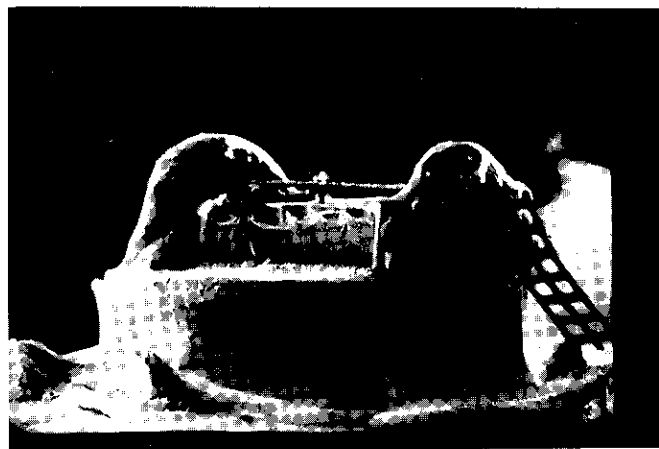
In early 1969, because of difficulties with tunnel diode amplifiers in INTELSAT III, the Applied Sciences Laboratory of COMSAT Laboratories launched a research program to elucidate the failure mechanism in germanium (Ge) tunnel diodes. In this work, tunnel diodes of various types were subjected to step stress (time and temperature) testing. It was shown

This paper is based upon work performed in COMSAT Laboratories under the sponsorship of the International Telecommunications Satellite Organization (INTELSAT). Any views expressed in this paper are not necessarily those of INTELSAT.

that the failure mode in diodes with contact mesh supports was increased valley current associated with the generation of defects near the junction during mechanical creep [1]. Further insight into the nature of tunnel diode p-n junctions was obtained by developing techniques to measure junction capacitance in the negative resistance regime of the I-V characteristic [2] as well as from electron microprobe and electron microscope analysis [3]. As a result of this work, prescreening criteria were developed for flight Ge tunnel diodes. A long-term life test verified the merits of the prescreening technique and the step stress results. The results of this test are reported here.

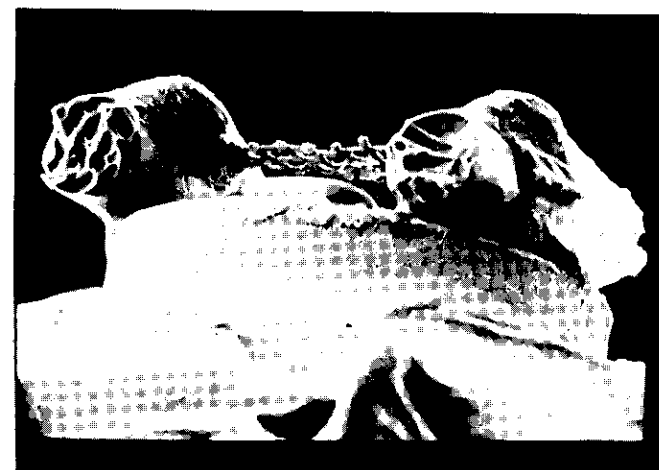
Step stress results

Microwave ball alloy tunnel diodes are unique among microwave solid-state devices in that they are available with and without mesh supports. Because of the small junction diameters ($\sim 2.5 \mu$), flight diodes are often supplied with mesh supports as a constructional feature. These supports are fairly massive compared to the tunnel diode pinnacle, and their differential thermal expansion relative to Ge plays an important role in stressing



71 μ

Figure 1a. SEM Picture of Ge Tunnel Diode with Glass Rod Supports



60 μ

Figure 1b. SEM Picture of Ge Tunnel Diode with Epoxy Supports

the junction. Figures 1a and 1b are scanning electron micrographs of diodes with glass rod supports and epoxy mesh supports, respectively. The thermal expansion coefficient of a general-purpose epoxy such as Ecobond 51 is $50 \times 10^{-6} \text{C}^{-1}$, while that of the glass ($\sim 3.9 \times 10^{-6} \text{C}^{-1}$) presents a better match to that of germanium ($\sim 5.7 \times 10^{-6} \text{C}^{-1}$). Diodes without mesh supports are available on request and have been incorporated into the step stress testing.

Diodes of the three types were subjected to temperatures between 100°C and 220°C in 1-hour steps. The results of the step stress are shown in Figure 2. In general, straight line fits on such plots indicate a log normal life distribution. The slopes indicate the variance for each distribution. It should be noted that median values are generally insensitive to such data variations and form a valid basis for comparing the diode types. These values are summarized in Table I. It is interesting to note that diodes without supports gave the best step stress performance.

Step stress data of this type, in conjunction with constant stress testing, are normally used to predict device life at some elevated junction temperature at which temperature stress is primarily responsible for the failure

TABLE 1. MEDIAN TEMPERATURE VALUES FOR THREE TYPES OF DIODE

Diode Type *	Median Temperature
Diodes with No Supports	185°C
Diodes with Glass Rod Supports	175°C
Diodes with Epoxy Supports	160°C

* Diodes with no supports and diodes with glass rod supports were obtained from Aertech Industries, Sunnyvale, California. Diodes with epoxy supports were obtained from KMC Semiconductor Corporation, Long Valley, New Jersey.

mechanism. Tunnel diode junctions normally operate (without significant power dissipation) at ambient temperature. Step stress tests can quickly indicate the range of stress and time for a particular failure mechanism involved in a given construction technology. Analysis of the step stress data indicates that, in diodes with mesh supports, the dominant failure mechanism is an increasing valley current, while in diodes without supports this failure mode is not dominant. The results shown in Figure 3 suggest that the presence of the supports plays a role in stressing the junction. To understand the mechanism, a relationship which involves mechanical and thermal stress is required. This relationship is provided by the theory developed for the creep failure mode [1].

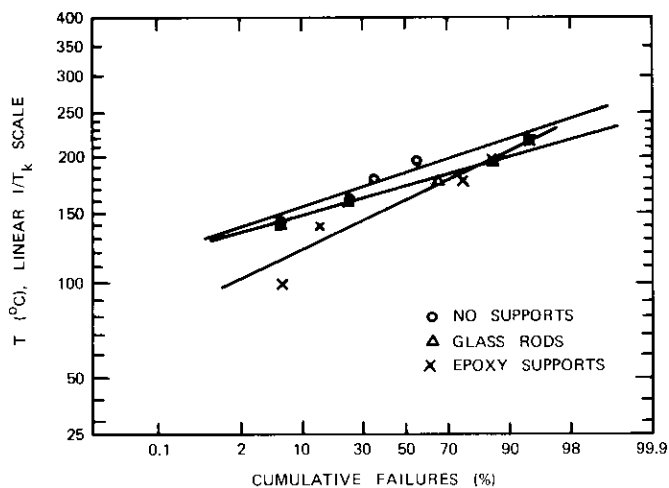


Figure 2. Step Stress Data on Three Types of Ge Tunnel Diodes

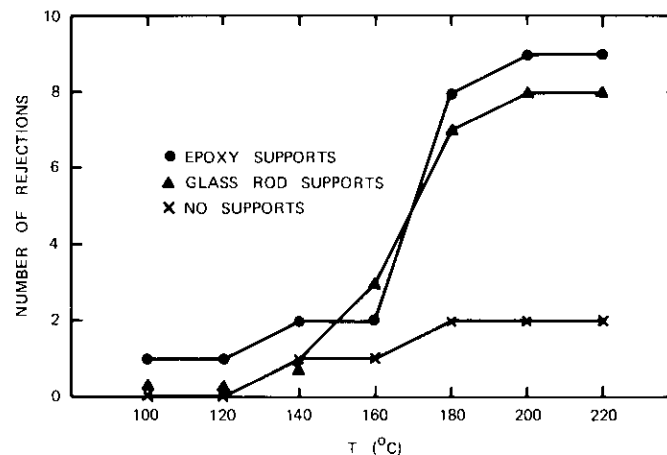


Figure 3. Number of Cumulative I_v Rejections vs Temperature Step (100°C to 220°C) for Three Types of Diodes

Background physics of the creep failure mode

Ball alloy tunnel diodes, by virtue of their construction, are subject to stresses on the junction which can exceed the elastic limit. In this instance, after an incubation period which is very sensitive to the internal stress and the temperature, plastic deformation occurs. The initial phase of this deformation, called creep, results in generation and motion of dislocation and point defects [4]. Arrival of these defects in the junction region introduces allowed energy states in the forbidden band which lead to excess valley current. Under constant stress, creep is characterized by an incubation time, t :

$$t = cd \exp\left(\frac{Q_1 - a_1\sigma}{kT}\right) \tag{1}$$

where a_1 and c are constants, and

- t = time (s)
- d = junction diameter (cm)
- Q_1 = activation energy (erg)
- σ = stress (dyne cm^{-2})
- T = temperature (K)
- k = Boltzmann's constant (erg K^{-1}).

Using values for a_1 , c , and Q based on experimental observations of creep in Ge [4] makes it possible to write equation (1) in the form

$$\log t_1 = -5.367 + \log d + \frac{1}{T} [(8.52 \times 10^3) - (3.78 \times 10^{-6}) \sigma] \quad (2)$$

Equation (2), which is a useful guide for developing prescreening techniques, is plotted in Figure 4 for 25°C and 100°C. The junction diameter used (2.5 μ) is typical of microwave tunnel diodes at 6 GHz. The plot shows the strong dependence of incubation time on temperature. Hours at 100°C are nearly equivalent to years at 25°C. It should also be noted that the incubation time is an extraordinarily sensitive function of the stress level. As a minimum, a 7-year mission at 25°C requires that diodes with a stress level of 0.88×10^9 dynes cm^{-2} be screened out. With screening to achieve some safety margin in the stress level, i.e., $\sigma \cong 0.80 \times 10^9$, 100°C for 1.0 week (168 hours) is a reasonable screen level for a 7-year mission.

Indicators of creep

As mentioned previously, a microwave technique has been developed to measure junction capacitance [2] in the negative resistance region as a function of bias. Junction capacitance profiles for representative microwave tunnel diodes are shown in Figures 5 and 6. Previous experimental

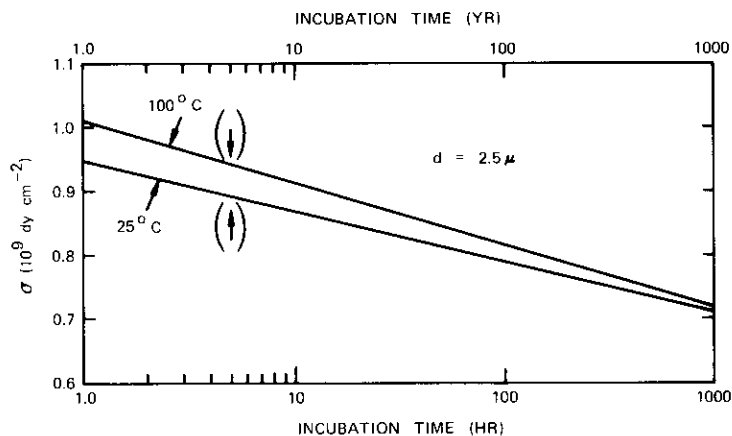


Figure 4. Stress vs Incubation Time for 25°C and 100°C

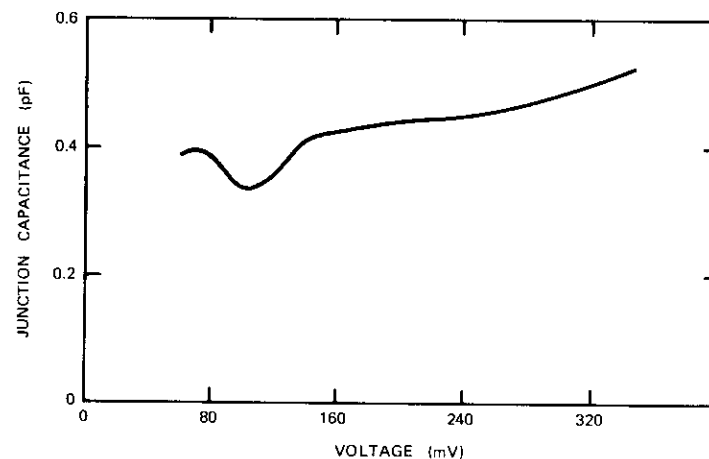


Figure 5. Junction Capacitance vs Forward Voltage for a Ge Tunnel Diode with Glass Rod Supports at 25°C

work has detected junction capacitance changes prior to the onset of valley current growth. This is rather significant in amplifier use, since junction capacitance change affects RF tuning and stability. These changes may well be associated with the generation and propagation of defects to the junction and indicate progression of creep failure.

The diodes in Figures 5 and 6 were not heat treated. It is believed that the relative dips in the capacitance profile are related to the respective stresses on each junction (and hence the number of defects) at 25°C, where the incubation time for creep failure is of the order of years.

The capacitance method provides new information for understanding tunnel diodes. As a test indicator for creep, it represents a complexity which is not warranted by a simple screening procedure. The valley current is easily measured and provides a hard and fast indicator of creep failure [1].

Life test verification of the prescreening technique

It was determined that Ge catalog diodes with the proper ratio of peak current (I_p) to junction capacitance (speed index) to ensure 20-GHz cutoff were entirely suitable for test purposes. The 6-GHz application could be approximated with a normal I_p of 2.0 mA. The manufacturer was allowed to perform the manufacturing preconditioning which normally precedes a

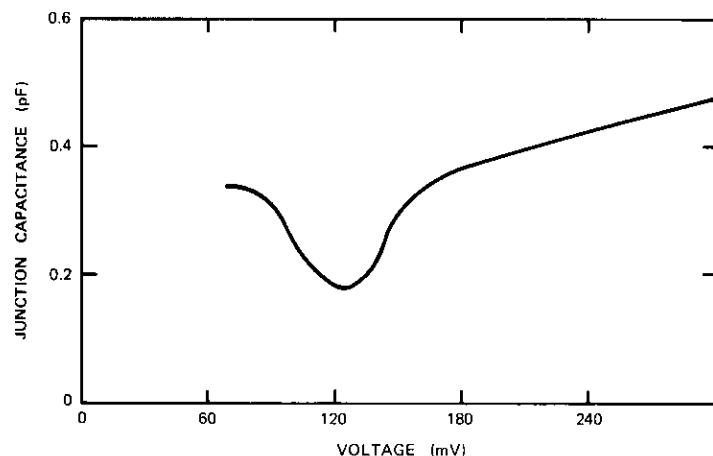


Figure 6. Junction Capacitance vs Forward Voltage for a Ge Tunnel Diode with Epoxy Supports at 25°C

high-reliability program for flight procurement. The features of the test are summarized as follows:

- a. All diodes were stabilized as amplifiers.
- b. Diodes with glass rod mesh supports were employed.
- c. Ribbon contacts (very low stress on the package) were used.
- d. Diodes were not handled after the test started (specifically, diodes were not removed from sockets).
- e. The life test was performed at 25°C at $I = I_p/2$.
- f. I-V plots were taken at 25°C at various check periods (1-percent accuracy); diodes were rejected if $|\Delta I_p|$ or $|\Delta I_v|$ exceeded 10 percent.

The test setup is shown in Figure 7.

One group of 12 diodes was screened and another group of 12 diodes remained unscreened. The creep screen for the screened group was accomplished by using the following procedure:

- a. The peak and valley current of the tunnel diodes were measured at room temperature to at least 3-digit accuracy.
- b. The diodes were heated at 140°C for 1.0 hour.*

* It should be noted that 140°C for 1.0 hour is equivalent to 100°C for 1.0 week.

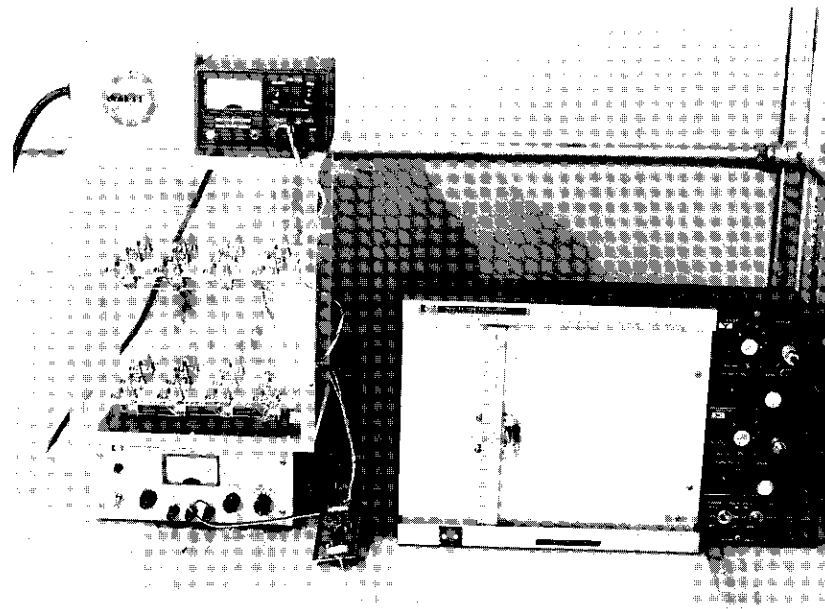


Figure 7. Photograph of Life Test Setup

- c. The diode peak and valley current were then remeasured at room temperature to the same accuracy as in step a. Any diode exhibiting a change exceeding ± 10 percent in either peak or valley current was rejected.

The test status is summarized in Table 2. The failure percentage in the unscreened group was approximately what was expected from the step stress results in Figure 2 (~ 10 percent).

Figure 8 is an I-V plot of the failed diode on test in the unscreened group for $t = 0$ and 7,540 hours. The diode has since exhibited an irreversible change in valley current. If a simplified microwave equivalent circuit had

TABLE 2. TEST STATUS AFTER 24,000 HOURS

Unscreened Group (12 Diodes)	Screened Group (12 Diodes, 140°C, 1 hr)
1 ΔI_v reject (7,540 hr)	no ΔI_v exceeding 1%

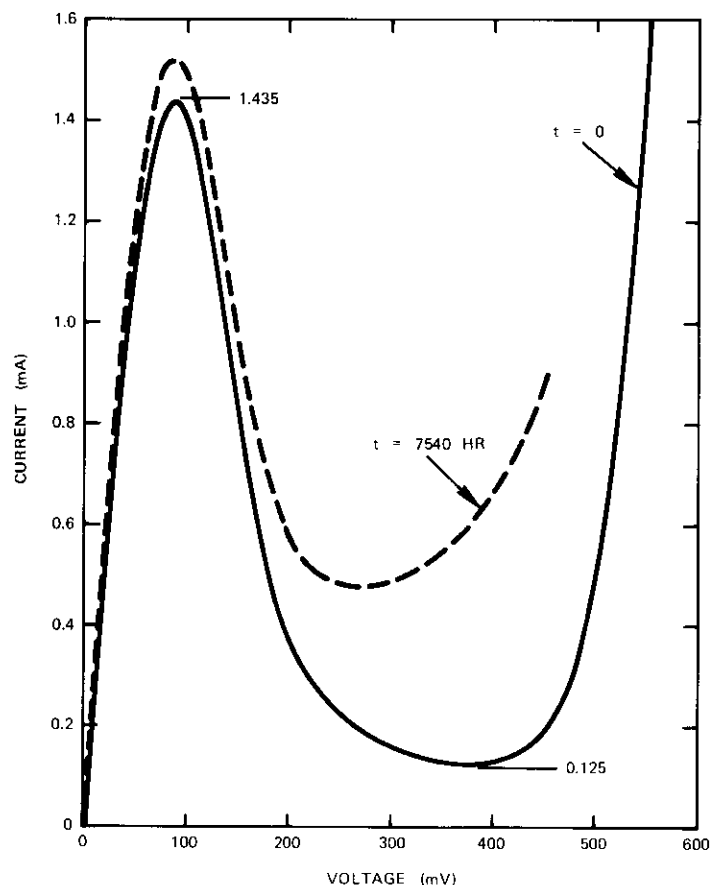


Figure 8. *I-V Characteristic of Test Diode 7 at $t = 0$ and 7,540 hr*

been used, this diode would have exhibited a 5.6-dB gain change in an amplifier whose nominal gain was 13 dB.

Conclusion

The onset of the "creep" failure mode, with subsequent capacitance and valley current change, causes gain and noise degradation in a tunnel diode amplifier. Capacitance change alone can cause detuning of the amplifier. An increasing valley current with time results in a decreasing gain as well

as an increased shot noise in the diode. In some cases, depending on amplifier design, amplifier instability can result from diode changes.

The creep screen can be easily implemented. The use of an accelerated incubation period eliminates stress-sensitive diodes, especially when the supports play a role in stressing the junction.

An in-house life test has verified the merits of the prescreening technique. For various missions, the equivalent screening criteria can easily be derived. The results of this investigation have been incorporated in the ATS-F transponder program at COMSAT Labs and provided to Hughes Aircraft Corporation for incorporation into the INTELSAT IV-A program.

Acknowledgments

The author wishes to acknowledge useful discussions with Dr. E. S. Rittner, Dr. A. Revesz, J. H. Reynolds, and I. Dostis. T. Kirkendall and J. Hannsen provided the appropriate tunnel diode SEM views. L. Foltzer provided fine technical support throughout the program.

References

- [1] A. G. Revesz, J. Lindmayer, and J. Reynolds, "New Aspects of Failure Mechanism in Germanium Tunnel Diodes," *Solid State Electronics*, Vol. 14, No. 11, November 1971, pp. 1137-1147.
- [2] P. L. Fleming and L. E. Foltzer, "Measurement of Negative Capacitance Component in Microwave Tunnel Diodes," *IEEE-GMTT International Microwave Symposium*, Washington, D.C., May 16-19, 1970.
- [3] P. F. Varadi and T. D. Kirkendall, "Physical and Chemical Analysis of Germanium Tunnel Diodes," *COMSAT Technical Review*, Vol. 3, No. 1, Spring 1973, pp. 35-55.
- [4] H. G. Van Bueren, *Imperfections in Crystals*, Chapter 30, North Holland, Amsterdam, 1961.



Paul Fleming is Manager of the Device Physics Department at COMSAT Laboratories. He received a B.S.E.E. degree from the City College of New York in 1957 and an M.S.E.E. degree from Columbia University in 1960. He previously served as a VHF radio specialist with the Marines in South Korea. He spent 10 years with the IBM Corporation, where he received an Invention Achievement Award. His work has included microwave memories, microwave modulation of light, digital microwave, 12-GHz propagation, bulk effect devices, and more recently, state-of-the-art devices in GaAs. He is a member of Eta Kappa Nu.

Index: ionospheric projection, scintillation, statistical distributions.

Ionospheric scintillation at frequencies above 1 GHz

R. R. TAUR

(Manuscript received March 1, 1974)

Abstract

This paper presents preliminary results of simultaneous L- and C-band scintillation measurements at Tangua, Brazil, along with a brief review of the existing literature pertaining to ionospheric scintillation at frequencies above 1 GHz. Specifically, it discusses the morphology and statistics, including fading rate, frequency dependence, and cumulative amplitude distributions of gigahertz scintillation.

It has been found that gigahertz scintillation occurs mainly in the equatorial and polar cap regions, with strong diurnal and seasonal variations. It also appears to have a positive correlation with the variation in the number of sunspots. In the equatorial region, for frequencies between 1.5 and 4 GHz, the frequency dependence of the scintillation index is directly proportional to the wavelength, and for frequencies above 4 GHz, the scintillation index varies as the square of the wavelength. Based upon the observed frequency dependence and fading rate, some possible space wave number spectra of the density fluctuation of the F-region irregularities are discussed to explain theoretically gigahertz scintillation in the equatorial region.

This paper is based upon work performed in COMSAT Laboratories under the sponsorship of the International Telecommunications Satellite Organization (INTELSAT). Views expressed in this paper are not necessarily those of INTELSAT.

Introduction

Before the actual use of microwave frequencies in satellite communications, it was believed that ionospheric irregularities would not cause noticeable signal fluctuations at such frequencies. However, in equatorial regions, severe fading at 2.2 GHz, with peak-to-peak fluctuations as large as 20 dB, has been reported by Christiansen [1]. Furthermore, at high latitudes (auroral zone), scintillations at 1.7 GHz have been observed by Pope and Fritz [2]. Ionospheric scintillations at 1.5, 2.3, 4, and 6 GHz have also been reported by Sessions [3], Maynard [4], [5], Craft and Westerland [6], Taur [7], and Paulson and Hopkins [8]. According to Taur [7], at latitudes below 50°, the occurrences of microwave scintillations are limited in the geomagnetic equatorial region and peak near the equinoxes. The diurnal variations of the observed scintillation have a strong peak approximately one hour after local sunset. The characteristics of the gigahertz scintillations are similar to those of the scintillations observed at lower frequencies in the equatorial region [9]. It is believed that F-region irregularities are responsible for the observed scintillations.

The primary reason for the failure to predict gigahertz scintillation was the application of a λ^2 dependence to the VHF-UHF scintillation data. The λ^2 variation is applicable only to the case of weak scattering for certain types of spatial spectra of the electron density fluctuation. This frequency dependence is not valid when the scintillation occurs at saturation or in the process of focusing and defocusing [7].

Taur [7] has reported the results of measurements made over a 15-month period at 22 different locations around the world with geomagnetic latitudes ranging from 20°S to 53°N to study the global morphology, cumulative amplitude probability, and distribution function of the ionospheric scintillations at 4 and 6 GHz. Paulson and Hopkins [8] have reported on extensive measurements at 250 MHz, 2.3 GHz, and 7.3 GHz made at about the time of the fall equinoxes of 1970, 1971, and 1972 in the Pacific, while Sessions [3] has reported the results of simultaneous VHF and L-band measurements at Arcon, Peru. Additional L-band measurements at Churchill and Ottawa, Canada, have been reported by Maynard [4], [5]. Finally, in 1972 simultaneous L- and C-band (1.5- and 4-GHz) measurements were made at Tangua, Brazil, using the ATS-E geostationary satellite. The preliminary results of this last experiment will be discussed in this paper.

Signal statistics and morphology

Fading rate

The fading rate of data collected in the equatorial region has a range of 4 to 30 fades per minute [3], [7], [8]. Koster [9] has reported that the fading rate of the VHF equatorial scintillation has a maximum value of 6.5 fades per minute at 2200 hours local time, which is the time at which maximum gigahertz scintillation is observed [7]. According to theory [10], [11], scintillations at higher (SHF) frequencies are produced by ionospheric irregularities of a smaller scale with more pronounced electron density fluctuations. Irregularities of this type also increase the level of scintillations at lower frequencies (VHF).

If it is assumed that irregularities of various sizes exist in the ionosphere, then gigahertz scintillation will correspond to a narrower range of power spectrum density fluctuations. Results of the simultaneous VHF and 2.3-GHz measurements agree with this prediction [8]. Analysis of the data from the simultaneous 1.5- and 4-GHz measurements indicates that the power spectrum of the 1.5-GHz scintillation is wider than the power spectrum of the 4-GHz scintillation. Therefore, it can be seen that the fading rate of gigahertz scintillation is limited to a range which is narrower than that of the scintillation at lower frequencies and that, as the frequency increases, the width of this range decreases.

Simultaneous 136-MHz and 1.55-GHz measurements [3] revealed another interesting phenomenon. On a few occasions, the VHF signal was first scintillating at a relatively slow rate and no apparent 1.5-GHz scintillation was observed. Then, within a short time, the rate of scintillation increased to equal that of the gigahertz scintillation observed in Reference 7. At the same time, the VHF signal fluctuation decreased, yet the 1.5-GHz scintillation became noticeable. This indicated that there was a sudden change in irregularity size distribution, possibly due to the breaking up of the large patches that caused the slow scintillations. From the observed change in the fading rate and the assumption that the drift velocity of the irregularities is constant, it can be deduced that gigahertz scintillation is caused by the smaller ionospheric irregularities, as predicted by theory.

The observed fading rate of auroral region scintillation of the signal from a geostationary satellite [4], [5] ranges from 2-6 fades per minute. For such a satellite, the fading rate reflects the motion of the ionospheric irregularities. When either the transmitter or the receiver is moving, the fading rates should be determined by the relative motion between the ray path and the irregularities.

Frequency dependence

In 1972 simultaneous ionospheric scintillation measurements were made at 1.5 and 4 GHz at Tangua, Brazil, to study frequency dependence. The frequency dependence of the ionospheric scintillation is directly related to the power spectra of the electron density fluctuation; therefore, unless the spectra are known, no theory can accurately predict the frequency dependence. The frequency-dependent exponent of ionospheric scintillation, denoted as ν , is normally expressed as

$$\frac{SI|_{\text{at } f_1}}{SI|_{\text{at } f_2}} = \left(\frac{f_2}{f_1}\right)^\nu = \left(\frac{\lambda_1}{\lambda_2}\right)^\nu \quad (1)$$

where SI is the scintillation index [12], f_1 and f_2 are the frequencies of two radio waves, and λ_1 and λ_2 are their free-space wavelengths.

Three scintillation events which covered a total of 86 minutes of the simultaneous 1.5- and 4-GHz measurement were studied. To eliminate slow power level variations due to the receiving equipment, data were divided into periods of 4 to 10 minutes during which the received signals were relatively stable. Scintillation indices of each of these periods were calculated. Equation (1) was used to obtain the corresponding value of ν . The results are shown in Figure 1 as functions of peak-to-peak scintillation at 1.5 GHz. It can be seen that the values of ν are generally less than or equal to 1.

Between 4 and 6 GHz, the scintillation index is found to vary approximately with λ^2 [6]. However, this result must be further investigated because the 6-GHz signal is the up-link signal to the geostationary INTELSAT satellite and the 4-GHz signal is the down-link signal. Since the distances between the receiver and the irregularities are different for the up- and down-links, this difference might affect the observation. Briggs and Parkin [12] state that the distance effect can be expressed as $Z_1 Z_2 / (Z_1 + Z_2)$, where Z_1 and Z_2 are the distances from the irregularities to the receiver and transmitter, respectively. The validity of this expression depends upon the frequency, sizes of the irregularities, and Z_1 and Z_2 . Therefore the range of its validity should be carefully examined. However, when the irregularities are sufficiently small in comparison to the distances, the difference between the up-link and down-link scintillations is expected to be small. Since all the scintillations observed at 6 GHz have scintillation indices less than 0.3, i.e., weak scattering, the λ^2 dependence should theoretically remain valid for higher frequencies.

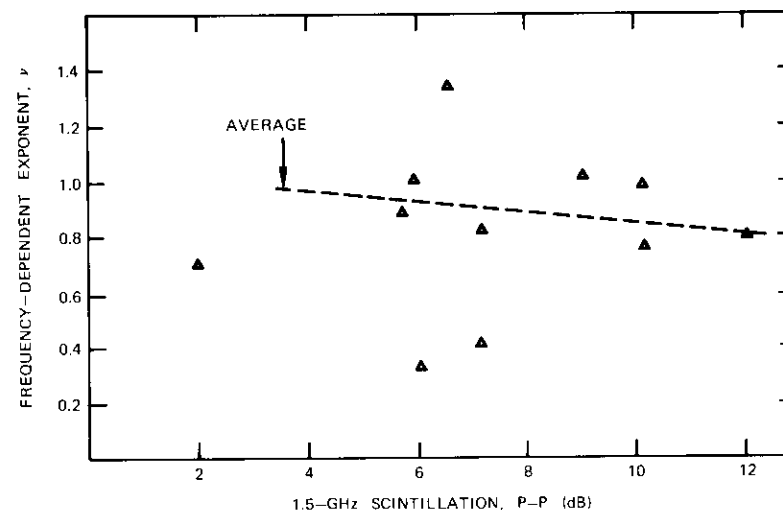


Figure 1. Frequency Dependence of Scintillation Between 1.5 and 4 GHz as a Function of Peak-to-Peak Scintillation at 1.5 GHz

The available information on the frequency dependence of the gigahertz scintillation suggests that, for frequencies below 4 GHz, the scintillation index is proportional to λ ; for frequencies above 4 GHz, the scintillation index scales as λ^2 .

Diurnal variation

In the geomagnetic equatorial region all the measurements have shown that gigahertz scintillation is a nighttime phenomenon that occurs mainly between 1900 and approximately 2400 hours local time. The ionosound spread-F and VHF scintillation measurements have shown that ionospheric irregularities exist throughout the entire nighttime. Hence, there is apparently a difference between the types of irregularities that cause spread-F and gigahertz scintillation. The difference is believed to be in the irregularity sizes. A possible explanation has been given by Taur [7].

In the auroral region, based upon a limited amount of information, gigahertz scintillation occurs between 1900 and approximately 2400 hours local time [4], [5].

Seasonal variation

The seasonal variation of gigahertz scintillation in the equatorial region is given by Taur [7], who shows that gigahertz scintillations occur near the vernal and autumnal equinoxes. The results of the 1.5- and 4-GHz measurements made over a period of one year agree with this observation. In auroral regions, gigahertz scintillation also peaks during the equinoxes and minimum fading occurs during solstices [4], [5].

Sunspot number variation

Measurements at Bahrain, Hong Kong, and Brazil indicate a noticeable decrease in gigahertz scintillation activities from the 1970–1971 measurements (see Table 1) to the 1972–1973 measurements. This observation appears to have a positive correlation with the sunspot activity, which also declines over this period. However, until measurements covering 11 years of average solar cycle are made at the same location, the correlations between the gigahertz scintillation and sunspot activity cannot be verified.

TABLE 1. TOTAL NUMBER OF MINUTES OF MEASURABLE SCINTILLATION OBSERVED IN 1970 AND 1972 AT BAHRAIN, BRAZIL, AND HONG KONG

Location	Month	Total Number of Minutes of Measurable Scintillation	
		1970	1972
Bahrain	October	772	43
Brazil	November	4,039	2,120
	December	2,816	1,865
Hong Kong	October	3,131	1,505
	November	80	0

Geomagnetic latitudinal variation

The result of an extensive worldwide measurement program in 1970–1971 indicates that, for latitudes below 50° , scintillation at 4 and 6 GHz is limited to the region of $\pm 30^\circ$ geomagnetic latitude [7]. The dependence of scintillation on geomagnetic latitude is not very clear. It is found that some stations with approximately the same geomagnetic latitude have quite different degrees of scintillation activity.

Because there has been a noticeable decrease in scintillation activity

since the last worldwide measurements were made, the equatorial scintillation boundary, i.e., $\pm 30^\circ$ geomagnetic latitude, may have moved to a lower latitude. More measurements are needed to investigate the correlation between the solar activity and the equatorial scintillation boundary.

Cumulative amplitude probability distribution statistics

For the equatorial region, the cumulative amplitude probability distributions of scintillation at 4 and 6 GHz at 12 locations have been given by Taur [7]. For high-latitude L-band scintillations, the cumulative amplitude probability distributions at Ottawa, Ontario, and Churchill, Manitoba, have been given by Maynard [4], [5].

Discussion and additional theory

Earlier theory [12] fails to predict and explain the observed gigahertz scintillation for two principal reasons:

- the assumed Gaussian spatial spectrum of the electron density fluctuation of the ionospheric irregularity is not appropriate [10],
- weak (single) scattering theory may not be applicable to the observed strong scintillation at 1.5 GHz in the equatorial region.

The Gaussian spectrum was chosen from other mathematical functions before the in-situ measurements and simultaneous observations at various frequencies were made. This particular function may have been chosen because it was a reasonable guess at the unknown spatial density variation of the irregularities and because a Gaussian function is easier to handle mathematically. In any case, a recent in-situ measurement indicates that the spatial spectrum of the electron density fluctuation of the F-region irregularities is closer to a power law variation than to a Gaussian function [13]. Calculations made by Rufenach [10] have shown that, on many occasions, the spectrum follows power law variations. However, whether the power law spectrum can truly describe the spatial density fluctuation of the F-region irregularities is still rather questionable, since the irregularities vary with location, time, and many other factors. Therefore, at the beginning of this section, no special form will be assumed for the power spectrum of the 2-dimensional electron density fluctuation, denoted as $N(q_x, q_y)$.

The 2-dimensional phase fluctuation, $\Phi(q_x, q_y)$, of a plane electromagnetic wave after passing through the slab of F-region irregularities of thickness L is

$$\Phi(q_x, q_y) = 2\pi(\lambda r_e)^2 LN(q_x, q_y) \quad (2)$$

where λ is the wavelength of the radio wave, r_e is the classical radius of the electron (2.8×10^{-13} cm), and q_x and q_y are the spatial wave number components transverse to the ray path. At a distance Z from the center of the slab of irregularities, the 2-dimensional power spectrum of the received radio wave $P(q_x, q_y)$ is given by [14]

$$P(q_x, q_y) = 4\Phi(q_x, q_y) \sin^2\left(\frac{\lambda Z q^2}{4\pi}\right) \quad (3)$$

where $q^2 = q_x^2 + q_y^2$.

For the equatorial region, the y -axis is assumed to be along the geomagnetic field lines. The equatorial F-region irregularities are found to be elongated along the field line (with axial ratios much greater than 5:1 [9], [15]) and often drift in the east-west direction. Thus,

$$\sin^2\left(\frac{\lambda Z q^2}{4\pi}\right) \cong \sin^2\left(\frac{\lambda Z q_x^2}{4\pi}\right) \quad (4)$$

If the irregularities are "frozen" as they move along the x direction with velocity V_x , then, from Lovelace [11],

$$\begin{aligned} P(f) &= \frac{1}{V_x} \int_{-\infty}^{\infty} dq_y \Phi\left(q_x = \frac{2\pi f}{V_x}, q_y\right) \\ &\cong \frac{4}{V_x} \sin^2\left(\frac{\sqrt{\pi\lambda Z} f}{V_x}\right)^2 \int_{-\infty}^{\infty} dq_y \Phi\left(q_x = \frac{2\pi f}{V_x}, q_y\right) \\ &= \frac{4}{V_x} \sin^2\left(\frac{\sqrt{\pi} f}{f_F}\right)^2 \int_{-\infty}^{\infty} dq_y \Phi\left(q_x = \frac{2\pi f}{V_x}, q_y\right) \end{aligned} \quad (5)$$

where f is the spatial frequency, and $f_F = V_x/\sqrt{\lambda Z}$ is the Fresnel frequency, i.e., the frequency of the first zero of the sine squared function.

Let r_f be the scale size of the irregularity traveling at a velocity of V_x . Then,

$$f \cdot r_f = V_x$$

and equation (5) becomes

$$P(f) = \frac{4}{V_x} \sin^2\left(\frac{r_f}{r_f}\right)^2 \int_{-\infty}^{\infty} dq_y \Phi\left(q_x = \frac{2\pi}{r_f}, q_y\right) \quad (6)$$

where $r_f = \sqrt{\pi\lambda Z}$ and is referred to as the "Fresnel dimension."

The scintillation index, SI , which is equal to the rms intensity variations divided by the mean received power, is given by

$$\begin{aligned} (SI)^2 &= 2\pi \int_{-\infty}^{\infty} df P(f) \\ &= 4 \int_{-\infty}^{\infty} \int_{-\infty}^{\infty} dq_x dq_y \sin^2\left(\frac{\lambda Z q^2}{4\pi}\right) \Phi(q_x, q_y) \end{aligned} \quad (7)$$

and the mean received power is unity. It is known that $\sin^2 X \leq X^2$; therefore equation (7) becomes

$$\begin{aligned} (SI)^2 &= 4 \int_{-\infty}^{\infty} \int_{-\infty}^{\infty} dq_x dq_y \sin^2\left(\frac{\lambda Z q^2}{4\pi}\right) \Phi(q_x, q_y) \\ &\leq 4 \int_{-\infty}^{\infty} \int_{-\infty}^{\infty} dq_x dq_y \left(\frac{\lambda Z q^2}{4\pi}\right)^2 \Phi(q_x, q_y) \\ &= \frac{1}{2\pi} \lambda^4 Z^2 r_e^2 L \int_{-\infty}^{\infty} \int_{-\infty}^{\infty} dq_x dq_y q^2 N(q_x, q_y). \end{aligned} \quad (8)$$

From equation (8), it can be seen that, during weak scattering, the frequency dependence of the scintillation index is limited by λ^2 . When $N(q_x, q_y)$ tapers off sharply for small irregularity sizes and $\pi\lambda Z \ll 1$ (i.e., in the near-field region), SI varies with λ^2 , which is the near-field case for a Gaussian spectrum [12]. In the far field a Gaussian wave number spectrum yields a λ dependence for the scintillation index. Detailed studies of

scintillation of a thin screen with Gaussian spatial electron density fluctuations have been performed by Briggs and Parkin [12], Singleton [16], and many others.

For a power law wave number spectrum, when the irregularities are elongated along the y -axis with an axial ratio η ,

$$\Phi(q_x, q_y) = 2\pi(\lambda r_e)^2 L(q_x^2 + \eta^2 q_y^2)^{-s/2}. \quad (9)$$

From equation (7),

$$\begin{aligned} (SI)^2 &= 8\pi(\lambda r_e)^2 L \int_{-\infty}^{\infty} \int_{-\infty}^{\infty} dq_x dq_y \sin^2 \left[\left(\frac{\lambda Z}{4\pi} \right) q^2 \right] (q_x^2 + \eta^2 q_y^2)^{-s/2} \\ &= 8\pi(\lambda r_e)^2 L \int_{-\infty}^{\infty} \int_{-\infty}^{\infty} dq_x dq_y \sin^2 \left[\frac{\lambda Z}{4\pi} (q_x^2 + q_y^2) \right] \\ &\quad \cdot (q_x^2 + \eta^2 q_y^2)^{-s/2} \\ &\cong \frac{8\pi(\lambda r_e)^2 L}{V_x} \int_0^{\infty} df \sin^2 \left[\pi \left(\frac{f}{f_F} \right)^2 \right] \int_{-\infty}^{\infty} dq_y \left(1 + \frac{\eta^2 q_y^2}{q_x^2} \right)^{-s/2} q_x^{-s} \end{aligned}$$

where

$$q_x = \frac{2\pi f}{V_x}. \quad (10)$$

In equation (10) let

$$\frac{\eta q_y}{q_x} = y$$

then

$$\begin{aligned} (SI)^2 &= \frac{8\pi(\lambda r_e)^2 L}{V_x} \int_0^{\infty} df \sin^2 \left[\pi \left(\frac{f}{f_F} \right)^2 \right] \int_{-\infty}^{\infty} dy \frac{q_x}{\eta} (1 + y^2)^{-s/2} \\ &= \frac{8\pi(\lambda r_e)^2 L}{\eta V_x^{s+2}} \int_0^{\infty} df \sin^2 \left[\pi \left(\frac{f}{f_F} \right)^2 \right] f^{-s+1} \int_{-\infty}^{\infty} dy (1 + y^2)^{-s/2}. \quad (11) \end{aligned}$$

The second integral in equation (11) is a function of s only. Therefore, if

$$\int_{-\infty}^{\infty} dy (1 + y^2)^{s/2} = Y(s)$$

equation (11) becomes

$$\begin{aligned} (SI)^2 &= \frac{8\pi(\lambda r_e)^2 L}{\eta V_x^{s+2}} Y(s) \int_0^{\infty} df \sin^2 \left[\pi \left(\frac{f}{f_F} \right)^2 \right] f^{-s+1} \\ &= \frac{2^{s/2} \pi^{(s/2)+1} f_F^{s+2} (\lambda r_e)^2 LY(s)}{\eta V_x^{s+2} \Gamma \left(\frac{s}{2} \right) \cos \left[\frac{\pi(s-4)}{4} \right]} \\ &= \frac{2^{s/2} \pi^{(s/2)+1} r_e^2 \lambda^{(s+2)/2} Z^{s-1} LY(s)}{\eta \Gamma \left(\frac{s}{2} \right) \cos \left[\frac{\pi(s-4)}{4} \right]}, \quad SI \propto \lambda^{(s+2)/4}. \quad (12) \end{aligned}$$

It should be noted that equation (12) is valid for $2 < s < 6$. In-situ measurements of the F-region irregularities indicate that the value of s lies between 3.5 and 4.5 [17]. From equation (12) it can be seen that, for a continuous power law spectrum, the scintillation index varies with $\lambda^{1.4}$ to $\lambda^{1.6}$ in both near and far fields. When the irregularities are isotropic, i.e., $N(q_x, q_y) = (q_x^2 + q_y^2)^{-s/2}$,

$$\begin{aligned} (SI)^2 &= 8\pi(\lambda r_e)^2 L \int_{-\infty}^{\infty} \int_{-\infty}^{\infty} dq_x dq_y \sin^2 \left(\frac{\lambda Z q^2}{4\pi} \right) (q_x^2 + q_y^2)^{-s/2} \\ &= 16\pi^2 (\lambda r_e)^2 L \int_0^{\infty} \sin^2 \left(\frac{\lambda Z q^2}{4\pi} \right) q^{-s+1} dq \\ &= \frac{\pi^3 \left(\frac{\lambda Z}{4\pi} \right)^{(s-2)/2} (\lambda r_e)^2 L}{2^{-s/2} \Gamma \left(\frac{s}{2} \right) \cos \frac{(s-4)\pi}{4}}, \quad SI \propto \lambda^{(s+2)/4}. \quad (13) \end{aligned}$$

Therefore, for irregularities with an isotropic power law spectrum, SI also varies with $\lambda^{(s+2)/4}$ for all values of Z .

For a power law spectrum, the irregularity size, a , which is an important factor for a Gaussian spectrum, becomes meaningless. Scintillations are determined by irregularities with sizes comparable to the Fresnel dimension ($\sqrt{\pi\lambda Z}$).

When a modified power law spectrum with a low wave number roll-off at q_0 is assumed, the far-field frequency dependence becomes λ [18]. This change can be explained as follows. For a continuous power law spectrum, as λZ increases, the scintillation index corresponds to the part of the spectrum with lower wave numbers. Since the lower part of the spectrum has the same slope as the higher wave numbers of the spectrum, frequency dependence should remain unchanged. For the "modified" power law spectrum, when r_F (Fresnel dimension = $\sqrt{\pi\lambda Z}$) is greater than $(2\pi)/q_0$ (outer scale), scintillations correspond to the flat section of the spectrum as the frequency decreases; therefore, the frequency dependence is expected to be different.

As mentioned previously, the measured frequency dependence varies with frequency. Between 1.5 and 4 GHz, SI scales as λ ; between 4 and 6 GHz, SI varies as λ^2 . These results indicate that, below 4 GHz, the observed gigahertz scintillations are apparently in the far field, while above 4 GHz they are in the near field.

The observed frequency dependence obviously cannot be explained by a continuous power law spectrum since the frequency dependence would be $\lambda^{(s+2)/4}$ regardless of the value of Z . A modified power law spectrum with a low wave number roll-off at $q_0 = (2\pi)/r_0$, where r_0 is the outer scale of the irregularities, may explain the gigahertz scintillation if $r_0 = r_F = \sqrt{\pi\lambda Z}$ and $s = 6$. This leads to the conclusion that the outer scale of the power law spectrum is approximately 280 m and the spectrum must taper off as q^{-6} to have a λ^2 dependence for frequencies above 4 GHz, as shown by experiment. In-situ measurements show that $s = 3.5-4.5$, which disagrees with the assumed value of s for gigahertz scintillation. However, it should be pointed out that these measurements are not made simultaneously; therefore they do not necessarily contradict each other.

If the spatial wave number spectrum of the irregularities is Gaussian, gigahertz scintillation can be theoretically explained by letting $(\lambda Z)/a^2 = 1$ at 4 GHz. This leads to the conclusion that, when $Z = 350$ km, the mean irregularity size, a , should be approximately 160 m. Below 4 GHz, $(\lambda Z)/a^2 > 1$ and $SI \propto \lambda$; above 4 GHz, $(\lambda Z)/a^2 < 1$ and $SI \propto \lambda^2$.

On many occasions during the simultaneous 1.5- and 4-GHz measurement, especially at the beginning of each scintillation event, high correlation has been found between the 1.5- and 4-GHz scintillations. Figure 2 is

a sample of these recordings. Since the radio frequencies (1.5 and 4 GHz) are well separated, this observation tends to suggest that, at least at that particular instance, scintillations are determined by irregularities of about the same size. Therefore, the spectrum is mathematically a delta function:

$$\Phi(q_x, q_y) = \phi_{av}^2 \left[\delta \left(q_x - \frac{2\pi}{a} \right) \delta \left(q_y - \frac{2\pi}{\eta a} \right) \right] \quad (14)$$

where ϕ_{av} is the rms phase shift due to the irregularities, a is the irregularity size, and η is its axial ratio. This is an extreme example of the Gaussian spectrum [11]. Therefore, for the near field, $SI \propto \lambda^2$, and for the far field, $SI \propto \lambda$. If it is assumed that $a = \sqrt{\lambda Z} \cong 160$ m at 4 GHz, the predicted frequency dependence in both the near and far fields also agrees with the observation.

Based upon the in-situ measurements of electron density fluctuation, the power law spectrum is quite possibly the spatial density distribution of the irregularities for most of the VHF scintillation. However, according to the

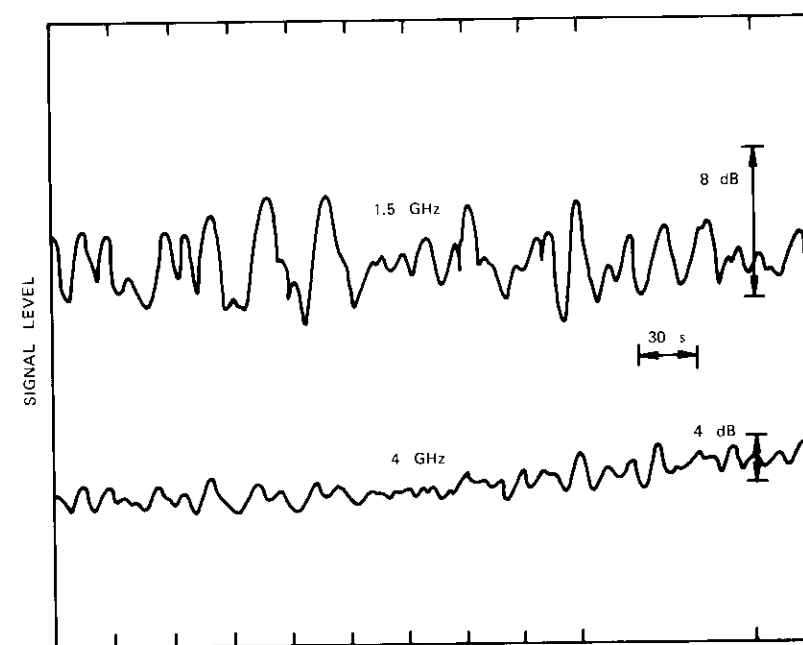


Figure 2. Simultaneous L- and C-Band Scintillation Measurement

theoretical calculation, a continuous power law spectrum simply cannot satisfactorily explain the observed frequency dependence of gigahertz scintillation. A modified power law spectrum with a low wave number roll-off at $(2\pi)/280 \text{ m}^{-1}$ and $s = 6$ can offer a better explanation. It should be noted that this type of spectrum is yet to be measured.

A Gaussian wave number spectrum with a scale size of about 160 m can also satisfactorily explain the gigahertz scintillation. Curves of these spectra are given in Figure 3. Since it is difficult to normalize the rms

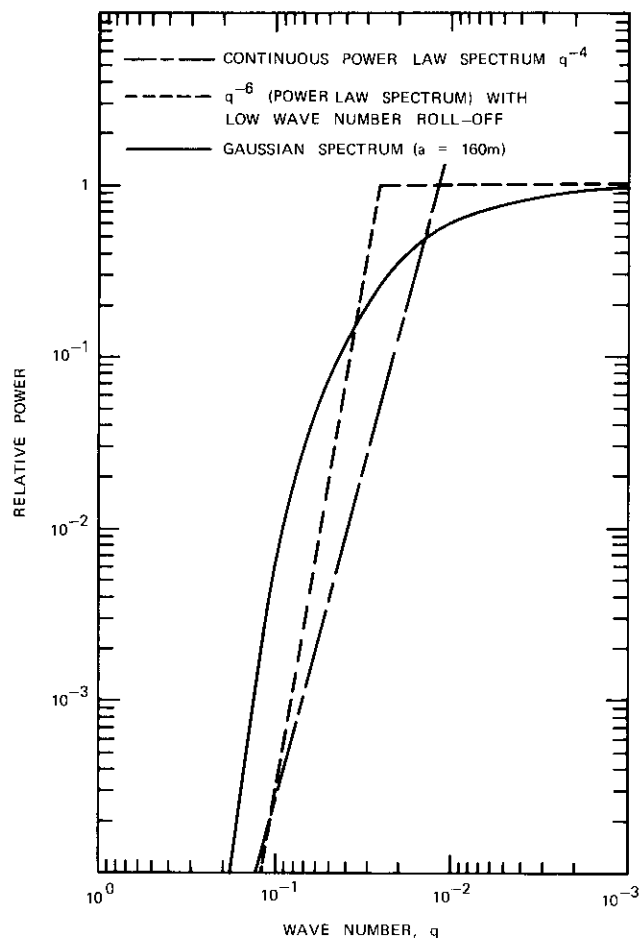


Figure 3. Various Power Spectra of the Spatial Electron Density Variation

electron density fluctuations for various spectra, the levels of relative power at low wave numbers of the modified power law spectrum and the Gaussian spectrum are both set at 1. Although their mathematical expressions are different, close agreement can be seen between the q^{-6} spectrum and the Gaussian spectrum, especially in the region of $10^{-3} < q < 2 \times 10^{-3}$, which corresponds to the Fresnel dimension of 4-GHz scintillation.

From Figure 3, it can be seen that the q^{-4} curve, which is derived from the in-situ measurements, is quite different from the other curves that can explain gigahertz scintillation more satisfactorily.

In some particular instances of gigahertz scintillation, a delta function spectrum is assumed to explain the high correlation between the 1.5- and 4-GHz scintillations. However, the validity of this assumption must be verified either by in-situ measurements or by simultaneous multifrequency measurement at VHF, UHF, and SHF.

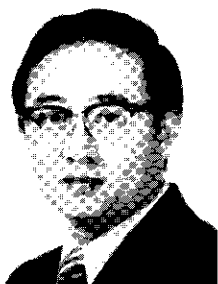
Acknowledgment

The author wishes to thank the engineering staff of the Tangua Earth Station (Brazil), who helped to collect the 1.5- and 4-GHz data.

References

- [1] R. M. Christiansen, "Preliminary Report of S-Band Propagation Disturbance During ALSEP Mission Support," Goddard Space Flight Center, NASA X-861-71-239, June 1971.
- [2] I. H. Pope and R. B. Fritz, "Observation of Simultaneous Scintillation on VHF and S-Band Satellite Transmissions at High Latitudes," NOAA TR-ERL-207-OD 6, November 1970.
- [3] W. B. Sessions, "Amplitude Fading of Simultaneous Transionospheric L-Band and VHF Signals Received at the Geomagnetic Equator," Goddard Space Flight Center, NASA X-810-72-282, June 1972.
- [4] L. A. Maynard, "L-Band Ionospheric Fading Measurements at Ottawa," presented at IMCO Panel of Experts for Maritime Satellites, November 6, 1972.
- [5] L. A. Maynard, "Ionospheric Fading Margins at 1550 MHz at Churchill," presented at IMCO Panel of Experts for Maritime Satellites, November 6, 1972.
- [6] H. D. Craft and L. H. Westerlund, "Scintillation at 4 and 6 GHz Caused by the Ionosphere," AIAA Paper No. 72-179, 1972.
- [7] R. R. Taur, "Ionospheric Scintillations at 4 and 6 GHz," *COMSAT Technical Review*, Vol. 3, No. 1, Spring 1973, p. 145.

- [8] M. R. Paulson and R. U. F. Hopkins, "Effects of Equatorial Scintillation Fading on SATCOM Signals," Naval Electronics Laboratory Center, TR-1875, May 8, 1973.
- [9] J. R. Koster, "Ionospheric Studies Using the Tracking Beacon of the Early Bird Synchronous Satellite," *Ann. Geophysics*, Vol. 22, 1966, p. 103.
- [10] C. L. Rufenach, "Power-Law Wavenumber Spectrum Deduced from Ionospheric Scintillation Observations," *Journal of Geophysical Research*, Vol. 77, 1972, p. 4761.
- [11] R. V. E. Lovelace, "Theory and Analysis of Interplanetary Scintillations," Ph.D. Thesis, Cornell University, September 1970.
- [12] B. H. V. Briggs and I. A. Parkin, "On the Variation of Radio Star and Satellite Scintillations with Zenith Angle," *Journal of Atmospheric and Terrestrial Physics*, Vol. 25, 1963, p. 339.
- [13] R. McClure, private communication.
- [14] K. G. Budden, "The Amplitude Fluctuations of the Radio Wave Scattered From a Thick Ionospheric Layer with Weak Irregularities," *Journal of Atmospheric and Terrestrial Physics*, Vol. 25, 1963, p. 339.
- [15] G. S. Kent and J. R. Koster, "Some Studies of Nighttime F-Layer Irregularities at the Equator Using VHF Signals Radiated from Earth Satellite," *Ann. Geophysics*, Vol. 22, 1966, p. 405.
- [16] D. G. Singleton, "Saturation and Focusing Effects in Radio-Star and Satellite Scintillations," *Journal of Atmospheric and Terrestrial Physics*, Vol. 32, No. 2, February 1970, pp. 187-208.
- [17] P. L. Dyson, J. P. McClure, and W. B. Hanson, "In-Situ Measurements of Amplitude and Scale Size Characteristics of Ionospheric Irregularities," *Journal of Geophysical Research*, 1973.
- [18] B. J. Rickett, "The Power Spectrum of Density Irregularities in the Solar Wind Plasma," *Journal of Geophysical Research*, Vol. 78, 1973, p. 1543.



Roger R. Taur received his B.S. in electrical engineering from Cheng-Kung University, Taiwan, and M.S. and Ph.D. in electrical engineering from Utah State University, where he was a research assistant in the Department of Electrical Engineering. Before joining COMSAT Laboratories in 1971, he worked on antennas and propagation with Computer Sciences Corp., Falls Church, Virginia. He is currently engaged in research on UHF-SHF wave propagation, ionospheric and tropospheric scintillation, and cross-polarization effects of propagation anomalies. Dr. Taur is a member of Sigma Xi, an associate member of URSI Commission III, and has been active in C.C.I.R. Study Groups V and VI.

Index: communications, satellites, statistical analysis, reliability (electronics).

The INTELSAT global satellite communications system

S. BROWNE

(Manuscript received April 30, 1974)

Abstract

The purpose of this paper is to highlight the practical results of satellite communications technology in the form of a growing worldwide satellite communications system which is currently carrying a significant portion of the world's transoceanic telecommunications. The growth of the system, from EARLY BIRD in 1965 to the present, is outlined, and future growth is projected.

Statistical information showing the overall reliability of satellite circuits indicates a high and improving reliability of service. A further breakdown of the data shows separately the reliability of the space segment, the earth stations, and the principal subsystems of the earth stations.

Introduction

The world's first commercial communications satellite—INTELSAT I, better known as EARLY BIRD—was launched on April 6, 1965, and placed into synchronous orbit over the Atlantic Ocean region. This satellite provided telephone service between North America and Europe com-

This paper is based upon work performed at COMSAT under the sponsorship of the International Telecommunications Satellite Organization (INTELSAT). Views expressed in this paper are not necessarily those of INTELSAT.

mencing on June 28, 1965, with 66 C.C.I.R. voice-quality circuits between an earth station in North America and another in Europe. In North America, the U.S. station at Andover, Maine operated in rotation with the Canadian station at Mill Village. In Europe, three earth stations operated in weekly rotation, namely, Goonhilly Downs, England; Pleumeur Bodou, France; and Raisting, Germany. Weekend service was provided in Europe by an earth station at Fucino, Italy. These stations were all interconnected via a terrestrial system. Satellite communications service was extended into the Pacific Ocean region in 1966, with the implementation of an INTELSAT II series satellite which, unlike its predecessor, provided for multiple access between a number of earth stations. The INTELSAT system became truly global in 1969 when an INTELSAT III series satellite commenced commercial operation in the Indian Ocean region.

From these milestone beginnings, the global satellite communications system has developed to such an extent that, as of May, 1974, there were over 5,130* transoceanic voice circuits in full-time operation between 89 earth station antennas in 54 countries over 321 separate paths. All real-time transoceanic TV is today transmitted via the INTELSAT satellite system.

A single-channel-per-carrier PCM multiple-access demand-assignment equipment system via satellite (better known as SPADE) has been implemented in the Atlantic Ocean region with 14 terminals currently in operation and 7 more scheduled by year end 1974. Direct digital transmission between a number of points has been established, and more such paths are planned.

The growth of the INTELSAT system

In 1965, of the 48 countries which were signatories to the interim agreements, 6 had earth stations operating in the INTELSAT system. Today there are 85 signatories of which 54 have operating earth stations, with a total of 89 operating antenna systems in May 1974. The number of pre-assigned discrete paths between earth stations is presently 321.

Figure 1 shows the growth in the number of operating earth stations to the present and those that are planned through 1978. It will be observed

* Including 412 circuits from the U.S. mainland to Hawaii via leased transponder.

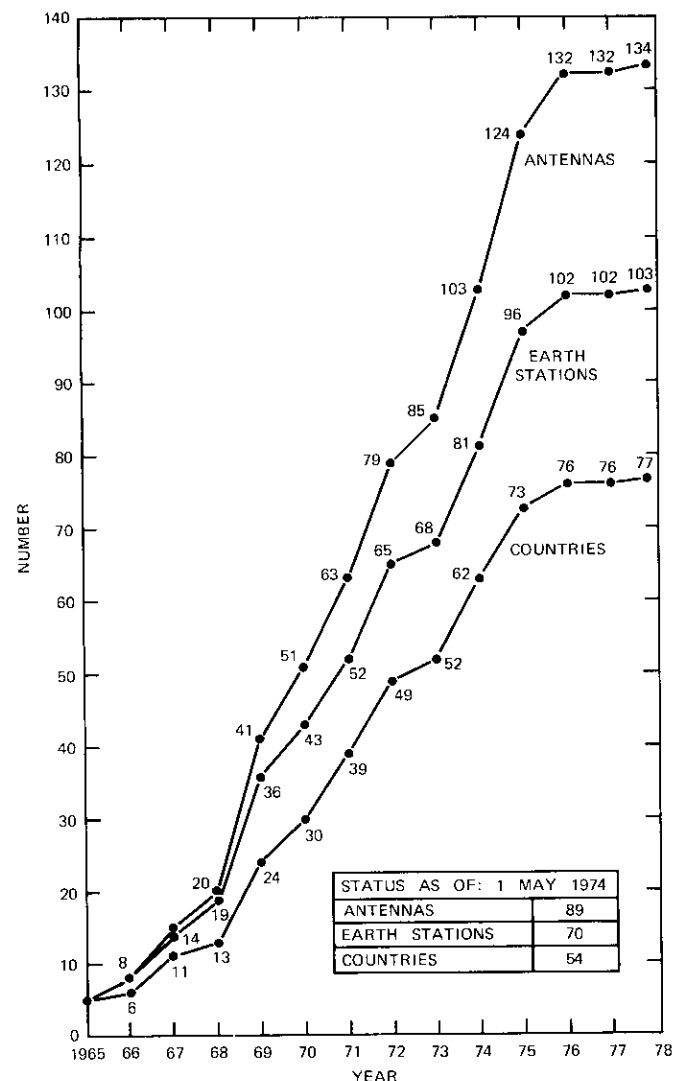


Figure 1. Growth of Earth Stations in the INTELSAT System (year-end totals)

from this figure that during 1975 the implementation of new earth stations will essentially level out, indicating that the "initial" phase of the implementation of the INTELSAT system will then be virtually complete; hence, a

period of "normal" growth is anticipated afterward. The additional earth stations beyond this time will, in the main, consist of the following:

- a. new countries entering the system;
- b. countries providing additional antennas to operate, where geographically possible, in more than one ocean region;
- c. countries providing additional antennas to achieve diverse routing via different satellites in the same region to given destinations;
- d. earth stations implemented to operate frequency bands higher than 6/4 GHz.

Figure 2 shows the actual growth of circuits in the INTELSAT global

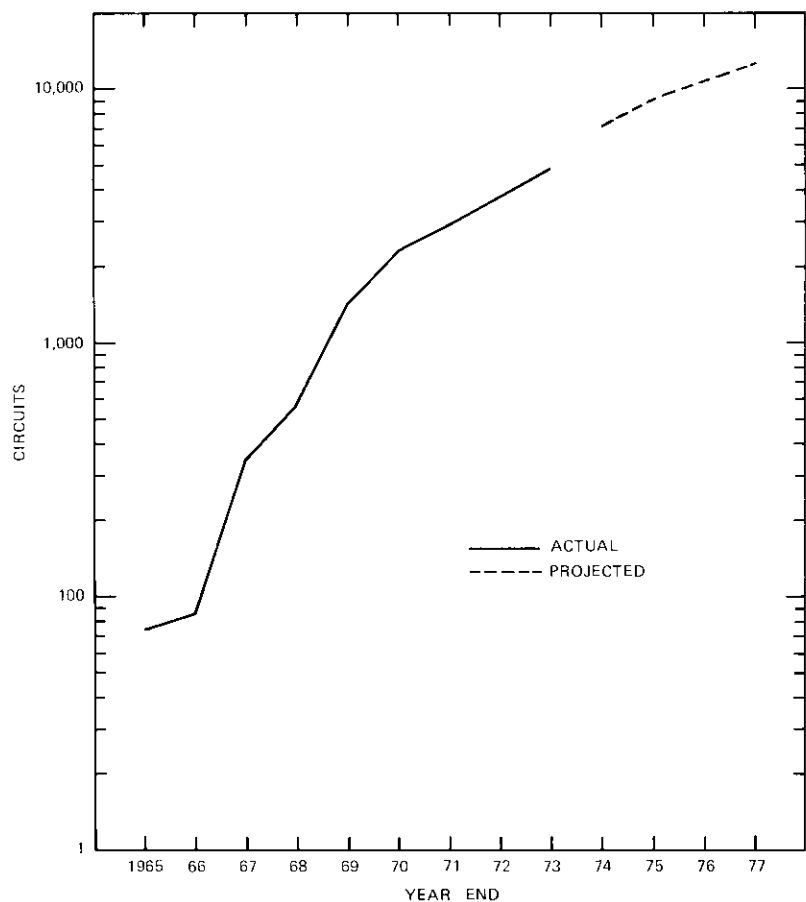


Figure 2. Growth of Full-Time Circuits in Service, Actual and Projected

system from year-end 1965 through year-end 1973. The projected number of circuits at year-end 1974-77 is also shown in Figure 2. The number of circuits is projected on the basis of bilateral agreements between corresponding administrations on the number of future circuits required between them.

With the implementation of an increasing number of earth stations throughout the world, the number of direct paths, point-to-point, has grown, significantly increasing the system complexity. The growth of the number of such paths is shown in Figure 3.

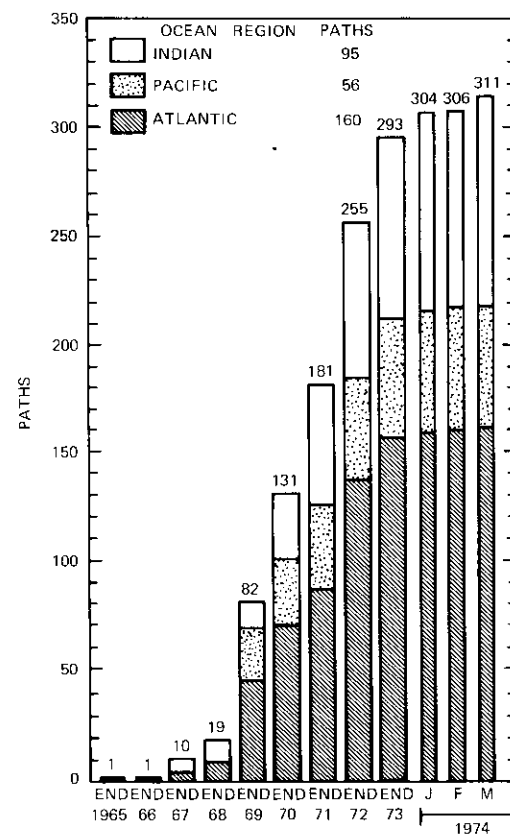


Figure 3. Earth-Station-to-Earth-Station Paths in the INTELSAT System

Satellite capacity

To meet the growth requirements so far realized, it has been necessary to implement satellites with successively increasing circuit capacity. Historically, at the time the first of a new series of satellite is being launched, the next series of satellite is generally well into the planning and implementation stage. INTELSAT types of satellite are known by a flight series, e.g., INTELSAT I and INTELSAT II. Currently, the INTELSAT IV series of satellite [1], [2] is providing all services on the INTELSAT system except for certain contingency capacity which is currently provided by predecessor satellites pending the completion of the INTELSAT IV launch schedule. The nominal capacity of the INTELSAT flight series is given in Table 1.

TABLE 1. INTELSAT FLIGHT SERIES CAPACITY

Flight Series	Nominal Capacity (circuits) ^a
I	240 ^b
II	240 ^c
III	1,500 ^c
IV	4,000 ^c

^a Exclusive of capacity reserve for TV and/or contingency use.

^b Communications between two points only; either telephony or TV.

^c Multiple-access communications between numerous earth stations.

It should be noted that the communications capacities given in Table 1 for each flight series are nominal and, in operation, may be greater or smaller depending upon the actual configuration which is used to meet the required traffic flow.

INTELSAT IV-A, a modified INTELSAT IV series of satellite with a higher circuit capacity, is now under construction for launch in 1975. The definition study phase for an INTELSAT V series of satellite is well underway.

Reliability of service

Earth-station-to-earth-station continuity of service

The INTELSAT satellite communications system has realized an especially high continuity of service. The earth-station-to-earth-station continuity of service* on a global basis was 99.87 percent over the first few months

* Continuity of service is computed by using the formula

$$\frac{\text{circuit-hours of operation} - \text{circuit-hours of outage}}{\text{circuit-hours of operation}} \times 100.$$

of 1974 and essentially the same (99.88 percent) in 1973. These figures reflect both scheduled and unscheduled outages and combine the outages for two earth stations in each path in addition to the space segment. The space-segment reliability is high compared to that of the earth stations.

The average circuit outage time, which may be attributable to an individual earth station can, therefore, be approximated as half of the total, or 0.06 percent. Reliability trends in terms of earth-station-to-earth-station continuity of service from 1970 to the present are shown in Figure 4.

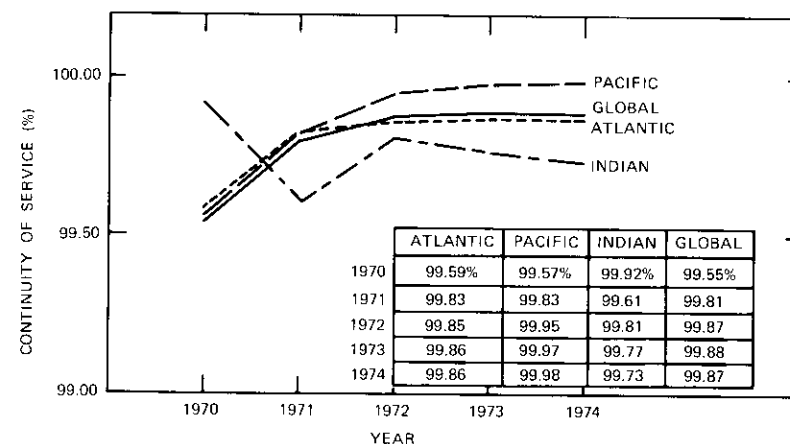


Figure 4. Continuity of Service, Earth-Station-to-Earth-Station Paths

Space-segment continuity of service

Reliability in this section is expressed as the total percentage of time that the space-segment resources actually provide the required services on a per-circuit basis. For example, if a satellite fails and services are restored half an hour later by directing all earth stations previously operating on the failed satellite to point to a spare or contingency satellite, then this half-hour is deducted from the total time under consideration for the statistical evaluation.

Table 2 shows the space-segment continuity of service* in the three regions since 1970, together with the global average. It will be seen that the reliability of the space segment, as defined previously, is very high.

* See "Earth-Station-to-Earth-Station Continuity of Service."

TABLE 2. SPACE-SEGMENT CONTINUITY OF SERVICE* (PERCENT)

Year	Atlantic	Pacific	Indian	Global
1970	99.963	100.000	100.000	99.988
1971	99.996	99.999	99.997	99.997
1972	99.998	99.999	99.998	99.998
1973	100.000	99.999	100.000	99.999
1970-73	99.993	99.999	99.999	99.995

* To develop these figures, all outages were included regardless of cause. The lower figure shown in the Atlantic in 1970 reflects the difficulty encountered with the III series of satellite. There has been no significant loss of service associated with the IV series of satellite, and the minor downtime indicated from 1971 through 1973 is due almost entirely to scheduled downtime for tests and changes in configurations.

Earth station availability

Figure 5 shows the earth station average monthly outages from 1971 through the first quarter of 1974, in minutes. Also shown in parentheses is the earth station availability. Availability is computed on a wideband basis and is a measure of the percentage of time that an earth station is available for service. It is computed by using the following formula:

$$\frac{\text{total operating time} - \text{total outage time}}{\text{total operating time}} \times 100.$$

These figures indicate the significant upward trend in reliability. Figure 6 shows a breakdown of earth station outages by subsystem for the year 1973. The antenna subsystem is the major factor in earth station outages. The breakdown shown is also typical of previous years.

The technical challenge

In earlier systems, satellite capacity was limited by the in-orbit power available. As the technology developed, the INTELSAT III series of communications satellite was substantially balanced in terms of power and bandwidth availability. In the INTELSAT IV series, the power available per unit of bandwidth in the available frequency spectrum is much greater than in earlier series, and the law of diminishing returns for satellite e.i.r.p. vs communications capacity becomes increasingly effective.

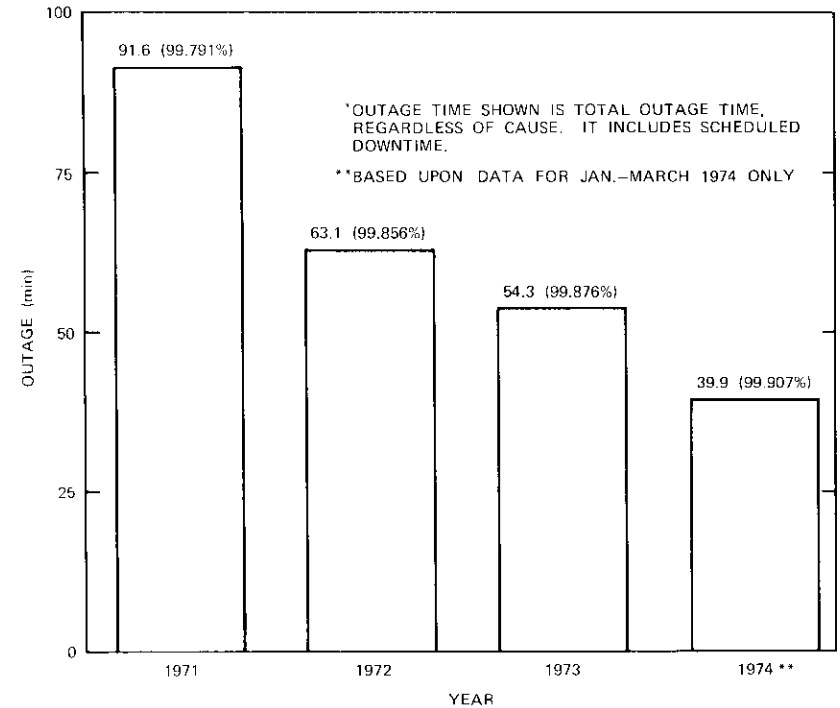


Figure 5. Average Outage Time* for All System Outages per Earth Station per Month

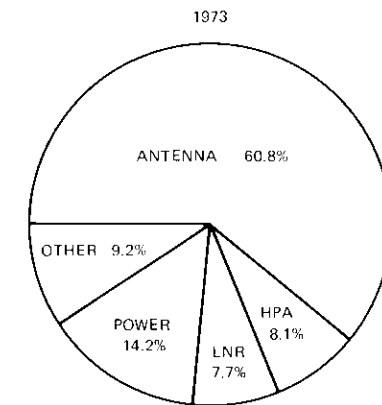


Figure 6. Distribution of Earth-Station Percentage of Total Outage Time by Subsystem

By means of frequency reuse, the INTELSAT IV-A satellite will effectively increase the frequency spectrum available, with the reused frequencies separated by satellite antenna beams pointing to different geographical areas. Nevertheless, some interesting challenges will have to be met during the next 15 years to provide for the projected traffic requirements within the frequency spectrum available with economically acceptable satellite payloads and earth station requirements.

A number of approaches are under intensive study, experimentation, or development [3]–[5]. These include the use of higher frequency bands, e.g., 11/14 GHz; frequency reuse by improved antenna beam isolation; and polarization isolation. New modulation and multiple-access techniques, notably time-domain multiple access (TDMA) with digital speech interpolation (DSI), can virtually double the communications capacity. It seems probable that, concurrent with the use of TDMA, an “adaptive” system will be developed. In this system the traffic flow of a geographical area covering a significant time zone difference on earth could be exploited by automatically time sharing a given amount of satellite capacity between these zones to match the traffic pattern and thus minimize inefficient satellite “slack periods.”

In the future it may be possible to implement intersatellite links which, among other advantages, would help to enable the communications capacity of, for example, two satellites, to be shared among a regional group of countries while reducing the requirement for these countries to have separate antennas pointing at each satellite.

Acknowledgment

The valuable assistance of Mr. W. N. Temple, Director, Analysis and Traffic Division, COMSAT, and his staff in furnishing the statistical data for this short paper is hereby acknowledged with thanks and appreciation.

References

- [1] *COMSAT Technical Review*, Vol. 2, No. 2, Fall 1972 (INTELSAT IV Issue).
- [2] J. L. Dicks, “Domestic and/or Regional Services through INTELSAT IV Satellites,” *COMSAT Technical Review*, Vol. 4, No. 1, Spring 1974, pp. 91–117.
- [3] W. L. Pritchard and P. L. Bargellini, “Trends in Technology for Communications Satellites,” *Astronautics and Aeronautics*, Vol. 10, No. 4, April 1972, pp. 36–42.

- [4] J. Knopow, “Next Generation Communications Satellites,” *Communications Satellite Systems (AIAA Progress in Astronautics and Aeronautics, Vol. 32, edited by P. L. Bargellini)*, Cambridge, Mass.: M.I.T. Press, 1974, pp. 63–86.
- [5] D. MacLellan, “Anticipated Developments in Communications Satellite Technology,” *Communications Satellite Systems (AIAA Progress in Astronautics and Aeronautics, Vol. 32, edited by P. L. Bargellini)*, Cambridge, Mass.: M.I.T. Press, 1974, pp. 145–171.



Sidney Browne obtained the HNC in electrical engineering with distinction in mathematics in London, England, in 1943. Joining the British Post Office in 1939, he was engaged in communications research and later in communications operations in West Africa. He joined the SHAPE Technical Center, The Hague, in 1957, where he became Deputy Chief, Communications. In 1963 he was appointed Technical Advisor to the President of Page Communications Engineers, Inc., Washington, D.C. With COMSAT since 1967, he is currently Director of INTELSAT System Management. Holder of a number of patents in the communications field, he is a chartered electrical engineer in the U.K., a member of the IEE, and also a Senior Member of the IEEE.

CTR Notes

Chemistry of the oxide cathode revisited

E. S. RITTNER

(Manuscript received March 11, 1974)

Over two decades ago, the writer carried out a comprehensive study [1] of the chemistry of the oxide cathode based upon chemical thermodynamics and diffusion theory. Out of this study emerged a satisfying picture of the chemistry of the cathode insofar as carbonate breakdown and cathode activation were concerned. However, an unresolved dilemma persisted in regard to the extremely long cathode lifetimes observed in practice as opposed to the extremely short period required for activation and the relatively short lifetimes calculated on the basis of several different models for the excess barium loss mechanism. A conjecture based upon the supposition that the low barium loss rate results from strong adsorption of a monolayer of barium on the oxide surface was advanced to explain the long cathode lifetime. However, the paucity of diffusion constant data available at the time for activator metals in nickel prevented integration of the conjecture into the otherwise satisfying overall picture. In the meantime, more diffusion constant data have become available [2], together with other experimental results on cathode lifetime [3] and on breakdown studies [4], which collectively shed additional light on the breakdown and activation processes and resolve the long cathode lifetime dilemma.

The thermochemical computations [1] permitted the following classification of about one-half of the elements of the periodic table as candidate activating agents for oxide cathodes:

This paper is based upon work performed in COMSAT Laboratories under the sponsorship of the International Telecommunications Satellite Organization (INTELSAT). Views expressed in this paper are not necessarily those of INTELSAT.

Dr. Rittner is Director of Applied Sciences, COMSAT Laboratories.

a. those elements reacting with BaO to yield an equilibrium pressure of barium as high as that above a BaO phase completely saturated with barium (for example, Th, Mg, Be, Zr, Al, and Si),

b. those elements completely inert in the presence of BaO (such as Ni, Co, Cd, Cu, Au, and Pd),

c. those elements of intermediate activity quantifiable in terms of the equilibrium partial pressure of Ba produced on reduction of BaO (such as Ce, Ti, C, Ta, and W, in order of descending reducing activity).

The maximum pressure of barium developed by the diffusion of activator in the core nickel and subsequent reaction with the oxide coating was found to be smaller than the equilibrium pressure for all of the elements in category *a* and for those in category *c* down to carbon. Hence, it was concluded that the reaction kinetics are limited by the diffusion mechanism. This conclusion was based upon diffusion constant data for carbon in nickel [5] which were considered reliable and representative by the writer. The Ba pressure was, however, sufficiently large to ensure the necessary solubility of excess barium in the oxide coating via Henry's Law, and the small activation time computed was in good agreement with observation.

With the advent of reliable diffusion constant data [2] for some of the commonly employed activators in nickel, namely (in order of increasing diffusion constant), aluminum, silicon, magnesium, and zirconium, it has become clear that carbon diffuses at least three orders of magnitude faster in nickel than these other metals at activation temperature. The diffusion time constant, τ , is given by the relationship

$$\tau = \frac{4l^2}{\pi^2 D}$$

where l is the thickness of the nickel substrate and D is the diffusion constant for the activator in the nickel. The value of τ for a typical nickel thickness of a receiver tube cathode and for the diffusion of carbon at an activation temperature of 900°C is only 2 minutes [1]. The corresponding values for the much thicker nickel substrate employed in a modern satellite TWT cathode with a zirconium activator* are 7×10^3 hours at 900°C and 4×10^4 hours at cathode operating temperature (730°C).

*The writer is indebted to H. W. Smith of the Hughes Aircraft Company for information on the TWT cathode nickel.

These time constants clearly imply that the metals commonly introduced into the nickel as activators cannot be responsible for the initial activation that occurs after carbonate breakdown because the maximum barium pressure reached will be too low to dissolve sufficient barium in the oxide coating. However, these metals (particularly magnesium and zirconium) function very well in maintaining an initially well-activated cathode in a high state of activation since the barium arrival rate to the surface of the oxide may easily be sufficient to keep the adsorbed monolayer intact, which in turn retards loss of barium from the interior of the oxide crystallites. For example, the minimum barium arrival rate required to maintain satellite TWT cathodes in a healthy state of activation, as judged from observed life times of the order of 10^5 hours, has been deduced to be about 3×10^{-9} micromoles/cm²s [3], which is a very low rate indeed.

Hence, the problem of explaining the very rapid activation together with the long observed cathode lifetime in well-processed tubes disappears, but the question now arises as to whether the rapid activation results specifically from carbon diffusion in the nickel [1]. Carbon in small quantities is a ubiquitous constituent of nickel and nickel alloys and could account for the rapid activation in many cases. However, there appears to be an additional source of carbon in oxide cathodes, namely decomposition products of the nitrocellulose binder commonly employed in coating preparation. It has been demonstrated [4] that nitrocellulose decomposes extensively in vacuo in the temperature range 175°C–250°C, leaving behind considerable black residue. Subsequent heating up to 500°C reduces the percentage of residue, which still constitutes 6–7 percent of the original binder. The residue is undoubtedly carbon or carbonaceous material of high reducing activity. Since the equilibrium partial pressure of barium above the carbon-barium oxide reaction and the barium pressure produced by carbon diffusion in nickel are about equal at 900°C, the carbon residue in intimate contact with the oxide crystallites can readily serve as the source of rapid activation.

References

- [1] E. S. Rittner, "A Theoretical Study of the Chemistry of the Oxide Cathode," *Philips Research Reports*, Vol. 8, June 1953, pp. 184–238.
- [2] H. W. Allison and H. Samelson, "Diffusion of Aluminum, Magnesium, Silicon, and Zirconium in Nickel," *Journal of Applied Physics*, Vol. 30, September 1959, pp. 1419–1424.
- [3] E. N. Sosa, L. E. Price, and H. W. Smith, "Hughes Model 1212H TWTA," Final Report to COMSAT, Phase I, Contract CSC-CC-278, July 15, 1972, p. 24.

- [4] K. Ettore and P. Varadi, "Breakdown Studies on Different Binders Used in Electron Tube Devices," *Sixth National Conference on Electron Tube Techniques*, New York: Pergamon Press, 1963, pp. 179-183.
- [5] J. J. Lander, H. E. Kern, and A. L. Black, "The Solubility and Diffusion Coefficient of Carbon in Nickel," *Physical Review*, Vol. 85, January 1952, p. 389.

A null technique for accurately determining the drive level required to saturate a TWT

A. STANDING

(Manuscript received March 19, 1974)

Introduction

The intermodulation performance of earth terminal transmitters under different carrier power and frequency plans is a critical factor in optimizing the system capacity. The current technique models the final TWT by referring its amplitude and phase transfer characteristics to its saturated output power. However, the success of this modeling depends upon the accuracy with which the saturated drive level is known.

Previous techniques for determining this saturated output power and associated drive power have resulted in considerable inaccuracy, since the tube's amplitude transfer characteristic exhibits a very flat maximum at saturation. While this effect allows an accurate determination of the saturated output power, the saturated drive power is difficult to measure, and the error may be in excess of 1 dB, resulting in 3-dB errors in intermodulation predictions. The proposed technique is based on the fact that the TWT amplitude transfer function is double valued; that is, an output power close to saturation can be produced by two input powers, one below and the other above the saturated drive level. It is possible to devise a saturated drive power measurement that determines the drive level required for saturation to any desired accuracy by capitalizing on this double-valued property.

Measurement technique

A null measurement for determining a parameter is a desirable technique. It offers high accuracy and is independent of the linearity of the

Mr. Standing is a member of the technical staff of the Earth Terminals Group at COMSAT Laboratories.

measuring equipment. The proposed null technique is capable of measuring the saturated drive level of a TWT with unsophisticated and readily available measuring equipment.

As shown in Figure 1, the TWT is driven by a carrier amplitude modulated with a square wave at a low level < 0.25 dB, and its detected output is fed to an oscilloscope. A null indication (no output modulation) is obtained when the power outputs at the two drive levels are equal. This condition occurs only when the two drive levels straddle the saturation drive level, as shown in Figure 2. At this point, the drive level can be measured on a power meter.

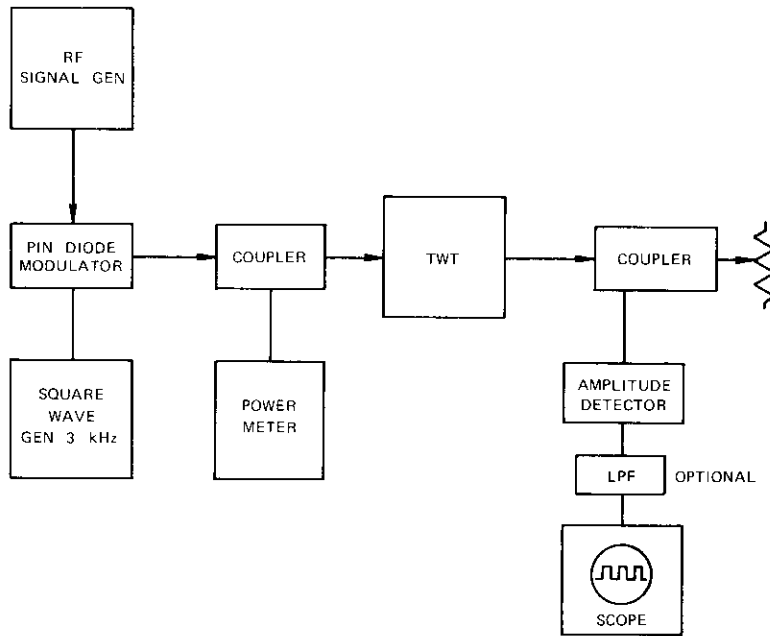


Figure 1. Test Configuration

The choice of square wave frequency is one of convenience. The suggested 3 kHz offers a reasonable compromise between the required bandwidth and sufficient oscilloscope gain.

Measurement errors

To establish the total error in the saturation drive level found by this technique, it is necessary to determine the contributing errors and their

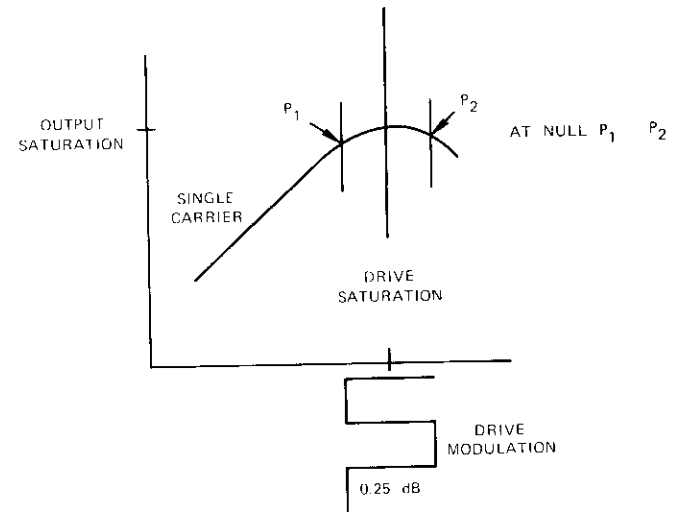


Figure 2. Null Condition

magnitudes. Consideration of the technique shows three major sources of error:

- a. asymmetry of the tube transfer characteristic;
- b. amplitude of the modulation, i.e., modulation depth;
- c. asymmetry of the modulating square wave.

Consider the effects of the first two errors. From Figure 3, where the asymmetry of the transfer function has been greatly exaggerated, it can be seen that the error cannot exceed plus or minus one-half of the modula-

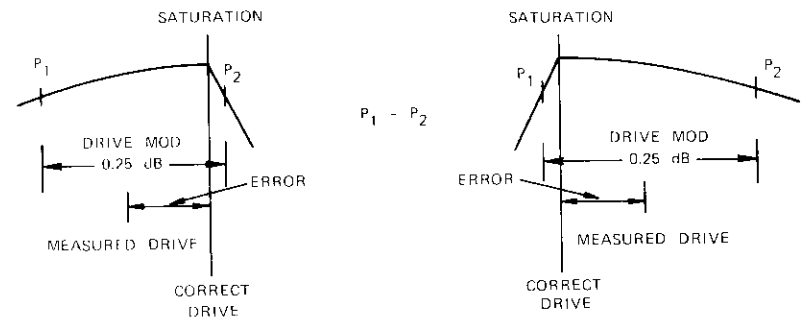


Figure 3. Error Due to Transfer Function Asymmetry

tion amplitude. Asymmetry of the modulating square wave can be readily held to within ± 5 percent of nominal, giving ± 5 percent of the modulation amplitude error. Since the modulation amplitude is less than 5 percent (0.25 dB) of the drive level, 5 percent of 5 percent can be neglected and the final error bounds are plus or minus one-half of the modulation amplitude. High gain in conjunction with suitable filters can be used to establish the null, resulting in modulation amplitudes less than 0.25 dB, and a corresponding accuracy of ± 0.1 dB.

TWT measurements

Measurements of both high- and low-power TWTs (Figures 4 and 5) show that the amplitude response referred to saturation does vary with frequency. Thermal effects on the amplitude response of the high-power

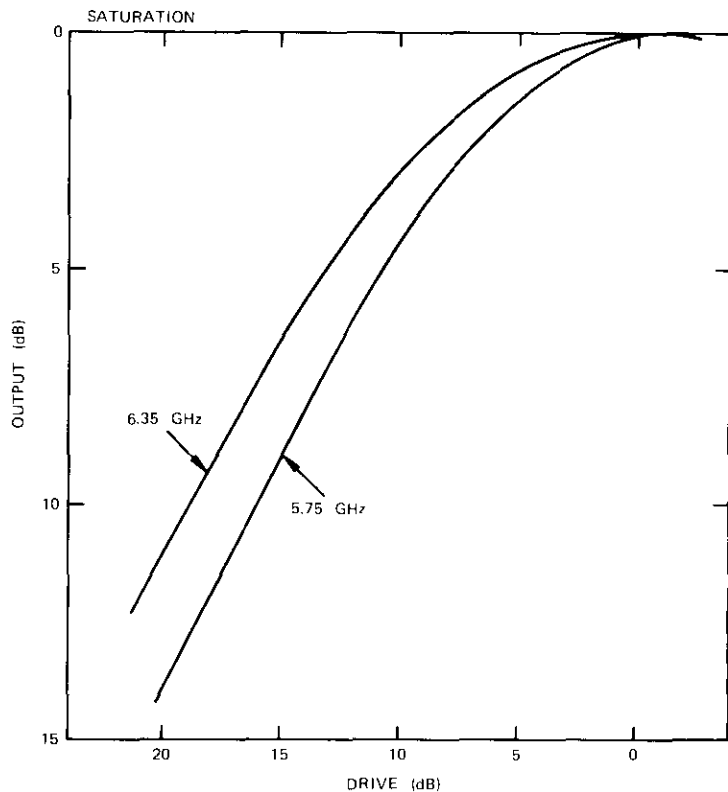


Figure 4. 8-kW TWT

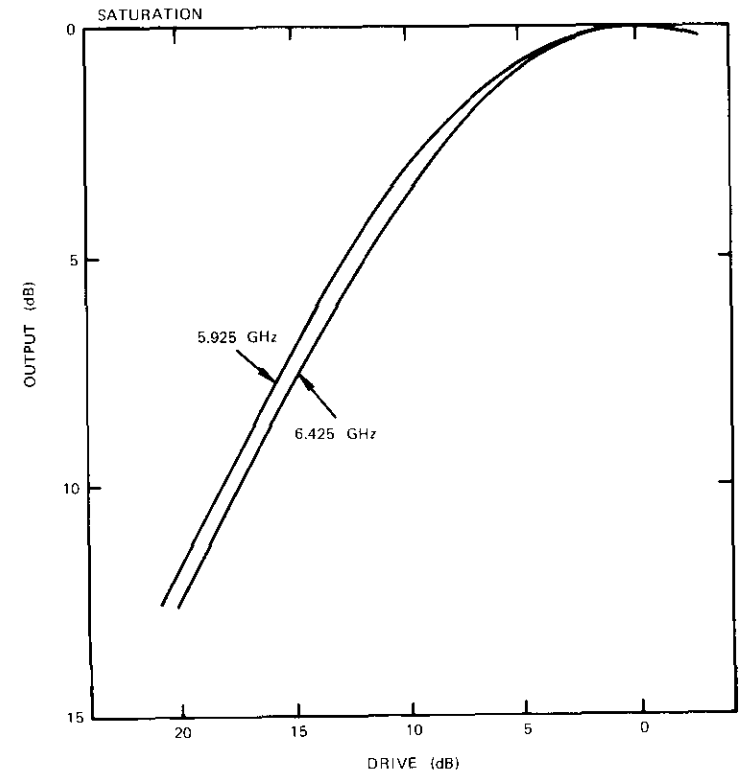


Figure 5. 400-W TWT

TWT can be examined by measuring the saturated drive as the TWT warms up due to the presence of RF.

Conclusions

The technique presented here eliminates the previous uncertainty in the drive level required for saturation and reduces the errors involved in C/I determination to those normally associated with microwave measurements.

Blocking bubbles in the INTELSAT IV fuel lines

G. D. GORDON, G. R. HUSON, AND V. J. SLABINSKI

(Manuscript received May 6, 1974)

Discovery

The INTELSAT IV F-3 spacecraft developed a slight wobble of 0.1° half-angle following a long firing of the system A axial thruster on February 14, 1973. This thruster firing used 8.8 kg of hydrazine propellant to change the orbit inclination by 0.5° . The spacecraft attitude sensors, mounted on the spinning rotor section of this dual-spin spacecraft along with the thrusters and propellant tanks, indicated a shift in the spin axis of 0.1° with respect to the rotor body-fixed axis.

Although the wobble had no effect on the spacecraft communications capability, it was also confirmed by an RF interferometer technique, by accelerometer data, and by radar signals reflected by the antennas. The direction and magnitude of the spin axis shift indicated a shift of the spacecraft mass center that would result if the 8.8 kg of propellant used for the firing had come from only one system A propellant tank (tank 1 in Figure 1) instead of in equal amounts from both tanks. Since blockage of the propellant line from tank 2 by dirt or corrosion seemed improbable, the hypothesis of a blocking bubble trapped in a thermal expansion loop in the propellant line was advanced and eventually proved to be correct.

This paper is based upon work performed at COMSAT Laboratories under the sponsorship of the International Telecommunications Satellite Organization (INTELSAT). Views expressed in the paper are not necessarily those of INTELSAT.

Dr. Gordon is Senior Staff Scientist in the Spacecraft Laboratory at COMSAT Laboratories.

Mr. Huson is a member of the technical staff in the Spacecraft Laboratory at COMSAT Laboratories.

Dr. Slabinski is a member of the technical staff in COMSAT Astrodynamics Department.

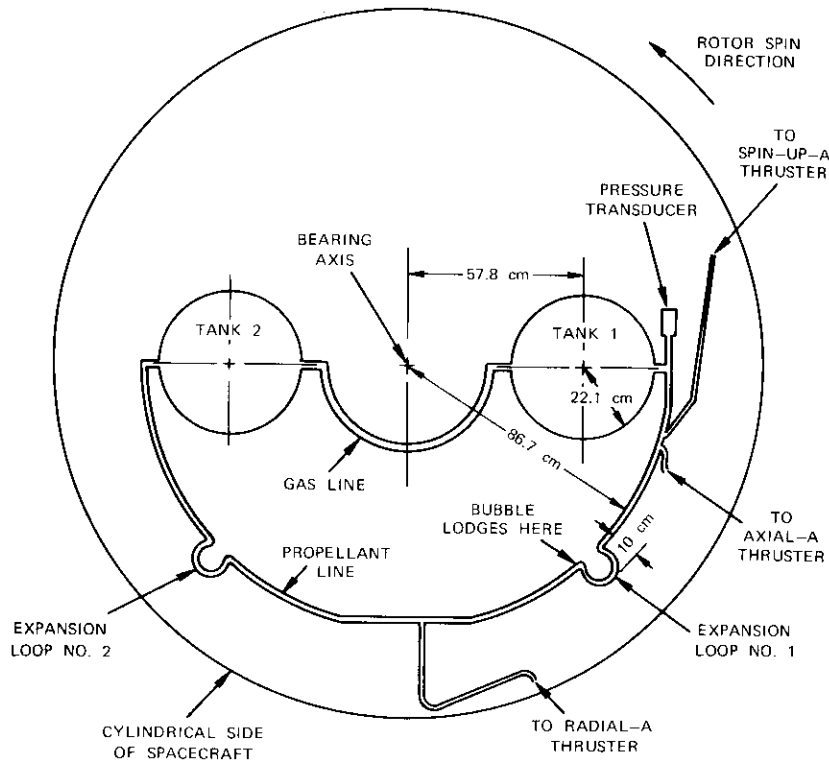


Figure 1. Rotor Showing Positioning and Orientation System A Viewed Along the Spin Axis from the Despun Antenna Platform

Blockage mechanism

In the laboratory the propellant system was modeled with glass tubing, and water was used to simulate hydrazine, since both liquids have nearly identical physical properties. The demonstration was intended to show that the bubble could block the flow of hydrazine and cause the observed wobble in the spacecraft, hence confirming the analysis.

The mechanism of propellant line blockage is illustrated by the laboratory analog of the propellant system shown in Figure 2, where gravity, acting downward, has the same qualitative effect on the liquid as centrifugal forces acting radially outward in the spinning rotor. Consider a large bubble in the propellant line between the tanks, as shown in the

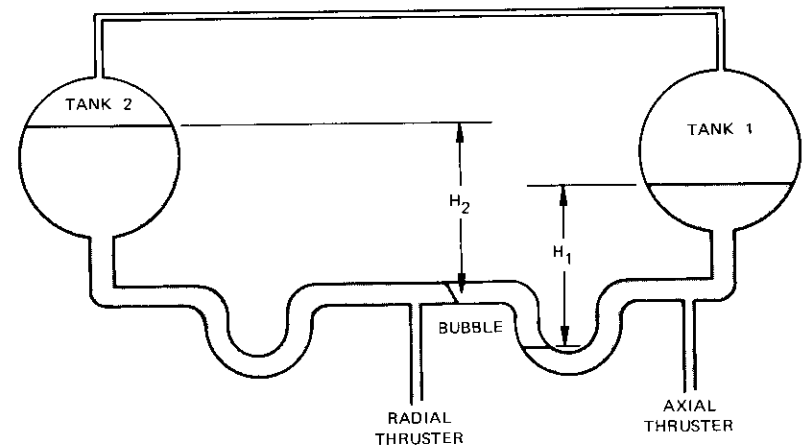


Figure 2. Laboratory Simulation of Fuel Line in Which Bubble is Pushed into "U" Bend Until $H_1 = H_2$ (not to scale)

figure. The continuous liquid column which extends from the propellant tank through the propellant line to one end of the bubble exerts a pressure on that end of the bubble. This pressure is equal to the gas pressure in the tank plus the hydrostatic pressure difference between the free liquid surface and the bubble end. It is assumed this is a static case; that is, no hydrazine is flowing.

Because of the negligible density of the gas in the bubble, the pressure throughout the bubble is expected to be constant. Since a gas pressure equalization tube between the two tanks results in equal gas pressure in each tank, the hydrostatic pressure difference in the two liquid columns must be equal, and the two height differences, H_1 and H_2 , must also be equal. Hence, in the static case each end of a bubble in pressure equilibrium can be at a different height only if the liquid level in each propellant tank is at a different height.

Now consider the motion of the bubble as propellant slowly drains out the axial thruster feed line. If the whole bubble is originally in the horizontal portion of the propellant line between the expansion loops, propellant drains from both tanks and the bubble moves to the right until it enters the expansion loop. The bubble can extend into the loop only until its vertical height equals the propellant level difference between the tanks. Thereafter, propellant draining out the axial thruster can come only from tank 1, as during the previously mentioned inclination maneuver of INTELSAT IV F-3.

Flow to the axial thruster decreases the propellant height in tank 1 until the difference in the tank levels exceeds the radial height of the bubble or the expansion loop. Then the bubble passes through the loop, and flow from the fuller tank 2 equalizes the propellant in the two tanks.

The results of an analytical study including the effect of frictional pressure drop in the tubes are shown in Figure 3, where a large bubble is assumed. The expected result is shown as a function of height difference between the two tank levels and gas pressure in the tanks. (The gas pressure decreases during the life of the satellite as hydrazine is used.) For height differences greater than about 12 cm, the bubble will be expelled when the axial thruster is fired; this is equivalent to a mass imbalance of 17.7 kg. For small height differences, the bubble can be expelled by continuous firing of the radial thruster. The analysis also indicates an intermediate zone in which it may not be possible to expel the bubble until the height differences are changed by fuel expenditures.

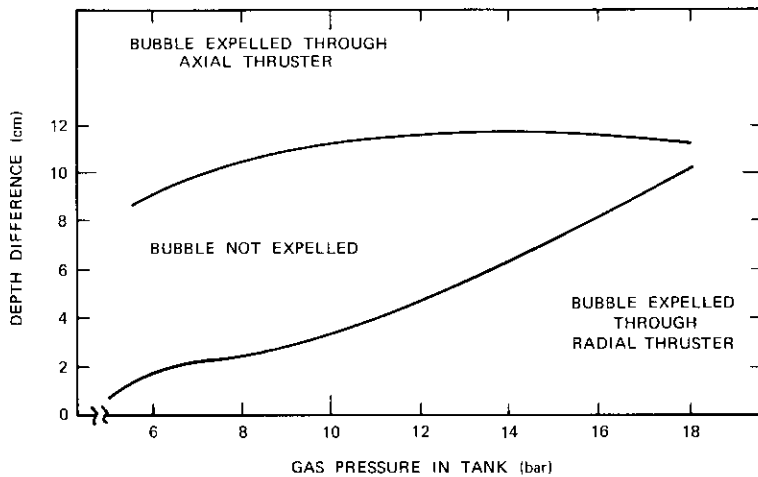


Figure 3. Modes of Bubble Elimination

Origin of bubble

It is most probable that the bubble originates in the loading process. Loading of the hydrazine through a fill-drain port in the line going to the axial thruster proceeds in four steps:

a. A vacuum pump is attached to the fill-drain port to evacuate air from the system.

b. Liquid hydrazine is put into the system through the fill-drain port. The amount of hydrazine loaded into the tanks is several kilograms more than that carried into orbit.

c. Nitrogen gas is blown through the fill-drain port and propellant feed line to pressurize the tanks and bubbles up through the hydrazine in the tanks.

d. Some hydrazine is drained out of the port in an attempt to purge any gas trapped in the propellant lines.

The last step was expected to purge all the nitrogen gas from the lines, but subsequent tests have shown gas bubbles remaining. One likely location is the line to the radial thruster at the T connection. A 5-cm section of this line comes up in a vertical direction from the plane of Figure 1. The line then makes a right-angle turn and proceeds radially away from the bearing axis. During the loading process, the 5-cm section comes up in a vertical direction from a horizontal tube that contains nitrogen gas. The hydrazine can easily drain down from the vertical section and the gas can penetrate up into the vertical tube and the connected radial section. After the spacecraft is injected into orbit and spun up, buoyant forces tend to move the bubble toward the spin axis, that is, out of the radial section and into the propellant line between the two tanks. If the first thruster to be fired following spin-up is the axial thruster, the bubble moves to expansion loop 1, where it lodges and blocks the flow from tank 2.

Two hypotheses for bubble formation after loading have been investigated. The nitrogen gas used for pressurization might dissolve in the hydrazine and then come out of solution when the pressure drops; however, nitrogen is not sufficiently soluble for this to create a significant bubble. The second possibility is that bubbles might be generated from localized decomposition of the hydrazine; such decomposition is unlikely, but cannot be completely ruled out.

Ejection of bubble

When the axial thruster is fired, the bubble remains lodged in expansion loop 1. However, when the radial thruster is fired, the flow of propellant from tank 2 to the radial thruster feed line reduces the pressure on end 2 of the bubble. This reduction might be sufficient to back the bubble out of the expansion loop and eject it through the thruster. However, the radial thruster is usually fired only in short pulses of 117 ms, which are not long enough for the bubble to move from the expansion loop to the

radial thruster feed line. (The propellant in the thruster feed line moves only ~ 5 cm during the pulse.) When the thruster pulse ends, the extra propellant in tank 2 pushes the bubble back into the expansion loop.

If the radial thruster is fired continuously, the bubble should move to the thruster feed line and be ejected as long as the depth difference between the two tanks is not excessive. The results of calculations for various amounts of propellant in the tanks are summarized in Figure 3. For small differences in depth, the bubble can be ejected by firing the radial thruster; this is easier to do (with a larger depth difference) early in the life of the satellite when the flow rate to the thrusters is higher. For large differences in depth (over 10 cm), a single bubble cannot support the pressure difference, and the bubble will be pushed through the loop.

Redistribution

Once the bubble is ejected, there is nothing to prevent the hydrazine from flowing from tank 2 to tank 1. This flow does take place, but rather slowly. The best indication of this flow is the variation in spin speed. As the hydrazine moves from one tank to the other, the distance of the liquid from the spin axis increases so that the moment of inertia of the spacecraft increases. The spin rate of the spacecraft decreases through the conservation of angular momentum.

The actual spin rate is plotted in Figure 4 for a bubble ejection maneuver. At the firing a sharp change in spin rate occurs because the thrust direction of the radial thruster does not pass exactly through the spin axis. After the firing, the spin rate shows an exponential decay with a time constant of 9 minutes. The spin rate decreases from 53.20 rpm to a final value of 53.176 rpm, from which an initial propellant mass imbalance of 6.7 kg is calculated.

A computer program has been used to predict the hydrazine levels during and after a normal thruster firing for an inclination change maneuver. It is assumed that no bubble exists, and that the difference in the level between the two tanks occurs because of the difference in the length of the feed lines. During the thruster firing (see Figure 5), more hydrazine comes from tank 1 than from tank 2. After the thruster stops firing, fuel flows from tank 2 to tank 1. The redistribution is in the form of two exponential curves with a time constant of 17.9 minutes. Theory shows that the redistribution time constant is twice the value of the spin rate time constant. There is excellent agreement between the results of the computer program and the observed spin rate time constant of 9 minutes.

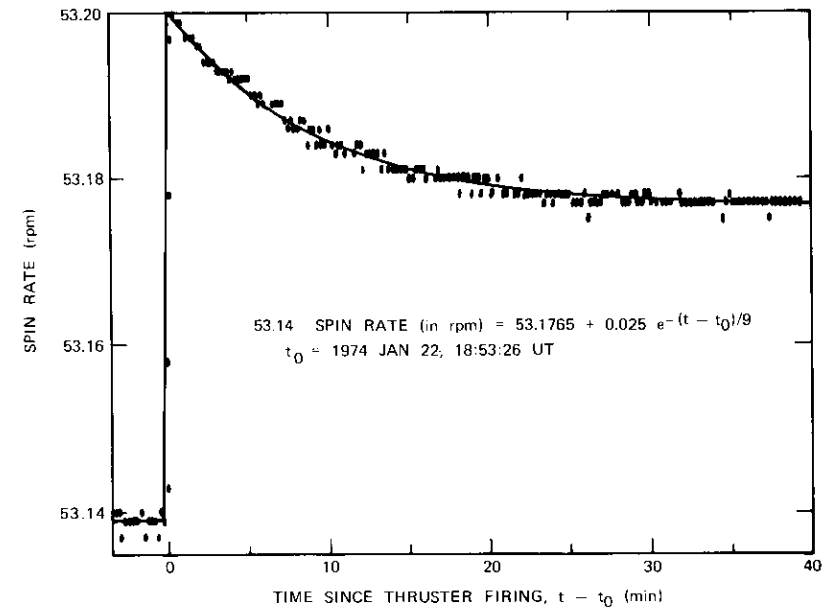


Figure 4. Spin Rate During Bubble Ejection and Fuel Redistribution

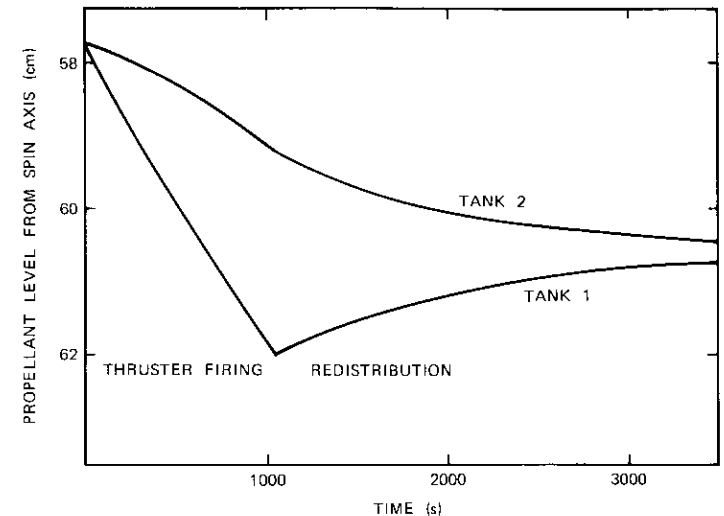


Figure 5. Computed Hydrazine Levels During and After Normal Firing (no bubble)

Conclusions

On the basis of the analyses described in this note, a continuous radial thruster firing to remove the bubble was recommended five weeks after the anomaly developed. This procedure would eliminate the observed 0.1° wobble and prevent increased wobble with later thruster firings. Two weeks later, on April 5, 1973, the radial thruster was fired continuously for 20 seconds. The slow change of spin speed after the firing showed that the moment of inertia was changing as a result of hydrazine redistribution. The existence of a bubble in the fuel line was thereby substantiated and a method of bubble removal demonstrated.

Bubbles have subsequently appeared in other INTELSAT IV spacecraft; in all cases, these bubbles have been removed by continuous firing of the radial thruster. While it is most probable that bubbles are generated during the initial loading, this mechanism seems improbable in certain cases; analysis of the origin of the bubbles is still proceeding.

Acknowledgments

This work was the joint effort of a number of individuals from different organizations at COMSAT. The early analysis and hypothesis of the bubble was done by Hakan Holm, in collaboration with Jeremiah Salvatore and Herbert Pass of the Hughes Aircraft Company. The analysis of the sun sensor data was done by Anthony J. Corio of COMSAT.

Reference

- [1] M. A. Vonnegut, "The INTELSAT IV Spacecraft, Positioning and Orientation Subsystem," *COMSAT Technical Review*, Vol. 2, No. 2, Fall 1972, pp. 360-365.

Translations of Abstracts in this Issue

Une station terrienne sans personnel pour communications par satellites

L. POLLACK et W. SONES

Sommaire

Les changements qui se sont produits dans les exigences des systèmes et les développements dans la technologie des microondes ont conduit à une nouvelle idée: une station terrienne pour communications par satellites conçue au fin de fonctionner sans personnel.

Les principaux facteurs qui ont conduit aux antennes toroïdales à faisceaux multiples (MBTA), qui représentent une partie intégrale des stations terriennes sans personnel (UET) furent: des tolérances de moins de $\pm 0,5^\circ$ pour la position orbitale des satellites, le groupage des satellites en 10° à 20° d'arc orbital pour servir les centres des stations terriennes et la nécessité où l'on se trouve de travailler avec deux satellites, ou plus, tout en répondant aux exigences des connections et en assurant la continuité des services.

L'antenne à réflecteur fixe est alimentée par des sources orientables associées à: plusieurs émetteurs de basse puissance refroidis à l'air et multiplexés par filtres; un récepteur à conversion de fréquence à large bande et à faible bruit, sans refroidissement et entièrement en état solide; un amplificateur à moyenne fréquence et un équipement de modulation avec circuits de microondes intégrés. Avec l'assurance d'une qualité garantie en cours d'installation, cette conception offre une grande fiabilité.

Ce document décrit les caractéristiques principales de la conception d'ensemble et le fonctionnement de la station.